THE GENERATION AND EXPERIMENTAL STUDY OF MICROSCALE DROPLETS IN DROP-ON-DEMAND INKJET PRINTING

LI ERQIANG
(B.Eng., Xi'an Jiaotong University)

A THESIS SUBMITTED

FOR THE DEGREE OF DOCTOR OF PHILOSOPHY
DEPARTMENT OF MECHANICAL ENGINEERING
NATIONAL UNIVERSITY OF SINGAPORE

2010

Acknowledgements

First I would like to express my deepest appreciation to my advisor Professor Jerry Fuh Ying Hsi for his guidance and supervision throughout this project. This thesis would never been written without his continuous support and encouragement. He is very helpful, generous and is very considerate of and patient with his students. Becoming his student is my great honor.

I most sincerely thank my co-advisor Professor Wong Yoke San, for his constructive guidance and valuable time on my research. He is very kind, helpful, considerate, enthusiastic and productive. Furthermore, his hands-on approaches for research will have a lasting impact on my career in the future.

I would like to express my deepest appreciation to my co-advisor Professor Sigurdur Tryggvi Thoroddsen, for his continuous support, endless encourage, constructive guidance and supervision throughout this project. I have learned from him not only knowledge but also rigorous attitude towards scientific research.

I am very grateful to Associate Professor Loh Han Tong for his concern and suggestions in project related issues.

My sincere thanks go to Dr. Zhou Jinxin for his support and enthusiastic encouragement. During nearly the whole process of my research, he gave me a lot of advice and help. My sincere gratitude should also go to Dr. Sun Jie, Dr. Wang Furong, Dr. Feng Wei, Miss. Xu Qian, Miss. Wu Yaqun, Mr. Thian Chen Hai Stanley, Mr. Zhang Fenghua, Mr. Wang Shouhua, Mr. Ng Jinh Hao and Mr. Yang Lei for their assistance and knowledge in carrying out the project.

I had the privilege of working with exceptional students from the department, including Chang Lei, Li Jinlan, Tan Wei Qiang Emil, Wu Yong Hao Benjamin, Tan Eng Khoon, Ng Lai Xing, Shareen Chan and Lim Wei Ren Farand. They have all worked together with me and given me great help in the development of my research project. They are also my friends and made my graduate study in Singapore colorful and memorable.

My sincere gratitude should also go to the members of the Fluid Mechanics Lab, Advanced Manufacturing Lab (AML), Workshop 2 (WS2), Impact Mechanics Lab, Tissue Engineering Lab, Cellular and Molecular Bioengineering Lab, and the various Laboratories and Workshops of IMRE and NUS and their technical staff for their support and technical expertise in overcoming the many difficulties encountered during the course of the project.

Lastly, but most important, I would like to thank my grandparent, my parents, my brother, and my girl friend Li Xinxiu (all I can say is that I have the best girl I could ever hope to have), for their unconditional love and support. They always believe in me and have done all they can to support my choices.

Table of Contents

Summary

For environmental conservation and the realization of a sustainable society, it is necessary that industrial manufacturing processes undergo a transformation with reduction of environmental impact. From this viewpoint, additive manufacturing technologies have attracted considerable attention because they have the potential to greatly reduce ecological footprints as well as the energy consumed in manufacturing. Inkjet printing is one of the most successful additive manufacturing technologies. It develops at a rapid pace and has been expanded from conventional graphic printing to various new applications, such as organ printing, displays, integrated circuits (ICs), optical devices, MEMS and drug delivery. Accordingly, the dispensed liquids have been expanded from the conventional pigmented ink (or standard dye-based ink) to polymers, gels, cell ink or other materials which often have higher viscosities or even contain large particles or cells. Consequently, the traditional inkjet printer designed for graphic printing is unable to fulfill the new challenges, one of which is to dispense fluids of very high viscosities. For most of the commercial inkjet printheads, only liquids with viscosities lower than 20 cps can be consistently dispensed. Fluids with even higher viscosities have to be diluted before printing or warmed up during the printing, which will adversely affect the properties of the liquids. Another challenge is raised by nozzle clogging. Fluids containing particles, or cells, can easily block the nozzle orifice, resulting in time-consuming nozzle cleaning or even damage of the entire conventional printhead. To solve the problem, the easiest way is to use a nozzle with a bigger orifice, as bigger orifices are less likely to clog. However,

this is often not desirable in inkjet printing as bigger nozzles result in bigger droplets and lower printing resolution. The poor printability and nozzle clogging may result in unreliable or failed dispensing when using the traditional inkjet printhead design for complex liquids.

In this research, a PET/PTFE-based piezoelectric DOD inkjet printhead with an interchangeable nozzle design was proposed and fabricated by the authors. The printhead chamber is made of PET or Teflon tube, which is much softer than the commonly used glass tube. The ejecting capacity of this novel printhead was compared with commercial printheads, and found to have superior performance and versatility. Our printhead succeeded in dispensing aqueous glycerin solutions with viscosity as high as 100 cps, while the corresponding commercial printheads could only dispense liquids with viscosities lower than 20 cps. PTFE-based printhead provides excellent anti-corrosive property when strongly corrosive inks are involved. The interchangeable nozzle design largely alleviates the difficulty in cleaning of clogged nozzles and greatly reduces the occurrence of printhead damage. The effects of operating parameters, including voltage pulse amplitude, pulse width and jetting frequency, on droplet size and droplet velocity were characterized. The new printhead shows excellent repeatability.

The formation of fine jets during the piezoelectric drop-on-demand inkjet printing was investigated using ultra-high-speed video imaging. The speed of the jet could exceed 90 m/s, which was much higher than the general droplet velocity during inkjet printing. The diameters of the thinnest jets were of the

order of a few microns. The generation of such fine jets was studied over a wide range of viscosities, using 7 different concentrations of water-glycerin solutions. This jetting was associated with the collapse of an airpocket which was sucked into the nozzle during the printing. This occurred for longer expansion times for the piezo-element. Two types of jet were identified during the printing. The relationships between the speed of the fine-jet and other parameters like the diameter of the jet and the physical properties of the liquid, were also characterized. The study provides a possible way to improve inkjet printing resolution without reducing nozzle diameter.

The in-house-developed printhead was also used for cell printing. The study has demonstrated that piezoelectric DOD inkjet printing is able to successfully deliver L929 rat fibroblast cells through nozzles as small as 36 μm. There was no significant cell death when dispensing the cells through the 81 μm and the 119 μm nozzle, with the mean survival rates only reducing from 98% to 85%. This is in good agreement with the existing study, in which a commercial printer was used to print human fibroblast cells. When the orifice was reduced to 36 μm, the corresponding cell survival rates fell from 95% to 76% when the excitation pulse amplitude increased from 60 V to 130 V. These results indicate that the droplet ejection out of the nozzle has exerted large shear stresses on the cells and possibly disrupted the cell membrane and killed about 20% of the cells. Mean shear rate was estimated by combining the effects of droplet velocity and orifice diameter and was correlated with the cell survival rate. A large range of mean shear rates from 1.3×10^{4} s^{-1} to 9.2×10^{5} s^{-1} were generated and cell survival rates were found to be strongly affected by the

higher mean shear rates, especially when the shear rate exceeds 5×10^5 s^{-1}. The distribution of the number of cells within each droplet was also investigated. This was done to find out the minimal cell concentration in the medium, which is required to avoid the appearance of empty droplets, since droplets containing no cells may be detrimental to pattern printing. The distribution of cell numbers is found to have a binomial form, which consistent with a uniform distribution of cells inside the medium in the reservoir.

For pattern printing, L929 fibroblast cells were delivered by using a 60 μm nozzle. Printed cells successfully kept their patterns in the crosslinked gel made from 1.0% (w/v) alginate and 0.5% (w/v) calcium chloride. However, it was found that the cells failed to adhere to alginate. On the other hand, cells dispensed onto collagen gel were found to successfully maintain their viability, adhere to the gel, spread and proliferate, forming a denser pattern. However, unlike the crosslinked calcium-alginate which can immobilize cells quite rapidly, cell adhesion to collagen needs a relatively long time to get established. Therefore, some of the printed cells were slightly moved from their initial position when the sample was disturbed, by the addition of fresh medium or unintended shaking of the sample, which will reduce the resolution of the printing. The smallest nozzle, with orifice diameter of 36 μm, was not used for pattern printing, due to issues concerning the reliability of the printing process, as it can easily get clogged.

List of Tables

List of Figures

List of Symbols

f	Jetting frequency
c	Sound speed
v	Droplet velocity
d	Droplet diameter
μ	Dynamic viscosity of liquid
σ	Surface tension of liquid
ρ	Density of fluid
d_{31}	Piezoelectric strain constant
ν	Kinematic viscosity of liquid
N	Average cell concentration per unit volume
V_d	Droplet volume
N_d	Average number of cells per droplet volume
U_i	Droplet impact velocity
θ	Contact angle
F^σ	Surface tension force at the liquid-gas interface

1. INTRODUCTION

1.1 Background

For environmental conservation and the realization of a sustainable society, it is necessary that industrial manufacturing processes undergo a transformation with reduction of environmental impact. From this viewpoint, additive manufacturing technologies have attracted considerable attention because they have the potential to greatly reduce ecological footprints as well as the energy consumed in manufacturing. An additive manufacturing process is one whereby a product is made by adding successive layers of material onto a substrate. Examples are electron beam melting, laser sintering, aerosol jet printing and inkjet printing. Rapid Prototyping (RP) is the name generally given to the various additive processes. Besides the above mentioned advantage of environmental benignity, additive manufacturing process is also a low cost production method for reducing the material wastage, especially for the specialty polymers and precious metals.

Drop-on-Demand Inkjet Printing (DOD IJP) is an additive manufacturing process, a data-driven process that patterns directly onto the substrate with ejected droplets. It is capable of precise deposition of picoliter volumes (down to 2 pL, 15 μm in diameter) of liquids at high speed (up to 60 kHz [1]) and accuracy (< 5 μm) on a target surface, even onto non-planar surface. Due to its advantages in high resolution, automation, low cost, non-contact, flexible, environmental benignity and ease of material handling, the application of

DOD inkjet printing technology has been expanded from conventional graphic printing to new areas, such as organ printing, displays, integrated circuits (ICs), solar cells, memory devices, optical devices, MEMS and drug delivery.

One of the aims of tissue engineering is to position cells into 3-D structures and arrange them in a specific pattern. The generation of such structures forms the basis of tissue regeneration and possibly, organ building [2]. Inkjet printing is a suitable candidate for this purpose. It has been used successfully in a similar manner for automated rapid prototyping technology which precisely positions droplets onto a substrate. To date, many different cell types have been printed successfully by different printing methods and their viability has been verified [3-10]. The power of inkjet printing lies in its ability to deliver picoliter volumes of materials at high speed and accuracy on a target interface (probably non-planar surface), and to deliver active substances to a developing structure in timing sequence. By using different cell types as different bio-inks, and delivering them to exact positions to mimic tissue structures of the original tissue, inkjet printing offers a possible solution for building whole structures such as bone, cornea, ligament, cartilage etc, to solve the organ transplantation crisis.

With improving living standards, requirements for low-power, fast response time, lightweight, wide viewing angle and portable communication devices are rising and galvanizing the display industry to loot at a new technology known as polymer light-emitting-diode (PLED) display. Monochromatic displays can be prepared by spin-coating; however, to fabricate a full-color PLED flat-

panel display (FPD), a micro-patterned array of red, green, and blue PLED subpixels must be fabricated on the display backplane. This requires the three differently colored electroluminescent polymers to be deposited onto the exact position of the substrate [11, 12]. The spin-coating technique is clearly not suitable for such displays. Subtractive patterning, such as the photolithographic technique, is also not appropriate for such task due to its high cost, and complicated process as a multi-stage approach. Among all the manufacturing processes, inkjet printing has been proved to be the most promise technique for full-color PLED displays fabrication, and PLED devices have been demonstrated by plenty of companies such as Seiko-Epson, Philips, CDT, DuPont, Samsung SDI, TM (Toshiba-Matsushita) Display and Delta.

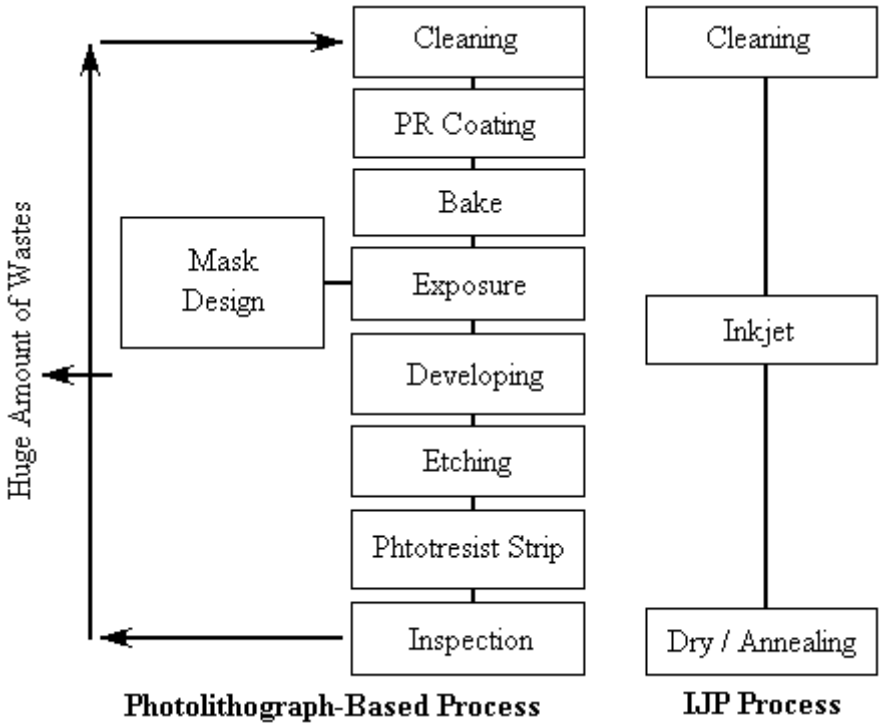

Fig. 1.1: A typical flow diagram of photolithograph-based and inkjet printing based process.

Applying inkjet printing technology to electronics patterning is quite straightforward, as material can be deposited on-demand, which reduces material wastage. It is also well-known that a conventional silicon patterning

process usually involves photolithography and etching processes (either reactive ion etching or anisotropic wet chemical etching), which consist of many sub-processes and lead to long processing time and high cost, as shown in Fig. 1.1; all these complicated processes are avoided in inkjet printing as it is a non-lithographic patterning method. Besides saving the cost of lithography masks and materials, DOD inkjet printing also has many other advantages. Firstly, as a low temperature process, micro-patterning process can be even performed on paper or plastics, which makes it well suited to roll-to-roll fabrication and makes it especially attractive for fabricating large-area, ultra-low cost electronic circuits on flexible substrates [13, 14, 15]. Secondly, applications of the above photolithographic patterning and etching processes to polymer multilayer structures is difficult because of the plasma-induced degradation of electroactive polymers and the lack of suitable anisotropic etching techniques for polymers [16]. However, inkjet printing can handle a wide range of materials including solution-based materials, suspended nano-particles and polymers; it also allows the use of inviscid ink without added binders [17]. This feature makes it a possible technique for low-cost fabrication of solution-processible polymer field-effect electronics devices [18]. Thirdly, inkjet printing is a data-driven process that can directly transfer computer-aided designs into device patterns, which can greatly save the process time and accommodate customization. To conclude, electronics fabricated by direct inkjet printing of functional electronic materials has gained significant interest as an alternative to conventional silicon integrated circuit (IC) process.

1.2 Challenges

As discussed in above section, because of its unique advantages, DOD inkjet printing has emerged as an attractive patterning technique for a variety of new areas in the last two decades. Accordingly, the dispensed liquids have been expanded from the conventional pigmented ink (or standard dye-based ink) to polymers, gels, cell ink or other materials which often have higher viscosities or even contain large particles or cells. For simplicity, the word "ink" is still used to represent the liquid to be dispensed. Ink viscosity is the most crucial parameter which will affect printing. When the actuator is activated, energy goes into kinetic energy, viscous flow and surface tension of the free-surface flow. Viscous dissipation causes partial energy loss in the printhead. As a result, ink viscosity must be low enough to ensure the success of droplet dispensing. For most of the commercial inkjet printheads supplied by companies like Microdrop, Microfab, Dimatix and XAAR, only liquids with viscosities lower than 20 cps [12] can be consistently dispensed. Fluids with even higher viscosities have to be diluted before printing or warmed up during the printing, which will either adversely affect the properties of the liquids or lead to long processing times in printing.

Another major concern in inkjet printhead design is the "first drop problem", which is the clogging of nozzles by dried ink at the nozzle tip. Especially, when inkjet printing is applied to the above new areas, inks containing particles, or even cells, can easily block the nozzle orifice, resulting in time-consuming nozzle cleaning or even damage of the entire printhead. To solve

the problem, the easiest way is to use a nozzle with a bigger orifice, as bigger orifices are less likely to clog. However, this is often not desirable in inkjet printing as bigger nozzles result in bigger droplets and lower printing resolution. Especially, for applications such as fabricating organic transistor circuits or MEMS devices, the resolution of current inkjet printing is still too low (normally limited to 20 μm by droplet size and the spreading of the droplet on the substrate [19, 20]) and droplet size needs to be further reduced. Besides reducing the nozzle size, when using piezoelectric-based DOD inkjet printhead, it has been proved that smaller droplets could be produced by judiciously controlling the piezoelectric parameters [21, 24, 25]. These studies reveal a possible way to alleviate the nozzle clogging problem without sacrificing printing resolution. However, these methods only work over a limited range of Ohnesorge numbers and their effects are also limited: the diameter of the dispensed droplets can be only reduced to a maximum of 60 % of the orifice diameter. Consequently, reducing nozzle size seems the only efficient way to reduce droplet size, to fulfill the resolution requirement by the new applications of inkjet printing, such as fabrication of organic transistor circuits or MEMS devices. As can be foreseen, the clogging problem would become even worse during printing.

The poor printability and nozzle clogging may result in unreliable or even failed dispensing and thus impose tremendous challenges on the printhead design and printing process.

1.3 Objectives

Main objectives of this research are:

- To study drop generation conditions and ejection nozzle requirements in DOD inkjet printing. Two methods for fabricating microscale inkjet nozzles, based on micro-pipette fabrication technology and silicon micro-machined technology, will be proposed and tested.

- To design and fabricate a new type of PET/PTFE-based piezoelectric squeeze mode inkjet printhead. The new printhead should have the ability to dispense liquids with much higher viscosities (> 100 cps). The new printhead should also have interchangeable nozzle design, so the clogged nozzle can be easily removed and cleaned. Especially, the damaged nozzle can be easily changed, avoiding the destruction of the whole printhead assembly.

- To characterize the in-house-developed printhead: investigating the printability and the printing repeatability of the new printhead by comparing it with the conventional glass-based printheads; investigating the effects of printing parameters (pulse amplitude, pulse width, nozzle size, jetting frequency etc.) on droplet velocity and droplet diameter; optimizing the printhead design to improve the maximum jetting frequency.

- To investigate the efficiency of three different methodologies on generation of microscale droplets: reducing the droplet size by directly reducing the nozzle size down to 1 to 2 microns; carefully controlling the piezoelectric waveforms to generate droplets smaller than the nozzle size; generating much smaller droplets or fine jet by combining DOD inkjet printing with the conventional electrospinning technique.

- To carry out the cell printing experiments. Investigate the survivability of the cells subjected to the large stresses during the printing process. Fibroblast cells will be printed onto different substrates (alginate, collagen etc) and cultured over a period of days to verify their long-term viability. Pattern printing, cell agglomeration in the cell ink, cell number in each printed droplet and cell location inside the dried-droplet will also be studied.

1.4 Organization

The layout of this thesis is organized as follows:

- Chapter 2 presents an essential introductory knowledge on the inkjet printing technology, which includes the classification of different DOD inkjet printing methods and their work principles, conditions for dispensing a droplet from an inkjet nozzle, different ejection nozzle fabrication methods and different criteria for evaluating printing

quality. It also presents the state-of-the-art work in the areas of generating ultra-small droplets and cell printing.

- Based on our theoretical study, a PET/PTFE-based piezoelectric squeeze-mode DOD inkjet printhead with interchangeable nozzles, has been designed and fabricated, which will be discussed in Chapter 3. The detailed printhead chamber design and the ejection nozzle fabrication process will be given. The advantages of the in-house-developed printhead, as well as its characterizations will also be discussed in detailed.

- In Chapter 4, the fine jet generated in DOD inkjet printing will also be systematically studied, with the help of an ultra-high-speed, high space-resolution video camera system.

- Chapter 5 presents the results of the cell printing experiments. The effects of shear stresses on cell survivability, the long-term viability of the cells printed onto different substrates (coated by alginate or collagen), and the results of pattern printing will all be discussed in detailed.

- Chapter 7 outlines future working directions that could further improve the printhead resolution and the maximum jetting frequency, based on the theoretical and experimental work presented in this dissertation.

2. LITERATURE REVIEW

2.1 Introduction to Inkjet Printing

Inkjet printing is a contact-free dot-matrix printing technique in which an image is created by directly jetting ink droplets onto specific locations on a substrate [26]. The concept of inkjet printing can trace its history to the 19th century and the inkjet printing technology was first developed in the early 1950s. Inkjet printers that capable of reproducing digital images generated by computers were developed in the late 1970s, mainly by Hewlett-Packard, Epson and Canon. The booming of the personal computer industry in 1980s has led to a substantial growth of the printer market and nowadays personal printer is present in almost every office and home. Inkjet printing technology is developing at a rapid pace. It has been expanded from conventional graphic printing to various applications, such as organ printing, displays, integrated circuits (ICs), optical devices, MEMS and drug delivery.

2.1.1 Classification of Inkjet Printing Techniques

Inkjet printing technology has been developed in a wide variety of ways. In Fig. 2.1, the inkjet tree structure shows a layout for most of the better known inkjet printing techniques and some of the corresponding adopters. As can be seen, there are two categories of inkjet printing technology: Continuous inkjet printing and Drop-on-Demand inkjet printing.

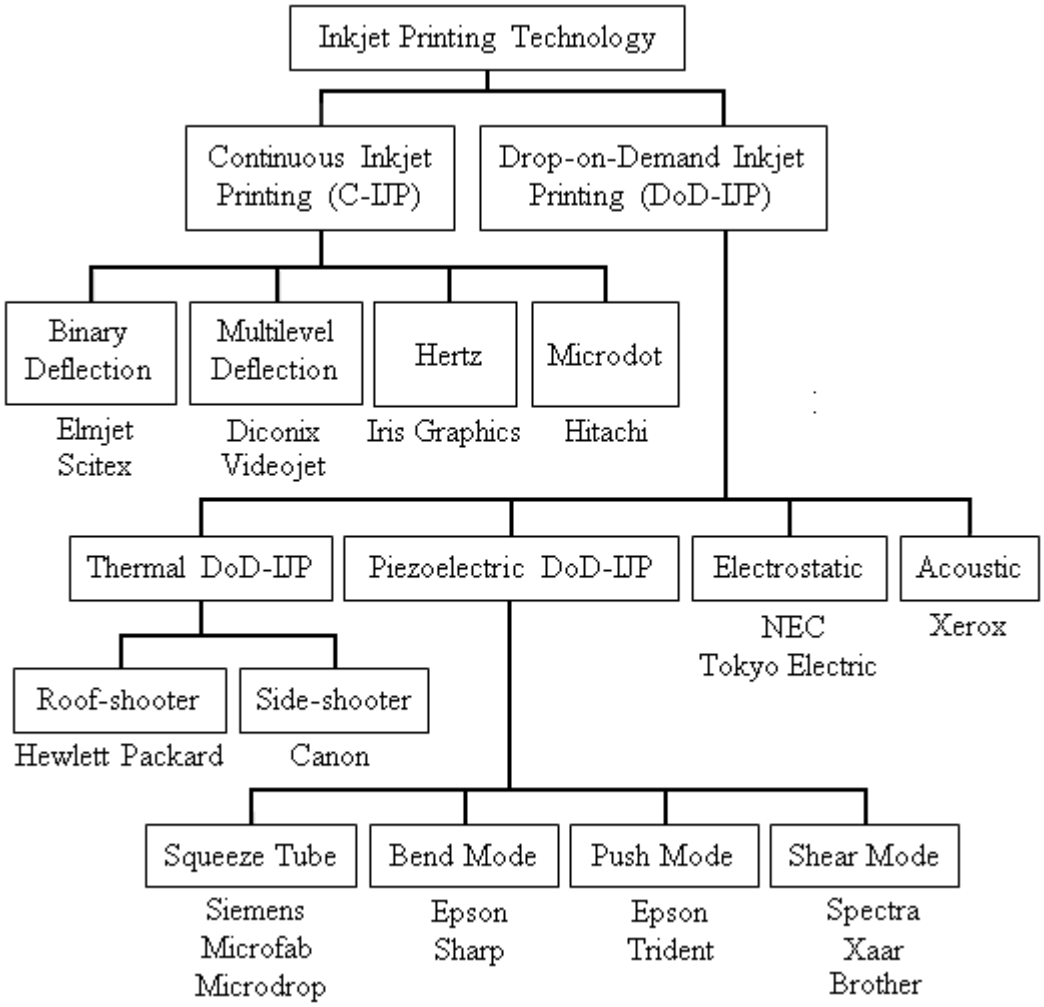

Fig. 2.1: Layout of the different inkjet printing technologies.

2.1.1.1 Continuous Inkjet Printing

The earliest inkjet devices operated in a continuous mode. The idea was first patented by Lord Kelvin in 1867 and the first commercial model was introduced by Siemens in 1951. In this technique, a continuous jet of the liquid ink is formed by applying pressure to the ink chamber with a small orifice at one end. A fluid jet is inherently unstable and will break up into droplets, which is entirely a consequence of the surface tension effects. This phenomenon was firstly noted by Savart in 1833 and described mathematically by Lord Rayleigh [27]. If surface tension force is the only force acting on the

free surface of the jet, it will break up into droplets of varying size and velocity; when a periodic perturbation of an appropriate frequency is applied to the liquid, typically using a piezoelectric transducer, the jet will break up into droplets of uniform size and velocity. The droplets separate from the jet in the presence of a properly-controlled electrostatic field which generated by an electrode that surrounds the region where break-off occurs. As a result, an electric charge can be induced on the drops selectively. Subsequently, when the droplets pass through another electric filed, the charged droplets are directed to their desired location on the substrate to form an image; those uncharged droplets will drift into a catcher for recirculation. Continuous inkjet can be classified into binary deflection or multilevel deflection according to the drop deflection methodology, as can be seen in Fig. 2.1.

Fig. 2.2 and Fig. 2.3 schematically show streams of droplets generated from binary deflection and multilevel deflection mode continuous inkjet, respectively. A piezoelectric transducer is used to generate a periodic perturbation onto the jet. In the both modes, the charged droplets are directed to deposit onto the substrate, while in the multilevel, the charged droplets are allowed to deposit onto the substrate at different levels. By using the multilevel deflection system, a small image swath can be created by a single nozzle. Fig. 2.4 shows droplets generated by a continuous inkjet system with multi-nozzles. Continuous inkjet is widely used in the industrial coding, marking, and labeling markets [26]. Extensive studies, both theoretical and experimental, have been conducted to analysis different continuous inkjet systems, especially the process of disturbance growth on the jet stream which

leads to droplet formation. Typically the droplets generated by a continuous inkjet system have a diameter of approximately twice of the orifice diameter. Droplets sizes range from 20 μm to 500 μm can be generated at rates of up to 1 MHz by continuous inkjet.

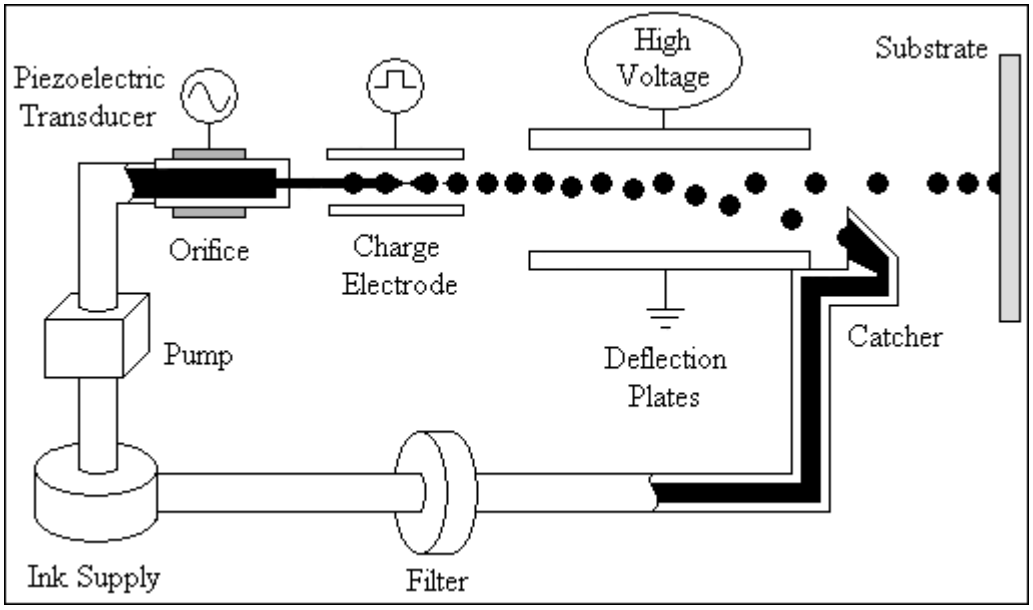

Fig. 2.2: A Binary-Deflection continuous inkjet system.

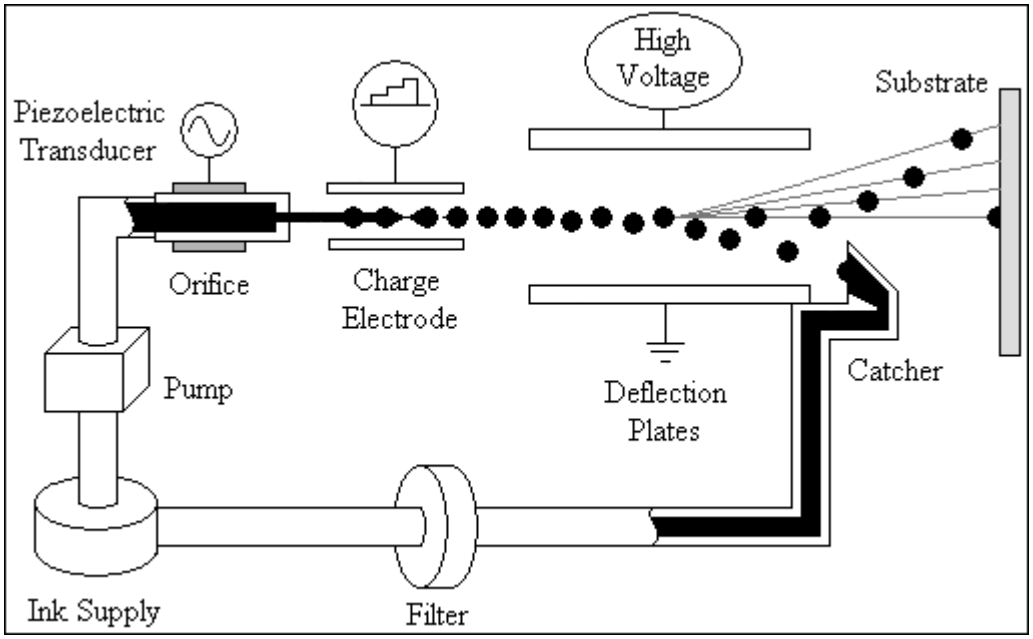

Fig. 2.3: A Multilevel-Deflection continuous inkjet system.

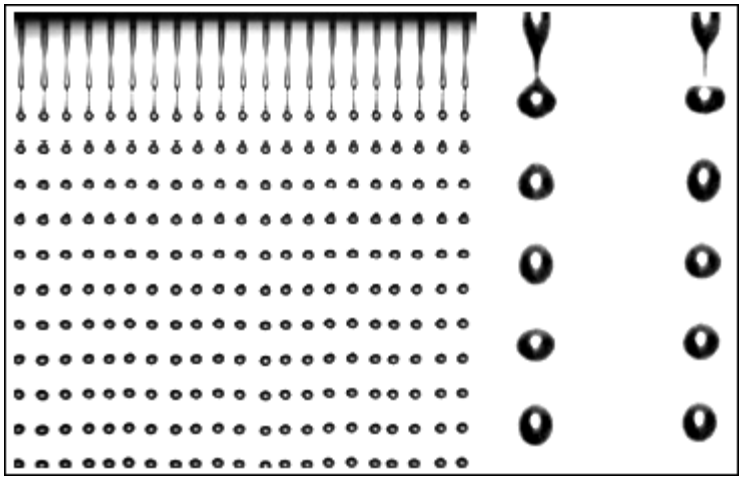

Fig. 2.4: Droplets generated from a continuous inkjet system with multi-nozzles.

The major advantage of continuous inkjet is that it can generate ink droplets with very high velocity, which can reach to 50 m/s. This feature allows for the usage of a relatively long distance between printhead and substrate. It also allows for rapid droplet formation rate, also known as high speed printing. Another advantage of continuous inkjet is no waste of ink, due to droplet recycling. Furthermore, since the jet is always in use, nozzle clogging can be avoided in continuous inkjet. Therefore volatile solvents such as alcohol and ketone can be employed to promote drying of droplets onto the substrate.

The major disadvantage of continuous inkjet is that the ink to be used must be electrically conducting, to ensure that ink droplets can be charged and directed to the desired location. Furthermore, due to ink recycling process, ink can be contaminated.

2.1.1.2 Drop-on-Demand Inkjet Printing

Drop-on-Demand inkjet systems were developed in the 1970s, when different actuation principles were utilized [28]. In this technique, ink droplets are

produced only when they are required. According to the mechanism used during the droplet formation process, DOD inkjet can be categorized into four major types: thermal mode, piezoelectric mode, electrostatic mode, and acoustic mode, as can be seen from Fig. 2.1. Most of the DOD systems in the market are using the thermal or the piezoelectric modes. Nevertheless, no matter which mode is used, the basic principles of all these different inkjet methods are similar: a transducer, normally a piezoelectric element or a thermal heater, generates a pressure pulse into the ink and forces a droplet out of the orifice, as schematically shown in Fig. 2.5. The only difference lies in that the way how this pressure pulse is generated.

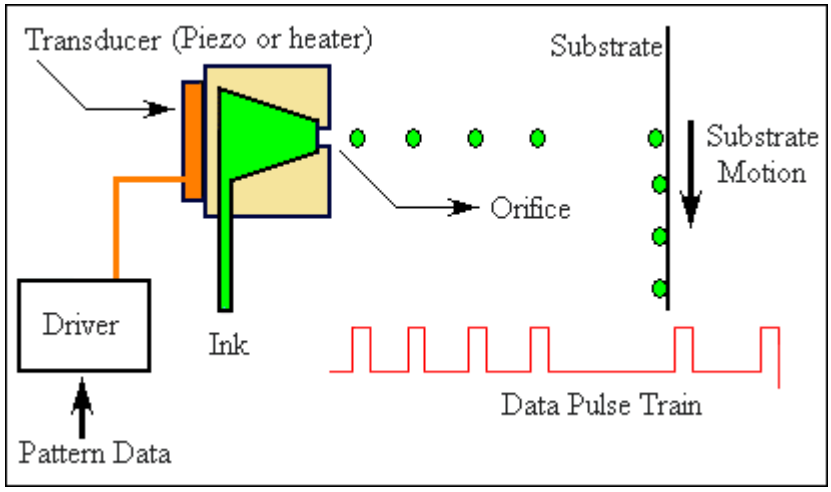

Fig. 2.5: Schematic of the DOD inkjet printing process.

The first thermal inkjet device was designed in 1977 by Canon engineer Ichiro Endo. In this technique, when a droplet is required, a current pulse of less than a few microseconds is produced and passes through a heating element located nearby the nozzle. Heat is transferred from the heater to the ink, causing a rapid vaporization of the ink to form a vapor bubble inside the ink chamber. As the ink chamber volume is fixed, this instantaneous expansion of bubble will cause a large pressure increase inside the chamber, propelling the ink out

of the nozzle. Simultaneously with the later bubble collapse, the pushed-out ink column will break off from the nozzle and form a droplet, flying to the substrate. The duration of the air bubble formation and collapse is less than 10 μs. Fig. 2.6 schematically shows the droplet formation process in a thermal inkjet chamber. As the bubble collapses, a vacuum is created. The ink then flow back into the chamber and recover to its equilibrium state, waiting the next round of jetting. According to its configuration, thermal inkjet device can be classified into a roof shooter or a side-shooter type. The orifice is located on top of the heating element in a roof-shooter thermal inkjet, while it is located on a side nearby the heating element, as shown in Fig. 2.7 and Fig. 2.8.

Most of the consumer inkjet printers designed by companies such as Hewlett-Packard and Canon are in thermal bubble type.

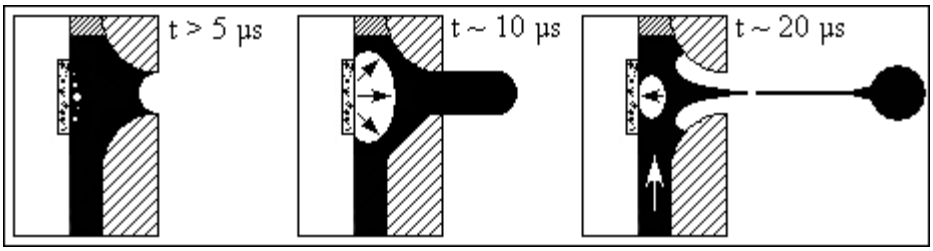

Fig. 2.6: Droplet formation process within the ink chamber of a thermal inkjet device.

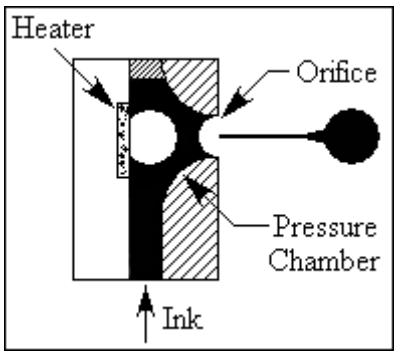

Fig. 2.7: Roof-shooter Thermal inkjet.

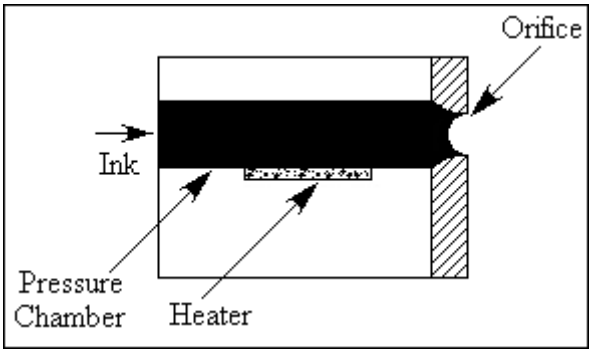

Fig. 2.8: Side-shooter Thermal inkjet.

The earliest piezoelectric inkjet printhead was designed by Zoltan in 1972. In this technique, when a droplet is required, an electric pulse will be applied to a piezoelectric element located behind the nozzle. Then the piezoelectric element changes its shape, causing a pressure pulse inside the ink that propelling a droplet from the nozzle. Depending on the deformation method of the piezoelectric element used in the device, piezoelectric inkjet printing can be classified into four categories: squeeze mode, bend mode, push mode and shear mode.

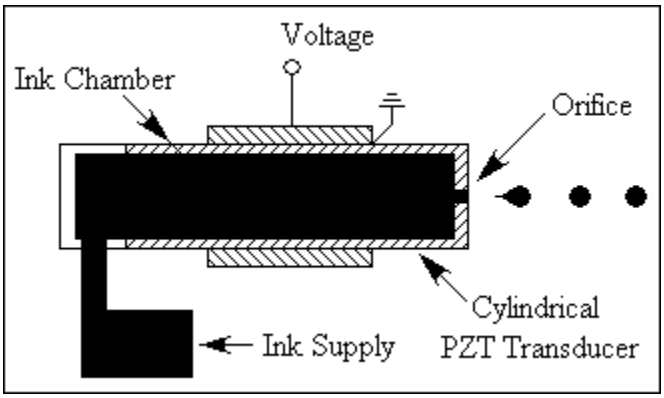

Fig. 2.9: Schematic of the squeeze-mode inkjet.

In squeeze mode piezoelectric inkjet, a thin piezoelectric tube is tightly attached onto a glass tube which with an orifice at one end, as shown in Fig. 2.9. The piezoelectric tube is radially polarized and is with electrodes on its outer and inner surfaces. When a droplet is desired, an electrical pulse will be

applied to the piezoelectric transducer, the polarity is selected to cause a contraction of the transducer. As a result, the glass tube as well as the ink will also be squeezed, and a droplet of ink will be ejected from the nozzle. Squeeze mode piezoelectric inkjet is implemented by companies, such as Siemens, Microdrop and MicroFab.

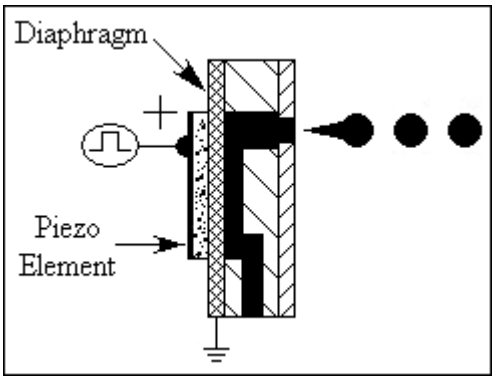

Fig. 2.10: Schematic of the bend-mode inkjet.

Fig. 2.10 schematically shows a piezoelectric actuator operating in bend mode. The device consists of an ink chamber with one side of it formed by a conductive diaphragm. A piezoelectric plate is tightly bonded to the diaphragm. When an electric pulse is applied, the piezoelectric element will contract in the radial direction, causing the diaphragm to flex inwardly into the ink chamber. This instantaneous motion of diaphragm will cause a large pressure increase inside the chamber and forces a droplet to be jetted from the orifice. Successful implementation of the bend mode piezoelectric inkjet can be found in printheads from companies, such as Epson and Sharp.

In a push mode piezoelectric design as shown in Fig. 2.11, when the piezoelectric rod expands in the horizontal direction, it pushes against the ink to eject a droplet from the orifice. Similar as in the bend mode, a thin

diaphragm is incorporated between the piezoelectric element and the ink, to prevent undesirable interaction between ink and the piezoelectric materials [29]. Push mode inkjet is implemented by companies, such as Epson and Trident.

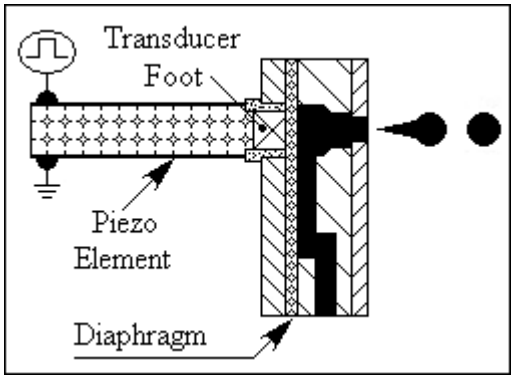

Fig. 2.11: Schematic of the push-mode inkjet.

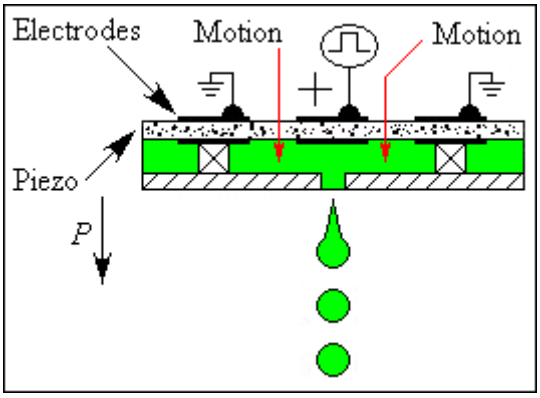

Fig. 2.12: Schematic of the shear-mode inkjet.

In all above 3 types of inkjet devices, the electric field generated between electrodes is parallel with the polarization of the piezoelectric plate. However, in the shear mode piezoelectric inkjet device, the imposed electric fields are orthogonal to the polarization direction of the piezoelectric element [30]. As schematically shown in Fig. 2.12, *P* denotes the polarization directions; the electrodes are mounted on the different locations of the piezoelectric plate. Therefore, the resulting shear motion of the transducer decreases the volume

of the ink chamber and pushes the ink, ejecting a droplet from the orifice. In shear mode piezoelectric inkjet, since the piezoelectric transducer directly forms one wall of the ink chamber, thus interaction between ink and piezoelectric materials is typically inevitable. It is also one of the key parameters of shear mode inkjet [26]. Successful implementation of the shear mode piezoelectric inkjet can be found in printheads from companies, such as Spectra and Xaar.

Most of the industrial inkjet printers and some of the consumer printers (those produced by Epson) are designed in piezoelectric type.

As can be seen from above discussion, the DOD actuation principle eliminates the need for droplet charging system, droplet deflection system and ink recycling system, thus the whole jetting device is more compact as compared to continuous inkjet device. Furthermore, wider range of inks can be used in DOD system as droplet charging is not required. Finally, since ink recirculation is avoided, thus ink contamination can be eliminated. Currently the majority of interest in inkjet printing is in the DOD methods.

The main disadvantage of DOD inkjet is the clogging of jet nozzles. Clogging may result from particles inside the ink, especially when pigment-based ink is used. Therefore, fine filters must be adopted upstream from the nozzle to prevent relatively big particles from reaching the nozzle. Furthermore, during the off working state, a solid deposit in the nozzle will form due to dry of ink, which will also lead to nozzle clogging. This is well known as the “first drop

problem" [31]. Another disadvantage of DOD inkjet is the lower droplet velocity. Typically DOD inkjet produce droplet with velocity lower than 10 m/s. Finally, DOD inkjet also has the advantage of low jetting speed. When a droplet is produced, acceleration of a mass of ink is always required, and this acceleration is created only by the actuating signal itself. Thus the droplet generation rate, as well as the printing speed is limited for DOD devices [28].

2.1.2 Advantages and Disadvantages of Inkjet Printing

As a Rapid Prototyping technique, inkjet is an additive manufacturing process. It ejects droplets only when required and hence reduces the material wastage. This implies a lower cost for the applications that requires expensive materials, which is sponsored for conservation and the realization of a sustainable society.

As compared to the traditional photolithography-based patterning process, which consists of many sub-processes and leads to long processing time and high cost, inkjet printing is much more compact. It avoids all those complicated sub-processes. Furthermore, it also saves the cost for lithography masks as well as the huge work for storing the hundreds of masks.

Inkjet printing is a data-driven direct-write process that can directly transfer Computer Aided Design (CAD) into device patterns, which can greatly save the process time and accommodate customization.

Inkjet printing offers the advantage of non-contact between the nozzle and the substrate, thus there is no mechanical wear on the printed sample. The possibility of cross-contamination is also reduced to a minimum.

To conclude, inkjet printing offers advantages in low cost, compact, automation, non-contact, environmental benignity and ease of material handling. It is a highly flexible technology that is able to accurately deposit small volumes of materials in almost any pattern.

There are two main disadvantages in inkjet printing. Firstly, the anisotropic nature of the inkjet process, due to the intrinsic pinhole nature of the deposited ink, results in the uneven surface roughness of the printed features [32]. Furthermore, this film non-uniformity can also be produced by the inevitable "coffee stain" effect, which arises from interaction of multiple effects of the solvent drying process [33, 34, 35]. This disadvantage in film uniformity does not exist in planar processing currently used in industry. Secondly, the resolution of inkjet method is limited by the dispensed droplets size. The minimum diameter of an inkjet droplet for a state of the art inkjet printhead is around 10 μm. The resulting printing resolution is enough for document printing use, but for nanotechnology use and many other industrial applications, such resolution is not good enough and a more precise inkjet device needs to be developed. Furthermore, the attainable feature size of a component fabricated by inkjet printing is also affected by how the droplet interacts with the substrate. Thus the impact behaviour of the droplets onto a substrate also needs to be carefully studied.

2.1.3 Printing System Evaluation

2.1.3.1 Print Resolution

Print resolution is normally measured by the number of individual dots that can be placed in a line within the span of 1 inch, namely DPI (dots per inch). It represents the spatial printing dot density and indicates the available printed fine-feature size. Obviously, print resolution is greatly influenced by the printed droplet volume. Smaller droplet size is able to provide a higher resolution printing. Another ongoing measurement of the resolution of inkjet printing is to use *drop pitch* in favor of metrication. Drop pitch gives the spacing between the two adjacent printing dots, and has a direct relationship with DPI as below:

$$Drop\ Pitch\ (\mu m) = \frac{25.4 \times 10^3}{DPI} \quad (2.1)$$

For example, a resolution of 720 DPI equals to a drop pitch of about 35 μm, indicating the inter-dot spacing of 35 μm. The resolution of drop-on-demand inkjet printing is usually in the range of 70-100 μm. However, the droplet size of commercial inkjet printers has been decreasing in order to achieve higher print resolution. Droplets of 8-30 picoliters in volume, i.e., droplet size about 25-40 μm, can be generated by commercial inkjet printheads [36, 37].

In practice, due to the changes in droplet size and shape during the droplet spreading and drying process, resolution of inkjet printing is also greatly influenced by surface energy of the substrate and the conditions of the ink solvent evaporation. By heating the substrate near or over the boiling point of the ink solvent, the liquid in the droplet can be evaporated immediately upon

contact and providing a finer resolution than one in printed at room temperature. However, it should be noted that by applying higher substrate temperature also increases the risk of the nozzle clogging at the printhead. Fundamental studies to obtain a constant width and shape of printed droplet, lines and areas on the solid substrate are not fully developed.

2.1.3.2 Jetting Frequency

As a manufacturing tool in industry, product throughput or productivity for inkjet printing systems is an important requirement, which is closely related to the droplet jetting process and printing speed. The productivity of an inkjet printhead is mainly determined by the jetting frequency, defined as the number of droplets jetted from a nozzle within a certain time. As such, high jetting frequency is desirable to attain high throughput for inkjet printing system.

On the other hand, print speed (the traveling distance in a unit time for a printhead or motion stage) has the relationship with jetting frequency and printing resolution (DPI), given as below:

$$Print\ Speed\ (mm/s) = \frac{Jetting\ Frequency\ (Hz)}{DPI/25.4} \tag{2.2}$$

This is shown that with the increase of the maximum jetting frequency, the maximum print speed of an inkjet printer will be increased accordingly, and thus extremely high throughput can be achieved. In 2009, Kyocera claimed the world's fastest inkjet printhead (KJ4B-JF06) with the jetting frequency up to 60 kHz [1]. With binary printing mode, each nozzle can eject 60,000 dots per second (40,000 dots per second in multiple-value printing); with the 2,656 nozzles per printhead, the printhead can print approximately 150 million dots

per second. Its corresponding print speed can reach 150 m/min at the ultra high resolution of 1200 × 1200 DPI.

Reliability is another important requirement for an inkjet printhead. For a reliable jetting, a subsequent droplet should not be dispensed until the meniscus oscillation from the previous droplet ejection cycle has sufficiently damped [38, 39]. As this damping takes time, the maximum jetting frequency is limited for the printhead. For a specific printhead, its maximum jetting frequency is mainly dependent on the printhead construction and its driving pulse signal [40]. Thus to obtain higher frequency jetting, a proper driving waveform needs to be designed such that residual meniscus oscillation can be effectively suppressed after each droplet ejection cycle. Typical drop-on-demand inkjet printheads generate droplets at rates in the range of 0.1 to 10 kHz.

2.1.3.3 Drop Positioning Error

Inkjet printing process usually requires accurate placement of ink droplets into predefined regions. Many of the error sources, affecting drop placement accuracy, are applied in the design process to improve the stability and precision of inkjet printing system [41]. Jet straightness and the location error of the jet onto the substrate are two critical factors producing drop positioning error. In Fig. 2.13, per nozzle straightness of the Spectra SX-128 inkjet printhead is measured as shown for example. Jet straightness error less than ±5 mrads, i.e. ±0.3°, shows a good performance in display applications [42].

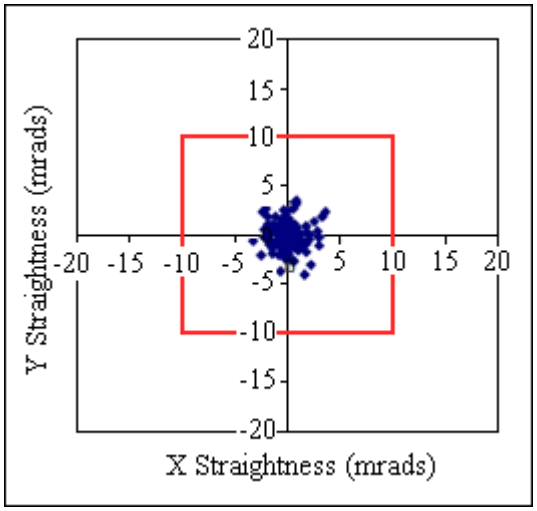

Fig. 2.13: Jet straightness error in both X and Y directions for Spectra SX-128 printhead [42].

The total positioning error is a function of jet straightness, machine inaccuracy and deviations in drop velocity, respectively [43]. Shimoda *et al.* [43] also demonstrated that positioning errors derived from jet straightness and mechanical inaccuracy can be compensated by a surface wetting effect caused by a droplet and a substrate. It is worth pointing out that the flatness of the precision substrate allows for small stand-off distances, which can reduce the effect of flight-trace errors.

2.1.3.4 Nozzle Hydrophobicity Treatment

To improve printing performance of the printhead, the ink has to be jetted in the form of complete droplets in a stable manner. Due to repeated droplet ejection, the surface of a nozzle is wetted by the ink. As such, a nozzle surface without proper hydrophobic treatment will be suffered from wetting. When such wetting takes place, the droplet being jetted may be accumulated together to form a lump on the nozzle surface, which will adversely affect the droplet formation process. Both the size and placement accuracy of the ink droplets

ejected are then influenced. And finally, the quality of the printing is deteriorated. Therefore, to guarantee a reliable inkjet printing, it is essential to provide effective hydrophobicity treatment on the nozzle surface of an inkjet printhead.

Fig. 2.14 shows total different inkjet printing behavior, for inkjet nozzles both with and without hydrophobic treatment. It can be clearly seen that without hydrophobic treatment, the jetted droplets are likely to accumulate on the nozzle surface, which will deteriorate the printing or even totally stop the printing.

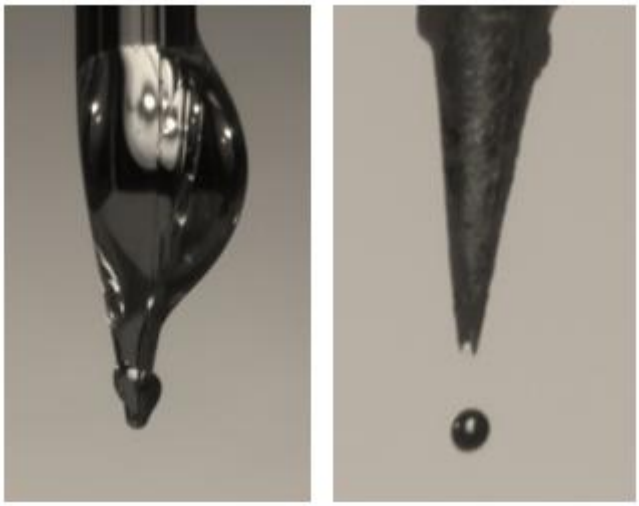

Fig. 2.14: Two nozzles to show the effects of hydrophobic treatment. (a). Nozzle without hydrophobic treatment. (b). Nozzle with hydrophobic treatment.

2.1.3.5 Inkjet-Printed Droplet Feature after Drying

Inkjet printing onto a nonabsorbent hard substrate is quite different from printing onto absorbent paper due to the complex wetting and drying processes. The shape or surface morphology of droplets and formed patterns are greatly influenced by surface energy of the substrate and the ink solvent evaporation

process. The evaporation can be controlled by changing drying environment such as substrate temperature, vapor pressure, etc. Generally, a circular droplet on the solid surface evaporates from the boundary and flows outward. This capillary flow tends to carry most of the dispersed materials to the boundary, a phenomenon well-known as the coffee-stain effect [34]. It should be noted that fundamental studies to obtain a constant width and shape of printed droplets, lines and even areas on the solid substrate are not fully developed. In practice, a considerable variety of the conditions of substrate surface and drop drying can produce various dried droplet patterns. They are introduced in the following sections.

- **Influence of Substrate Surface Wettability**

Surface wettability of the substrate has a great influence on the printed droplet feature after drying. Fig. 2.15 shows different shapes of printed droplets after the ink solvent has evaporated, for both hydrophobic and hydrophilic substrate surfaces [44]. On the contrary, the hydrophobic surface constrains the spread of the droplet and gives a smaller drying droplet in diameter without the coffee-stain effect.

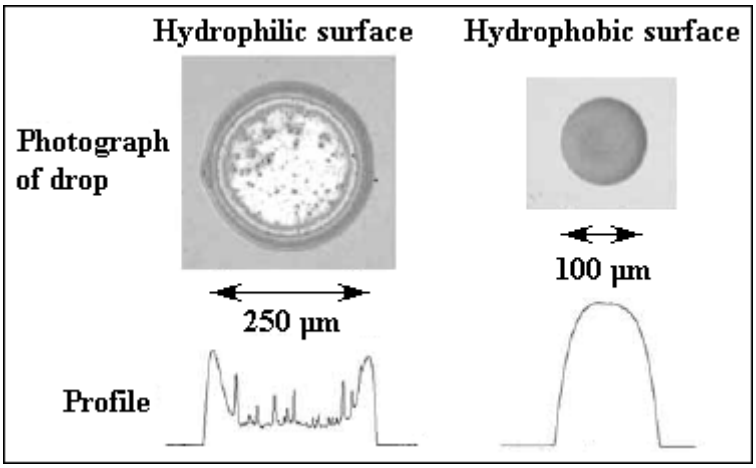

Fig. 2.15: Image showing profiles of dried droplets printed on hydrophobic and hydrophilic surfaces [44].

- **Influence of Drying Temperature**

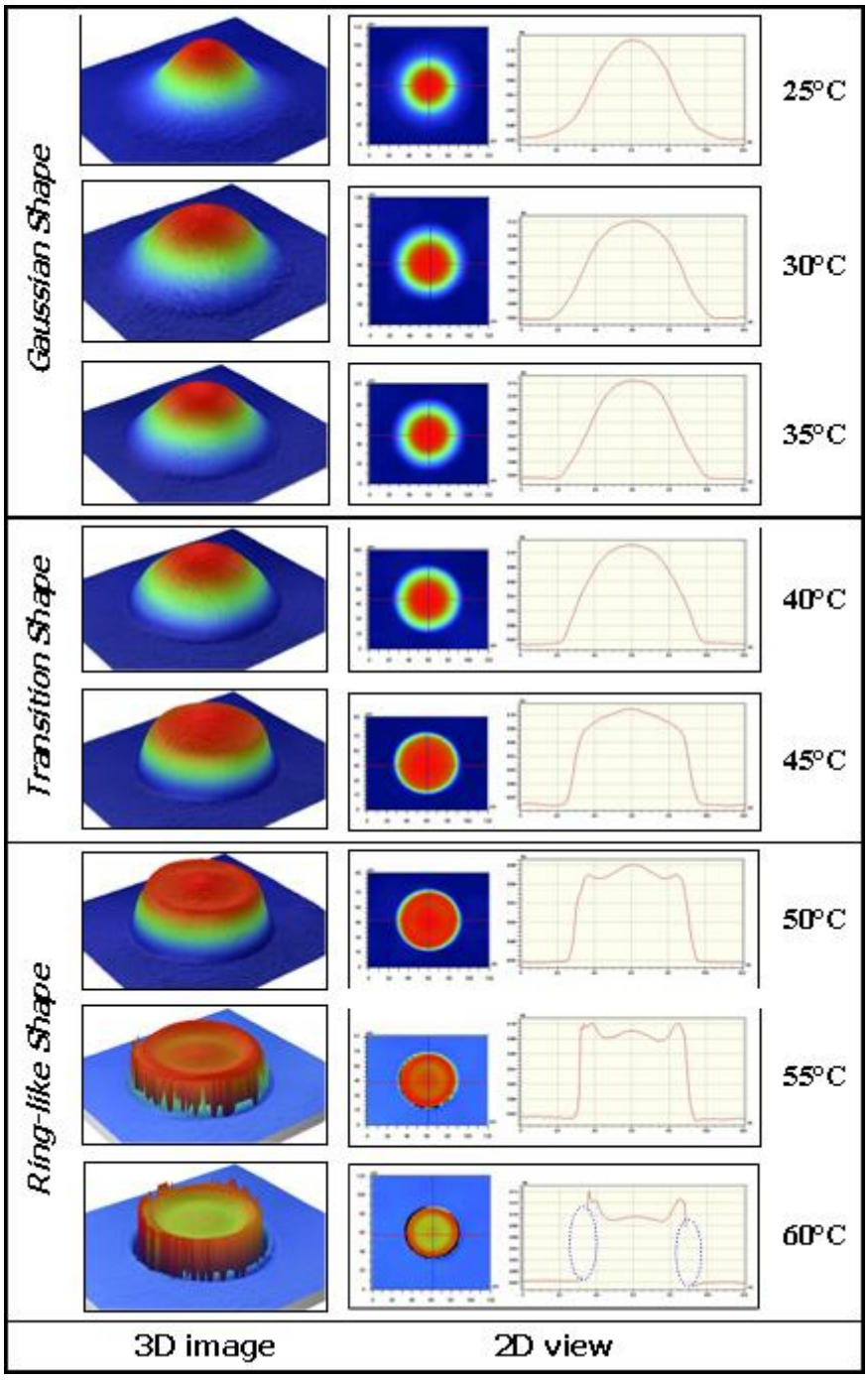

Fig. 2.16: Distinct dried droplet patterns under different temperature [45].

For super fine droplets such as ≤ 10 pl, the drying behavior of the droplets is extremely sensitive to the substrate temperature. Under different range of temperatures, printed droplet may achieve different dried patterns. Representative images of dried droplet 3D profile and 2D cross-sectional

profile through their center are shown in Fig. 2.16 [45], wherein dried profile of inkjet printed droplets under different substrate temperatures from 25 ℃ to 60 ℃ is characterized in order to obtain some reference information on making a uniform thin film.

Dried droplet profiles that are achievable are categorized into three types: Gaussian shape, transition shape and ring-like shape corresponding to low temperatures (< 40 ℃), medium temperatures and high temperatures (> 50 ℃), respectively [45]. At lower temperatures between 25 ℃ to 35 ℃, droplets finished their spreading stages before drying. Hence, the profiles obtained are of Gaussian shapes. At temperatures between 40 ℃ to 45 ℃, a change occurs in shape of the dried profiles. This could be due to the higher evaporation rates that prevented the droplet from spreading fully before it dried. At higher temperatures above 50 ℃, droplets are dried immediately upon impact before droplet spreading can occur. Therefore, droplets splash and simply solidify on impact so as to form a ring-like structure.

2.1.3.6 Inkjet-Printed Line Morphology

Ideally, inkjet-printed straight lines would be smooth and even. But sometimes it is difficult to fulfill all these features (straight, smooth and even) concurrently. A few different behaviors come out when examining inkjet-printed line formation under the various conditions such as droplet spacing, droplet frequency, and substrate temperature. Fig. 2.17 shows five typical line

morphologies [46]. They can be labeled respectively as individual drops, a scalloped line, a uniform line, a bulging line, and stacked coins.

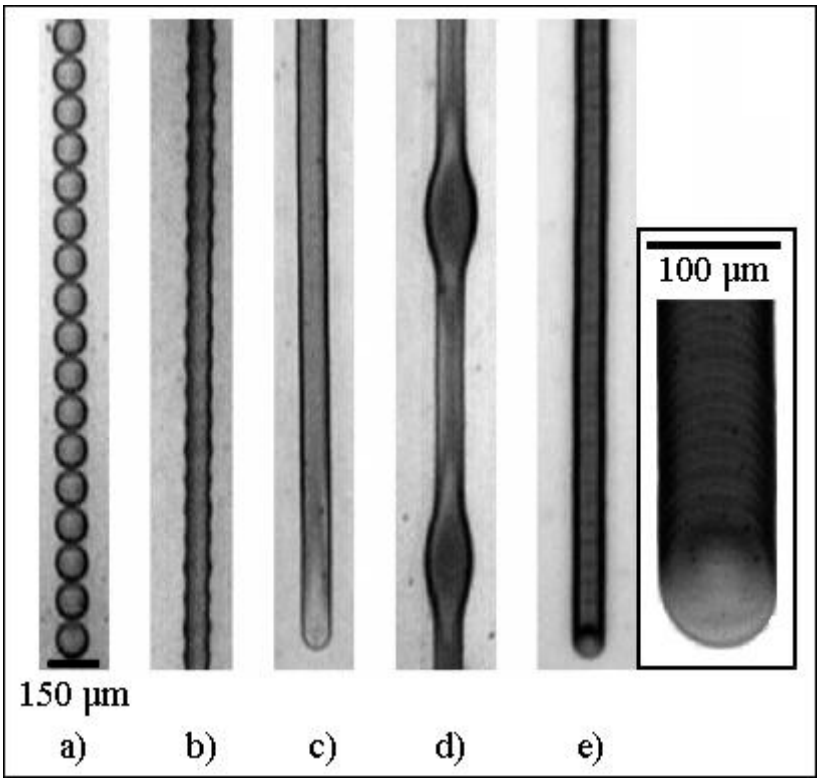

Fig. 2.17: Examples of five typical inkjet-printed line morphologies. (a). Individual droplets. (b). Scalloped line. (c). Uniform line. (d). Bulging line. (e). Stacked coins. Droplet spacing decreases from left to right [46].

In the case of Fig. 2.17(c), Smith and Shin *et al.* [47] provided a calculation to estimate the width of the printed line:

$$w = \sqrt{\frac{\frac{\pi d^3}{6(L/N)}}{\frac{\theta}{4sin^2\theta} - \frac{\cos\theta}{4\sin\theta}}} \tag{2.3}$$

where d is the droplet diameter, w is the line width, θ is the contact angle, N is the number of droplets printed for a line length L.

2.2 Squeeze Mode Piezo-Driven Printhead

As have been discussed in Section 2.1.1.2, there are four types of piezoelectric drop-on-demand inkjet: squeeze mode, bend mode, push mode and shear mode. This research is focused on squeeze mode piezo-driven DOD inkjet printing.

2.2.1 Theory of Droplet Formation

2.2.1.1 Principle of Squeeze Mode Piezo-Driven Printhead

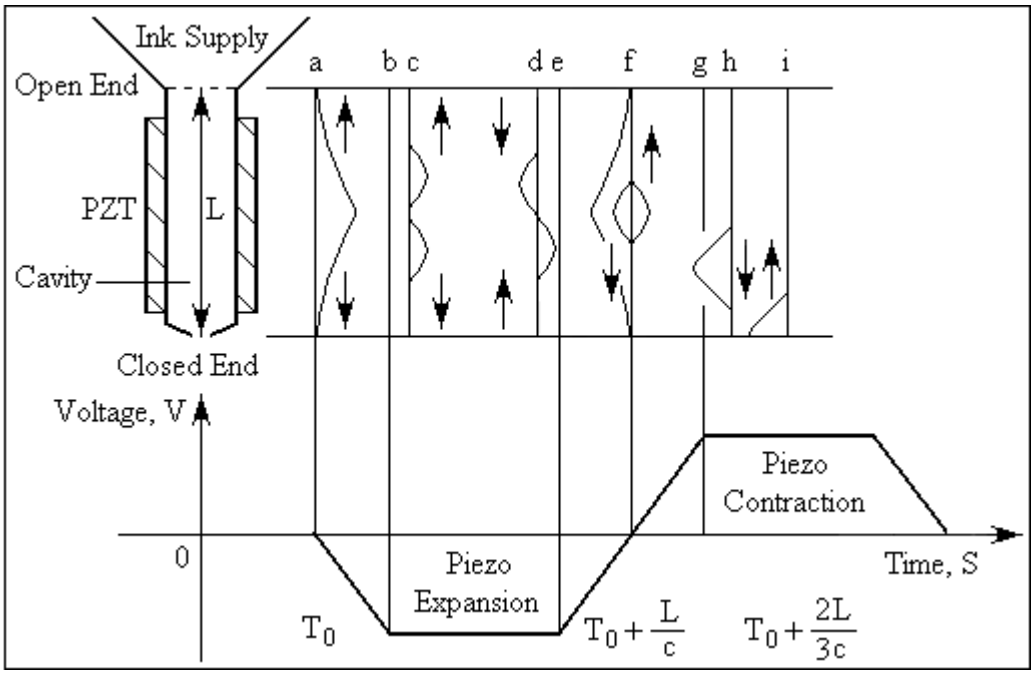

Fig. 2.18: Schematic representation of wave propagation and reflection in a squeeze-mode piezoelectric inkjet printhead.

A typically squeeze mode piezo-driven DOD inkjet printhead is schematically shown in the left top part of Fig. 2.18. The operating principle can be basically explained as follows: when a voltage pulse is applied to the piezoelectric actuator, it causes a sudden, quasi-adiabatic reduction of the ink chamber

volume, resulting in the generation of positive pressure waves inside the chamber. These pressure waves propagate throughout and reflect inside the chamber. Ink is propelled outwards when a positive pressure wave approaches the nozzle. A droplet is ejected when the amount of kinetic energy transferred outwards is larger than the viscous energy dissipation plus the energy needed to form the surface of the droplet [48]. Besides the above two parts, the kinetic energy left determines the initial velocity of the ejected droplet. For reliable jetting, this initial velocity of a droplet needs to be several meters per second, to overcome the drag action of ambient air [49].

The droplet formation process can be explained in more detail by referring to the phenomena of wave propagation and deflection in the inkjet printhead, which is a function of fluid properties, printhead design, and constituent materials [50, 51]. The first investigation of such phenomena was conducted by Bogy and Talke [52], followed by the extensive studies of other researchers [53, 54]. As can be seen from Fig. 2.18, a typical bio-polar voltage signal which normally used for printing is shown in the bottom of the diagram. In the top part of the diagram is the propagation and reflection of the acoustic waves related to each portion of that voltage signal.

At time “a”, the piezoelectric actuator moves radially outward due to a sudden fall in the voltage. As a result, a negative pressure wave is produced inside the ink. Point “b” represents that this pressure wave splits into two halves and propagate in opposite directions to the reservoir side and nozzle side. According to acoustic wave theory, the reservoir side can be treated as being

open since the inner diameter of the ink supply tube is comparable to that of the ink chamber. Whereas the nozzle end can be treated as being closed since the orifice diameter is negligible as compared to that of the ink chamber. The pressure wave keeps its phase after reflecting from the closed end while changes its phase to reverse after reflecting from the open end. The reason is: for the open end, the boundary condition is zero pressure and this condition is satisfied by superimposing an opposite phase pressure wave on the incident pressure wave; the nozzle end is simply treated as a dead end with no flow rate passing through it, to satisfy the governing equations for wave propagation, pressure wave only changes its direction after reflecting from this end [50]. After travelling a distance of *L*, the two halves pressure waves travel back and meet in the middle of the printhead chamber. At the same time "f", an increase of the voltage pulse causes the piezoelectric actuator to move radially inward, which in turn producing a positive pressure wave propagating to the two ends. The newly generated positive pressure waves coincide with the former two halves reflected waves ("f" in Fig. 2.18) and superpose with them. As a result, the negative pressure wave traveling to the open end is annihilated while the positive pressure wave traveling to the closed end is doubled ("h" in Fig. 2.18). This enhanced positive pressure wave propagates to the closed end and reflects again from it at time $t = T_0 + {}^{3L}/_{2c}$, where *c* represents the speed of sound in the ink. The drop ejection also occurs at this time "i".

Bogy and Talke calculated the pressure history at the orifice and concluded that the operation of DOD inkjet depends strongly on the length of the cavity. They also found that the four important quantities in wave propagation were

linearly dependent on the cavity length and the sound speed in the ink. These four quantities are: the optimum pulse width for generation of maximum droplet velocity, which equals to l/c; the delay time for the first protrusion of the meniscus, which equals to $3l/2c$; the period of meniscus oscillation, which equals to $4l/c$; and the period of low-frequency resonant and antiresonant synchronous operation, which also equals to $4l/c$. The calculations of these quantities have been extensively verified [40, 55].

The acoustic wave propagation theory is also utilized to help the printhead design for high-speed inkjet. It is worthy to note that as a manufacturing tool, high speed jetting is required to increase productivity of inkjet printing technology. Thus there is a continuous requirement for increasing the maximum jetting frequency for inkjet printing devices. However, for a reliable jetting, a subsequent droplet should not be ejected until the pressure wave from the previous pulse signal has sufficiently damped. This damping takes time and thus limits the maximum jetting frequency [38, 56]. By utilizing the self-sensing capability of the piezoelectric element, Kwon *et al.* proposed a way to effectively measure the pressure wave inside the ink chamber through the piezo current. Based on the measurement results, they designed a two-pulse waveform which could greatly improve the jetting speed of the printhead [40].

2.2.1.2 Droplet Generation Conditions

The governing equations for the 3-D drop-on-demand inkjet printing are:

$$\frac{\partial u}{\partial x}+\frac{\partial v}{\partial y}+\frac{\partial w}{\partial z}=0 \tag{2.4}$$

$$\frac{\partial}{\partial t}(\rho u)+\nabla\cdot\rho\vec{V}u=-\frac{\partial p}{\partial x}+\frac{\partial}{\partial x}\left[2\mu\frac{\partial u}{\partial x}\right]+\frac{\partial}{\partial y}\left[\mu\left(\frac{\partial v}{\partial x}+\frac{\partial u}{\partial y}\right)\right]+\frac{\partial}{\partial z}\left[\mu\left(\frac{\partial u}{\partial z}+\frac{\partial w}{\partial x}\right)\right]+F_x^{\sigma}+\rho g_x \tag{2.5}$$

$$\frac{\partial}{\partial t}(\rho v)+\nabla\cdot\rho\vec{V}v=-\frac{\partial p}{\partial y}+\frac{\partial}{\partial x}\left[\mu\left(\frac{\partial v}{\partial x}+\frac{\partial u}{\partial y}\right)\right]+\frac{\partial}{\partial y}\left[2\mu\frac{\partial v}{\partial y}\right]+\frac{\partial}{\partial z}\left[\mu\left(\frac{\partial v}{\partial z}+\frac{\partial w}{\partial y}\right)\right]+F_y^{\sigma}+\rho g_y \tag{2.6}$$

$$\frac{\partial}{\partial t}(\rho w)+\nabla\cdot\rho\vec{V}w=-\frac{\partial p}{\partial z}+\frac{\partial}{\partial x}\left[\mu\left(\frac{\partial u}{\partial z}+\frac{\partial w}{\partial x}\right)\right]+\frac{\partial}{\partial y}\left[\mu\left(\frac{\partial v}{\partial z}+\frac{\partial w}{\partial y}\right)\right]+\frac{\partial}{\partial z}\left[2\mu\frac{\partial w}{\partial z}\right]+F_z^{\sigma}+\rho g_z \tag{2.7}$$

where $\vec{V}$ is the velocity vector with *u*, *v* and *w* in the *x*-, *y*- and *z*-axes; *p*, ρ and μ represent the pressure, density and dynamic viscosity of liquid, respectively; ρg and F^{σ} denote the gravitational force and the surface tension force at the liquid-gas interface [57]. There are hydrostatic pressure, viscosity force, fluid inertia and surface tension force which will dominantly influence liquid flow in a drop-on-demand device. It can be seen from Fig. 2.19 that to eject a droplet out of the nozzle, the acoustic energy obtained from the piezoelectric actuator must be sufficient to compensate the energy loss due to viscous dissipation and the formation of liquid free surfaces.

In a fluid system with characteristic velocity *V* and characteristic length *L*, the Weber number, $We = \rho V^2 L/\sigma$, is a measure of the relative importance of the fluid's inertia compared to its surface tension. Wang *et al.* [19] claimed that it was reasonable to choose $We \geq 10$ as the condition for droplet generation, giving a initial droplet velocity $V \sim (k\sigma/\rho r)^{1/2}$. For simplicity, the acoustic pressure was treated as a square hydrostatic pressure pulse with a

magnitude of P_0 and a pulse width of t_0. According to the law of conservation of energy, the kinetic energy of the ejected droplet with such a velocity *V*, should equals to the work done by the acoustic pressure. As a result, P_0 can be estimated. Later this hydrostatic pressure was refined by adopting a commercial inkjet simulation tool: Conventor Inkjet Developer. Table 2.1 shows the minimum hydrostatic pressure required to generate different size of water droplets. The results indicate that the required actuation pressure increase is almost directly inversely proportional to the droplet size, which is reasonable as surface tension is the dominant factor influencing droplet generation [58].

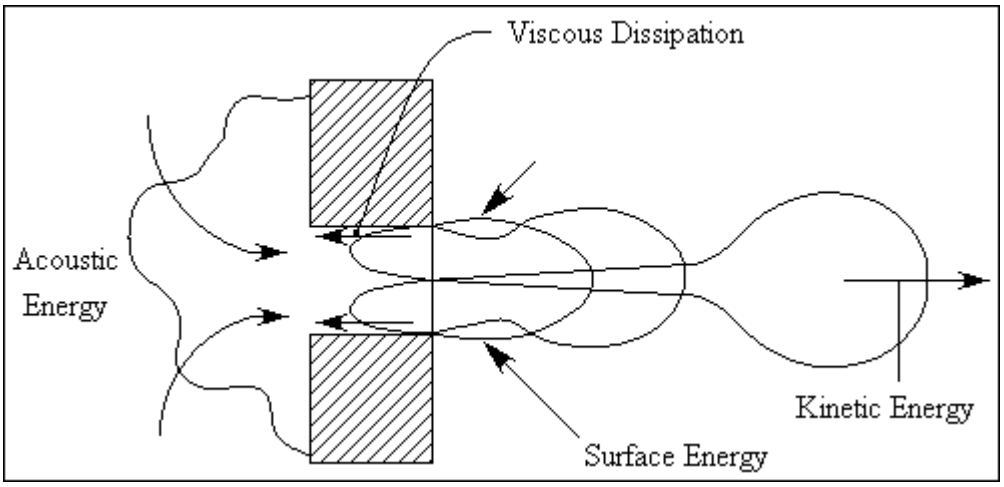

Fig. 2.19: Schematic representation the basic energy requirement for ejecting a droplet.

Table 2-1: The minimum actuation pressure for droplet generation in DOD inkjet devices [58].

d (μm)	10	2	0.4	0.1
Volume (pl)	$7.1e^{-1}$	$6e^{-3}$	$3.8e^{-5}$	$7.1e^{-7}$
P_0 (MPa)	0.2	1	4	20

Besides nozzle size, the fluid properties of the ink also influence droplet formation. Fromm rescaled the governing equations (eq. 2.4 to eq. 2.7) and

used the following grouping of fluid properties to provide a dimensionless analysis of the mechanics of drop formation in DOD inkjet [49]:

$$Z = (d\rho\sigma)^{1/2}/\eta = Oh^{-1} \quad (2.8)$$

The relation is equivalent to the inverse of the Ohnesorge number *Oh*, where η, ρ, and σ are the viscosity, density, and surface tension of the liquid, respectively, and *d* is the characteristic length. For an inkjet printhead, *d* is the diameter of the nozzle orifice. Fromm predicted that successful droplet ejection was only possible when $Z > 2$ and that for a given pressure pulse droplet volume increases as the value of *Z* increase [49]. This prediction was later refined by Reis and Derby, who carried out experiments for dispensing different concentrated alumina wax suspensions and then concluded that successful DOD printing could be achieved in the range $1 < Z < 10$ [51]. Here the lower limit represents no droplet ejection due to too much energy dissipated by viscosity forces, and the upper limit represents the formation of satellite droplets. In reality, inkjet printing can be reliably utilized for industrial applications even when satellite droplets are produced, just provided that the satellites can merge with the main droplet. For example, polymer solutions with *Z* numbers bigger than 50 have been successfully dispensed by Schubert *et al*. [59].

2.2.1.3 Droplet Velocity and Droplet Size

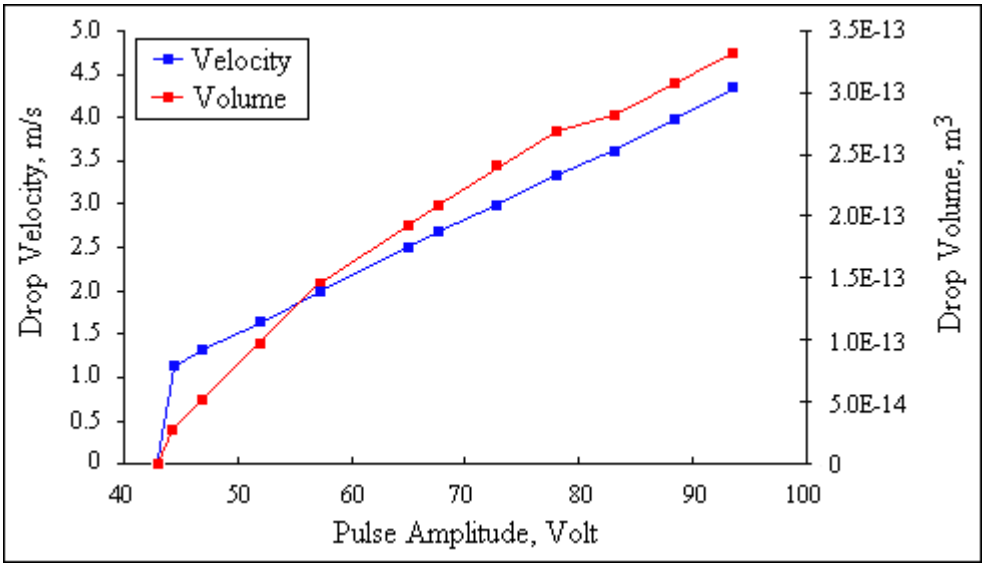

Fig. 2.20: Effects of pulse amplitude on droplet velocity and droplet volume [60].

The driving signal to the piezoelectric actuator has significant influence on droplet formation. Results from different research groups have shown that the droplet velocity and droplet volume are linearly dependent on the amplitude of the driving pulse (for simple rectangular input pulse), as shown in Fig. 2.20. This is understandable as referring to the fractional volume change due to the piezoelectric effect:

$$\Delta V/V = -3d_{31}U/t \tag{2.9}$$

where V is the volume of the piezoelectric actuator, d_{31} is the piezoelectric strain constant, U is the applied voltage and t is the thickness of the piezoelectric tube [61]. The negative sign indicates contraction when the applied pulse has the same polarity as the original polarizing voltage for the piezoelectric element. From eq. 2.9 is can be seen that the volume change of the piezoelectric tube is liner to the amplitude of the input pulse. An increase in voltage amplitude will lead to a greater volume change in the ink chamber

and correspondingly larger induced acoustic waves and fluid acceleration, ultimately, a bigger droplet with higher velocity.

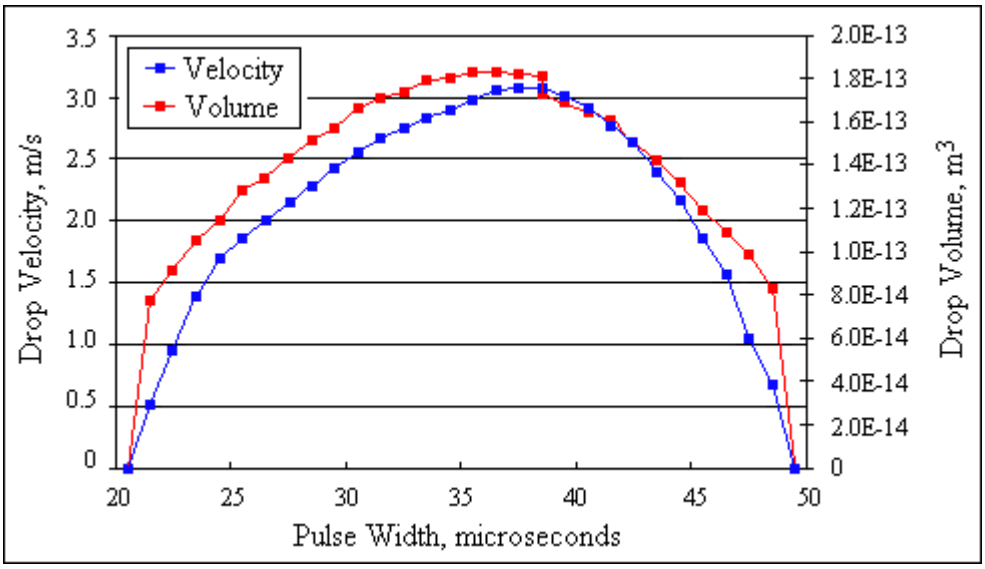

Fig. 2.21: Effects of pulse width on droplet velocity and droplet volume [60].

Fig. 2.21 shows the effects of pulse width on droplet velocity and droplet volume. Both of the quantities exhibit a maximum as the pulse width is varied. Derby *et al.* showed that the location of this maximum value of droplet velocity remained unchanged when the driving pulse amplitude was increased, but it shifted when the fluid properties were changed [62]. Similar behavior was also observed for droplet volume. Derby *et al.* also observed the periodic behavior of droplet as the driving frequency *f* of the piezo signal is varied, as shown in Fig. 2.22. The x-axis represents "inverse of the jetting frequency", rather than the "pulse width". They are two different parameters, although both of them have a unit of micro-second. In practice, pulse width is normally smaller than the "inverse of the jetting frequency" as there are intervals between successive piezo signals. From Fig. 2.22, this periodicity phenomenon is also dependent on the fluid properties. This is reasonable as the maximum in droplet velocity correspond to conditions of resonance, which

are dependent on the ink chamber geometry as well as the speed of acoustic wave in the ink, which is dependent on the ink properties.

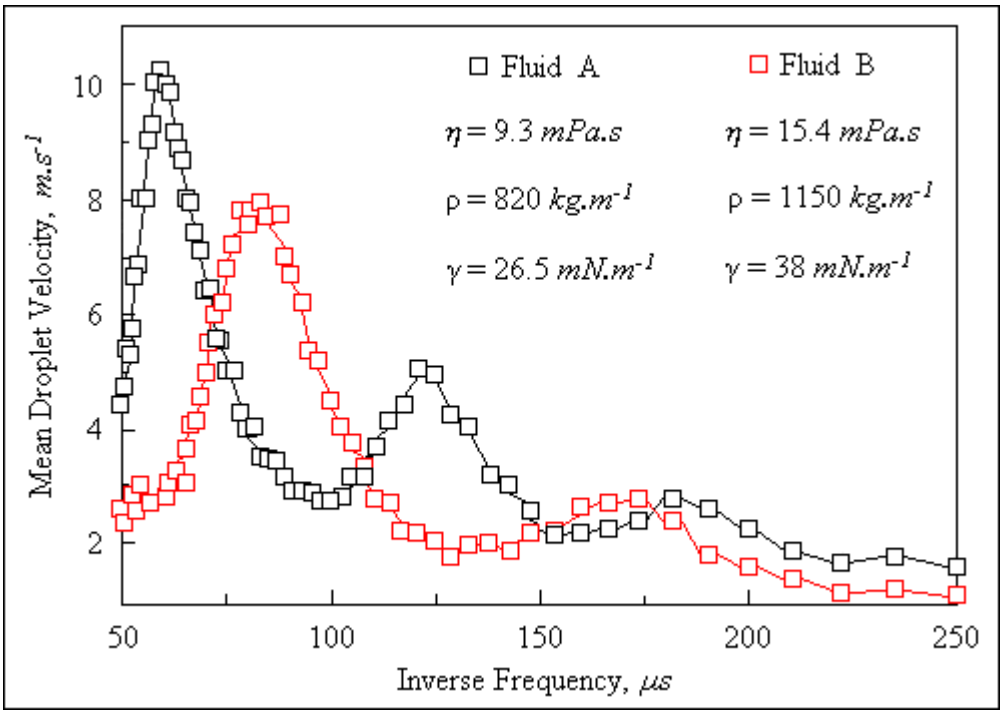

Fig. 2.22: Effects of jetting frequency on droplet velocity and droplet volume [62].

2.2.1.4 Satellite Droplet

As have been mentioned before, Reis and Derby predicted that satellite droplets would be produced during inkjet printing when the Ohnesorge number smaller than 0.1 [51]. Since satellite droplets can negatively impact the printing resolution, there has being a great interest in understanding the satellite droplet formation process, and also the methods to avoid it [63-65].

A sequence of images captured during DOD droplet formation is shown in Fig. 2.23, revealing the main features of this process. When the piezoelectric transducer contracts, ink inside the chamber is accelerated and squeezed out of the nozzle. Initially, the meniscus extends rapidly outward until a liquid

column with a round leading edge is formed (images 1-3 in Fig. 2.23). After a short time (normally several tens of micro-seconds after the contraction behavior of the transducer, starting at approximately 12 μs in the figure, as image 4), the outward flow rate decreases. The resulting difference in Z-axial velocity between the column head and the liquid at the nozzle exit causes the liquid column to stretch. The velocity of the liquid at the orifice continuously decreases until no flow into the column, or even decreases further due to some inverse flow caused by the extension of the piezoelectric transducer to its equilibrium position. The liquid column is continuously extended due to the inertia and this extension rate decreases with time as new surface is formed which resulting the increase of surface energy. With the extension and stretching of the liquid column, the liquid at nozzle exit necks, with a necking position at the nozzle exit. Almost concurrent with the liquid column stretching, a second necking point appears (image 5 in Fig. 2.23) at the top of the column head. Finally, the liquid thread pinches off from the nozzle, forming a free long liquid thread with a bulbous head [63]. Following the pinch-off, the tail recoils toward the bulbous head, to reduce the surface energy of the whole liquid column. As has been mentioned in above, there is a new neck near the bulbous head. The new necking continues to evolve until the liquid thread pinches off from the bulbous head, forming a primary droplet and a new free thin liquid thread. The lower end of this liquid thread recoils rapidly toward the upper end, again, to reduce the surface energy of the thread. Depending on its length, this new liquid thread may shrink into a smaller droplet (or satellite, image 16 in Fig. 2.23), or break up into two or even more droplets [63].

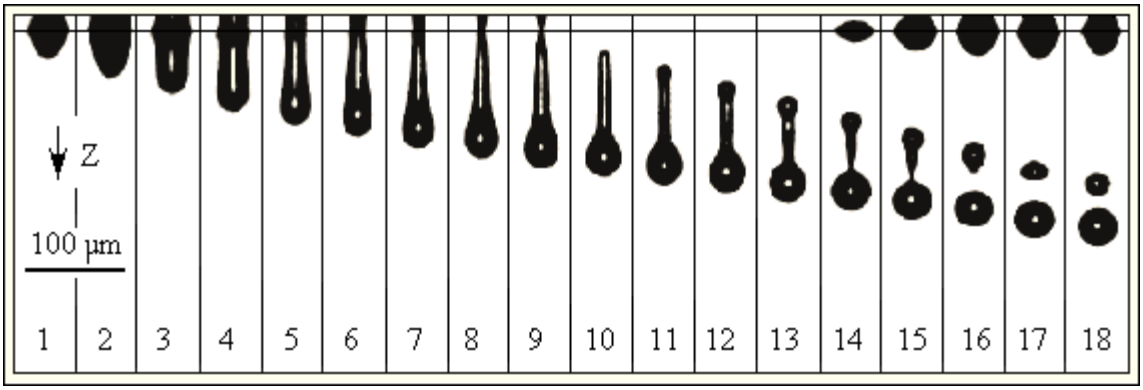

Fig. 2.23: Sequence of images of DOD droplet formation for water [63].

To conclude, the main reason for satellite generation is due to the existence and later break up of a long liquid thread which connecting the bulbous head with the nozzle exit, before the liquid column pinching off from the nozzle. Dong *et al.* [63] predicted that this liquid thread would contract and combine into the bulbous head without breaking up if the length of liquid thread at pinch-off, l_b, does not exceed a limiting value l_b^*.

$$l_b^* = R_{noz} \cdot \left[2 + a(C_2 - C_1)\frac{1}{\alpha_{max}^*}\right] \tag{2.10}$$

$$C_1 = \frac{t_{b1} - t_e}{t_{ca}/\alpha_{max}^*} \tag{2.11}$$

$$C_2 = \frac{t_{b2} - t_e}{t_{ca}/\alpha_{max}^*} \tag{2.12}$$

where R_{noz} is the nozzle radius, a is a constant for water, t_{b1} is the first pinch-off time, t_{b2} is the second pinch-off time, t_e is the ejection time (time from emergence of liquid form the nozzle until the ejected volume reaches its maximum), t_{ca} is the capillary time. α_{max}^* is the grow rate of the most unstable disturbances. To suppress satellite droplets formation, a bigger l_b^* is desired. According to Dong *et al.*, this can be achieved by increasing liquid viscosity and decreasing surface tension, or optimize the piezoelectric waveform. Another common attempt to eliminate satellite droplets generation is to reduce the magnitude of the piezoelectric pulse, which will decrease the

droplet ejection velocity and may shorten the liquid thread. However, droplets with low jetting velocity suffer from the droplet scattering and the loss of accuracy in positioning [66].

As can be imaged, the formation of the liquid thread connecting the primary droplet and the nozzle exit is related to the physical properties of the liquid itself. Shore *et al.* [65] found that by adding small amounts of polymers in Newtonian solvents, satellite droplets generation were effectively eliminated. This is understandable as when the polymer molecules are stretched out during the droplet formation, the elasticity of the solution will cause the liquid thread which connecting the primary droplet and the nozzle to snap back and combine with the primary droplet, forming a monodisperse droplet. While remember that this liquid thread normally pinches off from the primary droplet and breaks up into satellite droplets for a purely Newtonian fluid. Shore *et al.* also found that to efficiently suppress satellite droplets formation, there was a minimum required concentration for the polymers to be added, for a fixed molecular weight. Consequently, the resultant elasticity of the solution will increase and a stronger piezoelectric pulse is required to eject the droplet. The solution containing polymers will also have a longer liquid thread, a longer droplet separation time, and a lower droplet velocity as compared to the purely Newtonian fluids with similar shear viscosity [65]. Furthermore, the method requires the change of the ink properties, which might be undesirable for practical applications.

2.2.2 Printhead Fabrication

2.2.2.1 The Overall Printhead Structure

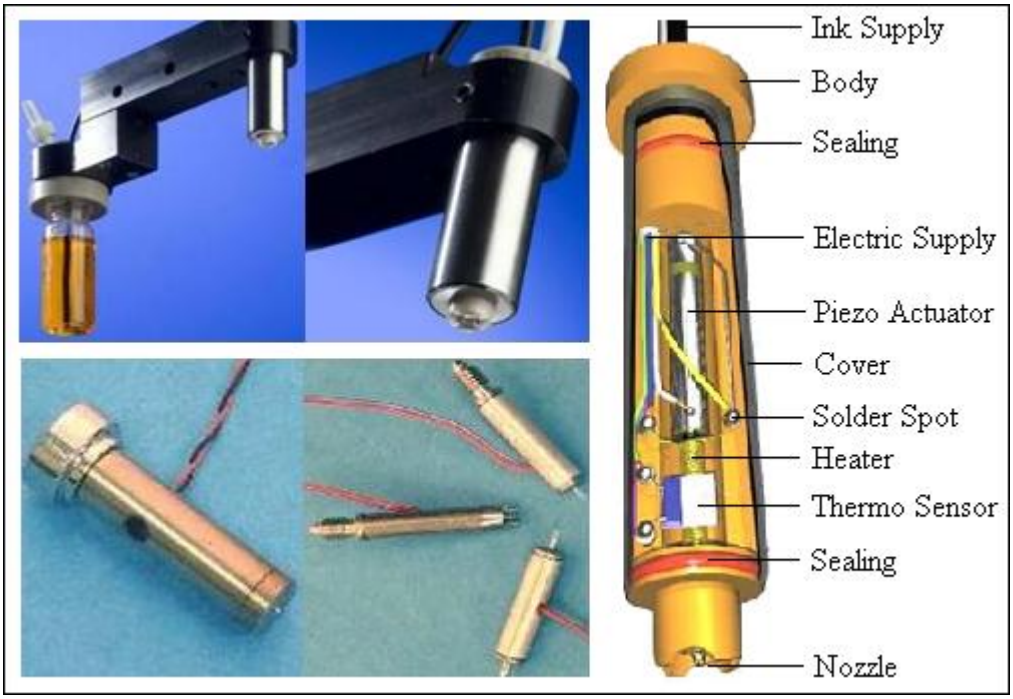

Fig. 2.24: Different kinds of commercial printheads.

Currently, printheads for research purposes can be bought from companies such as Microdrop and Microfab. Fig. 2.24 shows several dispensers from these companies. Regardless of the internal components it contains, the basic design idea for all the squeeze mode piezo-driven printhead is the same. Fig. 2.25 schematically shows the construction of a typical piezoelectric squeeze mode printhead. By using epoxy adhesive, a piezoelectric element is tightly attached onto a conventionally used glass tube which with an orifice at one end. When an electrical pulse is applied, the piezoelectric element will contract inward, squeezing the glass tube as well as the liquid inside, and ejecting a droplet from the nozzle. The piezo tube is made from a ceramic material that changes shape when a voltage is applied to it. There are several

kinds of piezoelectric ceramic materials: PZT-5H, PZT-5A, PZT-8 and PZT-4. Different materials have different piezoelectric constants thus have different stresses-strains relationships [67].

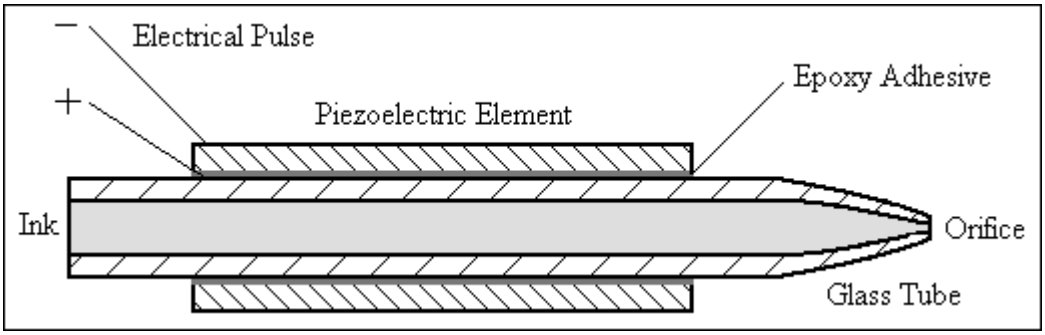

Fig. 2.25: Schematic of the construction of a piezoelectric squeeze mode DOD printhead.

A new printhead with interchangeable nozzles will be designed in this study. Accordingly, the printhead will be separated into two main parts: the printhead chamber and the interchangeable nozzle.

2.2.2.2 Ejection Nozzle Requirements

Lee [68] claimed that an ideal ejection nozzle should have a tapered cross section ending up in a short hole with an aspect ratio round one-to-one. The purpose of the overall conical taper is to minimize the flow resistance without compromising mechanical strength. To illustrate the effects of different aspect ratios on nozzle behavior, three types of nozzles, a tapered one with a proposed aspect ratio, a very thin one and a very thick one, are compared. As shown in Fig. 2.26, the left one in a proposed geometry works properly during the droplet generation cycle. However, air can be easily sucked into the ink chamber for the second nozzle, during the fluid withdrawal phase. The existence of air bubbles will cause an increase in the ejection threshold due to air bubbles absorbing the pressure impulse which is supposed to squeeze out

the ink. Worst case is the stop of jetting due to big air bubbles inside the ink chamber. Air entrapment will not occur for the nozzle has a high aspect ratio, as the third nozzle shown in the figure. However, the local flow resistance is too much for this nozzle and thus will also raise the threshold for jetting. To conclude, a desirable nozzle should have an orifice shape similar to that of the first one.

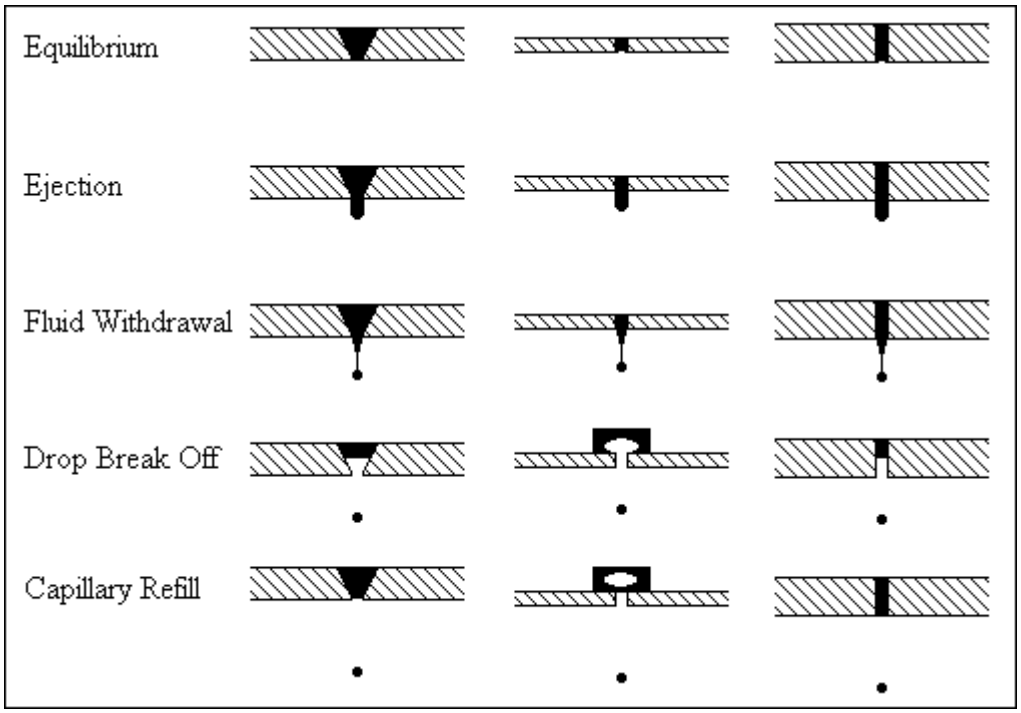

Fig. 2.26: Ejection nozzle orifice cross section requirements.

2.2.2.3 Ejection Nozzle Fabrication Methods

Various techniques can be used to fabricate small holes. A definitive paper on such techniques is published by [69].

- Thermally Tapered Glass Pipettes:

By simply heating a glass tube and pulling it while hot, a closed cone with an included angle will come out. This closed end is then polished until a hole of a desired diameter is produced. All the nozzles of the printheads shown in Fig.

2.24 are fabricated by this method. It is a simple and low-cost fabrication method. Meanwhile, it has following disadvantages. Firstly, it is difficult to achieve a perfectly axially symmetric nozzle, due to the polishing of a conical tip. This asymmetric nozzle will produce offset jets, which will destroy the accuracy of printing, especially when the jetting velocity is relatively low. Furthermore, glass material is so fragile that a simple touching or wiping the nozzle tip against a rigid object may destroy the orifice and, again, lead to an asymmetric nozzle. Secondly, the fabrication method is so sensitive to the heating process that it is virtual impossible to replicate the exact profile of the nozzle. This nonuniformity is obviously undesirable for industrial applications that require parallel, identically operating channels of interchangeable spare units [68]. For these reasons, a silicon micromachining method is proposed for fabricating inkjet nozzles.

- Silicon Micro-Machined Nozzles:

For crystal wafers, slice orientation is used to denote the crystallographic orientation of their surface. It is well-known that there are three most common used slice orientations for silicon wafers: (100), (110) and (111). Accordingly, the surfaces perpendicular to such orientations are denoted by (100) plane, (110) plane and (111) plane, respectively. For a (100) silicon wafer, such orientations and planes are shown in Fig. 2.27. Wet orientation-dependent etches (ODEs) can be used to etch silicon wafers for nozzle fabrication. It is an anisotropic etching method at rates that vary with crystallographic direction [70]. For example, for KOH etching at 85 ˚C,

$$R_{\langle 111\rangle}: R_{\langle 100\rangle}: R_{\langle 111\rangle} \approx 1: 300: 400$$

where $R_{\langle 111 \rangle}$, $R_{\langle 100 \rangle}$ and $R_{\langle 111 \rangle}$ represents the ODEs' etching rate at (111), (100) and (110) plane, respectively. Since $R_{\langle 111 \rangle}$ is negligible as compared to $R_{\langle 100 \rangle}$ and $R_{\langle 111 \rangle}$, for (100) a silicon wafer, the etching process will proceed downward until (111) planes are reached, forming a *V* shape, as shown in Fig. 2.27(b) and Fig. 2.27(c).

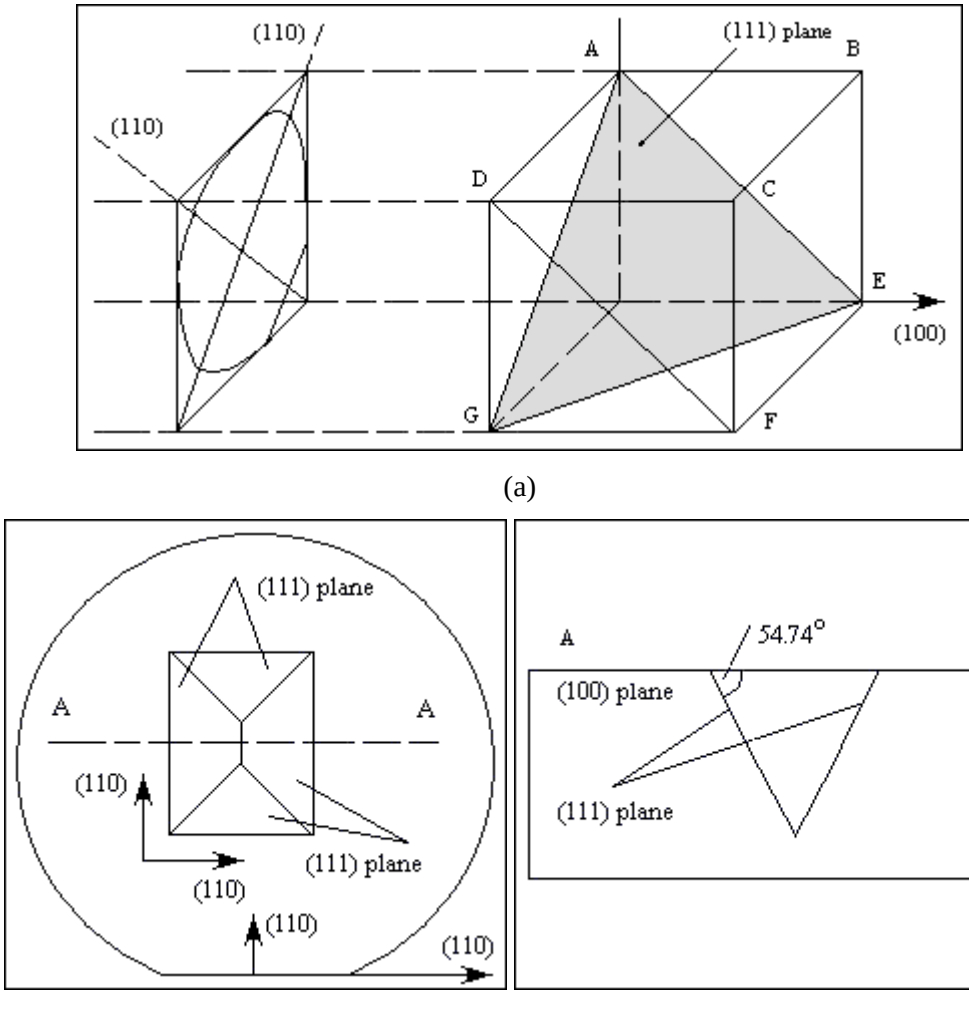

Fig. 2.27: KOH etching for a (100) silicon wafer. (a). Slice orientations for silicon material. (b). Slice orientations shown in a plan view of a (100) silicon wafer. Etching process proceeds downward until (111) planes are reached. (c). "A-A" cross-section view.

To obtain an inkjet orifice with a desired diameter, a silicon wafer is firstly etched by chemical anisotropic (KOH etching is normally used) method to form a deep pyramidal pit, just leaving a short distance to the opposite end of the wafer. Then Deep Reactive Ion Etching (DRIE) is used to form a

cylindrical aperture of a desired diameter through this thin layer, as shown in Fig. 2.28.

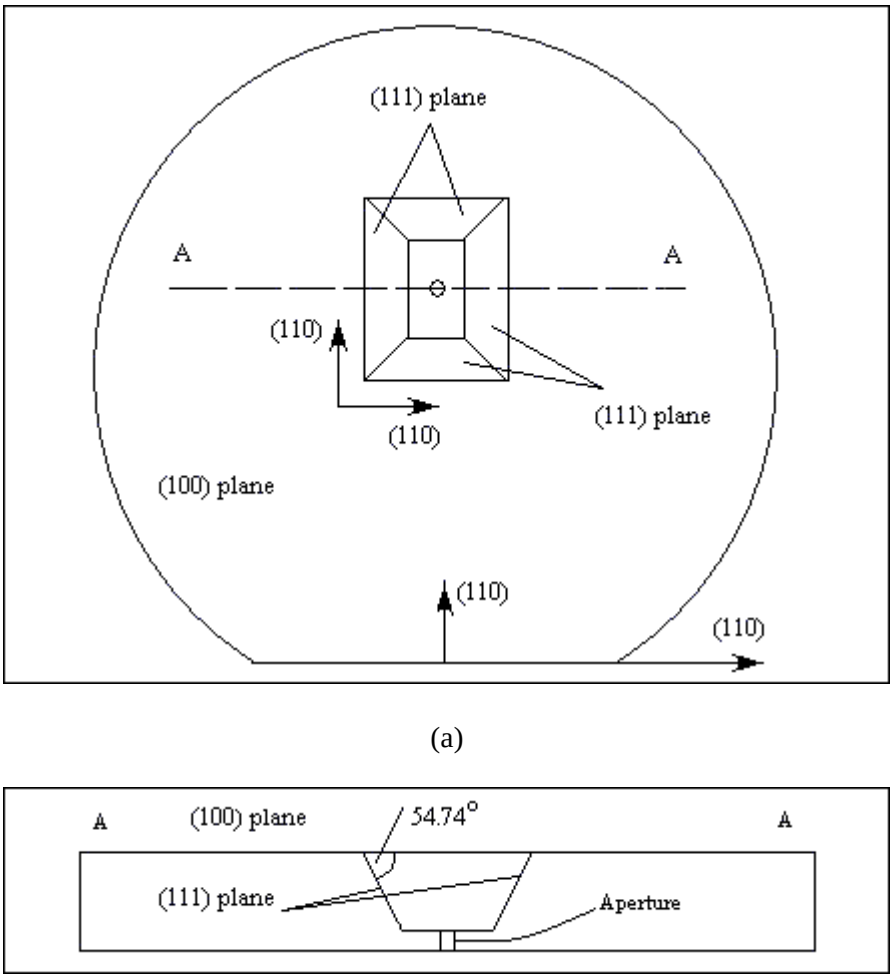

Fig. 2.28: Nozzle fabricated by silicon micromachining method comprising KOH etching and Deep Reactive Ion Etching. (a). Plan view of the etched wafer. (b). "A-A" cross-section view of the etched wafer.

The optimal thickness of this thin plateau, or the optimal thickness of the aperture, is determined by the diameter of the orifice. An aperture thickness of one to two orifice diameters is sufficient to suppress air entrapment. Another concern is the thickness of this plateau should be enough to ensure sufficient mechanical strength, avoiding nozzle damage due to the common nozzle cleaning process such as being immersed in an ultrasonic bath, or the accidental touching of the nozzle against a rigid object [68].

Silicon micromachining method is more complicated and more costly as compared to the glass heating and pulling method; however, the method provides good mass productability and exact reproducible desired nozzle profile for large production runs [71-73].

- Electro-Discharge-Machining (EDM)

In EDM method, a spark discharge between a cutting electrode and the workpiece is utilized to remove material. EDM can cut extremely hard material to very close tolerance, but it also has the disadvantages of inability to cut non-conductive materials and a slow cutting rate.

- Laser Drilling

To date, laser drilling can produce holes as small as 1 micron. Due to its non-contact feature, it can drill holes on curved surfaces and can handle both hard and soft material.

Plenty of methods have been adopted to fabricate nozzles for inkjet purpose. This research is more concentrated on the fabrication of glass nozzles.

2.3 Creation of Ultra-Small Droplets

2.3.1 Needs for Generation of Ultra-Small Droplets

The manufacture of flat panel displays (FPD) for computer monitors and televisions are a $ 60 billion industry. The state-of-the-art facilities are capable of fabricating panels on ~ 2 m × 2 m substrate, and the substrate size has doubled every two to three years since 1990 [44]. Traditional display manufacturing utilizes photolithography techniques, which is a well-established patterning method for silicon integrated circuits (ICs). However, to build the photolithography and etching systems for huge substrates is challenging and extremely expensive. From this viewpoint, emerging direct printing of functional electronic materials [74-77] has attracted consideration attention. Inkjet printing is a data-driven direct-write method without the complicated photolithography and etching processes, thus leading to a great reduction in manufacturing cost and processing time.

However, the requirements for patterning display pixel are more challenging than the traditional document printing: a document pixel element is formed by a drop of ink, while a display pixel is a circuit comprising different materials [44]. Currently, there is a wide gap between the resolution required for display manufacturing and the resolution of a typical inkjet device. Consequently, a more precise ink jet system that capable of producing subpicoliter or even subfemtoliter droplet is required. It is also the most critical requirement for applying inkjet printing to the fabrication of high-performance electronics

devices, in where thin-film transistors (TFTs) with a channel length of 1 to 2 μm is commonly required [78, 79].

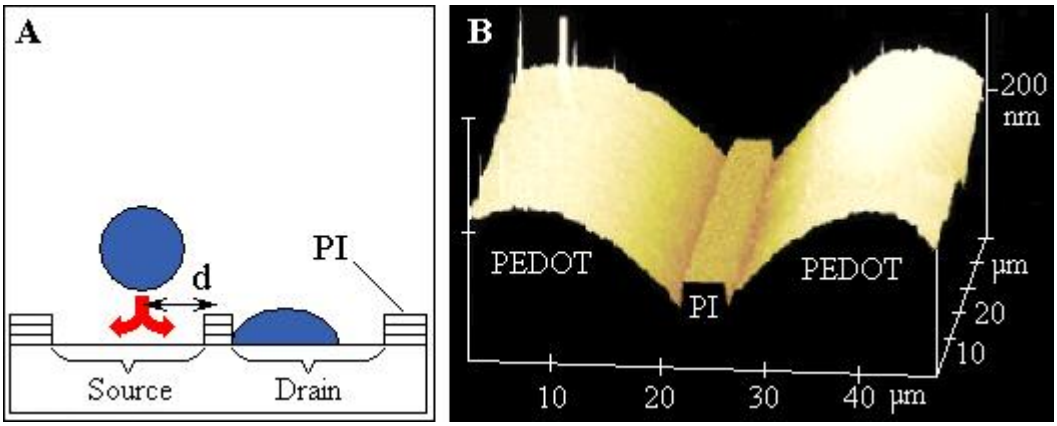

Fig. 2.29: Schematic of photolithographically predefined inkjet printing. (a). Schematic diagram of high-resolution inkjet printing onto a prepatterned substrate. (b). AFM showing accurate alignment of inkjet-printed PEDOT/PSS source and drain electrodes separated by a repelling polyimide (PI) line with L = 5 μm. [20]

Actually, several methods have been proposed and verified to eliminate such a gap between the resolution required for those high-performance electronic devices and the typical resolution of conventional inkjet printing devices. For example, photolithographically predefined features [18, 20, 80, 81] or surface pretreatment [15, 82] in the form of hydrophobic and hydrophilic patterns can confine and guide the flow and spread of the printed droplets when they land on the substrate. As shown in Fig. 2.29(a), a photolithographically predefined substrate was fabricated as follows: a glass substrate with a 500 Å hydrophobic polyimide film was spin-coated with photoresist. The photoresist above the source-drain regions on the bare glass was removed and the corresponding parts of polyimide were etched through. Then Oxygen plasma was used to burn up the hydrophobic groups of the source-drain regions and make it hydrophilic, whereas the polyimide line (PI line in Fig. 2.29(a)) defining the thin film transistor channel was still covered and protected by photoresist and remained hydrophobic [20]. Lines of PEDOT droplets were

deposited into the source-drain regions at a distance *d* from the mid polyimide line. This distance *d* was small enough to ensure that the spreading droplets could reach the repelling line. Atomic force microscopy (AFM) showed that the deposited PEDOT electrodes extended accurately up to the repelling polyimide line, without destroying the narrow gap (5 μm) between them.

With above methods [15, 18, 20, 80], the gaps between printed droplets can be controlled at the submicrometre level, which is important for electronics fabrication as such gaps define the transistor channel lengths. However, above methods do not offer a universal approach to high resolution. Furthermore, complicated photolithography and etching processes are required to deal with the substrate. By this token, reducing droplet size maybe the most general and direct way to obtain high printing resolution. Actually, inkjet printing technology is also developing at a rapid pace and the size of the dispensed droplets halved every four-and-half years during the last two decades, in a way similar to Moore's Law for transistors [83]. Thus, it can be foreseen that a more precise inkjet system that is capable of producing ultra-small droplet will be designed and fabricated in the near future.

2.3.2 Methods for Printing Ultra-Small Droplets

2.3.2.1 Reducing Nozzle Size

Typically drop-on-demand systems eject droplets with the radius roughly the same as the radius of the nozzles. To date the most direct and reliable way of reducing the droplet volume has been reducing the orifice size. Wang *et al.* [19, 58] have demonstrated the fabrication of inkjet nozzles with orifice size as small as 2.5 μm, based on silicon micro-machining technology. Their printhead was composed of a large array of inkjet devices, operated in the thermal bubble mode. Stable generation of water droplets down to 3.5 μm has been demonstrated. Kung *et al.* [84] have reported the generation of 3 to 4 μm water droplets by a piezo-driven printhead with a very small orifice measuring only 1 μm in diameter. Their nozzle tips were fabricated by heating and pulling 3-mm-diameter Pyrex tubing. The diameter of the dispensed droplets reduced from 4 to 1 μm after a short travel distance (several millimeters), due to evaporation. Although micro-scale droplets have been successfully generated by reducing the size of the printhead orifice, the problem of clogging and breaking of the nozzle becomes an obstacle to reliable operation. Thus there is a need for effectively reducing droplet volume without reducing nozzle radius in DOD inkjet printing.

2.3.2.2 Controlling of Waveform

The phenomenon of much smaller, faster droplets ejected from an inkjet printhead with a relatively bigger orifice was firstly described by researchers from Xaar. The mechanism was explained by Temple [85], who modeled the

acoustic waves of the fluid in the printhead chamber and claimed that a special configuration of interacting pressure pulses is responsible for the phenomenon.

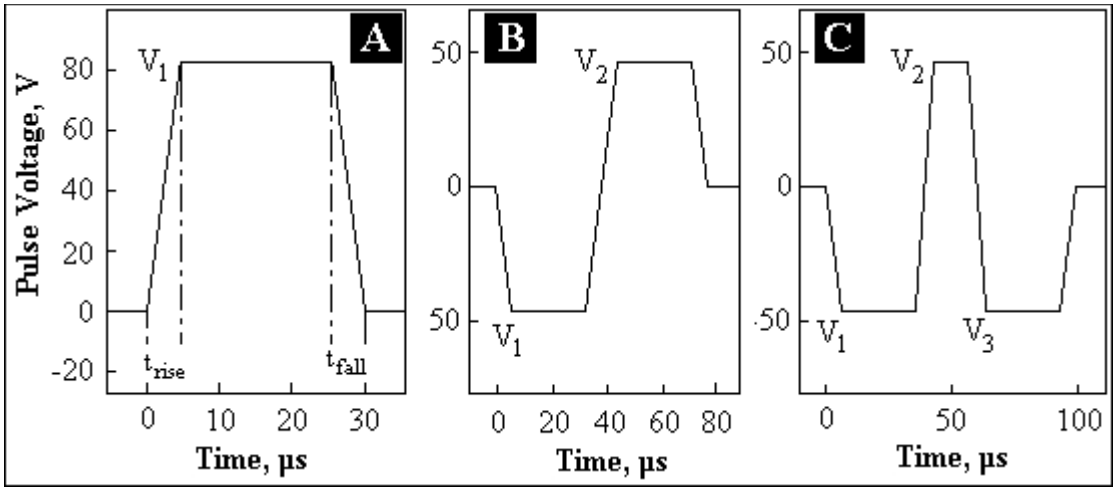

Fig. 2.30: Schematic of pulse waveforms used for driving the inkjet printhead. (a). A uni-polar waveform. (b). A bi-polar waveform. (c). The new waveform for small droplet generation. [21]

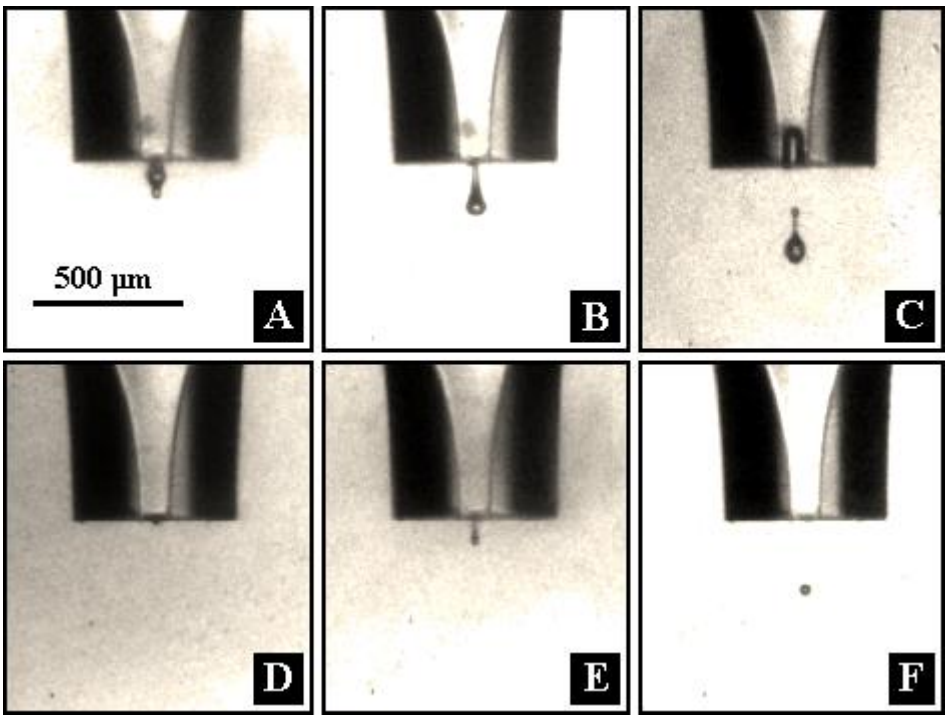

Fig. 2.31: (a) – (c) Images showing appearance and disappearance of a tongue and formation of droplet with a diameter similar to that of the nozzle. (d) – (f) Images showing formation of a droplet with a diameter much small than that of the nozzle orifice. [21]

Later Basaran *et al.* [21] confirmed that droplet with one order of magnitude reduction in its volume could be produced by judiciously controlling the capillary, viscous, and inertial time scales that govern the flow within the nozzle and the forming droplet. They investigated the effects of different piezo driving waveforms on droplet formation. Their results show that as compared to a conventionally used uni-polar signal (Fig. 2.30(a)), a bi-polar piezo (Fig. 2.30(b)) signal will cause a "tongue" protruding from the tip of the primary droplet, as shown in Fig. 2.31(a). The tongue is resulted from a small volume of liquid traveling at a high velocity relative to the surrounding liquid. However, the tongue was found to be absorbed into the primary droplet later, forming a droplet with a similar diameter to the nozzle orifice, as shown in Fig. 2.31(b). In order to suppress the formation of the large primary droplet and help the tongue detaching from the primary droplet, a new waveform (Fig. 2.30(c)) consisting of a succession of three square-wave pulses is suggested. As shown in Fig. 2.31(e), the tongue successfully detached from the primary droplet, forming a much smaller droplet.

Similar effects of reducing droplet size are also found when utilizing M-shaped, W-shaped, and other types of waveforms [23, 24, 25]. However, all above methods only work over a limited range of Ohnesorge numbers [21] and their effects are also limited: the diameter of the dispensed droplets can be only reduced to a maximum of 60 % of the orifice diameter. Different methods are required to reduce droplet size to micro-scale or even submicro scale.

2.3.2.3 Electrohydrodynamic Jetting

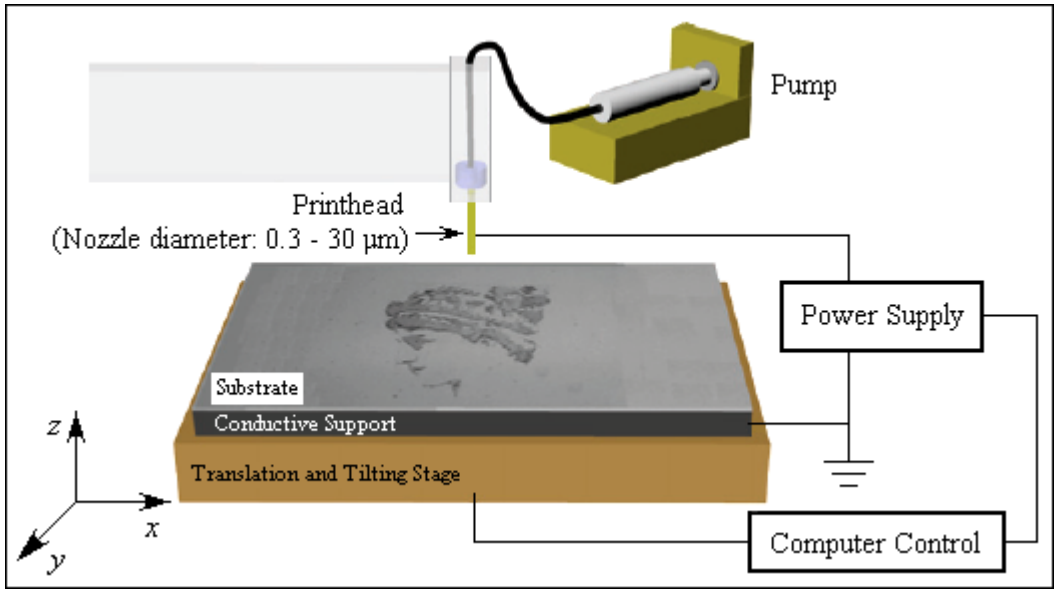

Fig. 2.32: Schematic of an electrohydrodynamic jet system. [86]

Electrohydrodynamic jet (E-jet) process is a unique and versatile jet-based technique, which utilizes electric field, rather than acoustic or thermal energy, to create the fluid flow required for ejection of liquid [86, 87, 88]. Fig. 2.32 shows a schematic diagram of a typical e-jet system. It comprises of a liquid reservoir, a pneumatic pressure controller connected to a needle, and a grounded electrode located centrally below the needle. By applying a potential difference between the needle and the grounded electrode, the liquid inside the needle can be charged. This charged liquid exits the needle and enters the high-intensity electric field, forming different liquid geometries from which a jet or multi-jets, or even dispersed droplets evolve. The size of these jets or droplets can be controlled by the intensity of the electric field, the liquid properties, and the flow rate into the needle. As has been mentioned before, conventional inkjet devices generate drops with diameter approximately the same as that of the nozzle orifice. In contrast, e-jet does not suffer from this

disadvantage and droplets of a few micrometers in diameter can be produced from needles that are a few hundred micrometers in diameter.

To better understand the fundamental dynamics of this electric-field-driven jetting behavior, sequential images of the liquid ejection process were obtained by reference Marginean *et al.* [89] with a high-speed-video camera. As shown in Fig. 2.33, the meniscus at the needle tip expands and contracts periodically due to the electric field. Correspondingly, a complete jetting cycle is divided into four stages: liquid accumulation, formation of the well-known Taylor cone [90, 91], droplet ejection (or jet ejection), and relaxation. The entire sequence takes about 0.5 ms.

During the first stage, the liquid accumulates at the end of the needle tip due to the net flow from the liquid reservoir. The almost spherical meniscus indicates that the surface tension is the dominant force during this stage. The application of the electric field will cause mobile ions in the liquid to accumulate near the surface of the liquid meniscus. Consequently, a tangential electrostatic stress, known as the Maxwell stress [86], will be induced on the liquid surface, due to the mutual coulombic repulsion between these ions. With the accumulation of surface charges, the initial spherical meniscus changes its shape gradually into a conical form under the tangential Maxwell stress, as shown in the second stage. The decrease in the radius of curvature at the cone apex continues until the Maxwell stress matches the maximum capillary stress. At sufficiently high surface charges, the Maxwell stress overcomes the capillary tension and jet (or droplets) ejects from the apex (the third stage, 252-412 μs) to expel some of

these surface charges (known as the Rayleigh limit). Both the cone volume and the charges decrease due to the ejection, resulting in a Maxwell stress less than the capillary tension. As a result, the ejection stops; a fast retraction of the liquid is observed and the cycle repeated, as shown in the fourth stage.

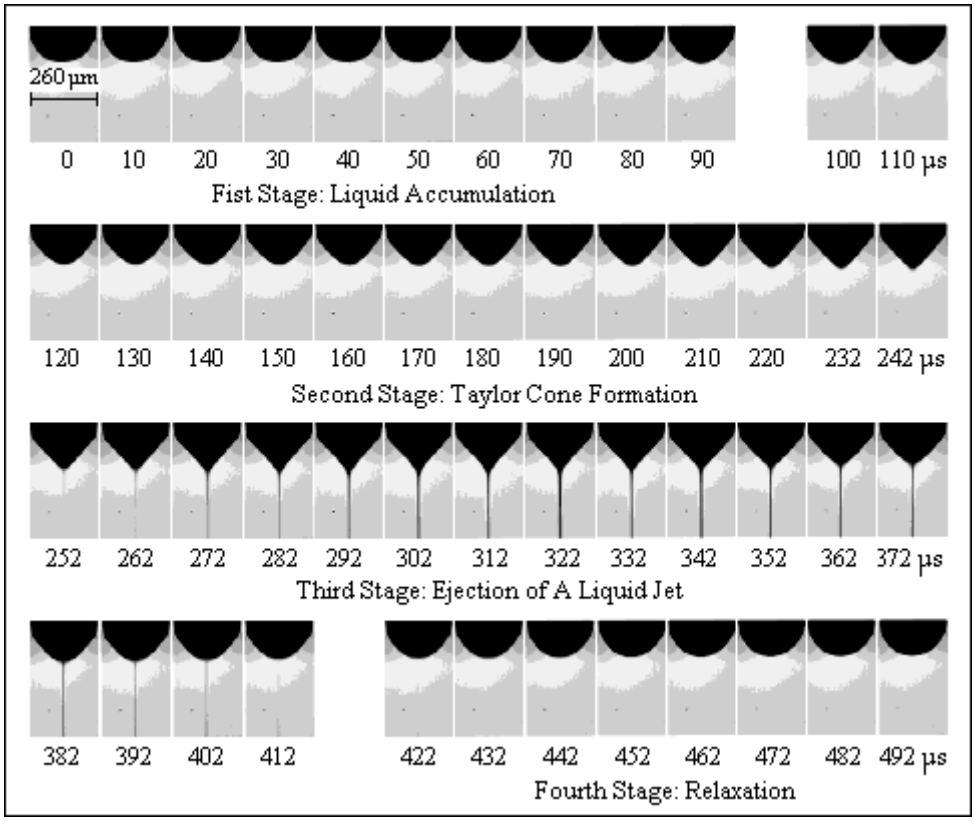

Fig. 2.33: Time-lapse images of the pulsating Taylor cone with the four stages of the complete jetting cycle. Each frame is an average of 100 exposures with the same delay. [89]

The above jetting process is well-known as the pulsating mode jetting. It is found that at sufficiently high electric field, a stable jet mode could be obtained, in which a continuous liquid stream rather than pulsating jet emerging from the needle. Both jetting modes can be used for high-resolution printing, while the pulsating mode jetting might be preferred in the sense of jet-on-demand, as in drop-on-demand inkjet printing. Different research groups [78, 86, 92, 93] have demonstrated the success of the method in

patterning structures with critical dimensions as small as 1 μm, as shown in Fig. 2.34.

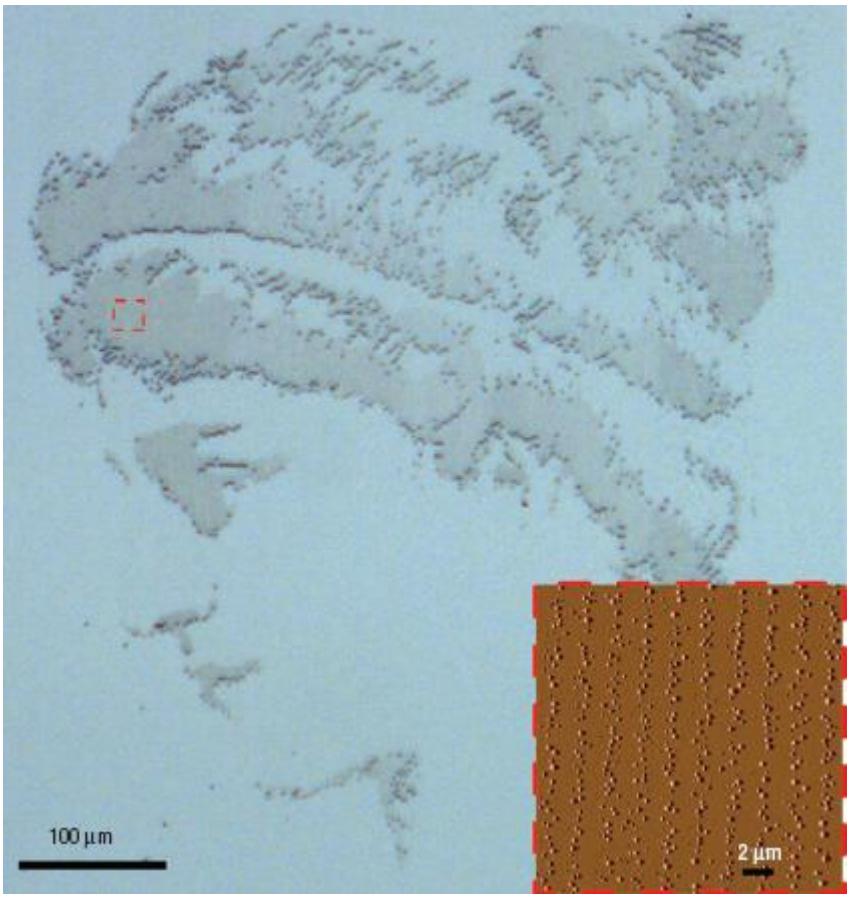

Fig. 2.34: High-resolution e-jet printing with printed feature size smaller than 1 μm. [86]

It is worth noting that the complete jetting cycle for above pulsating mode e-jetting normally lasts for 3 to 10 ms [86], which corresponding to a maximum jetting frequency of around 300 Hz. Unlike using DC high electric field in pulsating jetting, there is another type of e-jet, the pulsed-voltage mode, in which pulse waves of high voltage are used to switch electrohydrodynamic force ("on" or "off") [94, 95-98]. It also requires more than 3 ms [95] for Taylor cone formation, after applying the pulsed voltage. Consequently, it is also theoretically impossible to produce jets (or droplets) of a frequency higher than 300 Hz. Kim *et al.* [99] demonstrated that this maximum jetting

frequency could be increased to 5 kHz, by combining electrohydrodynamic force and the mechanical actuation from a traditional drop-on-demand printhead. The basic idea of this so-called hybrid jetting system (HJS) is: by utilizing the expansion and contraction of the piezoelectric element, to accelerate the "liquid accumulation", "Taylor cone formation" and the "relaxation" stages during the pulsating mode e-jetting. As a result, the jetting frequency can be increased [100]. However, this hybrid jetting technique is still of low throughput, as compared to the conventional drop-on-demand inkjet which generally has a maximum jetting frequency above 10 kHz.

To conclude, the e-jetting technique allows the generation of ultra-fine droplets (or jets) down to 1 μm; however, at the cost of reduced throughput. Furthermore, it has rigid restrictions on the liquid to be used, such as the conductivity and other physical properties.

2.4 Organ Printing - Science Rather Than Fiction

Positioning of living cells in a desired pattern onto a substrate is extremely important to cell-based technologies, including the fundamental investigation of cell functions and tissue engineering [101, 102]. The more exciting thing is that nowadays the self-organizing properties of cells and tissues are used by material scientists and tissue engineer to build 3-D living structures, as shown in Fig. 2.35. The generation of such structures forms the basis of tissue regeneration and possibly, the fabrication of implantable organs [2].

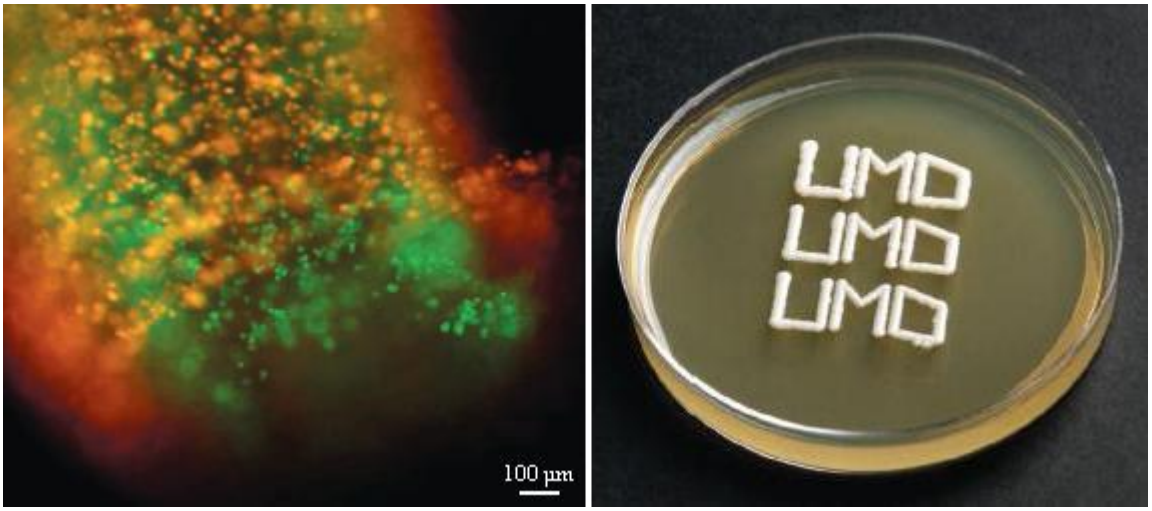

Fig. 2.35: Printed cells. (a). 3-D tube structure made from printed cells. The image shows an inner layer of human umbilical endothelial cells (green) and an outer layer of human aortic smooth muscle cells (red). (b). Printed yeast patterns after 3 days of culture. [2]

2.4.1 How to Realize

Inkjet printing is a suitable candidate for organ printing. The power of inkjet printing lies in its ability to deliver picoliter volumes of materials at high speed and accuracy on a target interface (probably non-planar surface), and to deliver active substances to a developing structure in a well-defined timing sequence. By using different cell types as different bio-inks, and delivering them to exact positions to mimic tissue structures of the original tissue, inkjet printing offers a possible solution for building whole structures such as bone, cornea, ligament, cartilage etc, to solve the organ transplantation crisis. It has been used successfully in a similar manner for automated rapid prototyping technology which precisely positions droplets onto a substrate. However, printing living cells into a desired structure which can ultimately grow to an implantable organ is a much more challenging task.

Firstly, cells have to survival from the shear stress during the printing, and keep their viability. Fortunately, to date, many different cell types have been printed successfully by different printing methods and their viability has been verified [3-10, 103]. By dispensing human fibroblast cells through a 60 μm nozzle, Saunders *et al.* carried out a comprehensive study to investigate the relationship between cell survivability and the inkjet printing parameters [9]. Their study supported previous claims [4, 5, 8, 10] that cell survivability was not significantly affected by the printing process since cell survival rates only fell from 98% to 94% when the excitation pulse was increased from 40 to 80 V. However, in all above studies, the printing process was carried out with relatively bigger nozzle diameters (normally bigger than 60 μm) and lower droplet velocities (1.0 to 3.0 m/s). These limitations may be of importance, because the shear stresses, which are expected to be the main factor in the killing of cells during the printing process, are proportional to the velocity gradients within the nozzle. In fact, shear stresses have been studied extensively to predict the damage of animal cells suspended in various laminar or turbulent flows [104-107]. To conclude, high rate of cell death might be possible during printing when smaller nozzle and high droplet velocity are required.

After verifying viability of the printed cells, the second step towards organ printing should be successful generating of 2D cell patterns. The number of cells inside each printed droplet will be one important factor for reliable cell printing, as "empty droplet" and cell-less droplets may be undesirable. For well prepared cell ink, this number mainly depended on the cell concentration of the cell ink as well as droplet volume [8, 103]. However, during the printing,

cell agglomeration or sedimentation may be occurs [9, 108], thus undesired variations in this number can be produced. The most direct and effective way to avoid such "empty droplet" should be increasing cell concentration of the cell ink. Another important issue is that the printed cells should be able to adhere, spread and proliferate on the substrate. Thus cells are normally printed on gels, such as alginate or collagen. Alginate has been increasingly utilized in tissue engineering to support encapsulated cells and to regulate cells function, in a manner similar to the extracellular matrices of mammalian tissues [109]. Alginate's popularity comes from its advantages of biocompatibility, nonimmunogenicity [110] and gentle gelling behavior [111]. However，the major limitation to its use as extracellular matrices is that alginate does not mediate mammalian cell adhesion [112, 113]. To promote cell adhesion within alginate gel, ligands such as arginine-glycine-aspartic acid (RGD) [114-117], GRGDY [118], KGD and VAPG [115] have been used. Collagen is another widely used hydrogel with a number of advantages including biodegradability, low immunogenicity and controllable stability. Furthermore, collagen contains cell adhesion domain sequences such as RGD, thus can facilitate cell adhesion for anchorage-dependent cell types [119, 120].

Thirdly, the most ambitious, also the most challenging step is to create 3D living structures. The conversion from cell suspension into 3D organ structures needs to be guided by 3D scaffolds as cells normally do not self-assemble into organ-like structures [122]. There are two possible ways to incorporate cells into such a scaffold. The first method is to create a degradable 3D scaffold first, and then seed cells into it, as shown in Fig. 2.36.

The scaffold has following important functions: serving as an adhesion substrate for the cell, promoting cell proliferation and cell-specific matrix production [123]; providing mechanical support in the initial tissue growth stage; guiding the development of new tissues with appropriate function [124]. The porosity and the internal pore organization of the scaffold have an important influence on its biodegradation dynamics, mechanical stability and nutrient diffusion, as well as on cell migration [125]. Conventional methods for fabricating scaffolds include phase separation [126], particulate leaching [127], gas foaming [128], freeze-drying [129, 130] and electrospinning [131].

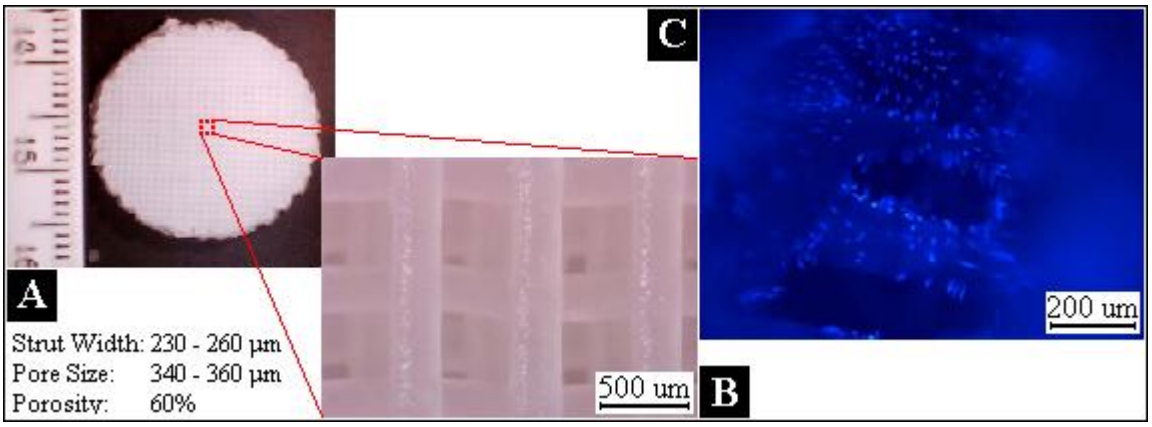

Fig. 2.36: 3D scaffold and the cells seeded into it. (a). A 3D scaffold fabricated by rapid prototyping method. (b). Big view of the scaffold shown in (a). (c). Human fibroblast cells seeded into a 3D scaffold, after 18 days of culture. [121]

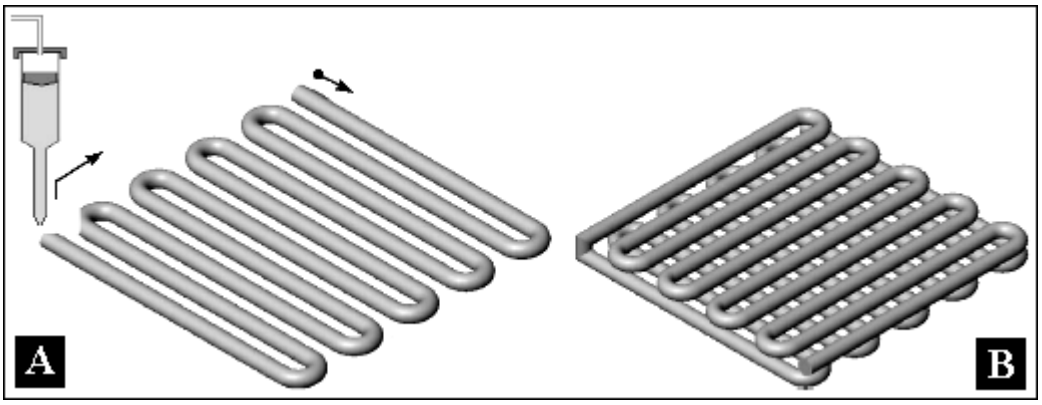

Fig. 2.37: Fabrication of a scaffold by 3D plotting. (a). One layer. (b). Two layers. [122]

However, above processing methods have inherent limitations in precise control of pore size, pore geometry, pore interconnectivity, spatial distribution of pores, and construction of internal channels within the scaffold [123]. Different new techniques have been proposed to eliminate these limitations, among them, a new Rapid Prototyping technology based upon 3D plotting technology, was developed to produce scaffold with complex architectures according to computer design [132]. A key feature of the technology is its ability to create 3D structures from liquids and pastes in liquid media. As shown in Fig. 2.37, by positioning individual microdroplets and in situ bonding them, it is possible to layer-by-layer fabricate scaffolds with desired interconnecting pore design, thus meeting the demands for cell attachment and cell growth. Currently this method has been widely used for 3D scaffold manufacture [123, 133, 134, 135].

It is worth noting that above method of creating 3D living structures is based on the premise that seeding cells into porous biodegradable scaffolds will be sufficient to generate organs. However, Boland *et al.* [136] claimed that there were at least four limitations for the method:

- cell penetration and seeding is still far from optimal;
- organs generally consist of several different cell types, it is a challenging task to "seed" different types of cells in specific positions of the 3D scaffold;
- the rigid, solid scaffolds are not optimal for engineering contractile tissue, such as heart and vascular tubes;

- absence of vascularization is the main problem with using solid scaffold seeding technology.

Consequently, there is an increasing interest in the using of the second method, in which the 3D living structures is fabricated by directly incorporating cells into the scaffold fabrication process. As shown in Fig. 2.38, cells and a kind of "thermo-reversible" gel are positioned by inkjet printheads, to form alternate layers onto a glass slide. This method is also termed as "organ printing" [137]. The closely packed layers will coalesce providing that the alternating layers are thin enough. After the whole tissue grows up, the gel will degrade by simply cooling it.

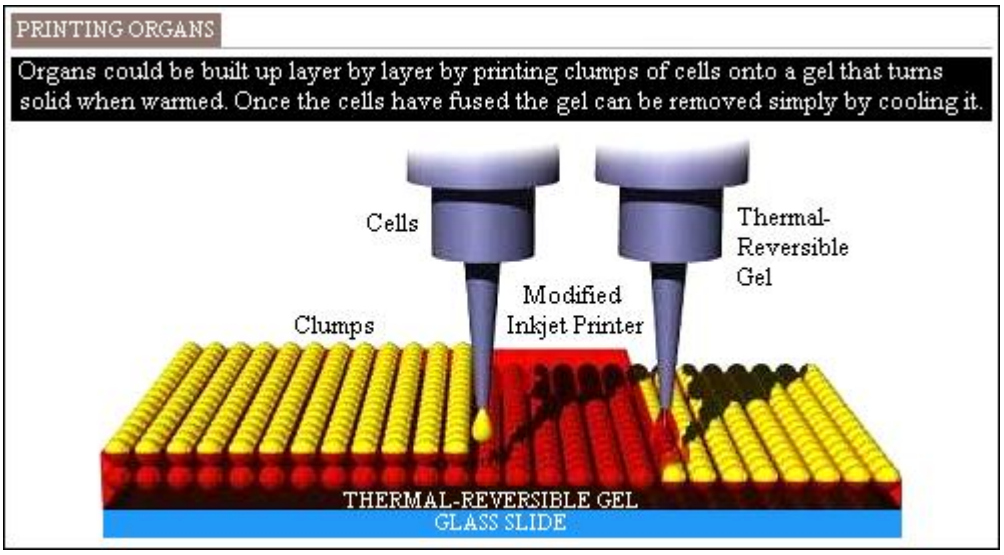

Fig. 2.38: Schematic diagram of organ printing. [138]

Herein the "thermo-reversible" gel, such as collagen, which behaves as extracellular matrix (ECM) to build 3D structures for long-term culture (similar to the 3D scaffold used in previous method), is generally squeezed out [139] from the nozzle rather than ejected by a printhead. The reason why not to directly print the thermo-reversible gel, or even straightforward, the cell-

laden gel is that the conventional piezo-based (or thermal-based) inkjet printhead is not easily adapted for solutions with high viscosity such as collagen. Solutions with quite low concentration of collagen (normally less than 0.5%, w/v), certainly, can be successfully printed, but is undesired when acting as extracellular matrix. To overcome this limitation, one method is to design and fabricate inkjet printhead that capable of printing liquids with high viscosities [140]. Another method is to utilize liquid materials that capable of solidifying after ejection, such as sodium alginate (SA) solution and fibrinogen solution [141]. For example, cell-laden alginate can be printed onto substrate which contains calcium chloride solution. Crosslink happens once the two liquids meet together, and the crosslinked alginate is able to control the position of the ejected cells.

Besides printing of cells, inkjet is also used to print different solutions [101], polymers [142], proteins [143-145] and growth factors into the living-structures, for mediating cell viability.

2.4.2 Challenges and Requirements

Although it has been widely acknowledged that "organ printing" is a promising technology for creating 3D living structures, plenty of challenges are still there and successful organ printing should most importantly fulfill the following requirements:

Cells in suspensions tend to agglomerate over around half an hour, which will lead to the non-uniformity in the cell ink. Moreover, bulks of cells can easily

clog the nozzle of the inkjet printhead and interrupt the printing process. Thus either the organ printing process should be rapid enough, or devices that can eliminate cell agglomeration should be designed and equipped into the cell ink chamber.

Despite the high resolution provided by inkjet printing method, it is difficult to exactly control a number of cells in one droplet, especially when small nozzle and/or low-concentration cell ink is used. To eliminate "empty droplet" and cell-less droplets, cell concentration in the ink, or the ink concentration, should sufficiently high.

Furthermore, cells should get rapid and continuous deposition and solidification onto the thermo-reversible gel; the gel must provide adequate mechanical support to the living structures; the gel should also allow adhesion, spreading and proliferation of multiple cell types; sufficient oxygen and nutrients have to be supplied to the cells which deep within the 3D structures; the gel should degrade in a regular and predictable fashion; mechanical strength of the grown-up tissue should also be considered as huge structure might not be strong enough to hold together by itself once the gel is removed.

To conclude, despite the various existing challenges, "organ printing" is feasible, fast-developing and predicted to be one of the most promising technologies in tissue engineering. It uses the principle of cellular self-assembly into tissues [146] and aims to build implantable organs to treat diverse diseases such as cancer, loss of tissue function, or organ failure. "It is

safe to predict that in the 21st century, cell and organ printers will be as broadly used as biomedical research tools as was the electron microscope in the 20th century". [137]

3. NOVEL PRINTHEAD DESIGN

The design and fabrication of a PET/PTFE-based piezoelectric squeeze-mode DOD inkjet printhead with interchangeable nozzles is presented in this section. The two methods, heating and pulling glass tubing, and silicon micro-machining, which are used to fabricate nozzles for the printhead, will also be reported. The characteristics of this novel printhead are studied by dispensing glycerin-water solutions and non-Newtonian sodium alginate (SA) solutions, and the experiment results with discussions are also documented in this section.

3.1 Introduction

As has been mentioned before, due to its unique advantages, the application of DOD inkjet printing technology has been expanded from conventional graphic printing to new areas, such as fabrication of integrated circuits (ICs) [20, 147], LED [44], rapid prototyping (RP) [148], MEMS, cell printing [2, 8, 9] and drug delivery [149]. Accordingly, the dispensed liquids have been expanded from the conventional pigmented ink (or standard dye-based ink) to polymers [12, 150-152], gels, cell ink or other materials which often have higher viscosities or even contain large particles or cells. Consequently, the traditional inkjet printer designed for graphic printing is unable to fulfill the new challenges, one of which is to dispense fluids of very high viscosities. For most of the commercial inkjet printheads supplied by companies like Microdrop, Microfab, Dimatix and XAAR, only liquids with viscosities lower than 20 cps [12] can be consistently dispensed. Fluids with even higher

viscosities have to be diluted before printing or warmed up during the printing, which will adversely affect the properties of the liquids.

Another challenge is raised by nozzle clogging. Fluids containing particles, or cells, can easily block the nozzle orifice, resulting in time-consuming nozzle cleaning or even damage of the entire conventional printhead. To solve the problem, the easiest way is to use a nozzle with a bigger orifice, as bigger orifices are less likely to clog. However, this is often not desirable in inkjet printing as bigger nozzles result in bigger droplets and lower printing resolution. In [21], Chen and Basaran reported that by judiciously controlling the piezoelectric parameters governing the flow within the nozzle and thereby the drop formation, droplets with diameters less than 40% of the orifice diameter could be produced. A similar study was carried out by Goghari and Chandra [22]. These studies reveal a possible way to solve this nozzle clogging problem without sacrificing printing resolution. However, their methods only work over a limited range of Ohnesorge numbers.

The poor printability and nozzle clogging may result in unreliable or failed dispensing when using the traditional inkjet printhead design for complex liquids.

In this section, we will present an in-house-developed PET/PTFE-based piezoelectric squeeze mode inkjet printhead with an interchangeable nozzle design. PET (polyethylene terephthalate) tubing, comprising of a much softer material, is used as the printhead chamber to substitute for the conventionally

used glass tubing [140]. Liquids with viscosities of up to 100 cps have been successfully dispensed by this novel printhead. When strongly corrosive inks are involved, Teflon tubing is served as the printhead chamber. The interchangeable nozzle design allows one to easily clean or change the clogged or damaged nozzle, avoiding the destruction of the whole printhead assembly.

3.2 Printhead Fabrication

Fig. 2.25 schematically shows the construction of a traditional piezoelectric squeeze mode printhead. By using epoxy adhesive, a piezoelectric element is tightly attached onto a glass tube which with an orifice at one end. When an electrical pulse is applied, the piezoelectric element will contract inward, squeezing the glass tube as well as the liquid inside. In order to eject a droplet from the orifice, the volume change within the piezoelectric transducer, due to the electrical pulse, must exceeds the volume of liquid to be ejected. Furthermore, the volume change must be sufficient to develop enough pressure inside the liquid to overcome the surface tension at the orifice. The fractional volume change due to the piezoelectric effect is approximately:

$$(\Delta V/V) = -3d_{31}U/t \tag{3.1}$$

where d_{31} is the piezoelectric strain constant, U is the applied voltage and t is the thickness of the piezoelectric tube [61]. The negative sign indicates contraction when the applied pulse has the same polarity as the original polarizing voltage for the piezoelectric element. Equation 3.1 shows that the printability of a printhead is mainly depended on the piezoelectric strain constant and the geometry of the piezoelectric transducer. In this study, we

focus on how to improve the printability of piezoelectric squeeze printheads without pursuing high piezoelectric strain constant. All the piezoceramic tubes (PZT-5H, from Boston Piezo-Optics Inc.) have the same piezoelectric strain constant d_{31}, approximately -275×10^{-12} m/V, at 25 ˚C.

The basic idea is to reduce the energy loss during the deformation of the liquid chamber, by replacing the traditionally used glass tube with PET or Teflon tube. Accordingly, the printhead is divided into two parts: a printhead chamber and an interchangeable nozzle attachment fitted tightly to the chamber by screw threading. These will now be described in turn.

3.2.1 Printhead Chamber

The design of the printhead chamber is illustrated in Fig. 3.1. The PET heat-shrink tubing has a relative low shrinking temperature ranges from 85 ˚C to 190 ˚C. Thus a hair drier is recommended to be the heat source, rather than a burner which could burn up the tubing if overheated. To get a uniform shrunken tubing with a desired diameter, a steel tube with 4.9 mm OD is inserted into the PET tubing during the heating process, as a mould. The PET tube with 6.0 mm OD and 0.1 mm wall thickness (230400CHGS, from Advanced Polymers, Inc.) is evenly heated, shrinking it to a tubing with approximately 5.2 mm OD, so that it can fit exactly inside the piezoceramic tube. This shrunken PET tubing is used as the inner wall for the printhead chamber, which directly contacts with the liquid to be dispensed. By using electrical conductive epoxy (CW2400, from ITW Chemtronics Inc.), the shrunken PET tubing is glued to the inner wall of the piezoceramic tube (PZT-

5H, from Boston Piezo-Optics Inc.) with 6.35 mm OD, 0.5 mm wall thickness and 25.4 mm in length.

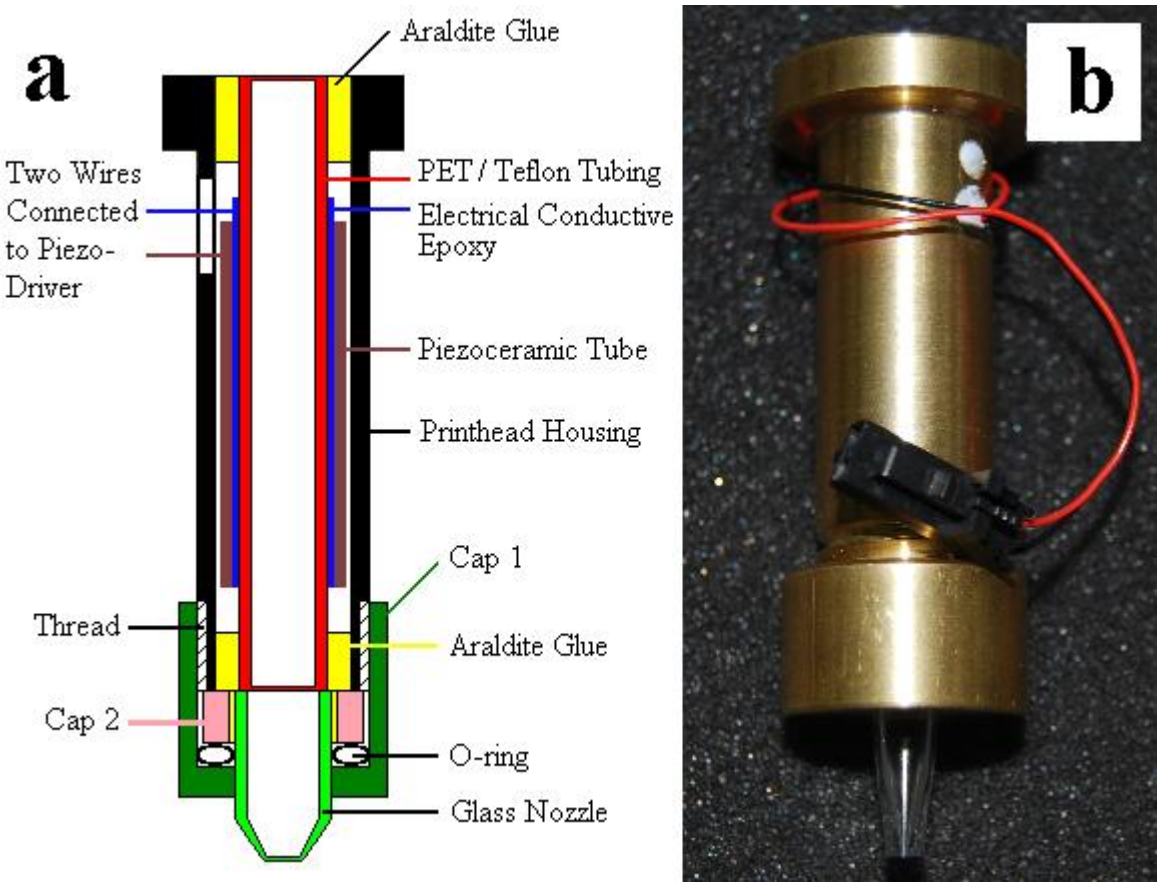

Fig. 3.1: The novel printhead. (a) Schematic showing of the design (out of proportion). (b) A self-fabricated printhead following the novel design.

Teflon tubing serves as the printhead chamber when strongly corrosive inks are involved, due to its perfect anti-corrsive property; however, it is such a non-stick material to be directly bonded to the inner surface of the piezoceramic tube. Fortunately, sodium-based chemical etchant can be used to etch the surfaces of the Teflon material, to make it bondable to another material. In this study, the PrimeEtch® Plus solution, provided by Plastomer Technologies, an EnPro Industries company, is used as the etchant. Teflon tubing (from Zeus, Inc.) with 5.22 mm OD and 0.25 mm wall thickness is dipped into the etchant for 5 minutes. The etching takes place to a depth of a

few hundred angstroms and modifies only the surface composition of the Teflon tubing, leaving other properties of the tubing unaffected, even the dimensions. The etched Teflon tube is then rinsed in alcohol for 2 minutes, dried, and glued to the inner wall of the piezoceramic tube by using electrical conductive epoxy (CW2400, from ITW Chemtronics Inc.), forming the printhead chamber.

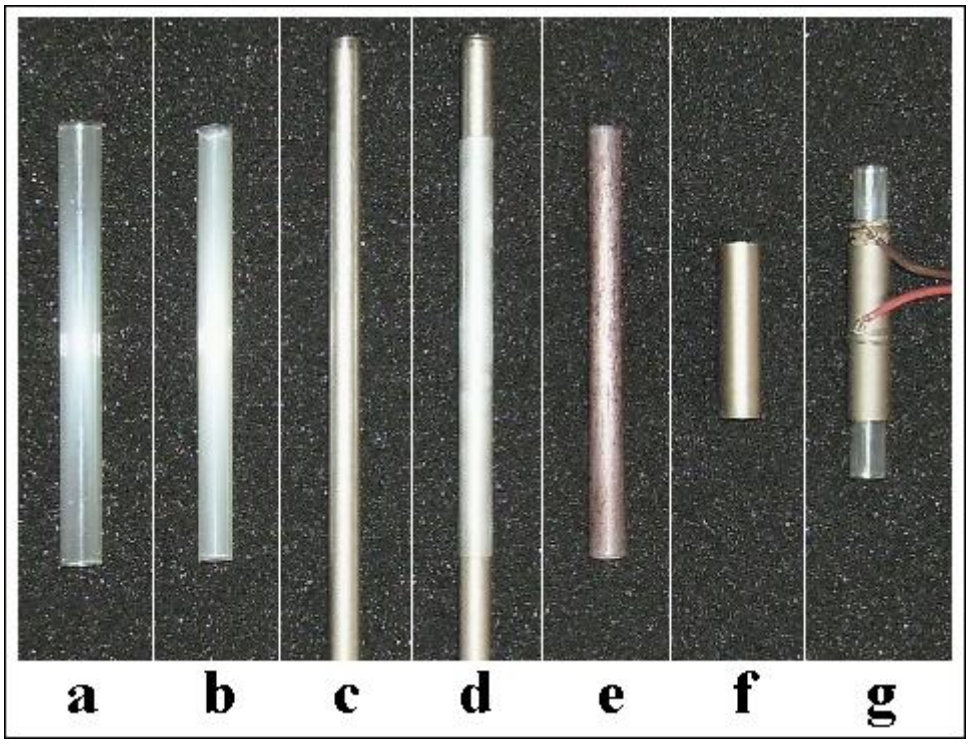

Fig. 3.2: Schematic showing the fabrication of the printhead chamber: (a) PET tube before shrink. (b) Teflon tube before etching. (c) The steel tube used as a mould during heating of PET. (d) PET tube after shrink. (e) Teflon tube after etching. (f) Piezoelectric tube. (g) Shrunken PET tube bonded to the piezoelectric tube.

In the next step, two wires are separately attached to the inner and outer wall of the piezoceramic tube by using electrical conductive epoxy, for connecting the printhead to the piezo–driver, as shown in Fig. 3.2(g). Then the whole part is fixed inside a brass housing by araldite epoxy adhesive for protection. The solidified araldite epoxy can also prevent short circuit which can be caused by liquid permeation to the piezoceramic tube. The two connecting wires are pulled out through a hole in the housing, and the hole is also sealed with

araldite epoxy, as shown in Fig. 3.1(b). An outside thread is cut on the bottom of the brass housing for connecting the housing to the nozzle adaptor. Fig. 3.3 schematically shows the design of the brass housing and the nozzle adaptor.

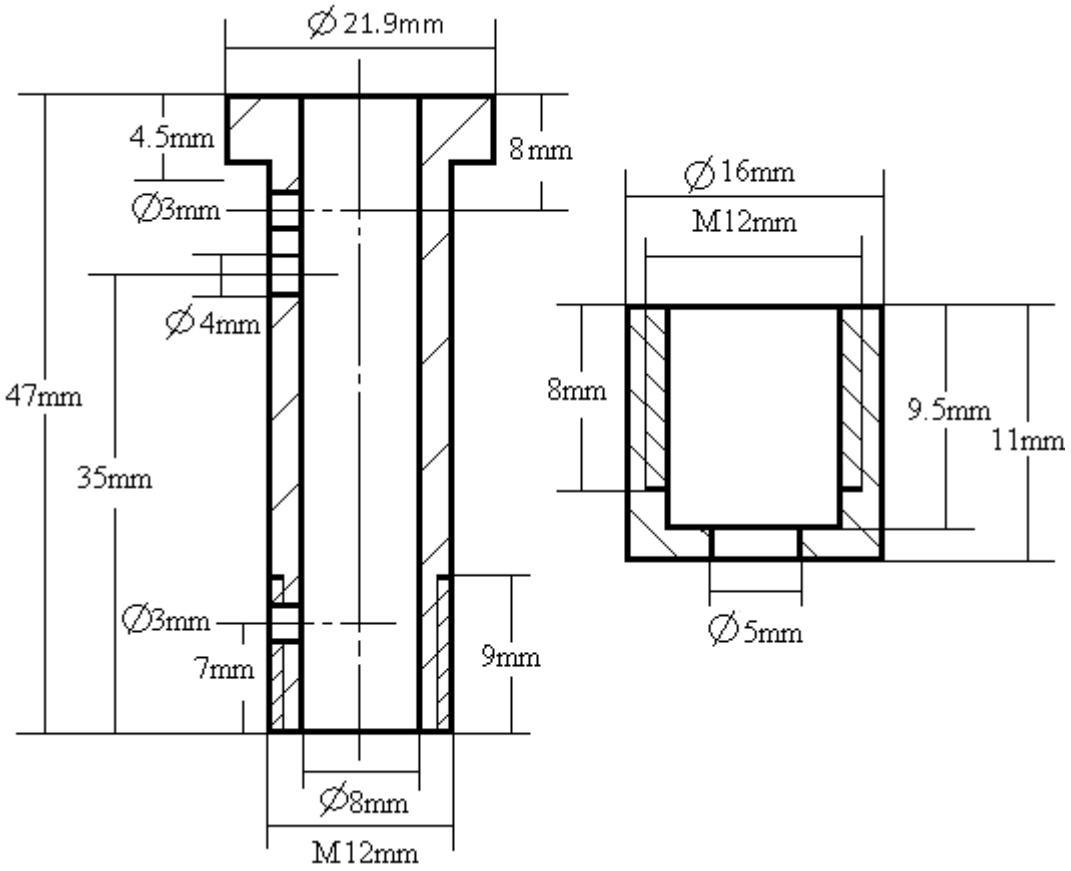

Fig. 3.3: Schematic showing the design of the printhead housing and the nozzle adaptor.

3.2.2 Interchangeable Nozzle Design

The glass nozzle is fabricated by heating and pulling a glass tube, as demonstrated by Lee [68]. The setup is graphically shown in Fig. 3.4(a). A glass tube with 5.0 mm OD and 3.5 mm ID is vertically fixed to a motor which rotates the tube about its axis. By applying local heat to the lower section of the rotating glass with a propane torch, the glass tube is melted at the location of the flame, and pulled longer by the weight of its lower portion until it

finally breaks into two parts, each of which contains a hollow cone with a closed end. The closed end is then polished by fine sand papers until an orifice of a desired diameter is exposed, as shown in Fig. 3.4(c). By this method, orifices of 13 μm to 300 μm have been fabricated in this study. A similar glass-fabricated nozzle was also adopted by Fan *et al.* [153].

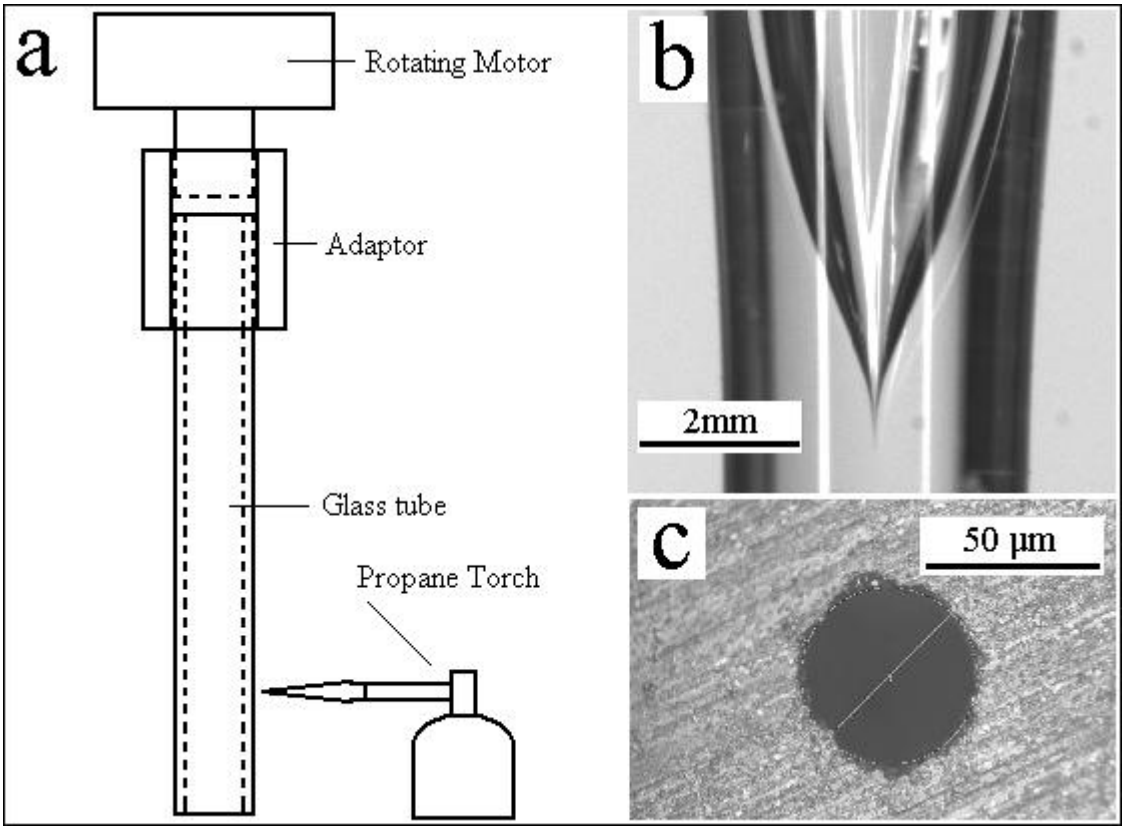

Fig. 3.4: Fabrication of a glass nozzle by heating and pulling glass tubing. (a) Drawing of the glass tubing heating system (out of proportion). (b) Glass tubing containing a hollow cone with a closed end. (c) A 50 μm orifice fabricated by polishing the end of the tubing showing in (b).

As recommended by Lee [68], to generate an axisymmetric conical nozzle profile, the rotation speed of the motor is maintained around 600 rpm.

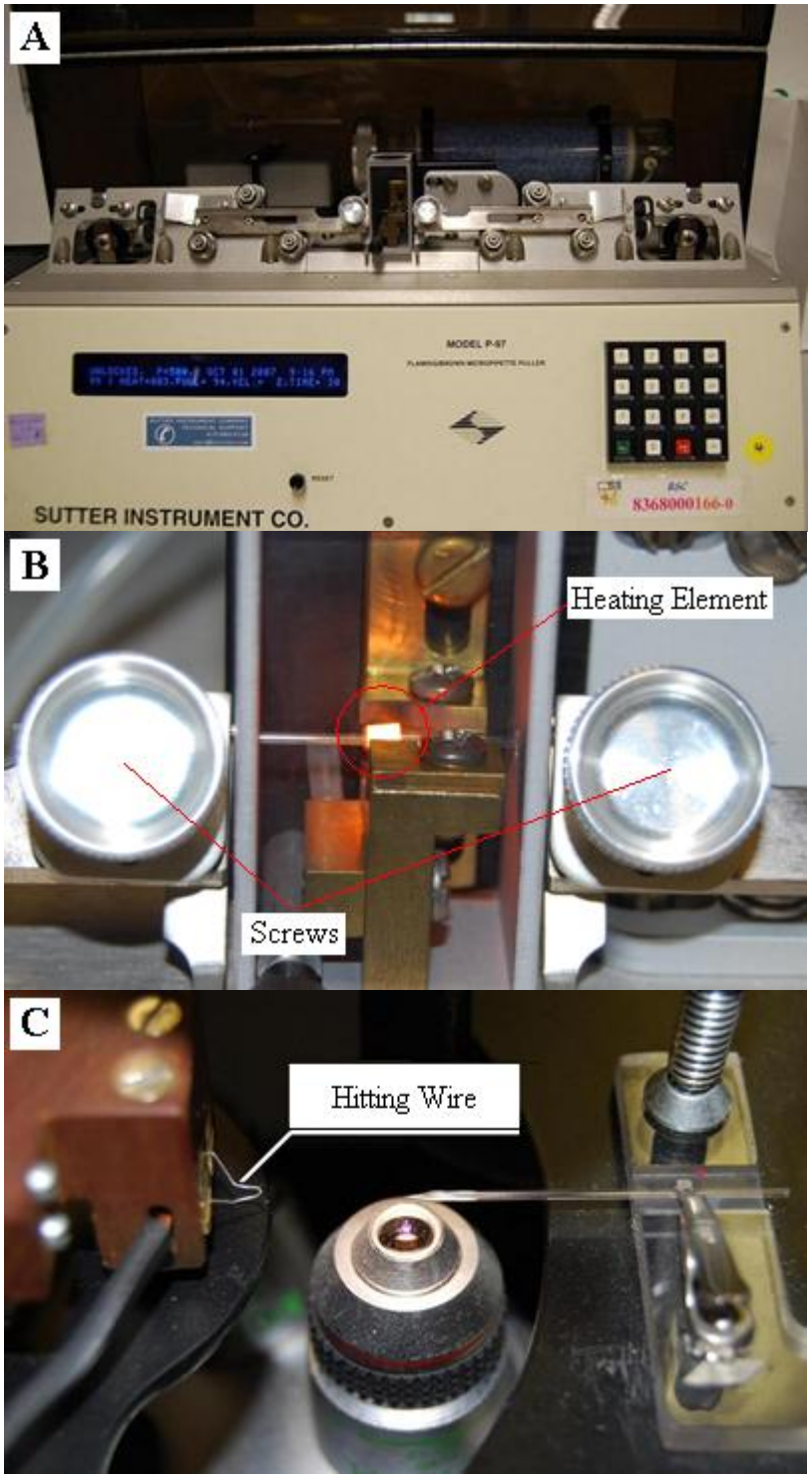

Fig. 3.5: Fabricating glass nozzle by heating and pulling 1.0 mm glass capillary with a micropipette puller. (a). The P-97 Flaming/Brown type micropipette puller. (b). Heating the capillary. (c). Hit the sharp tip to from an orifice.

The major advantage of this nozzle fabrication method is ease of manufacture and low cost. However, it is difficult to precisely control the taper angle of the nozzle.

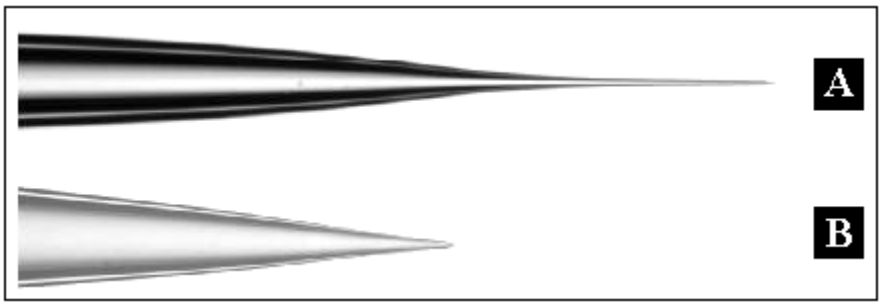

Fig. 3.6: Different shapes of tips fabricated by the micropipette puller. (a). A too "sharp" tip. (b). A tip with a moderate converging shape.

To eliminate this limitation, a professional micropipette puller (the P-97 Flaming/Brown type micropipette puller, from Sutter Instrument Company) can be used to heat and pull the glass capillary (TW100-4, from World Precision Instruments) with 1.0 to 2.0 mm OD diameter. As shown in Fig. 3.5(b), a glass capillary is inserted through the heating element. Two screws are used to fix the two ends of the capillary. Two separate springs are connected to the screws, thus the screws will pull the two capillary ends to opposite directions. After setting a desired program, the capillary is heated and pulled, breaking into two parts, each of which contains a hollow cone with a sharp tip. The sharp tip is then hit by a heated hitting wire under microscope, forming a tiny orifice, as shown in Fig. 3.5(c).

Using this method, a sharp tip with an outer diameter of even 60 nm can be fabricated. However, such a sharp tip normally has a slender shape, as shown in Fig. 3.6(a). It is not suitable for inkjet printhead nozzle usage as it has too much flow resistance, which will lead to difficult jetting even failure of jetting. Actually, the shape of the sharp tip can be controlled by setting different program, in other words, by changing the heating temperature and the pulling speed. Fig. 3.6(b) shows a desired tip shape for inkjet printhead nozzle

application. The second tip has a moderate converging shape and will have a lower flow resistance. However, in turn, leads to a relatively bigger orifice diameter. A tip with an orifice diameter of 13 μm is shown in Fig. 3.7. Tip with an orifice as small as 7 μm has been successfully adopted for jetting in this study.

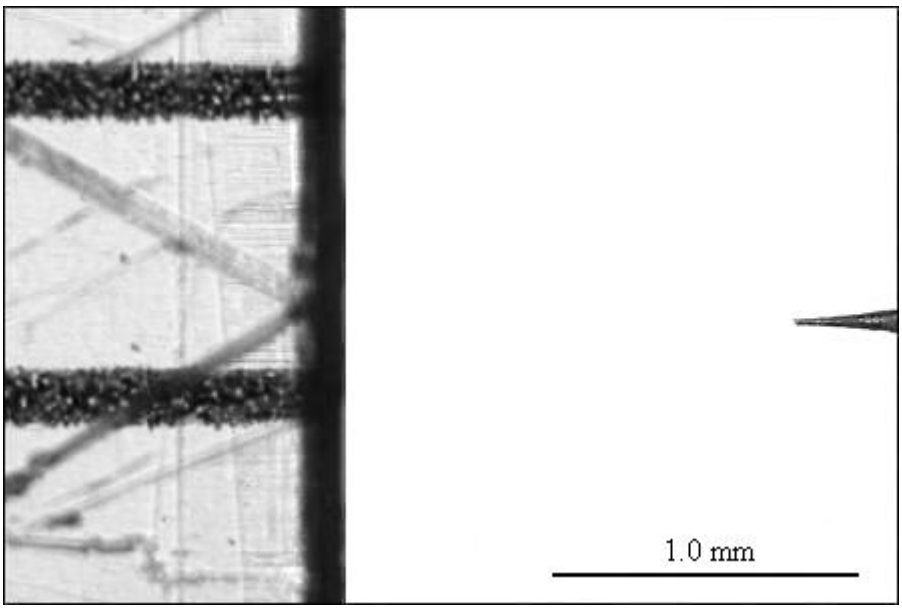

Fig. 3.7: A 13-micron-tip fabricated by the micropipette puller.

Fig. 3.8: Inkjet printhead nozzles fabricated from glass tube.

Fig. 3.1 also shows how the interchangeable nozzle design is implemented. After being fixed to a short brass cylinder (Cap 2 in Fig. 3.1) by araldite epoxy adhesive, the nozzle is placed inside another brass cap (Cap 1 in Fig. 3.1) that has an inside thread which is tightly fitted to the outside thread of the

printhead chamber. An O-ring must be used here to prevent cracking of the nozzle from overtightening of the threads. Fig. 3.8 shows different glass nozzles fabricated in this study.

Although tips with uniform shapes can be fabricated by this micropipette puller, nozzles fabricated from such tips are normally quite fragile. Furthermore, when it goes to the tip hitting process to form the orifice, non-uniformity emerges again. To obtain mass productability and exact reproducible desired nozzle profile for large production runs, silicon micromachining method can be used [68].

3.3 Experimental Testing of the New Printhead

3.3.1 Experimental Setup

Experimental tests were carried out to investigate the characteristics and repeatability of the PET/PTFE-based printhead, as well as to compare the ejection capacity of the PET/PTFE-based and the glass-based printheads.

The experimental setup is comprised of an air compressor, a pressure regulator, a liquid reservoir, a piezoelectric actuated printhead, a piezo driver, a stroboscope light and a CCD camera, as shown in Fig. 3.9.

The fluid to be dispensed is filled into a 60 ml stainless steel reservoir which is mounted on a XYZ motion stage. The combination of the air compressor and the pressure regulator (AD 3000D, from Iwashita Instruments Pte Ltd.)

provides a negative pressure in the reservoir to hold up and prevent the liquid from leaking out of the orifice of the printhead. Before getting into the printhead, the liquid is filtered by passing it through a syringe filter with 0.2 μm pore size membrane (Ref. 4652, from Pall Corporation) to remove large particles which might block the nozzle. Electric signals are sent by a JetDrive^{TM}III (from Microfab Technologies Inc.) to the piezoelectric transducer, causing alternating expansion and contraction of the transducer as well as the printhead chamber, ultimately, squeezing the liquid inside the chamber and ejecting a droplet from the orifice.

The inkjet process is produced by a periodic driving voltage and the resulting droplet ejection is repeatable from one droplet to the next. This allows for stroboscopic imaging to determine the formation and the ejection velocity of the droplets. Concurrently with the printing, signals are also sent by the driver to a stroboscope (MS-200, from Nissin Electronic Co., Ltd.) which has pulse duration of 2 μs and is therefore capable of freezing an image of the high-speed droplet with minimum blur. The droplet shape is illuminated by the flashing of the strobe light and the images are captured by a JAI CV-A11 camera (from Ultravision Pte Ltd.). To determine the droplet velocity, the stroboscope was operated at the same frequency as the printhead driver. By varying the time delay between the signal for the stroboscope and signal for the piezoelectric transducer, sequential images of the droplet during its motion are captured with known time differences. The droplet velocity can then be derived by dividing the spacing between the droplets by the time difference

between two frames. Fig. 3.10 shows a representative typical droplet formation sequence, the droplet is 50 μm and its velocity is 0.69 m/s.

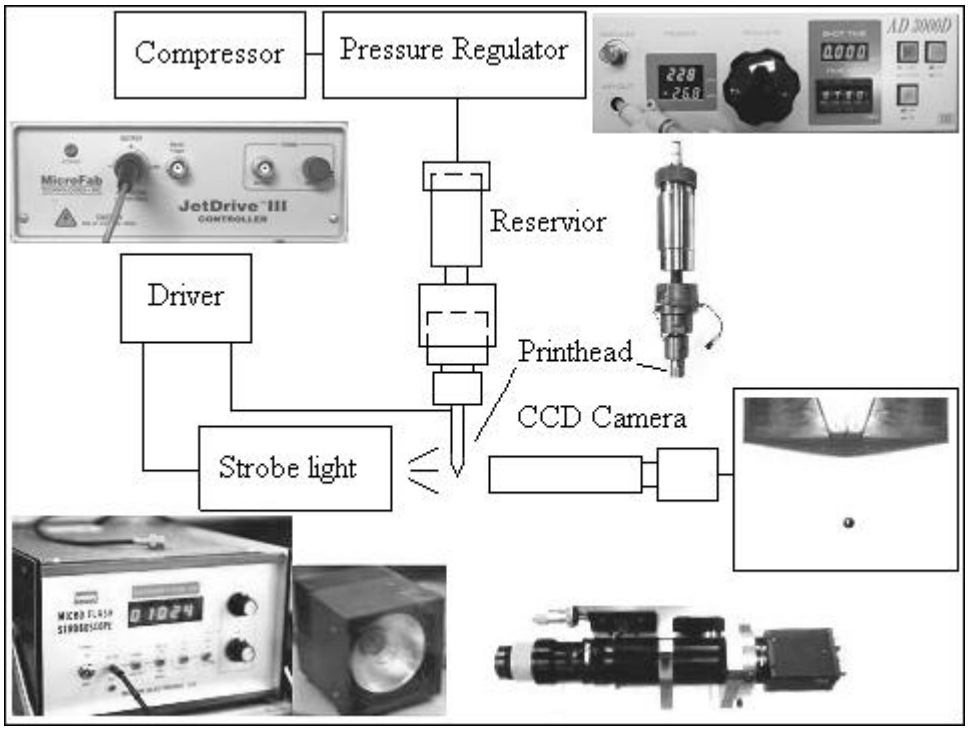

Fig. 3.9: Schematic showing of the drop-on-demand inkjet printing system used in the experiment.

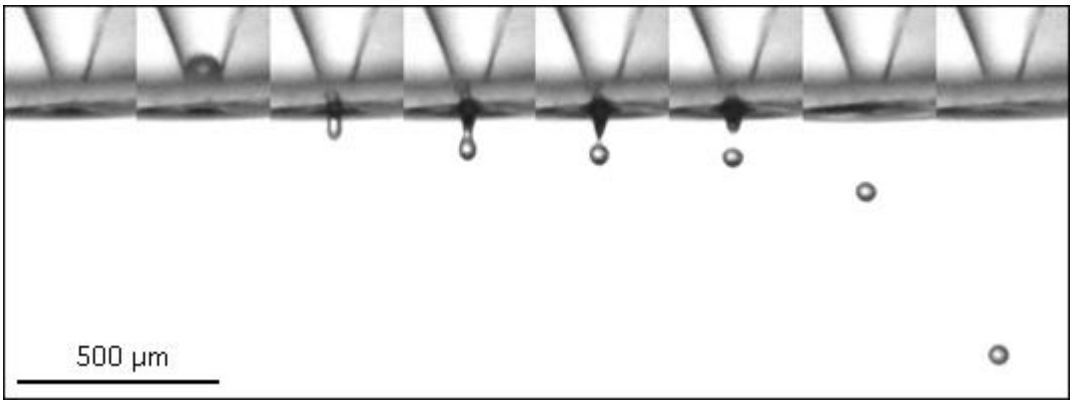

Fig. 3.10: Image sequences showing the formation of a 50 μm droplet from a 36 μm inkjet nozzle. The times shown are 0, 144, 322, 367, 389, 400, 522 and 1122 μs relative to the first frame. The droplet velocity is here determined to be 0.69 m/s.

The droplet size is determined by two different methods, i.e. either measured directly from the images, or by a weight method. In the latter method, printing is carried out in a vapor-saturated environment to suppress the evaporation of

the printed liquid, and then 7200 droplets are collected and then weighed for each test condition. Droplet diameter can then be calculated from its weight and the corresponding liquid density.

3.3.2 Experimental Conditions

The jet driver made by Microfab Technologies Inc. is able to send out voltage pulses with designed profiles. Up to 12 points can be set to form the signal waveform. Commonly used signals are of uni-polar, bi-polar or sinusoidal shape. The maximum allowable amplitude and frequency for the pulse is ±140 V and 30 kHz, respectively.

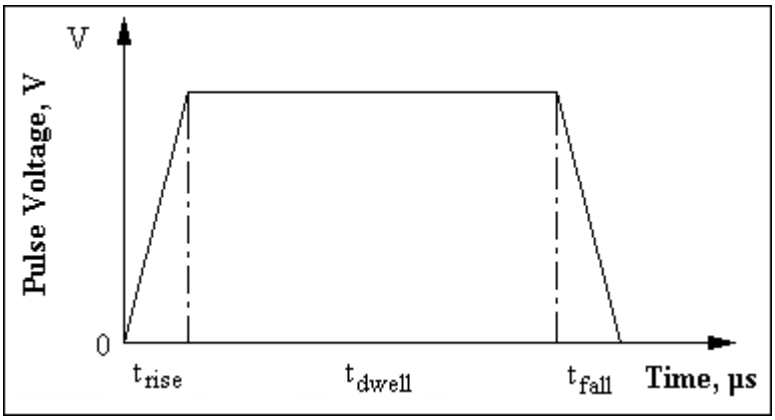

Fig. 3.11: Schematic showing of the uni-polar pulse waveform.

Fig. 3.11 shows a uni-polar pulse employed in the experimental study. The zero line represents the equilibrium state of the piezoceramic tubing, without any external voltage. During the time of t_{rise}, the piezoceramic tubing expands outward to its maximum inner volume and holds that state for a time of t_{dwell}. During the time of t_{fall}, the piezoceramic tubing contracts inward, to its equilibrium state. The expansion and contraction of the piezoceramic tubing causes negative and positive pressure waves propagating and reflecting inside the printhead, which ultimately leads to droplet ejection [52]. During all the

experiments, t_{rise} and t_{fall} were kept at 3 μs, which are the minimum permitted values of the jet driver, with the purpose of introducing instant action of the piezoeceramic tubing.

Static pressure needs to be applied to the reservoir, so that the liquid will not flow out of the nozzle under the hydrostatic pressure. The negative pressure applied to the reservoir was determined by direct observation showing no liquid leaking and no air entertainment.

3.3.3 Testing Liquids

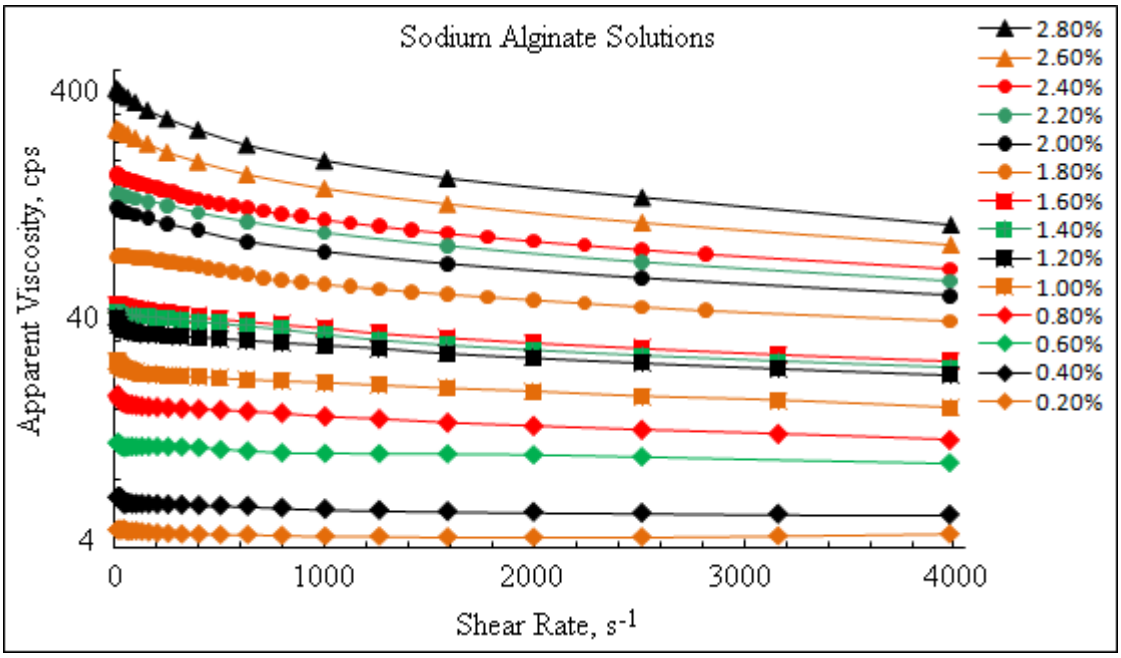

Fig. 3.12: Measured viscosities for different concentrations of sodium alginate solutions. Measurement at 20 ˚C.

The conventional pigmented ink or standard dye-based ink for graphic printing normally has a viscosity of less than 5 cps. However, to apply inkjet printing in the new areas mentioned earlier, various complex liquids like polymers, gels and other materials with much higher viscosities need to be effectively

dispensed. Thus, two types of liquids are used to test the new printhead: aqueous glycerin solutions with viscosities from 1 to 120 cps, and aqueous sodium alginate (A2158, low viscosity, Sigma-Aldrich) solutions with concentrations from 0.2% to 2.8% (w/v).

Aqueous solutions of sodium alginate were prepared by suspending the polymer in distilled water. After 6 hours of stirring by a magnetic stirrer, the solution was sterilized by sterile filtration, using 0.2 μm pore size membrane filters. The filtration did not change the concentration of the solution as the polymer has been totally dissolved.

The viscosity of the sodium alginate solutions was measured using the ARES Rheometer (TA Instruments, Inc.). The geometry involved consists of two parallel plates of 50 mm diameter with a gap of 0.5 mm. 1 ml sample was used for each measurement. The shear rates ranged from 1.0 to 4000 s^{-1}. As shown in Fig. 3.12, aqueous sodium alginate (A2158, low viscosity, Sigma-Aldrich) solutions behave as Newtonian fluids at low concentration of 0.2% to 1.6% (w/v) as the corresponding viscosities remain almost constant over a wide range of shear rates (1.0 to 4000 s^{-1}). The solution shows significant shear thinning behavior once the concentration exceeds 1.8% (w/v).

3.4 Experimental Results

3.4.1 Comparison of PET/PTFE-Based and Glass-Based Printhead

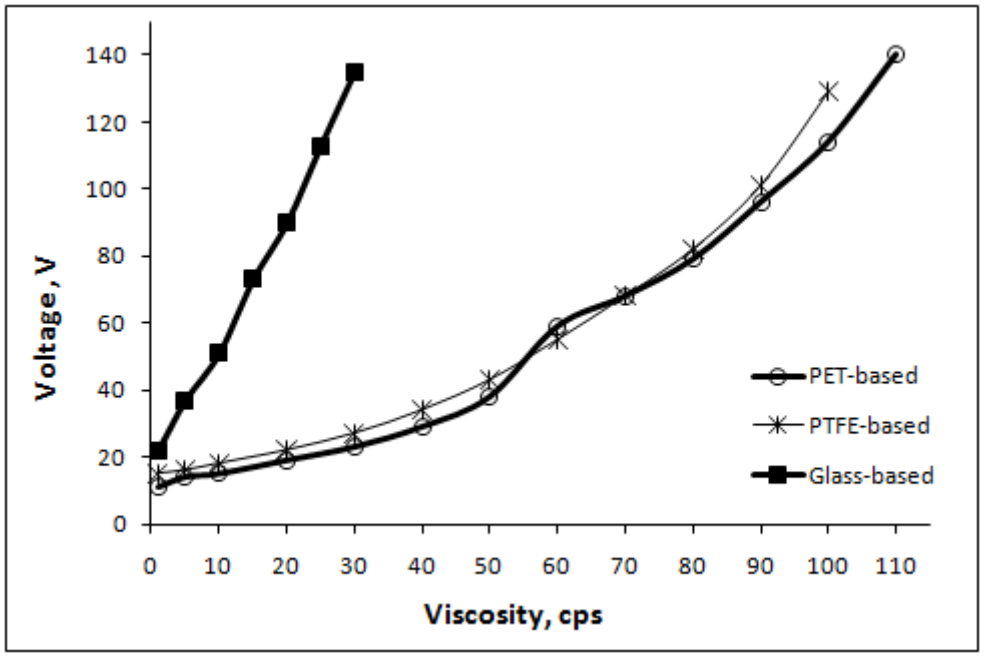

Fig. 3.13: Threshold voltages for PET-based printhead (–○–), PTFE-based printhead (–*–) and glass-based printhead (–■–). Nozzle diameter is 119 μm.

The commercial printheads fabricated by Dimatix, XAAR, Microfab and Microdrop can only dispense liquids with viscosity less than 20 cps [12]. In our printhead design, PET or Teflon tubing was used as the printhead chamber, but a separate glass-based printhead of similar configuration was also fabricated for this study to compare the dispensing capacity of the new type printhead and that of the glass-based printhead. Aqueous glycerin solutions with viscosities from 1 to 120 cps were used for the test. Fig. 3.13 shows the threshold voltage needed for dispensing glycerin solutions of different

viscosities. During the printing, the same nozzle of 119 μm diameter was used for both of the PET/PTFE-based and glass-based printheads.

It can be seen that the threshold voltage increases with the increase of fluid viscosity, for all of the printheads. However, for the same viscosity, the PET/PTFE-based printhead requires a much smaller threshold voltage than the glass-based printhead. Furthermore, the PET/PTFE-based printhead can dispense liquids with viscosity of up to 100 cps, which far exceeds the performance of the glass-based ones which are typically used in commercial printheads. The main reason for the lower voltage is that PET or Teflon is much softer than glass. When an electrical pulse is applied, the liquid chamber made of PET or Teflon tube is much easier to be squeezed by the piezoceramic element, thus less energy will be dissipated in the deformation of the liquid chamber. Consequently, a larger volumetric change will be achieved in the liquid, leading to a better dispensing capacity.

Furthermore, from eq. 3.1, for the piezoelectric tubes of the same wall thickness, the one with the larger diameter can generate a greater change in its volume. This is the reason why the self-fabricating glass-based printhead can only dispense glycerin solution with viscosity of 30 cps, which still exceeds the limitation of most commercial printheads. However, when the diameter of the piezoelectric tube increases, the diameter of the inner glass tube or PET/PTFE tube should also increase. Glass material is quite stiff and brittle; therefore, with the increase of its diameter, it becomes more fragile when the same wall thickness is used. However, with a thicker wall, more energy is absorbed in the glass and less volume change can be obtained. Fortunately,

PET or Teflon is quite pliable; by adopting them as the printhead chamber, the piezoelectric tube with a bigger diameter can be used to further improve the printhead behavior for dispensing materials with high viscosity.

3.4.2 Effect of Pulse Width

For PET-based printhead, the effects of pulse width on droplet diameter and droplet velocity were investigated by keeping the pulse amplitude constant at 50 V. Note that here the pulse width represents the duration of t_{dwell} in Fig. 3.11. The jetting frequency was kept constant at 120 Hz. The PET-based printhead and PTFE-based printhead behave almost the same, for simplification, only the results for PET-based printhead will be represented and discussed.

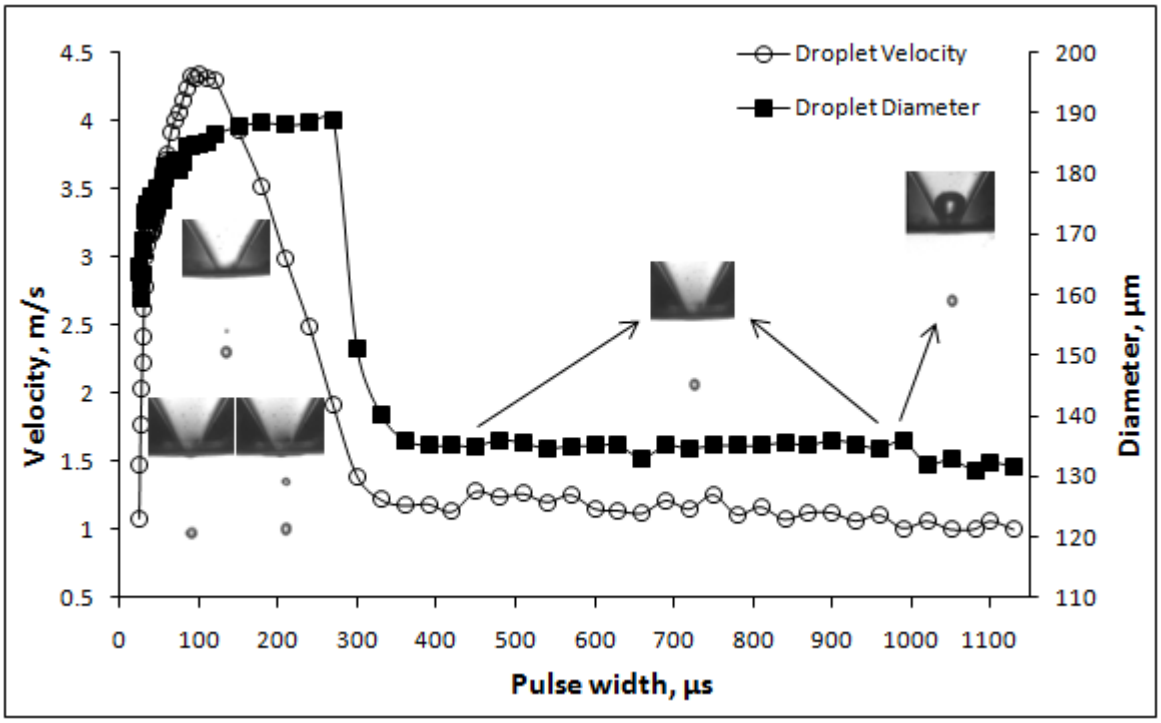

Fig. 3.14: Effects of pulse width on droplet velocity and droplet size. The pulse amplitude is 50 V. Nozzle diameter is 119 µm.

It is observed from Fig. 3.14 that both droplet velocity and droplet diameter initially increase with the increase of pulse width. The maximum droplet velocity 4.3 m/s is obtained when the pulse width reaches a value of 100 μs. Then droplet velocity rapidly decreases with a further increase of pulse width, reaching a minimum value of 1.2 m/s at 360 μs pulse width. The increase of droplet diameter continues until the pulse width is 120 μs. Then the droplet diameter is almost constant at a value of 188 μm until the pulse width reaches 270 μs, followed by a dramatic fall to the value of 135 μm. Both the droplet velocity and droplet diameter reach a near constant value after the pulse width exceeds 420 μs. With further increase of pulse width to 990 μs, air gets easily sucked into the nozzle, leading to a slight decrease of droplet velocity and droplet diameter.

According to De Jong *et al.* [154], there are two types or two reasons for this air entrapment. In the first type, the air entrapment is often related to the presence of an ink layer on the nozzle plate, especially for a nozzle plate without hydrophobic treatment. Within this ink layer, dust particles, which are deposited from the ambient air, can be transported toward the inkjet nozzle [155]. The reason for this transport lies in the fact that: during the time t_{rise} and t_{dwell}, the piezoelectric element has expanded outward, resulting in a negative pressure in the printhead which drives the ink (with the dust particles) toward the nozzle. Furthermore, according to Beulen *et al.* [156], the jet of droplets will transfer momentum to the ambient air, which will result in a suction of air towards the jet. Friction between the ink layer and the air flow induced by the

jet will also cause a flow of ink towards the jet nozzle. This so-called pulled back flow will also cause the transport of particles toward the inkjet nozzle.

When the particles reach the jetting nozzle, they will cause a local surface tension distortion and thus an asymmetry of the droplet formation. This asymmetry of the retracted meniscus in combination with the next symmetric pressure wave then will cause air entrapment [154, 157]. The entrained tiny bubbles will oscillate and coalesce with the neighbouring bubbles, moving along the inner wall of the printhead and growing through coalescence and rectified diffusion, forming a bigger bubble [158]. When this bubble grows big enough, normally much bigger than the diameter of the nozzle, it will absorb too much of the pressure energy generated by the piezoelectric element and thus stop the jetting. From this point of view, at a higher jetting frequency, more particles are likely to be driven toward the nozzle, thus air entrapment is more likely to happen.

In the second type, the air entrapment is also related to the presence of an ink layer on the nozzle plate. A void is formed once the meniscus is pulled back, due to the expansion of the piezo element. At the meantime, the pulled back ink from the ink layer closes the void, forming an air bubble inside the nozzle.

In this experiment, the nozzle plate does not have any hydrophobic treatment, thus a thin layer of ink will exist on the nozzle plate during printing. Furthermore, the jetting frequency was kept constant at 120 Hz here, while the air entrapment only happened when the pulse width exceeded 990 μs. Thus we

would like to say that the air suction in this experiment belongs to the second type of air entrapment. When a waveform of a very big pulse width is applied, the piezoelectric element expands for a longer time. As a result, meniscus is pulled too far into the nozzle during each dispensing process, allowing air to be easily sucked into the nozzle, forming a void inside the nozzle. At the same time, the pulled back ink from the ink layer on the nozzle plate closes the void, forming an air bubble inside the nozzle. Finally, a much bigger air bubble is formed inside the nozzle and totally stops the dispensing at a pulse width of 1160 μs. Single droplets without satellites can now be obtained in two ranges of pulse widths: 25 μs to 32 μs, and 420 μs to 1130 μs.

3.4.3 Effects of Voltage Pulse Amplitude

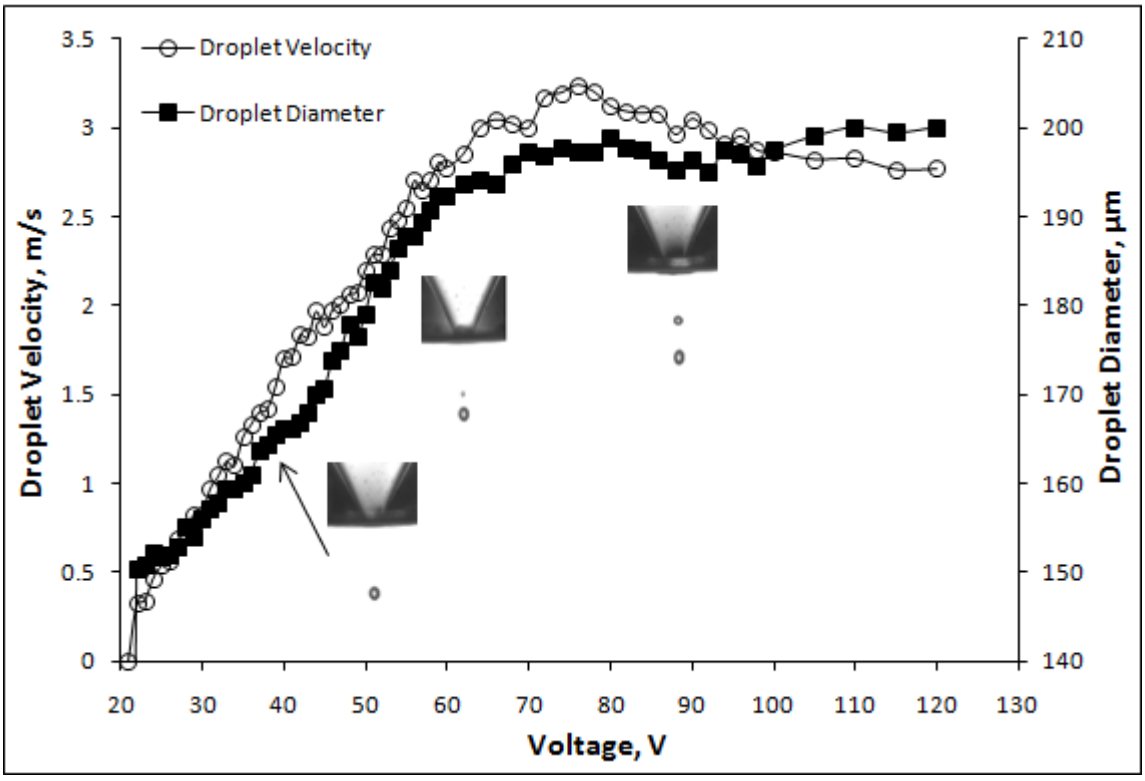

Fig. 3.15: Effects of pulse amplitude on droplet velocity and droplet size. The pulse width is 100 μs. Nozzle diameter is 119 μm.

The effects of the pulse amplitude on the behavior of the PET-based printhead were investigated by dispensing 5 cps aqueous glycerin solution through a 119 μm nozzle. From Fig. 3.14, it can be seen that the optimal t_{dwell} for generating a high velocity droplet is 100 μs. Herein the t_{dwell} was kept constant at 100 μs. The pulse amplitude was varied to the maximum which can be generated by the jet driver, i.e. 140 V. The jetting frequency was kept constant at 120 Hz.

As shown in Fig. 3.15, both drop velocity and drop volume increase initially with an increase of pulse amplitude. However, single droplets can only be obtained using pulse amplitudes from 21 to 40 V. Further increase in pulse amplitude generates a primary droplet followed by a small satellite droplet. This is understandable as a higher voltage causes a bigger volume change within the piezoelectric element, thus a longer column of liquid squeezed out and a satellite will be generated. The satellite droplet becomes bigger and tends to break into multiple satellite droplets as the pulse amplitude is further increased. The maximum droplet velocity is 3.24 m/s and the droplet diameter varies from 150 μm to 200 μm.

A slight decrease in droplet velocity is observed once pulse amplitude exceeds 76 V. The reason for this decrease lies in the fact that: during the time t_{rise} and t_{dwell}, the piezoelectric element has expanded outward, resulting in a negative pressure in the printhead which causes the meniscus to move into the nozzle. When very high voltage is applied, the piezoelectric element expands more. As a result, meniscus is pulled too far into the nozzle during each dispensing process, allowing air to be easily sucked into the nozzle. The sucked air forms

small air bubbles inside the nozzle which leads to the decrease of droplet velocity [159].

3.4.4 Nozzle Size

For a specific printhead with a fixed nozzle size, it is of interest to determine the smallest droplet and the biggest droplet that can be generated.

Eight different nozzle sizes were investigated for this printhead. For each nozzle size, the pulse width was 22 μs. Then the pulse amplitude was slowly increased from 10 V to 140 V in steps of 1.0 V, until the liquid can be regularly dispensed. The corresponding droplet diameter is recorded as indicating for the smallest single droplet. The pulse amplitude was further increased, until satellite droplet was generated along with the main droplet. Then the pulse amplitude was decreased by 1 V step length and droplets were collected. Droplet diameter was calculated and recorded as that for the biggest regular droplets, i.e. without a satellite.

To determine the largest droplet, irrespective whether a satellite was produced, a different approach was used. In accordance with the results of Fig. 3.14 and Fig. 3.15, to obtain the biggest droplet diameter, the pulse amplitude was set to be 140 V. The pulse width was increased from 25 μs to 625 μs at intervals of 50 μs. Droplets were collected and weighed to determine their size. The biggest value among the 13 samples was recorded as the biggest droplet diameter.

Fig. 3.16 shows the relationship between the droplet size and the nozzle size, for all nozzles tested. It is shown that all the above three types of droplet sizes increase monotonically with increasing nozzle sizes. The droplets are always larger than the nozzle diameter indicated by the broken line. An excellent rule-of-thumb states that the droplets are between 120 to 220% of the nozzle diameter.

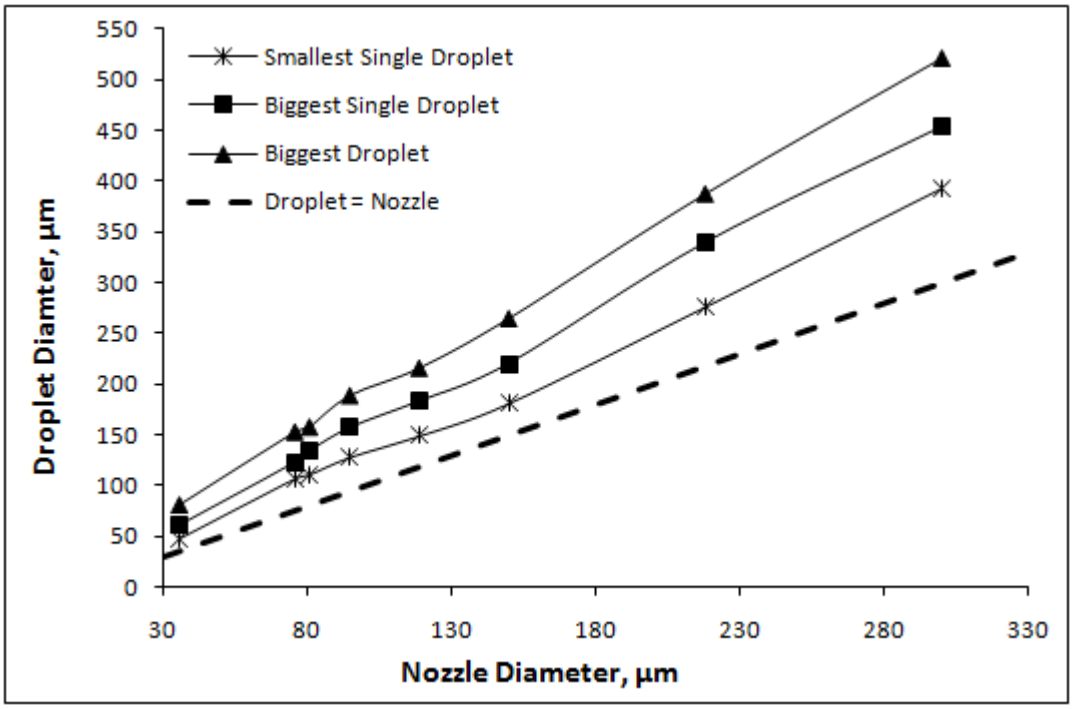

Fig. 3.16: Effects of nozzle size on droplet diameter. (–*–) denotes the diameters of the smallest single droplets can be generated; (–■–) denotes the diameters of the biggest single droplets can be generated; (–▲–) denotes the diameters of the biggest droplets which can be generated using the maximum voltage.

3.4.5 Repeatability

A good inkjet printhead should have nice repeatability, allowing generation of a rapid sequence of droplets without big variation in droplet velocity and droplet size. To test the repeatability of our novel PET-based printhead, water was dispensed through a 119 µm nozzle. In accordance with Fig. 3.14, to generate stable single droplets, the printing was carried out by using a signal

of 50 V pulse amplitude and 600 μs pulse width. As shown in Fig. 3.17, over a one hour test run at 120 Hz, the variation in droplet diameter is only 0.18% and 0.46% for droplet velocity.

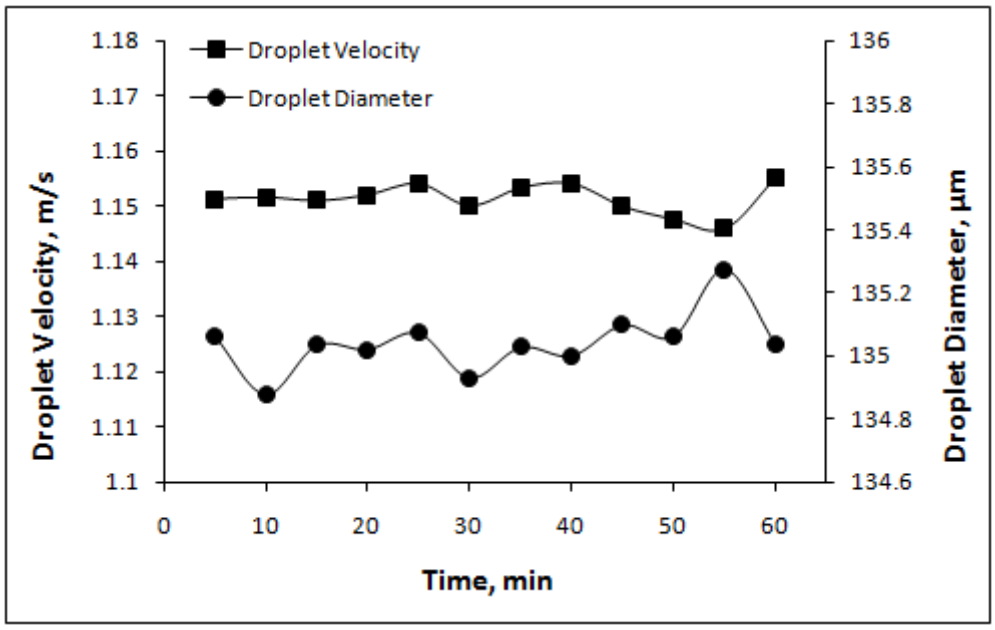

Fig. 3.17: Repeatability test of the PET-based printhead. Nozzle diameter is 119 μm.

3.4.6 Maximum Jetting Frequency

As a manufacturing tool, high speed jetting is required to increase productivity of inkjet printing technology. For industrial printer with multi-nozzle, this can be realized by increasing number of nozzles or increasing jetting frequency of each nozzle. While for printhead with single nozzle, as designed in this study (also for Microfab and Microdrop), jetting speed can only be improved by increasing jetting frequency. However, for a reliable jetting, a subsequent droplet should not be ejected until the pressure wave from the previous pulse signal has sufficiently damped. This damping takes time and thus limits the maximum jetting frequency [38]. For a specific printhead, its maximum jetting frequency is mainly depended on the construction of the printhead as well as

the driving signal [40]. Typical DOD printheads generate droplets at rates in the range 0.1-10 kHz.

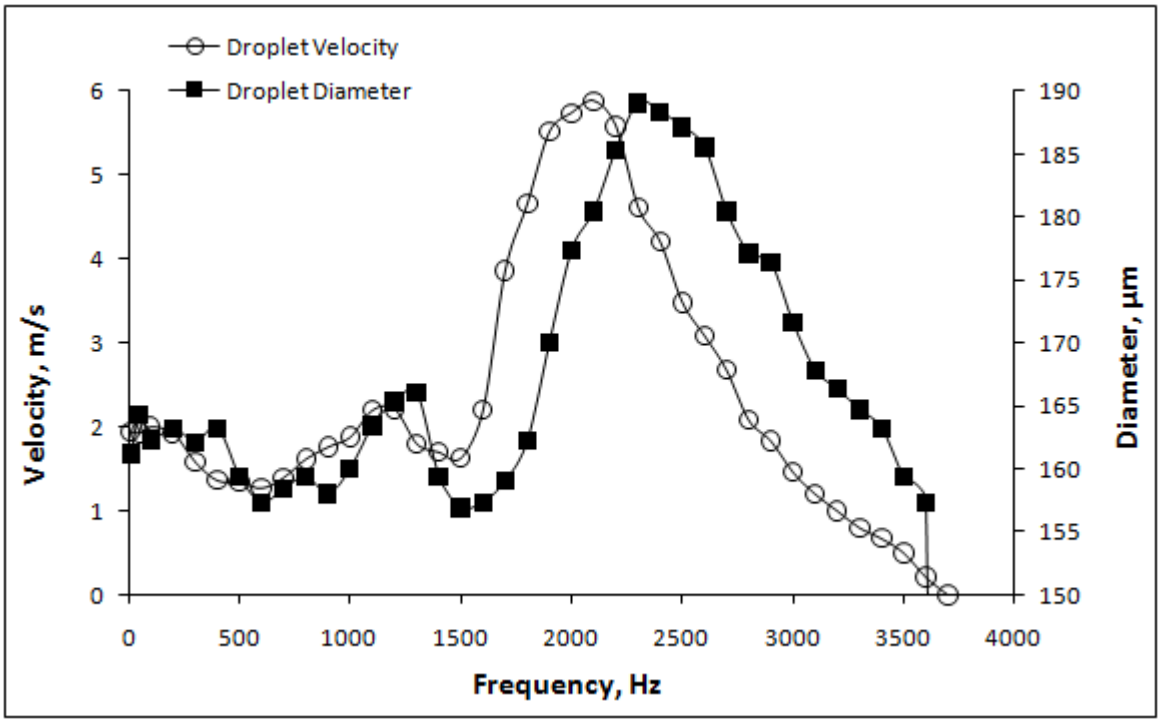

Fig. 3.18: Effects of jetting frequency on droplet velocity and droplet size. The pulse width is 100 µs. The pulse amplitude is 30 V. Nozzle diameter is 119 µm.

If a droplet is ejected before the pressure waves from the previous pulse signal have sufficiently damped, the new droplet ejection cycle will be affected by the non-zero flow field inside the printhead. Consequently, the droplet velocity and the droplet size will increase or decrease, depending on whether the residual movement of the meniscus is in-phase or out-of-phase with the new droplet ejection cycle [160].

Fig. 3.18 shows the effects of jetting frequency on droplet velocity and droplet diameter, for the PET-based printhead. Printing was carried out by dispensing water through a 119 µm nozzle. The t_{dwell} was kept constant at 100 µs, the optimal value for the printhead. The pulse amplitude was kept constant at 30 V.

The printing was operated with a variation in frequency between 1 Hz to 5 kHz. It is shown that below 1.5 kHz, jetting frequency has relatively small effects on drop velocity and drop diameter. The reason was that below this frequency, there was sufficient time (670 μs, according to a jetting frequency of 1.5 kHz) between droplet ejection cycles for the acoustic pressure waves to get damped. Thus the droplet ejection cycles were independent of each other and were irrelevant with the jetting frequency.

However, when jetting frequency exceeds 1.5 kHz, both drop velocity and drop volume rapidly increase with an increase of jetting frequency. The maximum droplet velocity 5.7 m/s is obtained when the jetting frequency reaches a value of 2.1 kHz. Then droplet velocity decreases with a further increase of jetting frequency. The increase of droplet diameter continues until the jetting frequency is 2.3 kHz. Then the droplet diameter also decreases with a further increase of jetting frequency. The dispensing is stopped at a frequency of 3.7 kHz. The maximum jetting frequency of 3.6 kHz is higher than that of the Microdrop printhead (2.0 kHz), while much lower than that of the Dimatix, XAAR, and Microfab printhead (20 kHz).

The strong variation of droplet velocity and droplet diameter with changing of jetting frequency indicates that, above 1.5 kHz, the time interval between two consecutive droplet ejection cycles was not sufficiently long for the acoustic pressure waves to get adequately damped. With the meniscus motion method proposed by Kwon [161], one can estimate the time needed for the damping of the pressure waves. For the printhead designed in our study, it has an optimal

t_{dwell} around 100 μs; and it takes around 800 to 1000 μs for the acoustic pressure waves to get sufficiently damped. As a result, our printhead should has a much lower threshold frequency [160], above which jetting frequency will have great effects on droplet speed as well as droplet volume. This is verified by the experiment results, as shown in Fig. 3.18. The threshold frequency for the designed printhead is only 1.5 kHz.

The maximum droplet velocity is produced with a driving frequency of around 2.1 kHz, corresponding to the resonance frequency of the inkjet channel. This resonance frequency is much lower as compared to other commercial printheads. The reason is that the first mode resonance frequency of the printhead is inversely proportional to the length of the pressure channel [160]; in the meantime, the designed printhead has a liquid channel of 50 mm length, which is much larger than that of the commercial printheads. As a result, a much lower resonance frequency is reasonably expected.

3.4.7 Jetting of Non-Newtonian Liquid

Aqueous sodium alginate (SA) solutions were used to estimate the printing behavior for non-Newtonian liquid of our PET-based printhead. The threshold voltages for different concentrations of SA solutions are compared with those values for glycerin solutions (which have been shown in Fig. 3.13). To do the comparison, the viscosity used for the non-Newtonian SA solutions is that predicted from Fig. 3.12, corresponding to the mean shear rate of 1.0×10^4 s^{-1}. The selection of this mean shear rate to represent the real values is reasonable. The reason is that the nozzle used in the test has a diameter of 119 μm, and the

velocity of the liquid thread ejected from the nozzle is around 1.5 to 3.0 m/s before the droplet formation. Thus the mean shear rate determined by $\dot{\varepsilon} = v/r$, where v and r are the drop velocity and radius, respectively, does have the order of 10^4 s^{-1}.

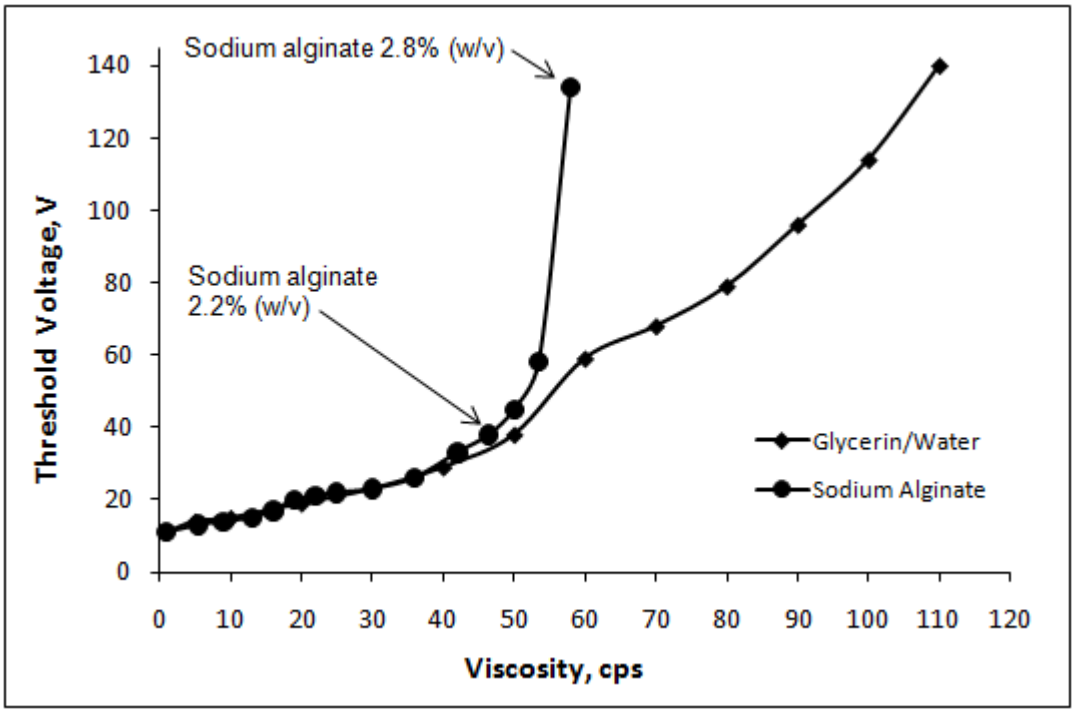

Fig. 3.19: Threshold voltages for sodium alginate solutions of concentrations from 0.2% to 2.8% (w/v).

Fig. 3.19 shows that for SA solutions, the threshold voltage increases from 13 V to 110 V when the SA concentration increases from 0.2% to 2.8% (w/v). In the initial stage, for the same viscosity, the threshold voltage required by the SA solution and glycerin solution is nearly the same. However, when the concentration of the SA solution further increases to 2.0% (w/v), the SA solution needs a larger threshold voltage than the glycerin solution having the same viscosity, especially when the SA solution concentration exceeds 2.4% (w/v). It is noticeable that although 110 cps glycerin solution is dispensable, the dispensing of 3.0 % (w/v) SA solution with a viscosity of 63 cps failed.

There is a big jump of threshold pulse amplitude from 58 V for 2.6% (w/v) SA solution to 134 V for 2.8% (w/v) SA solution, despite that the viscosity difference is only around 4 cps.

Fig. 3.20: Schematic showing of drop formation for 2.2% SA solutions.

The results indicate that during the inkjet printing, sodium alginate solutions behave more like a Newtonian fluid when its concentration is below 2.0% (w/v). However, with the increase of concentration, sodium alginate exhibits more non-Newtonian behavior. The dispensing of non-Newtonian liquid generates longer threads than the Newtonian fluids with similar viscosity [65], which has been observed from the experiment. A droplet formation for 2.2% (w/v) SA solution is shown in Fig. 3.20. It is shown that a quite long liquid thread is formed before the droplet separation from the nozzle. The breakup of the non-Newtonian liquid thread causes much energy dissipation due to the elasticity in the fluid, leading to a significantly lower droplet velocity. For the 3.0% (w/v) SA solution, energy dissipation is so much that the dispensed

liquid does not have enough kinetic energy to overcome the surface energy, leading to the failure of droplet separation.

It also can be seen that the long liquid thread snaps back and combines with the primary droplet, rather than pinching off from the primary droplet and breaking up into a satellite droplet. The phenomenon verifies the previous claim that an increase in elasticity of the solution will effectively eliminate satellite generation [65].

3.5 Conclusions

A PET/PTFE-based piezoelectric DOD inkjet printhead with an interchangeable nozzle design has been proposed and fabricated by the authors. The printhead chamber is made of PET or Teflon tube, which is much softer than the commonly used glass tube. The ejecting capacity of this novel printhead has been compared with commercial printheads, and found to have superior performance and versatility. Aqueous glycerin solutions with viscosity as high as 100 cps have been successfully dispensed, while the corresponding commercial printheads can only dispense liquids with viscosities lower than 20 cps. PTFE-based printhead provides excellent anti-corrosive property when strongly corrosive inks are involved. The interchangeable nozzle design largely alleviates the difficulty in cleaning of clogged nozzles and greatly reduces the occurrence of printhead damage. One of the printhead which was fabricated in 2007 still works properly now The effects of operating parameters, including voltage pulse amplitude, pulse

width and jetting frequency, on droplet size and droplet velocity have been characterized. The new printhead shows excellent repeatability.

Finally, non-Newtonian aqueous sodium alginate (SA) solutions with concentrations from 0.2% to 2.8% (w/v) have been successfully dispensed. For relatively low concentrations, the threshold voltages required by SA solutions and glycerin solutions take nearly the same values, implying that the printhead characteristics calibrated from dispensing Newtonian liquid can also be used as a reference to predict dispensing of the non-Newtonian liquids. However, for higher concentrations of the polymers there is a sharp transition where printing can no longer be achieved.

4. FORMING A FINE JET IN INKJET PRINTING

The formation of fine jet during the piezoelectric DOD inkjet printing will be presented in this section. An ultra-high-speed video camera is used to record the fast jetting process. The characteristics of this fine jet are studied by dispensing different concentrations of aqueous glycerin solutions, and the experimental results are presented and discussed in this section.

4.1 Introduction

Jet eruptions from free liquid surface can be found in a number of flow configurations. These include Worthington jets [162, 163], which are generated by the collapse of an impact crater; granular jets, discovered by Thoroddsen and Shen [164], which are generated by the impact of a solid sphere onto a deep bulk of granular material [165, 166]; the Cavity jets [167, 168], which are produced inside cavitation bubbles when they collapse and are capable of severely damaging a solid surface, such as the blades of turbines and kidney stones; apex jets [169], and many other kinds of jets [170, 171, 172, 173].

Over the years, there has been a consensus that jet formation in many different cases is related to a singularity on a free surface [174, 175]. Fig. 4.1 [168] shows a micro-jet formed by impact of a tube filled with perfectly wetting liquid, on a rigid floor. In the gravity-free reference frame, when the tube falls

axially under its own weight, surface tension deforms its liquid interface into a hemispherical shape. It is believed that the jet is generated by the violent reversion of the interface curvature resulting from the impact. This is a typical example to show that the jet formation is closely related to a singularity on a free surface. Now it is quite interesting to us whether such needle-like jet can also be produced by DOD inkjet printing, as the similar processes which existing in a typical droplet ejection cycle: firstly an inwards hemispherical meniscus is produced by the expansion of the piezoceramic element, then a positive acoustic pressure generated by the contraction of the piezoceramic element suddenly squeezes the liquid inside the printhead chamber, behaving as the impact in Fig. 4.1. This is the part which will to be covered in the next two subsections.

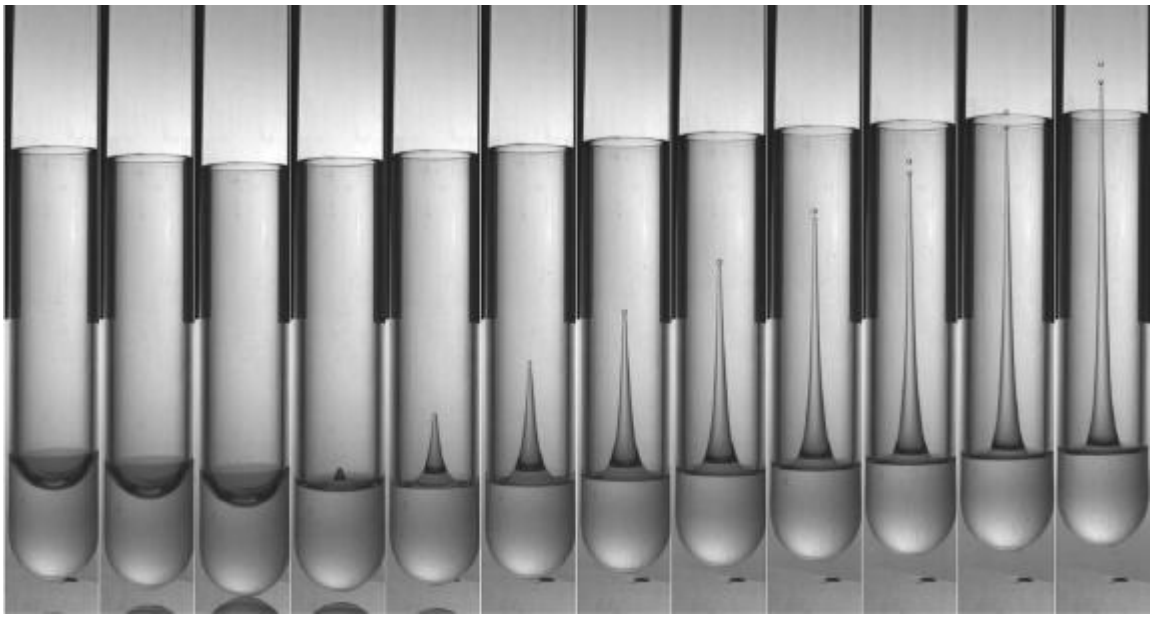

Fig. 4.1: Jet formation observed just after impact of the tube with a solid wall when the free surface is initially deformed with a meniscus [168].

4.2 Experimental Setup

Printing experiments were carried out by using the self-developed squeeze mode piezoelectric inkjet printing system. The setup is almost the same as that shown in Fig. 3.9. The only difference is that an ultrahigh-speed video camera (maximum frame rate: 1,000,000 fps) developed by Etoh *et al.* [176] is used to record the jetting process here. Eight different concentrations of aqueous glycerin solutions will be used as the ink, to obtain a wide range of viscosities.

4.3 Experimental Results

The jets are classified into two types: Type I is the typical fine jet, and Type II is the jet produced when there is a bubble locating inside the nozzle.

4.3.1 Jet I

Fig. 4.2 shows a typical process of Type I jet. In the first 4 frames, a backflow is generated by the expansion of the piezo-element and air gets sucked into the nozzle due to the negative pressure produced inside the liquid. Surface tension forces deform this liquid interface into a spherical shape, or a partial cavity. The later sudden contraction of the piezo-element squeezes the fluid and induces pressure gradients which in turn produce a sudden change in the liquid velocity, and, finally causes the collapse of the cavity and the generation of the fine jet. The principle is similar to that of the cavity jet shown in Fig. 4.1. Here the differences between these two jets are the way of generating the free surface (with singularity) and realizing the sudden change in the velocity field,

as well as the geometry of the liquid channels. Fig. 4.3 shows the converged inner profile of the nozzle used for the experiments to study the fine jet.

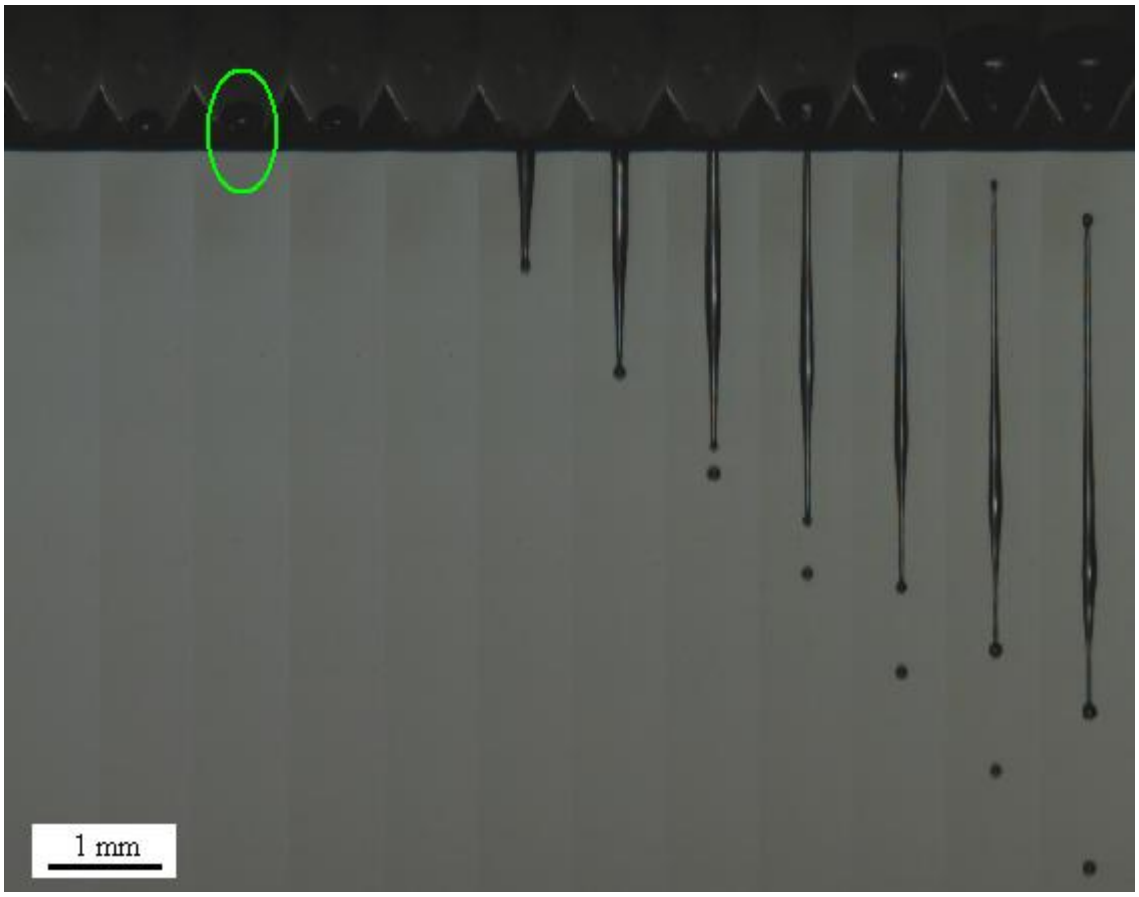

Fig. 4.2: A 93 μm jet with a velocity of 7 m/s. The diameter of the orifice $\boldsymbol{D_{noz}}$ is 150 μm. Liquid used is 70% aqueous glycerin (w/w) solution. Printing parameters: bi-polar piezo-driving signal with t_{dwell} and t_{echo} equal to 700 μs; driving pulse amplitude equals to 140 V. Negative pressure inside the reservoir is -2.2 kPa relative to the atmospheric pressure. Images were taken at a frame rate of 8 kfps. Ambient temperature is 25 ˚C.

As compared to the regular printing cycle shown in Fig. 3.10, here the time durations for the expansion and contraction of the piezoelement are much longer of around 700 μs. The jetting is found to be extremely sensitive to the negative pressure in the reservoir which is used to hold up and prevent the liquid from leaking out of the orifice of the printhead. Fig. 4.4 shows another jet process almost under the same conditions as that one shown in Fig. 4.2. As can be clearly seen, by slightly changing the negative pressure, a much finer jet with a much higher velocity can be produced.

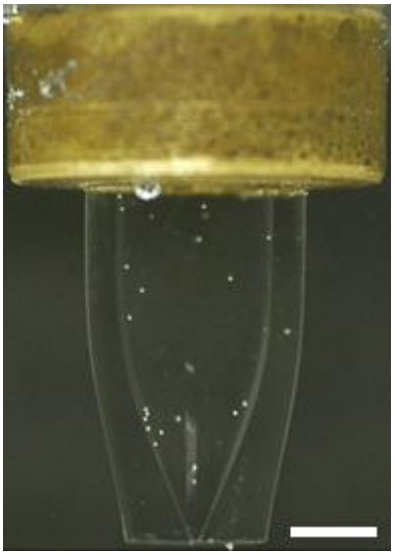

Fig. 4.3: The 150 μm nozzle used for fine jetting experiments. The scale bar is 2 mm. This image was taken when the nozzle was placed inside a 60% aqueous glycerin (w/w) solution, which had an index of refraction similar to that of the glass.

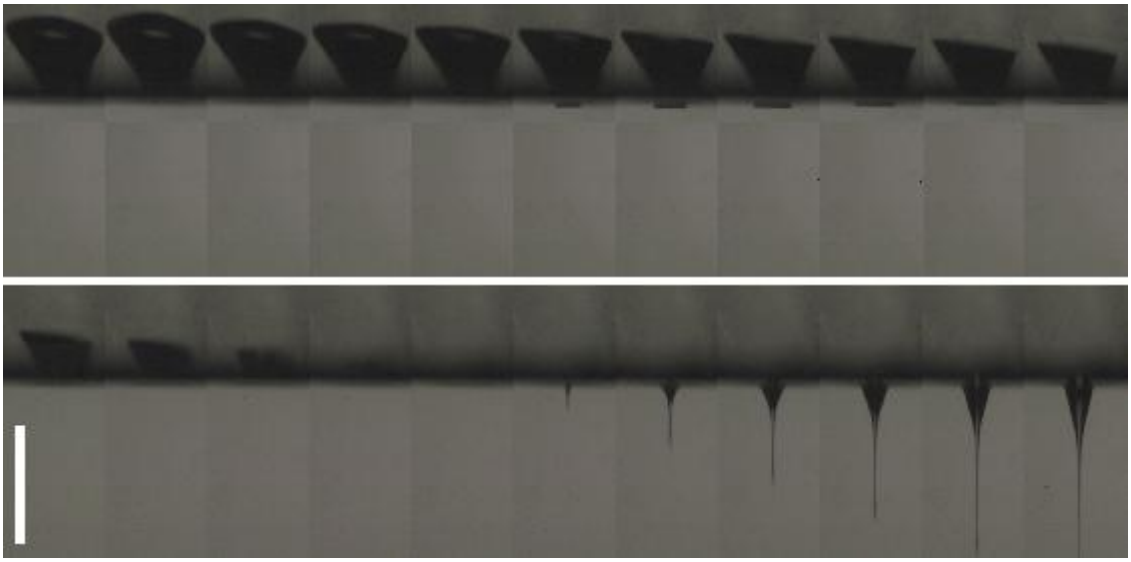

Fig. 4.4: An 8 μm jet with a velocity of 29 m/s. $\boldsymbol{D_{noz}}$ is 150 μm. The liquid used is 70% aqueous glycerin (w/w) solution. Printing parameters: bi-polar piezo-driving signal with t_{dwell} and t_{echo} equal to 700 μs; driving pulse amplitude equals to 140 V. The negative pressure inside the reservoir is -2.3 kPa relative to the atmospheric pressure. Images were taken at a frame rate of 165 kfps. Ambient temperature is 25 ˚C. The scale bar is 500 μm.

Fig. 4.4 also clearly shows the evolution of the cavity during the jet formation process, as a much higher frame rate is used. Frames 1 and 2 record the growth to maximum size of the cavity, as the liquid goes into tension due to

the expansion of the piezo-element. When the positive acoustic pressure arrives, the cavity rapidly collapses towards the free surface (start from frame 3 to frame 16), followed immediately by the formation of a downward thin liquid jet which rapidly grows in length (frame 17). It can be seen that the shock flattens the lower surface of the cavity. Similar jet behaviors have been also reported by Barrow *et al.* [177], in their study of cavitation damage.

4.3.2 Type II Jetting from Entrained Bubble

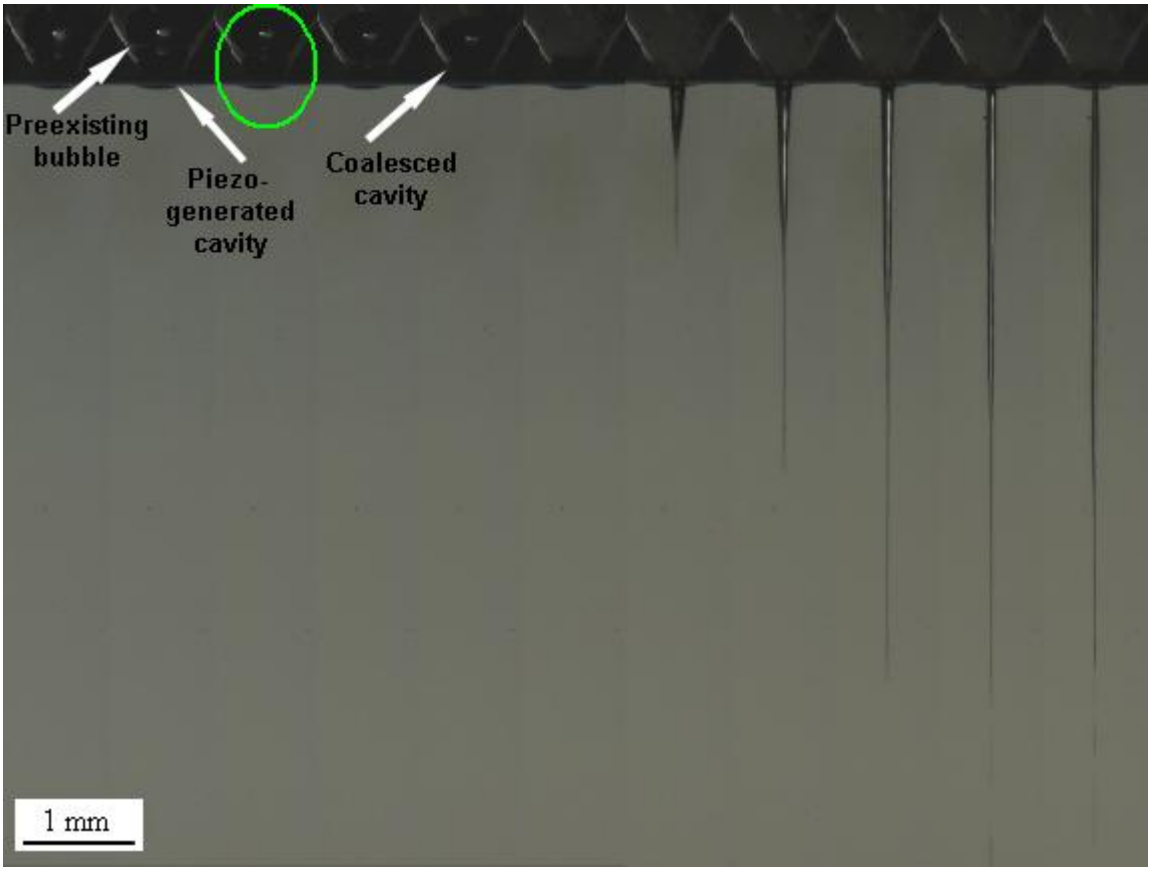

Fig. 4.5: A 16 μm jet with a velocity of 35 m/s. $\boldsymbol{D_{noz}}$ is 150 μm. The liquid used is 70% aqueous glycerin (w/w) solution. Printing parameters: bi-polar piezo-driving signal with t_{dwell} and t_{echo} equal to 700 μs; driving pulse amplitude equals to 140 V. Negative pressure inside the reservoir is -2.3 kPa relative to the atmospheric pressure. Images were taken at a frame rate of 16 kfps. Ambient temperature is 25 ˚C.

The jet in Fig. 4.2 and Fig. 4.4 result from the collapse of a hemispheric crater. In some cases, there is already an entrained bubble inside the nozzle before the

actuation of the piezo-element, the second type of jet will occur. This earlier bubble is entrained in the late stage of the previous droplet ejection cycle, due to the long duration of the piezo expansion. As shown in Fig. 4.5, the preexisting bubble coalesces with the new piezo-generated hemispheric crater, forming a new cavity which finally collapses and produces the fine jet.

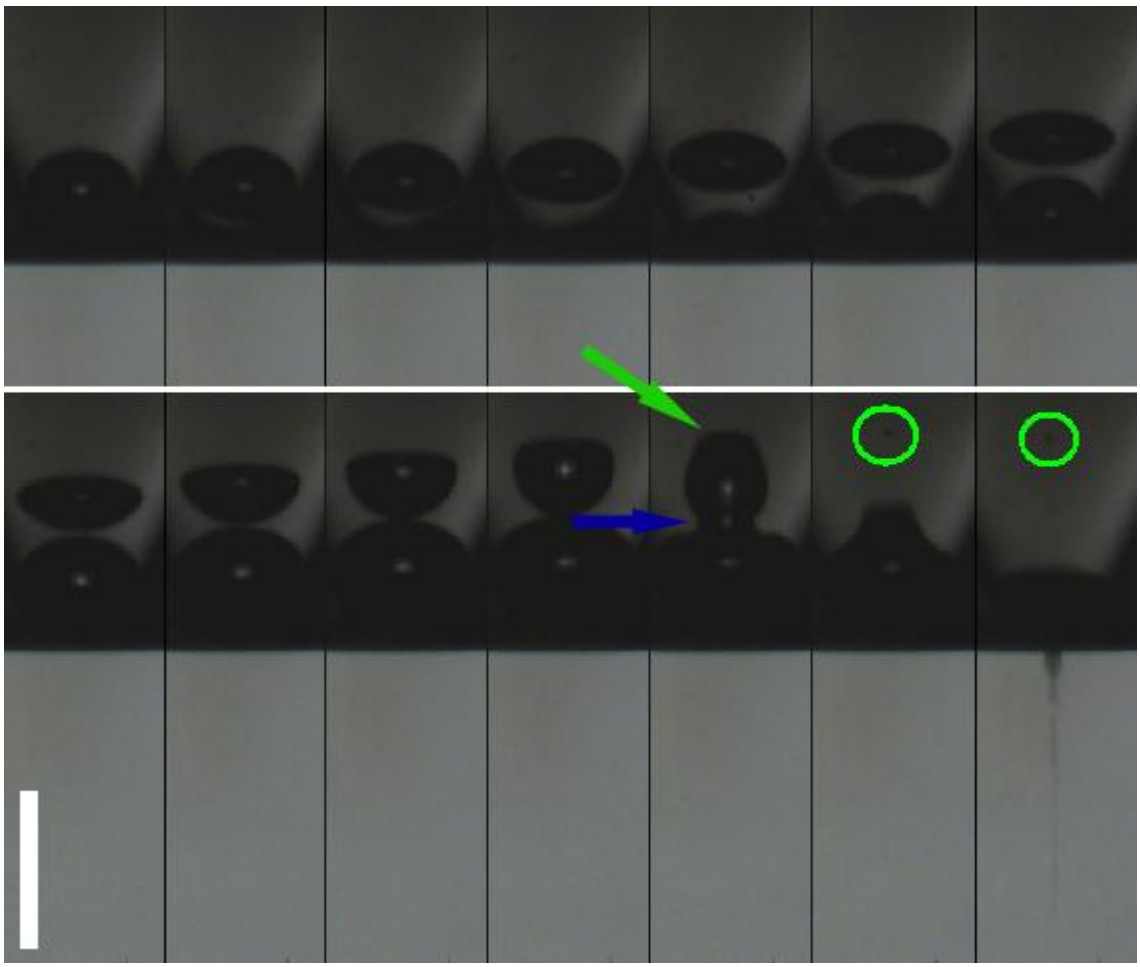

Fig. 4.6: A 10 μm jet with a velocity of 24 m/s. $\boldsymbol{D_{noz}}$ is 150 μm. The liquid used is 10% aqueous glycerin (w/w) solution. Printing parameters: bi-polar piezo-driving signal with 450 μs t_{dwell} and 70 μs t_{echo}; driving pulse amplitude equals to 140 V. The negative pressure inside the reservoir is -2.3 kPa relative to the atmospheric pressure. Images were taken at a frame rate of 27 kfps. Ambient temperature is 25 ˚C. The scale bar is 500 μm.

Fig. 4.6 provides a close view for the cavities evolution inside the nozzle. Frames 1 to frame 11 (a time duration of around 370 μs) record the growth to maximum size of the piezo-generated cavity, as the liquid goes into tension due to the expansion of the piezo-element. Concurrently, the preexisting

bubble is slightly pulled up. Starting from frame 10, the piezo-generated cavity contacts and coalesces with the preexisting bubble. The neck connecting the two cavities grows rapidly as studied by Thoroddsen *et al.* [178]. The neck shapes form perfect circular arcs (marked by a blue arrow), as demonstrated in Frame 12. A crest is developed when these circular arcs meet the undisturbed bubble, as marked by the green arrow. With the growing of the neck, this crest moves up the bubble and generates a series of capillary waves, which propagate along the bubble surface and converge at the apex, and finally, leading to the pinch-off of the small bubble (as marked by the green circles in frame 13 and 14). A similar pinch-off phenomenon during bubble coalescence has been comprehensively studied by Zhang and Thoroddsen [179], who also provided a nice view of the capillary waves focusing at the bubble apex, at a slight downwards angle. Finally, the shock waves produced by the piezo-element arrive and cause the collapse of the coalesced cavity, bringing about the fine jet. The jet is expelled out of the nozzle by the positive acoustic pressures.

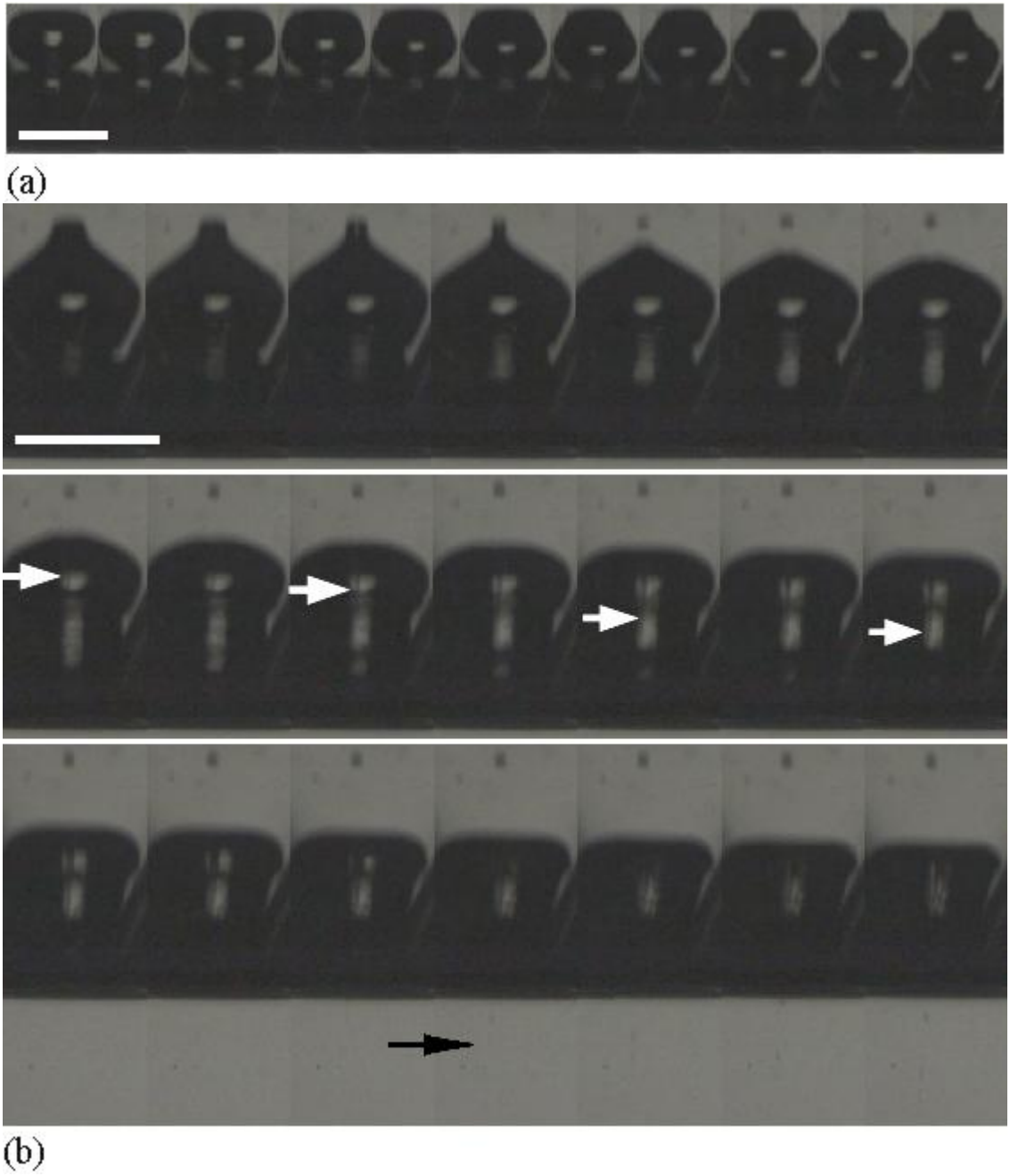

Fig. 4.7: A 9 μm jet with a velocity of 26 m/s. $\boldsymbol{D_{noz}}$ is 150 μm. The liquid used is water. Printing parameters: bi-polar piezo-driving signal with 700 μs t_{dwell} and 700 μs t_{echo}; driving pulse amplitude equals to 140 V. The negative pressure inside the reservoir is -2.3 kPa relative to the atmospheric pressure. Images were taken at a frame rate of 330 kfps. Ambient temperature is 25 ˚C. The scale bar is 500 μm. (a). The time interval between successive frames, *dt*, equals to 9.09 μs. (b). *dt* equals to 3.03 μs. (c). *dt* equals to 9.09 μs.

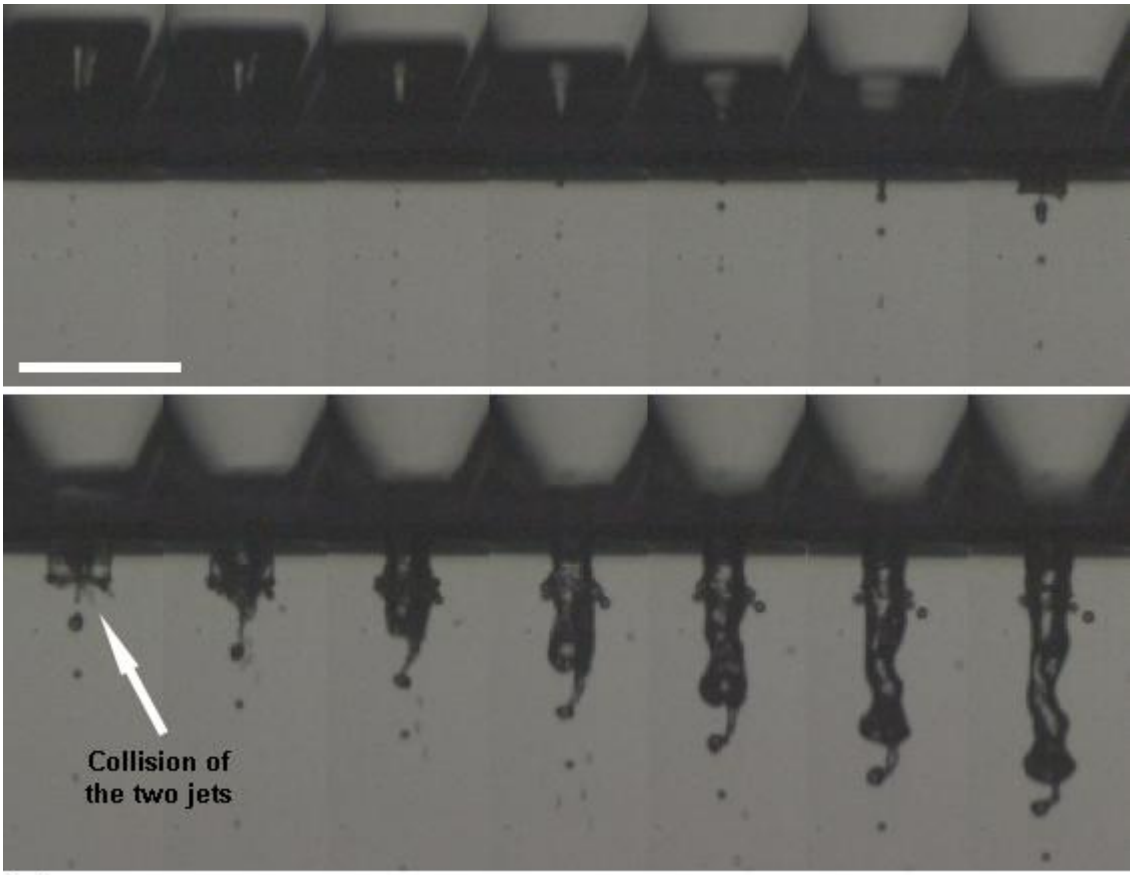

Fig. 4.7: A 9 μm jet with a velocity of 26 m/s. $\boldsymbol{D_{noz}}$ is 150 μm. The liquid used is water. Printing parameters: bi-polar piezo-driving signal with 700 μs t_{dwell} and 700 μs t_{echo}; driving pulse amplitude equals to 140 V. The negative pressure inside the reservoir is -2.3 kPa relative to the atmospheric pressure. Images were taken at a frame rate of 330 kfps. Ambient temperature is 25 ˚C. The scale bar is 500 μm. (a). The time interval between successive frames, *dt*, equals to 9.09 μs. (b). *dt* equals to 3.03 μs. (c). *dt* equals to 9.09 μs.

Fig. 4.7 shows the details of the coalescence process with a very high frame rate of 330 kfps. It is remarkable that we discovered that with the pinch-off of the small bubble, a downward fine jet was produced simultaneously, as marked by the arrows in Fig. 4.7(b). We conclude that this fine jet is different from the one which produced by the cavity collapse. As shown in Fig. 4.2 and Fig. 4.4, the cavity collapses when almost all the gas has been expulsed out of the nozzle (frame 5 in Fig. 4.2); then the jet is produced (frame 6 in Fig. 4.2). While here in Fig. 4.7(b), when this jet was produced (at frame 7 or frame 8)

inside nozzle, the big coalescence-generated cavity was still far away from collapsing. Thus we can conclude that rather than the cavity collapse, both the small bubble pinch-off and the jet formation are consequences of the local surface collapse during the radial focusing flow, perhaps in a singular (self-similar) fashion, as schematically shown in Fig. 4.8. Similar free surface geometries evolution has also been reported for others' study of cavity jet [180] and impact jet [171, 173]. Here we can name this jet as the "surfaces collapse" jet, to differentiate it from the cavity jet.

Cavity collapse occurs only after frame 6 in Fig. 4.7(c), followed immediately by the cavity jet. Frame 8 in Fig. 4.7(c) shows that this cavity jet finally catches up and collides with the first jet, forming a much thicker jet with a complicated structure. Fig. 4.9 provides a much more clear view of this collision.

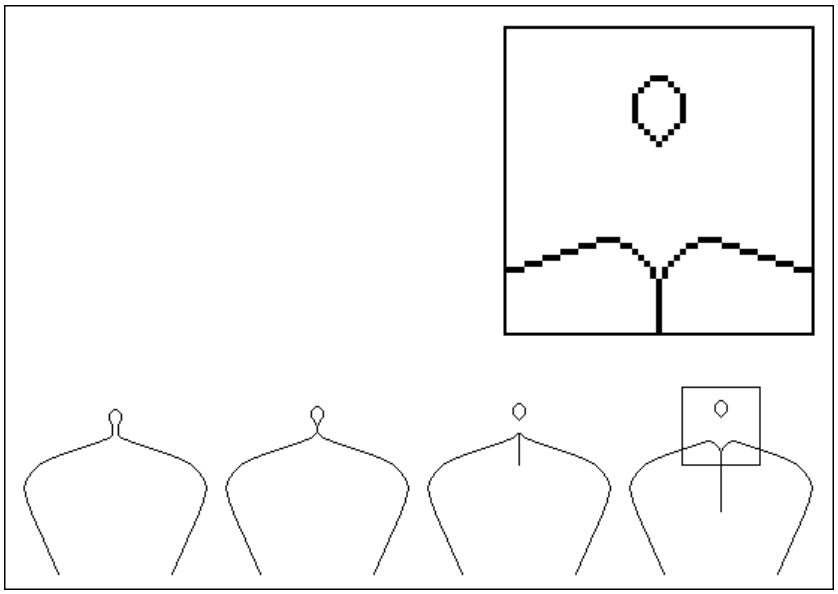

Fig. 4.8: Schematic showing the free surface shapes.

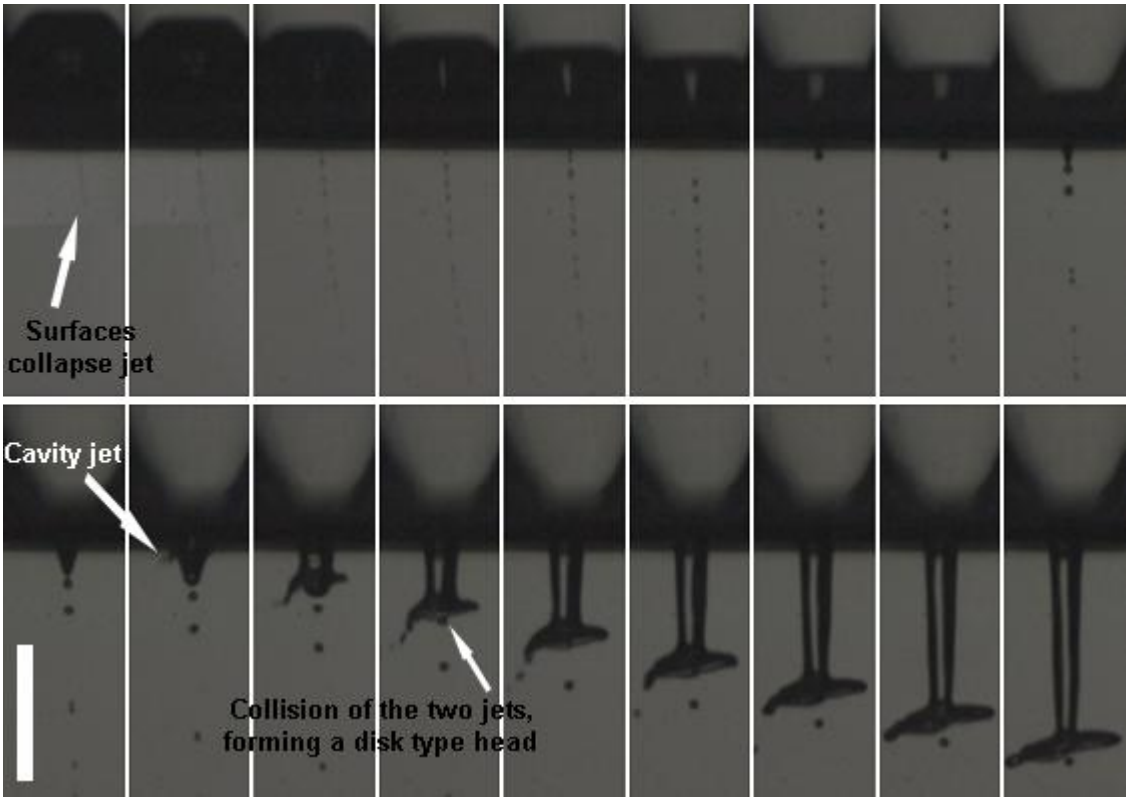

Fig. 4.9: A 8 μm jet with a velocity of 28 m/s. $\boldsymbol{D_{noz}}$ is 150 μm. The liquid used is water. Printing parameters: bi-polar piezo-driving signal with 500 μs t_{dwell} and 500 μs t_{echo}; driving pulse amplitude equals to 140 V. Negative pressure inside the reservoir is -2.3 kPa relative to the atmospheric pressure. Images were taken at a frame rate of 330 kfps. The numbers of the frames shown in the figure are *n* = 1, 4, 7 …… 52. Ambient temperature is 25 ˚C. The scale bar is 500 μm.

In Fig. 4.6 to Fig. 4.9, it was shown that a small bubble can be pinched off during the coalescence of the two cavities, for the 10% aqueous glycerin (w/w) solution and pure water. Fig. 4.10 shows a very complicated jetting process for the 70% aqueous glycerin (w/w) solution. From Fig. 4.10(b), we can conclude that the two cavities did not coalesce when they got into contact with each other, as a balloon-like bubble was generated here. So the process evolved as following: a piezo-generated cavity was sucked into the nozzle and got into contact with a preexisting bubble, without coalescing with it. The later piezo-generated radial focusing flow pushed out the lower cavity as well as the lower cap of the preexisting bubble, forming the balloon-like bubble extending

far out of the nozzle. This balloon-like bubble ruptures later close to its tip, followed by a cavity jet which has been shown in Fig. 4.4.

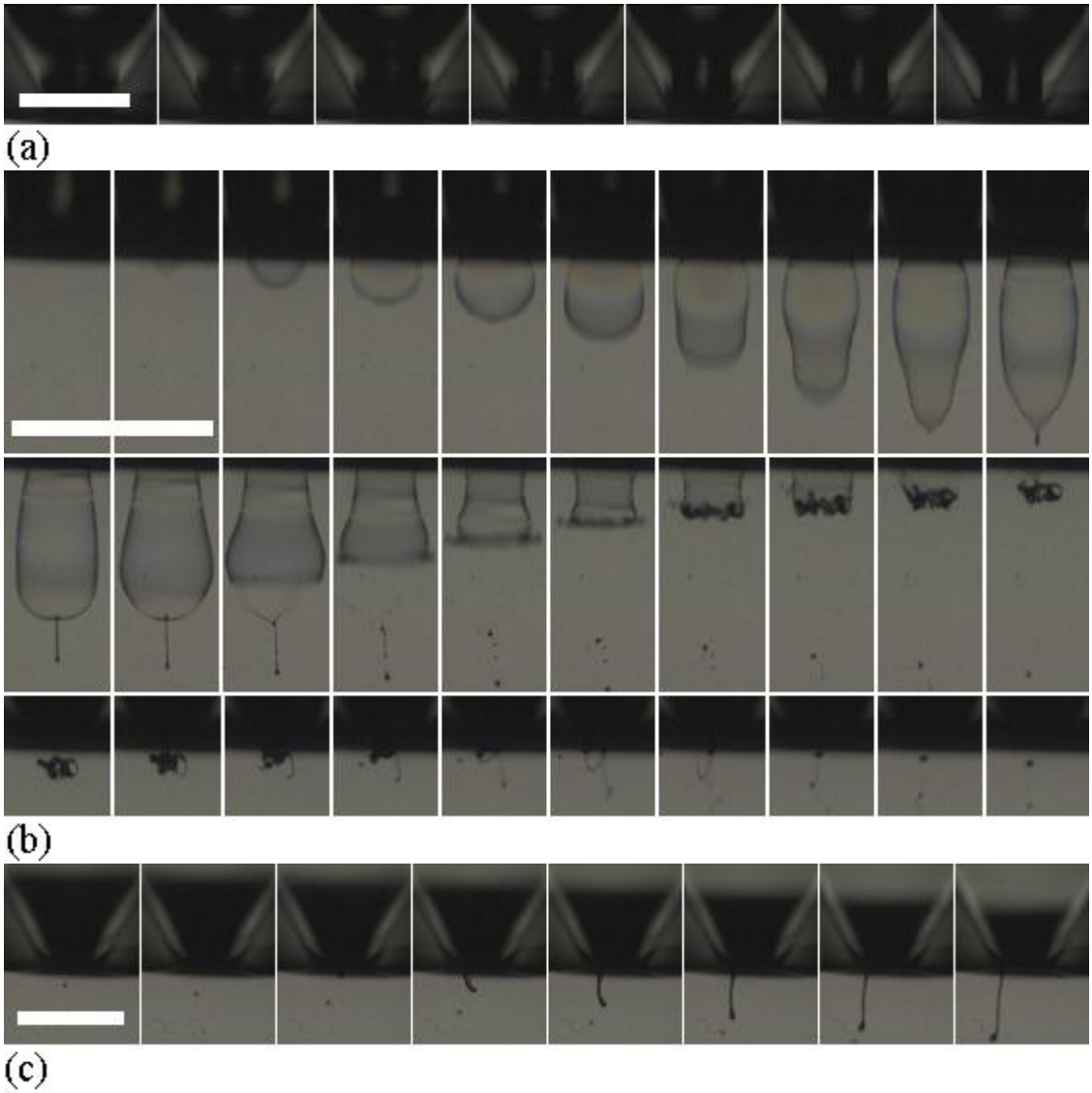

Fig. 4.10: Images showing jetting produced when no coalescence happens between the two cavities. D_{noz} is 150 µm. The liquid used is 70% aqueous glycerin (w/w) solution. Printing parameters: bi-polar piezo-driving signal with 550 µs t_{dwell} and 550 µs t_{echo}; driving pulse amplitude equals to 140 V. The negative pressure inside the reservoir is -2.3 kPa relative to the atmospheric pressure. Images were taken at a frame rate of 330 kfps. Ambient temperature is 25 ˚C. The scale bar is 500 µm. (a). *dt* equals to 6.06 µs. (b). *dt* equals to 3.03 µs. (c). *dt* equals to 9.09 µs. (c). *dt* equals to 6.06 µs.

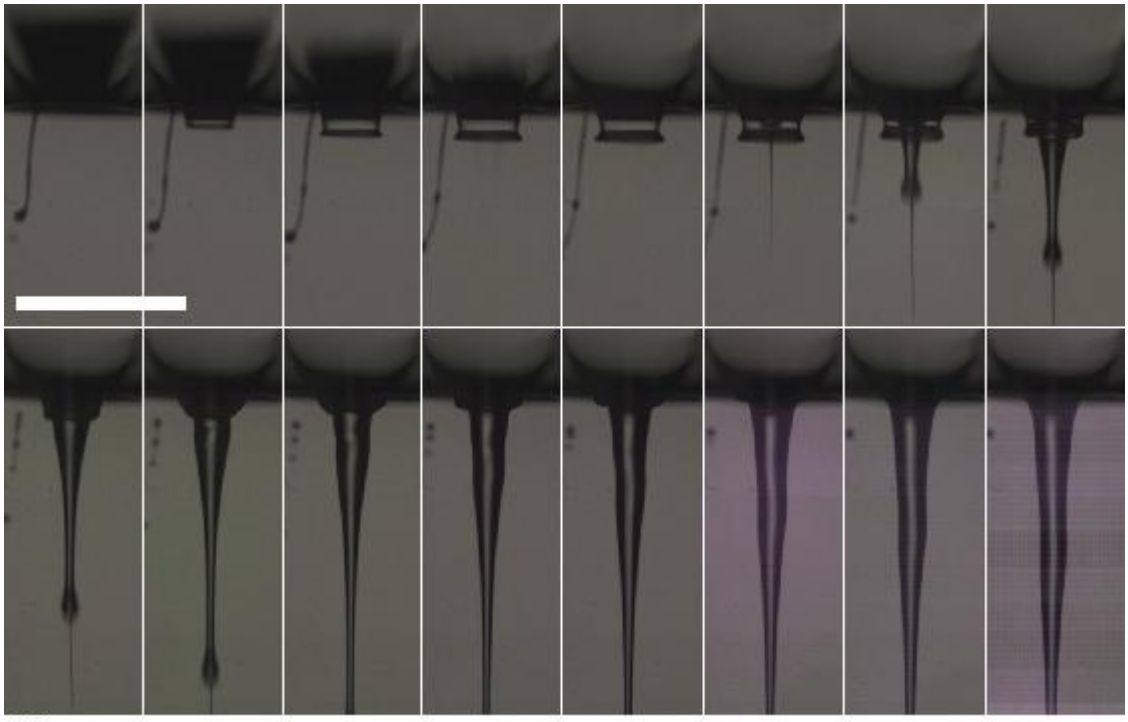

Fig. 4.10: Images showing jetting produced when no coalescence happens between the two cavities. $\boldsymbol{D_{noz}}$ is 150 μm. The liquid used is 70% aqueous glycerin (w/w) solution. Printing parameters: bi-polar piezo-driving signal with 550 μs t_{dwell} and 550 μs t_{echo}; driving pulse amplitude equals to 140 V. The negative pressure inside the reservoir is -2.3 kPa relative to the atmospheric pressure. Images were taken at a frame rate of 330 kfps. Ambient temperature is 25 ˚C. The scale bar is 500 μm. (a). *dt* equals to 6.06 μs. (b). *dt* equals to 3.03 μs. (c). *dt* equals to 9.09 μs. (c). *dt* equals to 6.06 μs.

Fig. 4.11 shows another jetting process with almost the same conditions as that in Fig. 4.10, but for a 30% aqueous glycerin (w/w) solution. It shows that the cavity jet occurs much earlier for the less viscous solution. As a result, the cavity jet pierced the balloon-like film before it becomes thin enough to rupture on its own. For comparison, the similar jetting process for a much higher viscosity liquid of 85% aqueous glycerin (w/w) solution is shown in Fig. 4.12. Here the jet passed through the viscous film, without piercing it.

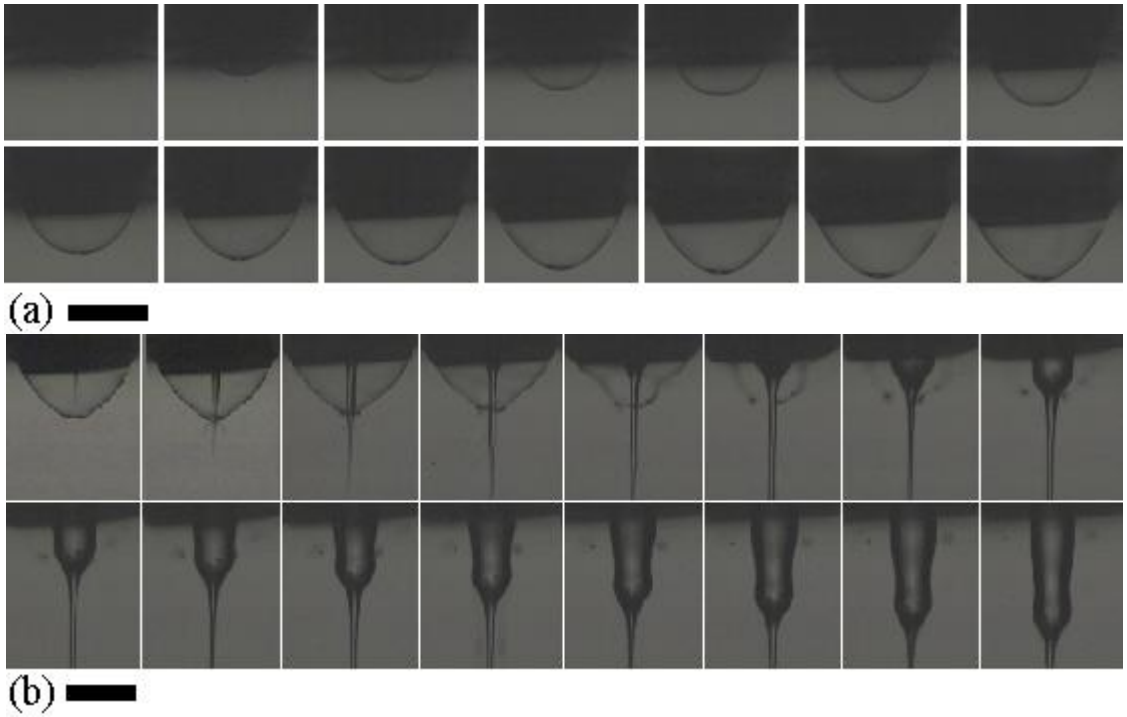

Fig. 4.11: Images showing the cavity jet pierces the thin liquid film. $\boldsymbol{D_{noz}}$ is 150 μm. The liquid used is 30% aqueous glycerin (w/w) solution. Printing parameters: bi-polar piezo-driving signal with 750 μs t_{dwell} and 750 μs t_{echo}; driving pulse amplitude equals to 140 V. The negative pressure inside the reservoir is -2.3 kPa relative to the atmospheric pressure. Images were taken at a frame rate of 330 kfps. Ambient temperature is 25 ˚C. The scale bar is 200 μm. (a). *dt* equals to 6.06 μs. (b). *dt* equals to 3.03 μs.

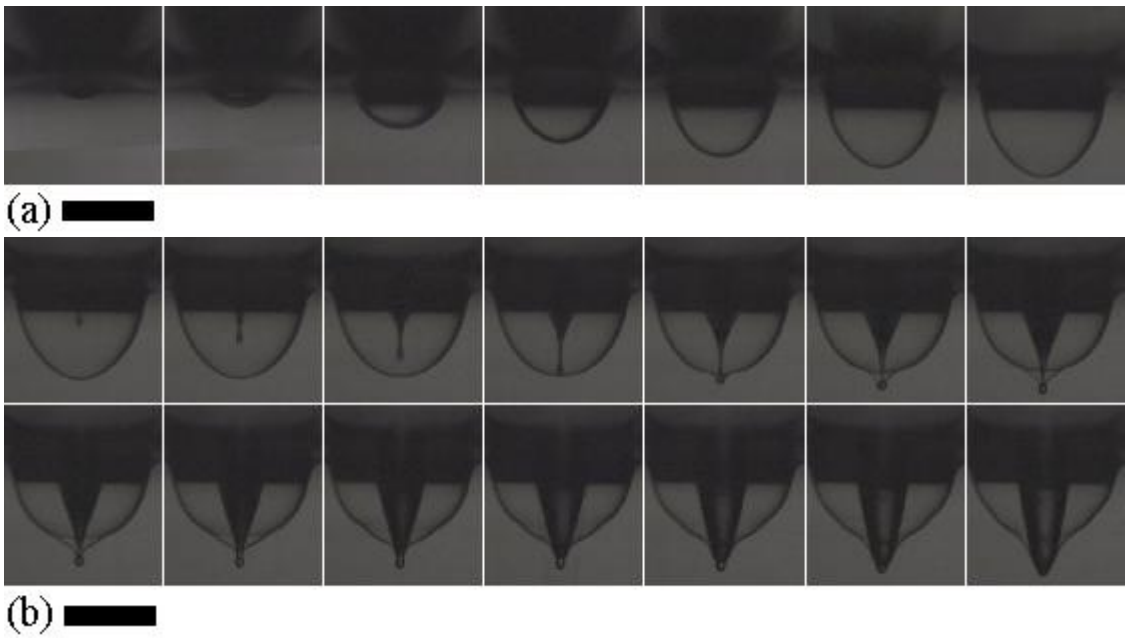

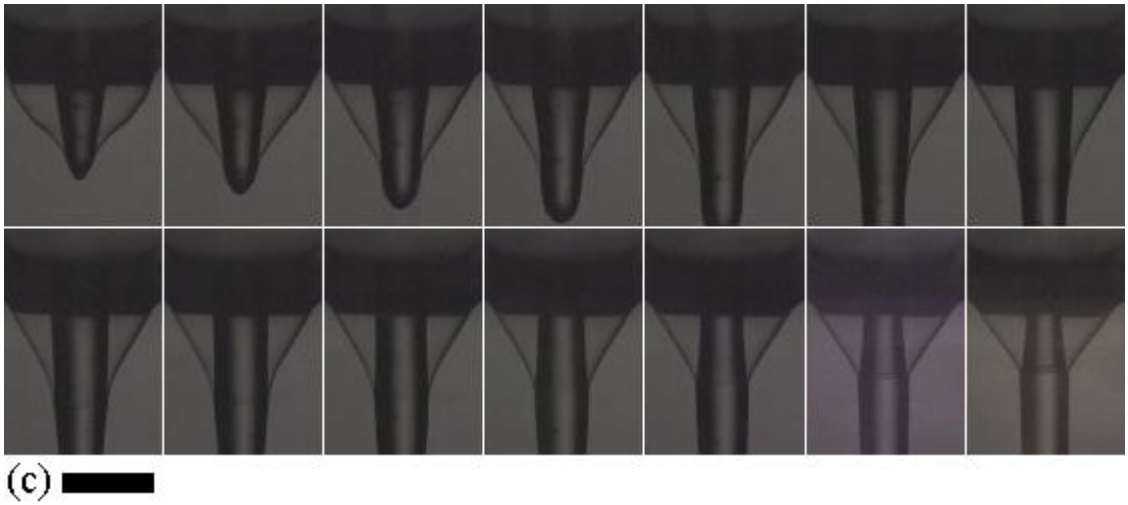

Fig. 4.12: Images showing the cavity jet fails to pierces the cavity. $\boldsymbol{D_{noz}}$ is 150 μm. The liquid used is 85% aqueous glycerin (w/w) solution. Printing parameters: bi-polar piezo-driving signal with 650 μs t_{dwell} and 650 μs t_{echo}; driving pulse amplitude equals to 140 V. The negative pressure inside the reservoir is -2.3 kPa relative to the atmospheric pressure. Images were taken at a frame rate of 330 kfps. Ambient temperature is 25 ˚C. The scale bar is 200 μm. (a). *dt* equals to 18.18 μs. (b). *dt* equals to 3.03 μs. (c). *dt* equals to 15.15 μs.

Fig. 4.13 shows a totally different kind of jet. It seems that two bubbles broke up during the printing cycle, and the most interesting thing was that, there emerged a long liquid thread between these two bubbles during the jetting. It is also remarkable that following the bursting of the first bubble, an upstream pressure wave was generated, which slightly deformed the lower head of the liquid thread (as marked by the arrow in Fig. 4.13(a)).

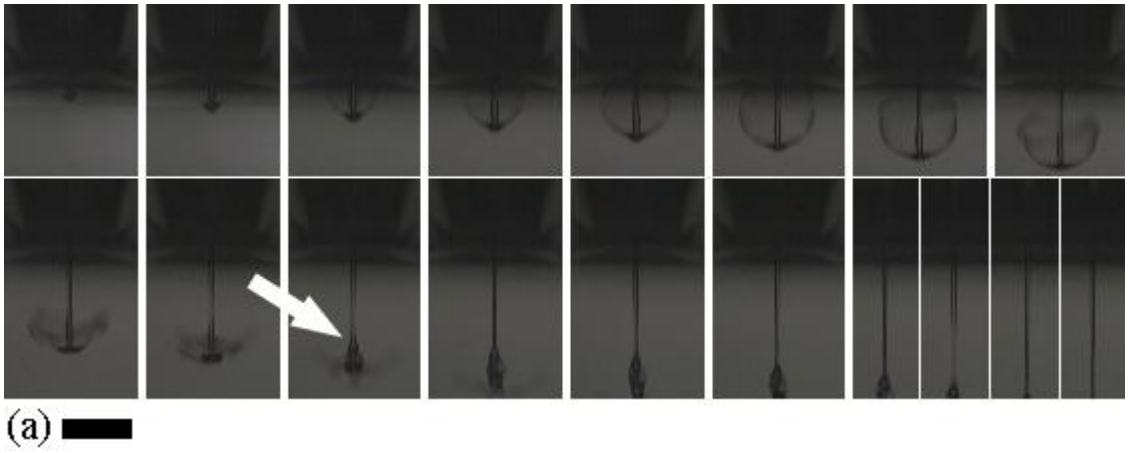

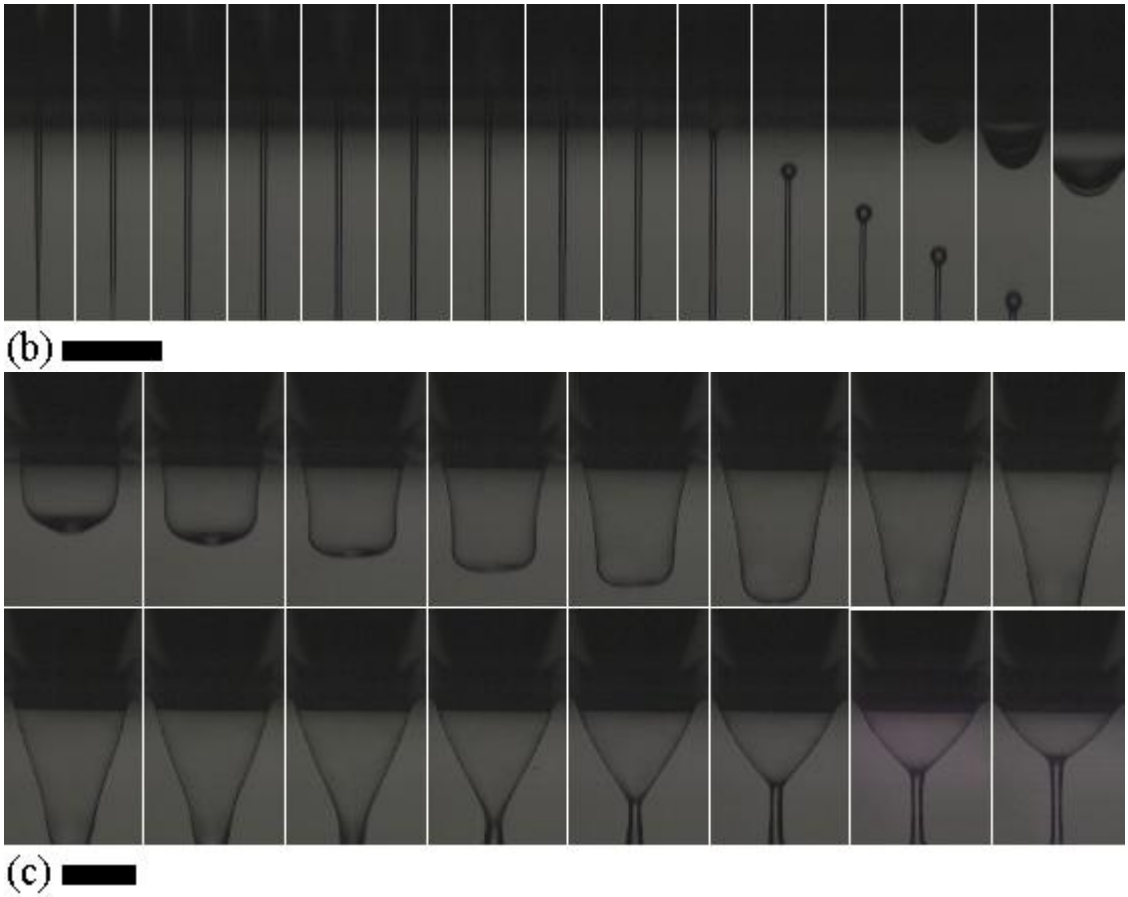

Fig. 4.13: A thin liquid thread generated during the jetting. $\boldsymbol{D_{noz}}$ is 150 μm. The liquid used is 70% aqueous glycerin (w/w) solution. Bi-polar piezo-driving signal with 550 μs t_{dwell} and 550 μs t_{echo}; 140 V. The negative pressure inside the reservoir is -2.3 kPa. Images were taken at a frame rate of 330 kfps. Ambient temperature is 25 ˚C. The scale bar is 200 μm. (a). *dt* equals to 3.03 μs. (b). *dt* equals to 12.12 μs. (c). *dt* equals to 6.06 μs.

It is obviously interesting to find out how this liquid thread was produced. However, the initial stage is missing here in Fig. 4.13, because the ultrahigh-speed video camera [176] used to capture the jetting process can only take 103 successive frames each time. Thus we captured another similar jetting process with a slightly earlier camera trigger and the result is shown in Fig. 4.14. As can be seen from frame 5 in Fig. 4.14(a), when the piezo-generated cavity gets sucked into the nozzle, a bulk of liquid was captured between it and the preexisting bubble. When the piezo-element contracted, the preexisting bubble pushed this bulk of liquid, deforming the bottom of the piezo-generated cavity, and finally expelled the liquid out of the nozzle, forming a long liquid thread.

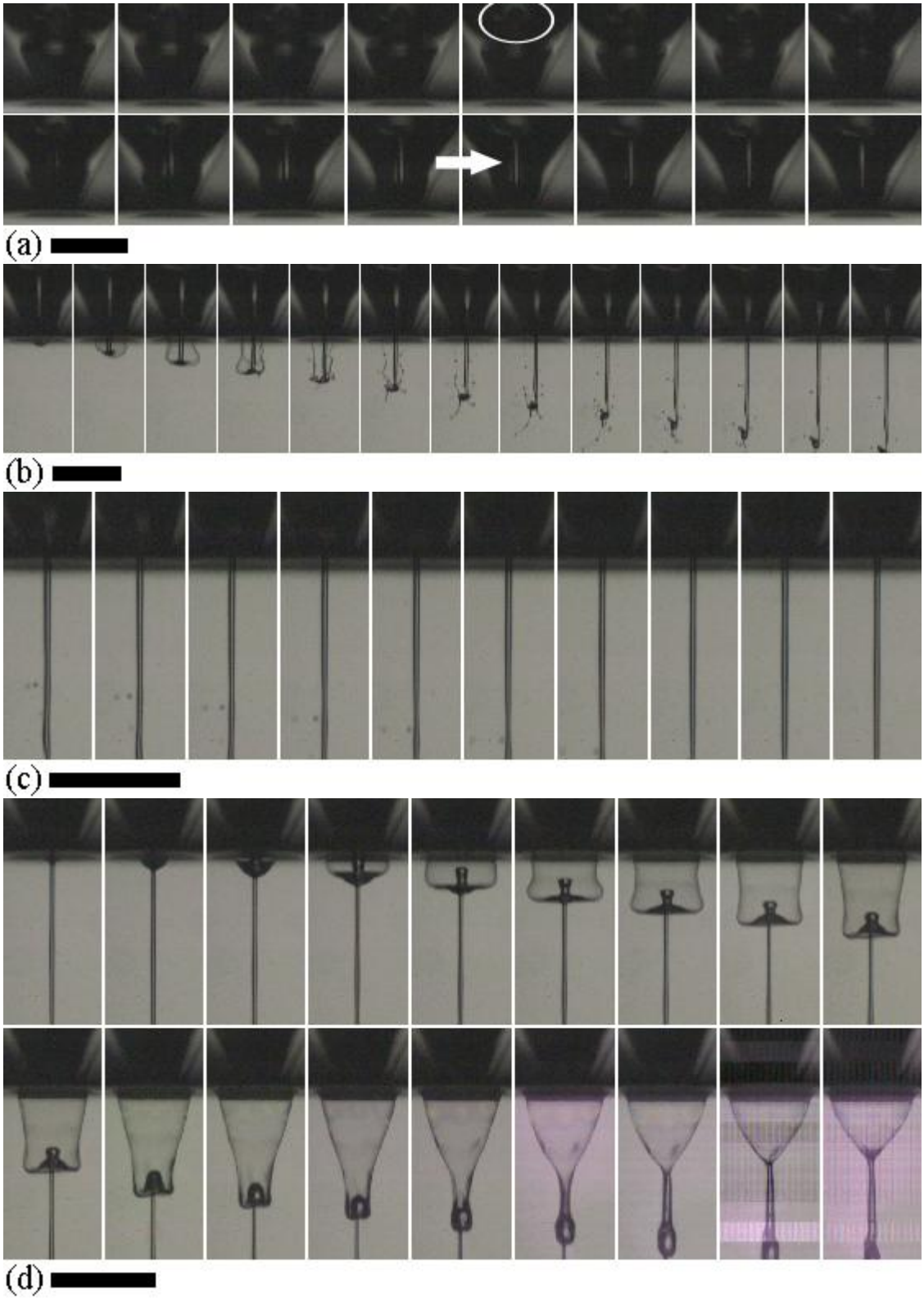

Fig. 4.14: Images showing the interaction between the piezo-generated cavity and the preexisting bubble inside the nozzle. $\boldsymbol{D_{noz}}$ is 150 μm. The liquid used is 75% aqueous glycerin (w/w) solution. Printing parameters: bi-polar piezo-driving signal with 550 μs t_{dwell} and 550 μs t_{echo}; driving pulse amplitude equals to 140 V. The negative pressure inside the reservoir is -2.3 kPa relative to the atmospheric pressure. Images were taken at a frame rate of 330 kfps. Ambient temperature is 25 ˚C. The scale bar is 500 μm. *dt* equals to 6.06 μs.

4.3.3 More on Surfaces Collapse Jets

Fig. 4.15 shows another type of "surfaces collapse" jet which occurs during inkjet printing. Initially an air bubble stays deep inside the nozzle. When the piezo-generated positive acoustic pressures reach the bubble, the focusing flow squeezes the bubble and causes part of the air and the liquid being expelled out of the nozzle. The squeezed air blows the liquid to an elongated crown shape and breaks it to release part of the air. Thus the pressure inside the cavity decreases rapidly. After only around 50 μs, the conical wall of the broken crown contracts on the lower sections and closes up again. Due to inertia, the expelled liquid, which constituting of the crown wall, will travel downward along the crown wall and accumulates at the vertex of the crown. Meanwhile, the piezo-element expands to its equilibrium state, causing a negative pressure inside the nozzle. Thus the atmosphere pressure squeezes the air inside the crown into the nozzle, as marked by the arrows in Fig. 4.15(b). The combination of these two effects causes a "necking" effect on the crown, with a decreasing in the crown height and a decreasing in the angle at the crown vertex, forming a cusp shown in closeup. The arrow in the first frame of Fig. 4.15(c) marks this angle at the crown vertex. Finally, the crown wall meets and collapses with itself, sending an upward fine jet into the nozzle, as can be seen clearly in frame 4 of Fig. 4.15(c). Furthermore, a tiny air bubble is also trapped by the collapse (frame 5 in Fig. 4.15(c)). Fig. 4.16 provides a close view of a similar kind of surfaces collapse jet. It clearly shows that the jets are produced when the hyperbolic surface collapses. Two jets are generated, one upward and one downward, as marked by the arrows.

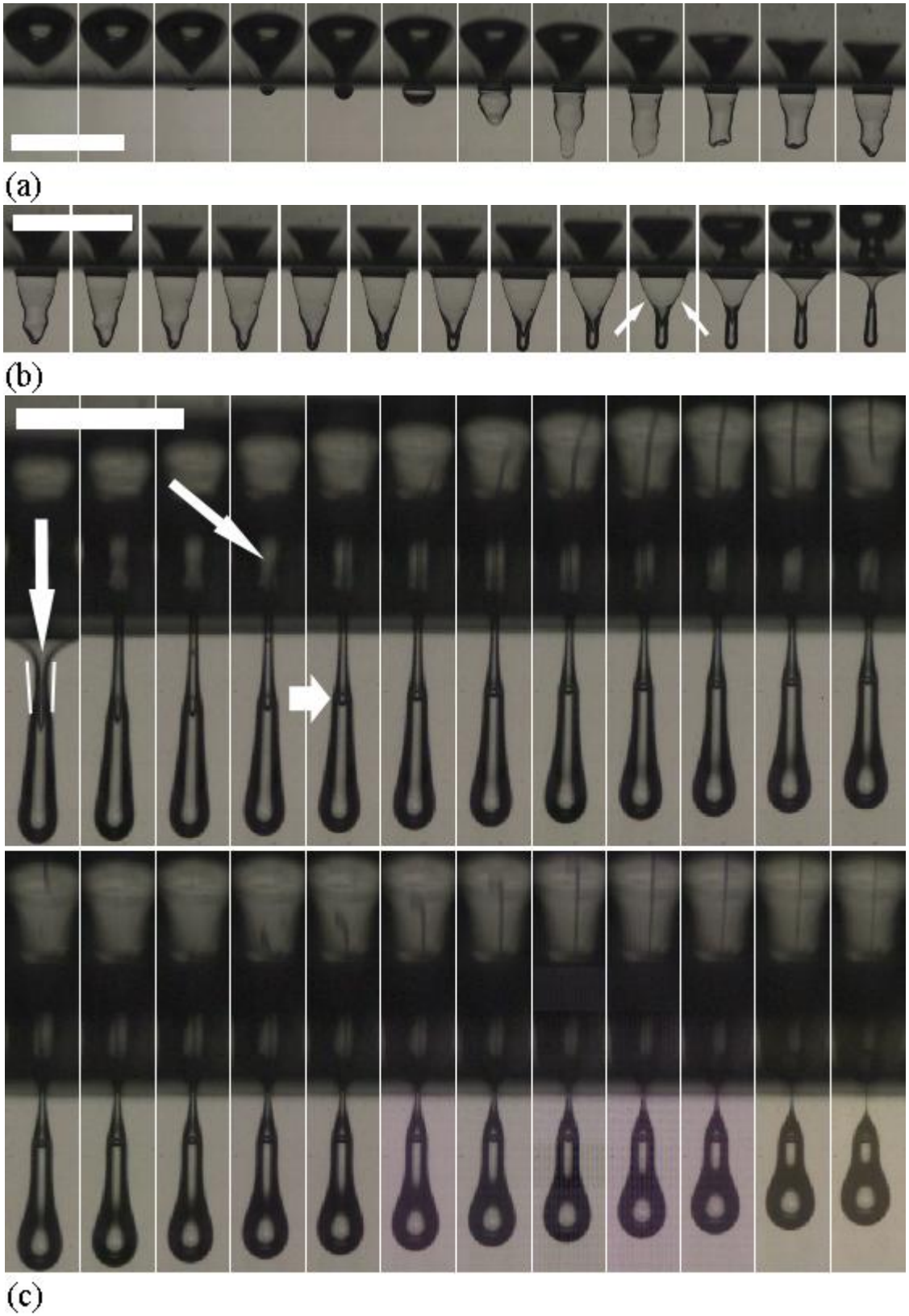

Fig. 4.15: Surfaces collapse jet upward into the nozzle. $\boldsymbol{D_{noz}}$ is 150 μm. 85% water glycerin (w/w) solution. Bi-polar piezo signal: 650 μs t_{dwell} and 650 μs t_{echo}; 140 V. The negative pressure inside the reservoir is -2.3 kPa. Images were taken at 165 kfps. Ambient temperature is 25 ˚C. (a). The scale bar is 1 mm. *dt* equals to 24.24 μs. (b). The scale bar is 1 mm. *dt* equals to 18.18 μs. (c). The scale bar is 500 μm. *dt* equals to 12.12 μs.

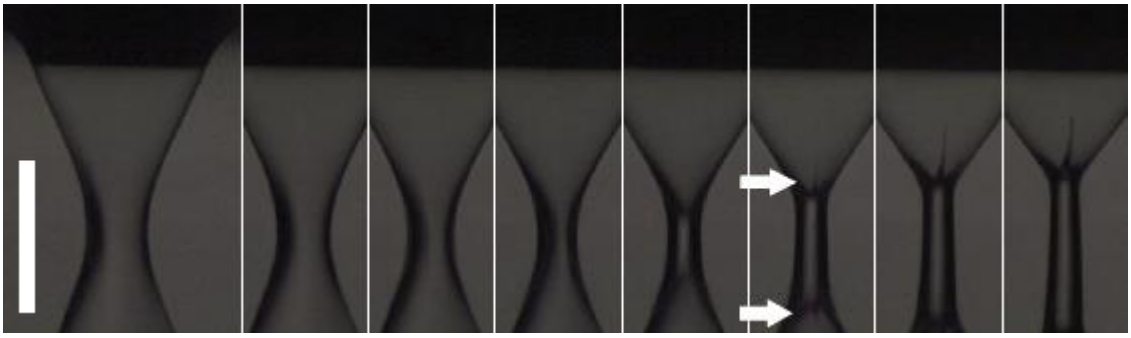

Fig. 4.16: Surfaces collapse jets. $\boldsymbol{D_{noz}}$ is 150 μm. The liquid used is 50% aqueous glycerin (w/w) solution. Printing parameters: bi-polar piezo-driving signal with 550 μs t_{dwell} and 550 μs t_{echo}; driving pulse amplitude equals to 140 V. The negative pressure inside the reservoir is -2.3 kPa relative to the atmospheric pressure. Images were taken at a frame rate of 330 kfps. Ambient temperature is 25 ˚C. The scale bar is 200 μm. Image for frame number n = 1, 3, 5 …… 13, 15.

4.3.4 Viscosity Effects on Jet Velocity

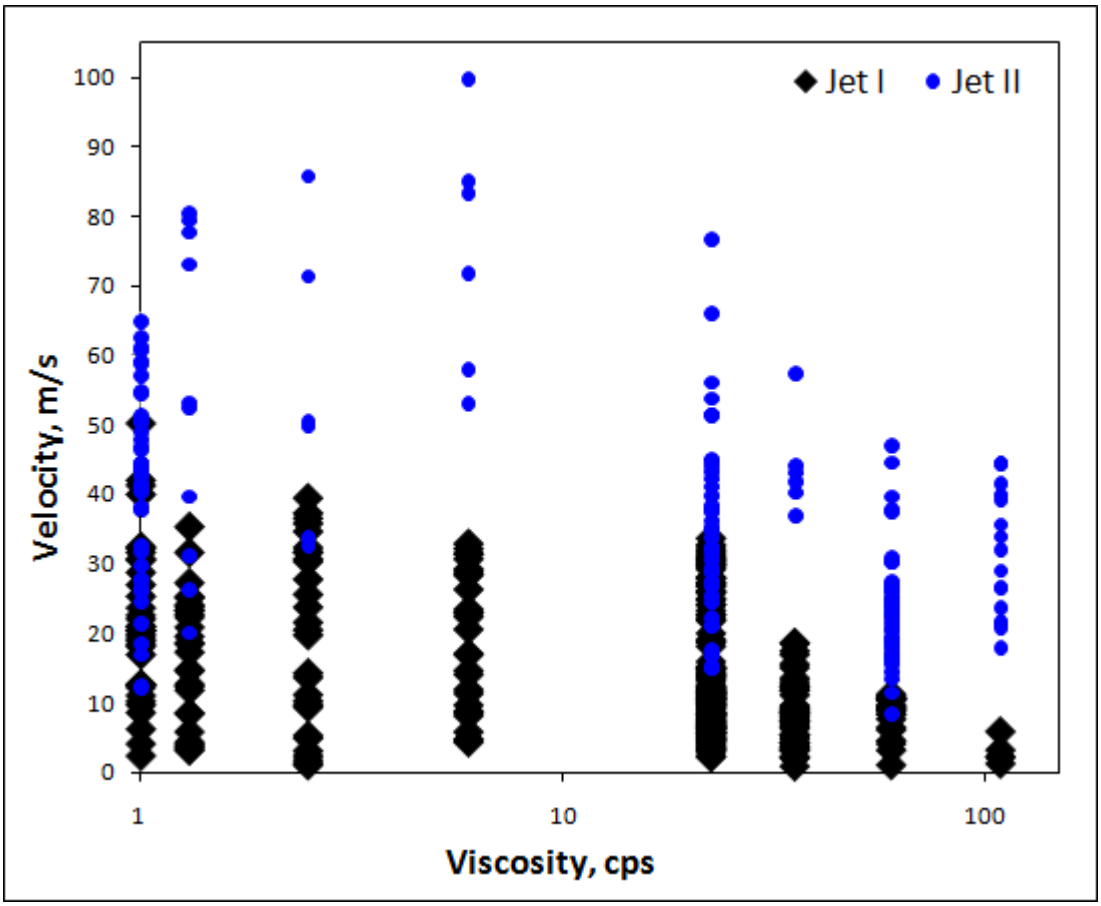

Fig. 4.17: Jetting velocities obtained for different concentration of aqueous glycerin solutions (w/w): 0%, 10%, 30%, 50%, 70%, 75%, 80%, and 85%.

For each concentration of the aqueous glycerin solution, the printing parameters were varied to obtain different jetting velocities as well as jet diameters. Fig. 4.17 shows the velocities obtained during the experiments. As can be seen, for the typical jet (Jet I), the highest jetting velocity for different solutions fairly decreases monotonously with the increase of viscosity. While for Jet II, the highest velocity occurs for intermediate, with a maximum peak when 50% glycerin-water solution is printed.

Fig. 4.18 shows the fastest jet generated in the experiment. The jetting process is similar to the one shown in Fig. 4.10(d). A piezo-generated cavity was sucked into the nozzle and got into contact with a preexisting bubble, without coalescing with it. The later piezo-generated radial focusing flow pushed out the lower cavity as well as the lower cap of the preexisting bubble, forming the balloon-like bubble. This balloon-like bubble collapsed later, followed by the cavity jet shown here.

From extensive experiment results, it became clear that the jets produced in this way normally have much higher velocities. Also from Fig. 4.17, it seems that a solution with a moderate viscosity is optimal to produce a fast jet. The reason may be due to the fact that for solutions with lower viscosities, the two cavities inside the nozzle are more likely to coalesce (as shown in Fig. 4.6); while for solutions with much higher viscosities, it becomes more difficult for the viscous balloon-like bubble (as shown in Fig. 4.12) to rupture. The bubble's oscillation dissipates much energy; the viscous film itself exerts flow resistance to the jet, and finally this two effects lead to a slower jet.

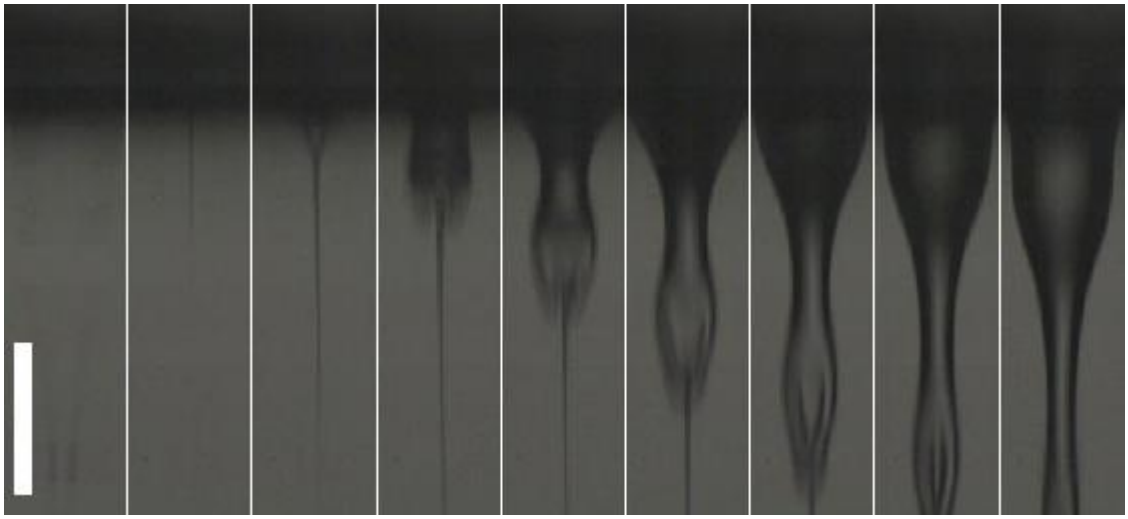

Fig. 4.18: The fastest jet observed in the experiment: a 9 μm jet with a velocity of about 100 m/s. $\boldsymbol{D_{noz}}$ is 150 μm. The liquid used is 50% aqueous glycerin (w/w) solution. Printing parameters: bi-polar piezo-driving signal with 550 μs t_{dwell} and 550 μs t_{echo}; driving pulse amplitude equals to 140 V. The negative pressure inside the reservoir is -2.3 kPa relative to the atmospheric pressure. Images were taken at a frame rate of 330 kfps. Ambient temperature is 25 ˚C. The scale bar is 200 μm. Time interval between frames is dt = 3.03 μs.

4.3.5 Relationship between Jet Velocity and Jet Diameter

Fig. 4.17 shows that the jets velocities generated during the experiments vary over a wide range; same is true for the diameters of the jets. Fig. 4.19 shows 3 jets with different diameters as well as velocities. The only difference in their printing conditions was slight change of the negative pressure inside the reservoir. As was mentioned before, both type I and type II jets are quite sensitive to this back pressure. As a result, big differences were obtained in jetting velocity. From Fig. 4.19, it appears that the jet velocity decreases with the increasing of the jet diameter. To verify this, Fig. 4.20 combines all the obtained jet velocities with their corresponding jet diameters into one graph. An inverse relationship can be clearly seen from the figure.

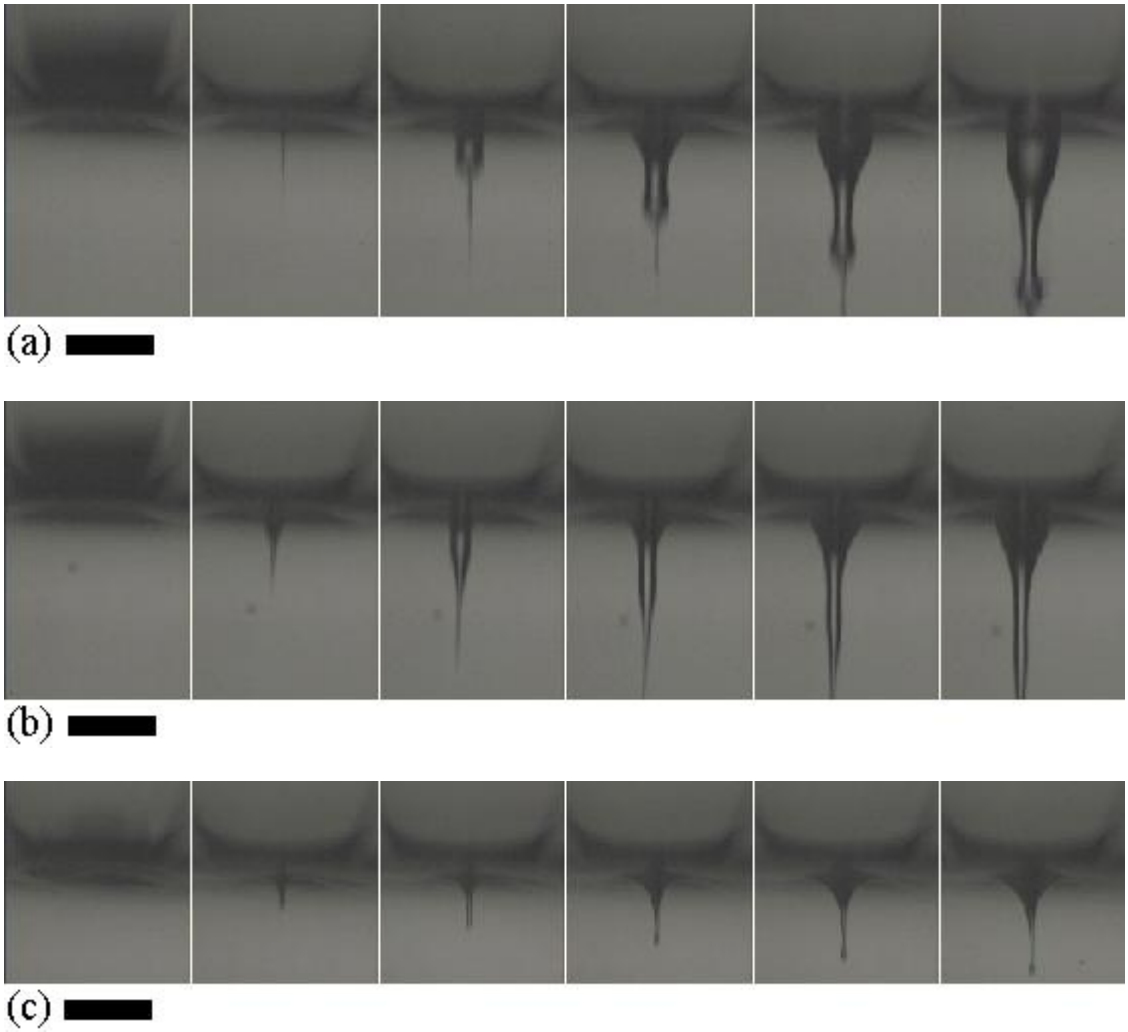

Fig. 4.19: Images showing the relationship between jet velocity and jet diameter. Jets belong to type II. $\boldsymbol{D_{noz}}$ is 150 μm. The liquid used is 70% aqueous glycerin (w/w) solution. Printing parameters: bi-polar piezo-driving signal with 550 μs t_{dwell} and 550 μs t_{echo}; driving pulse amplitude equals to 140 V. The negative pressure inside the reservoir is -2.3 kPa relative to the atmospheric pressure. Images were taken at a frame rate of 330 kfps. Ambient temperature is 25 ˚C. The scale bar is 200 μm. (a). A 1 μm jet with a velocity of 66 m/s. (b). A 3 μm jet with a velocity of 51 m/s. (c). A 10 μm jet with a velocity of 15 m/s.

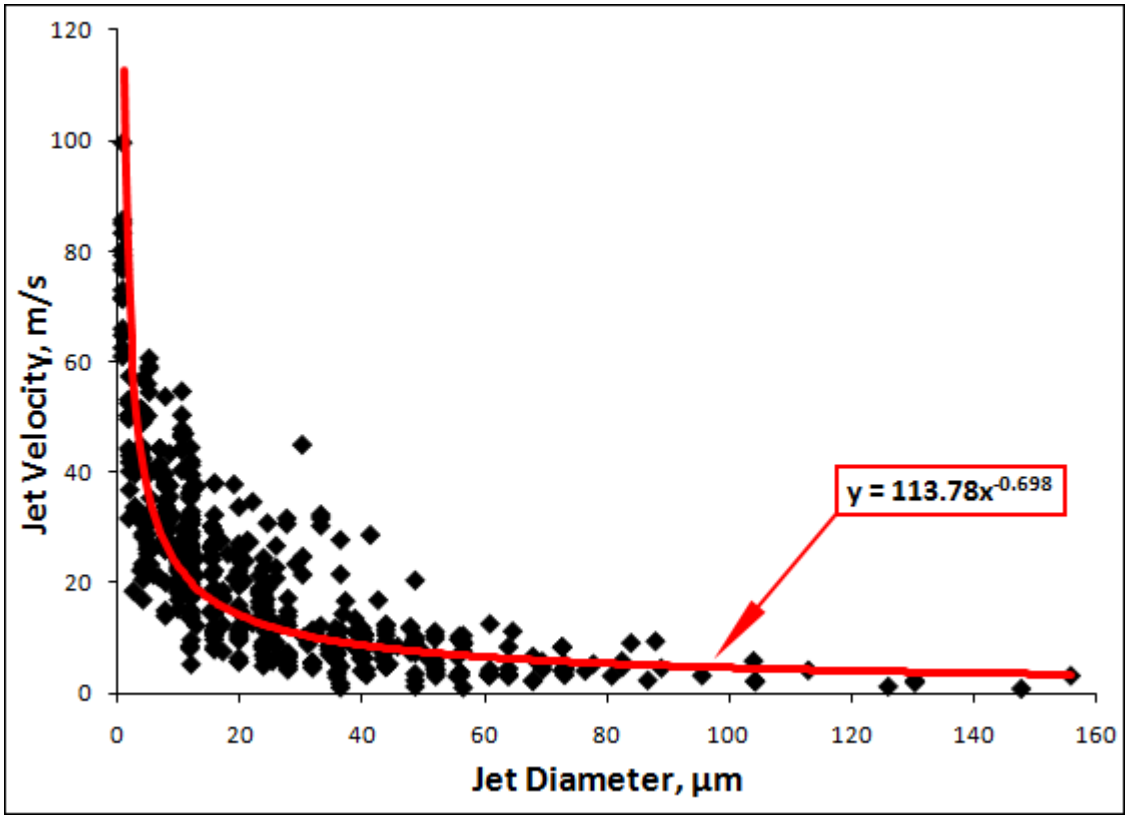

Fig. 4.20: Images showing the relationship between jet velocity and jet diameter. Data collected for both Jet I and Jet II. $\boldsymbol{D_{noz}}$ is 150 µm. Liquid used is 0%, 10%, 30%, 50%, 70%, 75%, 80% and 85% aqueous glycerin (w/w) solutions. Printing parameters: bi-polar piezo-driving signal; driving pulse amplitude equals to 140 V. Ambient temperature is 25 ˚C.

4.4 Conclusions

The formation of fine jets during the piezoelectric drop-on-demand inkjet printing has been investigated using ultra-high-speed video imaging. The speed of the jet can be as high as 100 m/s, which is much higher than the typical droplet velocity during regular inkjet printing. The generation of such fine jets has been studied over a wide range of viscosities, using 7 different concentrations of water-glycerin solutions, giving viscosities as high as 100 times that of water. This jetting is associated with the inertial focusing of an airpocket which is sucked into the nozzle during the printing. This occurs for longer expansion times for the piezo-element. Two types of jets have been

identified during these experiments. The relationship between the speed of the fine-jet and its diameter has also been characterized, over a range of viscosities.

These fine jets are very sensitive to slight variations of reservoir back-pressure, suggesting chaotic behavior. However, the diameters of the thinnest jets are of the order of a few microns, indicating the successful generation of smaller droplets (or jets) to diameters of smaller than 1 % of the orifice diameter. While in existing studies [21, 24, 25], the diameter of the dispensed droplets can be only reduced to a maximum of 60 % of the orifice diameter. Consequently, the study provides a possible way to improve inkjet printing resolution without reducing nozzle diameter.

5. CELL PRINTING

5.1 Introduction

Organ printing, is defined as "a rapid prototyping computer-aided 3D printing technology, based on using layer by layer deposition of cells and/or cell aggregates into a 3D gel with sequential maturation of the printed construct into perfused and vascularized living tissue or organ" [137]. It is a feasible and fast-developing technology which aims to build implantable organs to treat diverse diseases such as cancer, loss of tissue function, or organ failure. As has been mentioned in section 2.4, inkjet printing is a highly suitable candidate for organ printing. The power of inkjet printing lies in its ability to deliver picoliter volumes of materials (solutions, polymers, gels or cell ink) at high speed (a jetting frequency of 2-10 kHz is quite common) and accuracy (several tens of microns) on a target interface (probably non-planar surface, for example, an organ surface), and to deliver active substances to a developing structure in a well defined time-and-space sequence.

To guarantee successful organ printing, plenty of fundamental requirements must be fulfilled: cells should be accurately placed into desired patterns; cells have to survive the shear stresses experienced during the printing, and must keep their viability. The number of cells inside each printed droplet should also be well controlled as "empty droplet" and cell-less droplets are undesirable for building living structures. Printed cells should be able to

adhere, spread and proliferate on the substrate, which are generally different gels.

To date, different types of cells have been printed successfully and their viability has been verified [3-10, 103]. The most comprehensive studies was carried out by Saunders *et al.* [9], who used a commercial desktop printer to dispense human fibroblast cells, for the investigation of the relationship between cell survivability and the inkjet printing parameters. Their study supported previous claims [4, 5, 8, 10] that cell survivability was not significantly affected by the printing process since cell survival rates only fell from 98% to 94% in their case, when the excitation pulse was increased from 40 to 80 V. However, in their study, the entire printing process was carried out using a modified commercial printer, thus limiting their experiments to a fixed nozzle diameter (60 μm) and a small range of the drop velocities (lower than 1.0 m/s). These limitations may be of importance, because the shear stresses, which are expected to be the main factor in the killing of cells during the printing process, are proportional to the velocity gradients within the nozzle.

To eliminate above two limitations, a squeeze mode piezoelectric DOD inkjet printhead was designed and fabricated in-house, as has been represented in detail in Chapter 3. A much larger range of droplet velocities can be obtained by the novel printhead, compared to this earlier study [9]. Furthermore, the improved design of the printhead allows us to change the nozzles while using the same printhead main-body, thus enabling us to investigate the effects of varying the orifice diameters on cell survival rates. It will be shown that by

using a small diameter nozzle and a high excitation voltage, the printing process generates large enough shear stresses to cause significant decrease in the cell survival rates. In fact, shear stresses have been studied extensively to predict the damage of animal cells suspended in various laminar or turbulent flows. This part of our study provides quantitative estimate of these effects on cell survivability in DOD inkjet printing.

The number of cells in each printed droplet is one important factor in optimizing cell printing, as empty droplets may be undesirable. The probability distribution of cell numbers to ascertain desirable mean cell concentration in the medium has been studied, to avoid "empty droplets" and cell-less droplets. To form cell patterns, L929 rat fibroblast cells were firstly printed onto alginate. Alginate has been increasingly utilized in tissue engineering to support encapsulated cells and to regulate cell function, in a manner similar to the extracellular matrices of mammalian tissues. However, the major limitation to its use as an extracellular matrix is that alginate does not mediate mammalian cell adhesion. To promote cell adhesion within alginate gel, ligands such as arginine-glycine-aspartic acid (RGD), GRGDY, KGD and VAPG can be used. Collagen is another widely used hydrogel with a number of advantages including biodegradability, low immunogenicity and controllable stability. Furthermore, collagen contains cell adhesion domain sequences such as RGD, which facilitate cell adhesion for anchorage-dependent cell types. Therefore, in later part of the study L929 cells were printed onto collagen to form patterns.

5.2 Material Preparation and Experimental Procedure

5.2.1 Preparation of Cells, Alginate and Collagen

L929 rat fibroblasts were cultured in 1× Dulbeccos Modified Eagles Medium (DMEM, D1152). The medium was supplemented with 10% foetal bovine serum (FBS, Gibco) and 1% Penicillin Streptomycin. FBS is widely used in cell culture as cell growth promoting factor. Penicillin Streptomycin is a broad spectrum bacteriostatic and bacteriocidal, with activity against gram negative and gram positive organisms. Cells were cultured and sub-cultured in 150 cm^3 culture flasks at 37 ℃, 5% CO_2 and were observed under a microscope at intervals until they grew to a full layer in the flasks. Cells were harvested by trypsinizing with the utilization of 0.25%, 1 mM EDTA Na (Gibco) and washing with phosphate-buffered saline (PBS, Gibco). DMEM was mixed with the trypsinised cell solution and transferred to 50 cm^3 conical tubes which were then centrifuged at 1500 rpm for 5 min. After centrifugation, the supernatant liquid was removed leaving the cell pellet and fresh media was added. The final cell solution was gently agitated using a pipette to ensure uniform distribution as well as to disrupt cell clumps. The required cell concentrations of solutions for experiments were quantified by using a haemocytometer (Fisher Scientific UK, Loughborough, UK).

A 1.0% (w/v) aqueous solution of sodium alginate (A2158, Sigma-Aldrich) was prepared by suspending the polymer in distilled water. After 6 hours of

stirring by a magnetic stirrer, the solution was sterilized by sterile filtration, using 0.22 μm membrane filters.

The 3 mg/ml collagen solution, (C4243, Sigma-Aldrich) was prepared by mixing 8 parts of chilled collagen solution with 1 part of 10× PBS. The pH of mixture was adjusted to 7.2–7.6 using 0.1 M NaOH. The pH value was monitored carefully using pH paper. To prevent gelation, the resulting solution was then maintained at temperature of 4 ℃ until ready for use.

5.2.2 Printing Experimental Setup

Printing experiments were carried out by using the self-developed squeeze mode piezoelectric inkjet printing system. The setup is comprised of a compressor, a pressure regulator, a reservoir, a piezo-actuated printhead, a piezo driver, an Arrisun-5 lamp and a Photron Fastcam SA-1 camera (high-speed-video camera), as shown in Fig. 5.1. The present printhead design is a great improvement over conventional pintheads, as it allows for the use of interchangeable nozzles, for the same piezoelectric transducer. The interchangeable nozzle design allows one to easily clean or change a clogged or damaged nozzle. The details of the design can be referred to Chapter 3 or Ref. [140]. Before printing, all the components that will contact with cell ink during printing process, which include the liquid reservoir, the printhead chamber and the interchangeable nozzle, need to be properly sterilized by autoclaving to 121 ˚C at 15 psi (pounds per square inch) for 60 minutes. The inkjet process is highly periodic. Fig. 5.2(a) shows the droplet formation process in a time sequence. Drop velocity can be calculated by dividing the

spacing between two droplets by their time difference. Fig. 5.2(b) shows images of a few cells inside the nozzle.

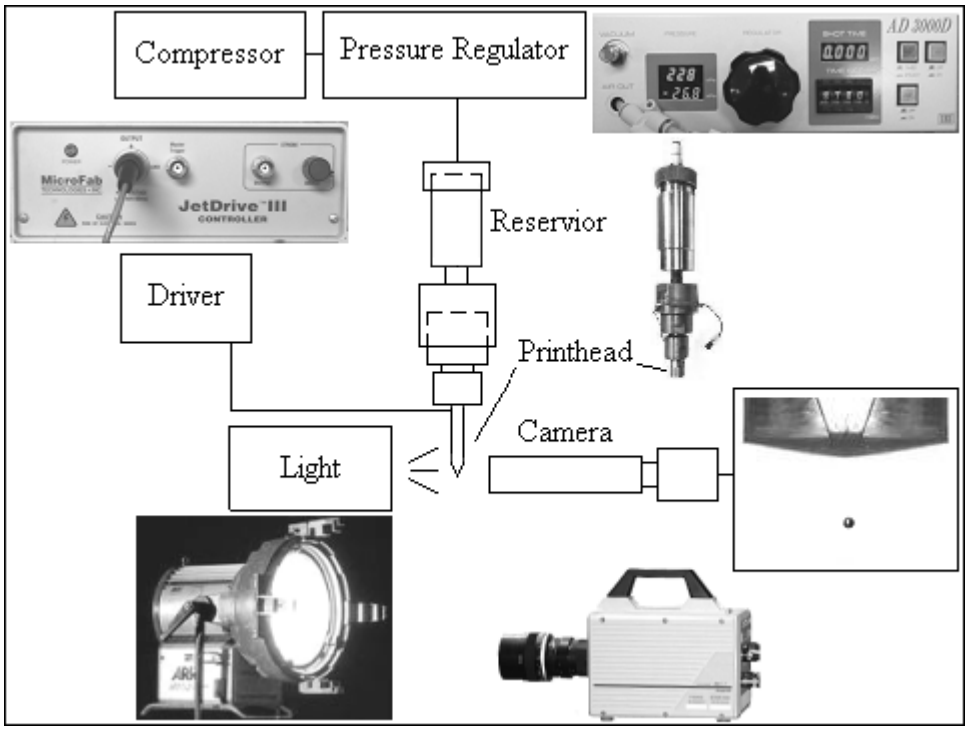

Fig. 5.1: Schematic showing the DOD setup for cell printing experiment.

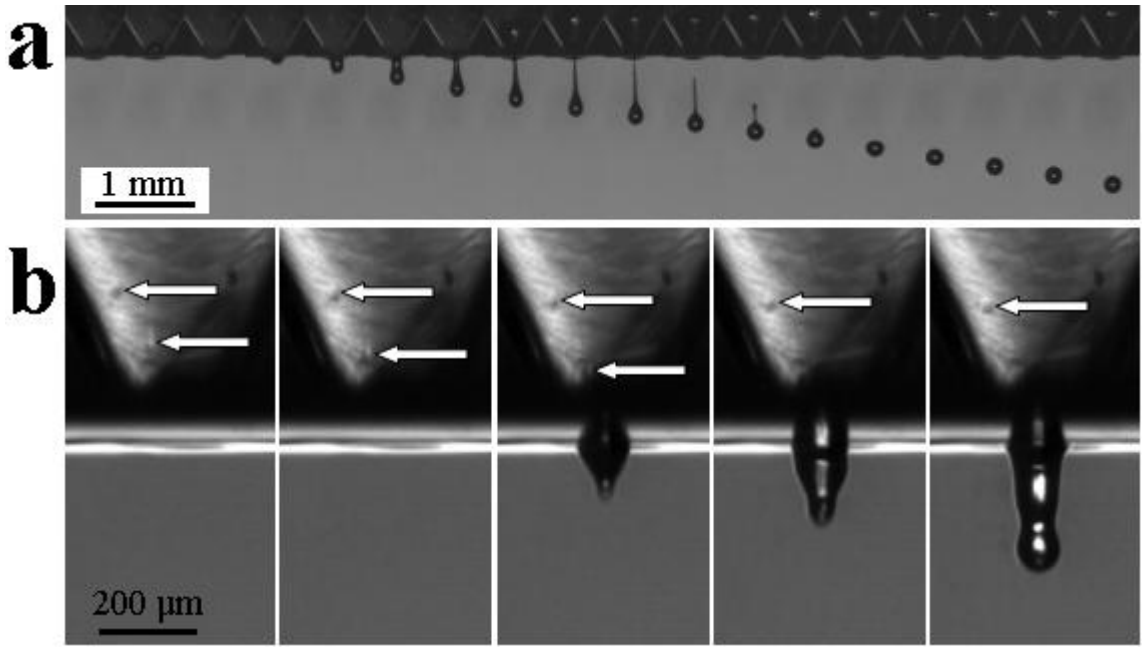

Fig. 5.2: Images taken by using the high-speed-video camera. (a). Image sequence showing the formation of a 160 µm droplet from a 119 µm nozzle, taken at a frame rate of 8,000 fps, giving time between frames of 125 µs. Liquid used was 1.0% (w/v) aqueous solution of sodium alginate. Drop velocity is 0.74 m/s. (b). Images showing cell motion inside the nozzle. Nozzle opening diameter is 119 µm.

For the study of cell survival rates, L929 rat fibroblast cell suspensions were printed through orifices of three different diameters (119 μm, 81 μm and 36 μm) onto well plates (Costars) which contained the live-dead assay solution. Preparation of the live-dead assay solution will be introduced later. The electric pulses which were used to drive the piezoelectric transducer were in the range of 52 to 140 V. Each sample was printed for approximately 20 s with a driving frequency of 1.5 kHz for the printhead. Prior to the printing process, a 15 μl cell suspension was deposited with a pipette into a well plate in the same environment as the printing system, to act as a control.

For pattern printing, either alginate or collagen served as the substrate. The 1.0% (w/v) alginate was coated onto well-plate surfaces (Costar) to form around 100-μm-thick film. Cells were dispensed onto this film using a cell ink which contained 0.5% (w/v) calcium chloride and had a cell concentration about 3×10^6 cells per ml. The crosslinking reaction occurs once the droplets contact the alginate film. Printed samples were immediately placed into an incubator. One hour after printing, fresh medium was carefully added into the well plates, covering the gel surface and protecting the cells from dehydration. Samples were transferred into incubator again and observed under a microscope at intervals. When collagen served as substrate, 0.3% (w/v) collagen solution was coated onto well plate surfaces to around 2-mm-thick films and warmed up to 37 ℃ for around 1 hour for gel formation. The well plates were then placed onto a XY motion stage and L929 cell suspensions were printed onto the gel according to the desired pattern. Printed samples were immediately transferred into an incubator. Fresh medium was carefully

added into the well plates 1 hour following the printing, preventing cells death from dehydration. Samples were transferred into incubator again and observed under a microscope at intervals.

5.2.3 Survivability Tests

A Live-Dead Viability/Cytotoxicity Kit (L3224, Molecular Probes, Invitrogen) was used to assess the survivability of the cells after the printing. The frozen vials containing the assay were thawed and centrifuged briefly before use. 20 µl of the supplied 2 mM EthD-1 solution and 5 µl of the supplied 4 mM calcein AM solution were added into 10 ml of 1× DMEM solution and mixed thoroughly, which gave an approximately 4 µM EthD-1 and 2 µM calcein AM working solution.

Cells were directly dispensed into well plates which each contained 100 µl of the assay mixture, then incubated for 30 min. For each printing condition, cells were dispensed into 5 separate petri dishes, to study the variation of survival rates. Controls were taken directly from the cell ink before printing and put on a set of separate petri dishes, undergoing the same environment and procedure. The stained samples were then partly transferred onto microscope slides and observed under a fluorescence microscope. Six images were captured from each perti dish for cell counting. Cells that remained alive after the printing were stained green and the damaged cells were stained red. The numbers of alive and dead cells for each sample were tallied with respect to that of the control which was taken prior to the printing.

5.3 Results and Discussion

5.3.1 Cell Survivability Study

5.3.1.1 Cell Printing

L929 cells were printed into Petri dishes containing the live-dead assay solution, through 3 different orifices with the diameters of 119 µm, 81 µm and 36 µm. Printing was carried out over a range of excitation pulse amplitudes from 52 to 140 V, while the rising/falling time was kept constant at 3 µs and the dwell time, i.e. the time duration of the excitation pulse, was kept at 70 µs. The driving frequency was held constant at 1.5 kHz. Each sample was printed for approximately 20 s. The concentration of the cell suspension was about 1 million cells per ml.

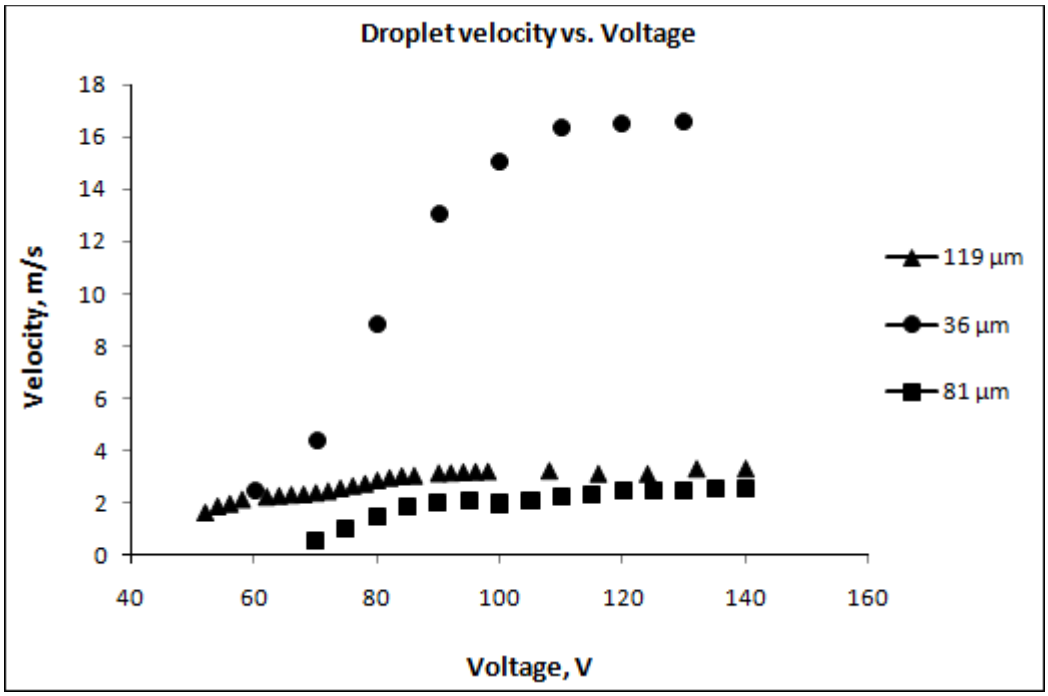

Fig. 5.3: Graph showing influence of excitation pulse on droplet velocity. The orifice diameters of the nozzles used were 36, 81 and 119 µm.

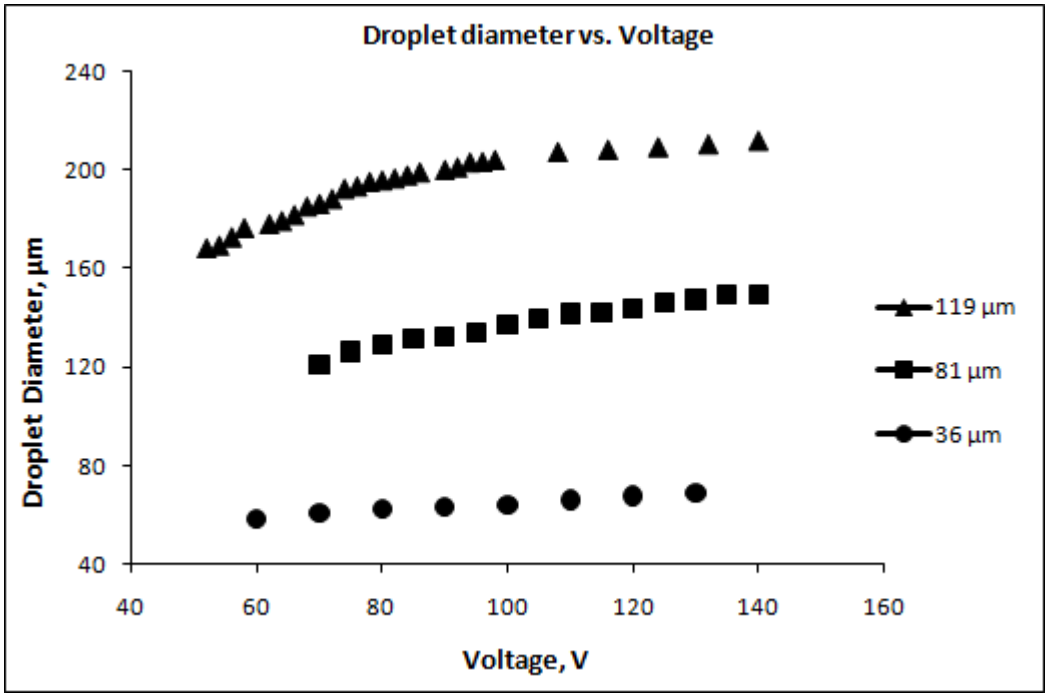

Fig. 5.4: Graph showing influence of excitation pulse voltage on droplet diameter. The orifice diameters of the nozzles used were 36, 81 and 119 µm.

The initial average number of cells inside each droplet is fairly independent of the voltage used to drive the piezo-element. This was verified by observations under the microscope done within 2 hours of the printing, i.e. before proliferation occurs. This result is consistent with the existing study [9]; however, the average number of cells depends strongly on the nozzle/droplet size, as discussed below.

Fig. 5.3 and Fig. 5.4 show the effect of the excitation pulse (which is imparted to the piezoelectric actuator) on the droplet velocity and droplet diameter, respectively. It is shown that for all of the three nozzles, drop velocity and droplet diameter increase with the increase of excitation pulse. This increase in droplet velocity is especially pronounced for the 36 µm nozzle, where droplet velocity increases from 2.4 to 16.6 m/s as the driving voltage increases from 60 V to 130 V. However, for the 36 µm nozzle, small satellite droplet is

generated once the driving voltage exceeds 70 V. To avoid satellite formation typical DOD inkjet printing cannot generate such high velocities as used herein. In fact, for specific nozzle size and pulse duration, there exists a critical pulse amplitude, above which satellite droplets are produced [63]. When a satellite droplet is generated, the drop velocity is determined based on the main droplet. The presence of the small satellite droplets is of no direct relevance to the survival study, but will interfere with pattern printing.

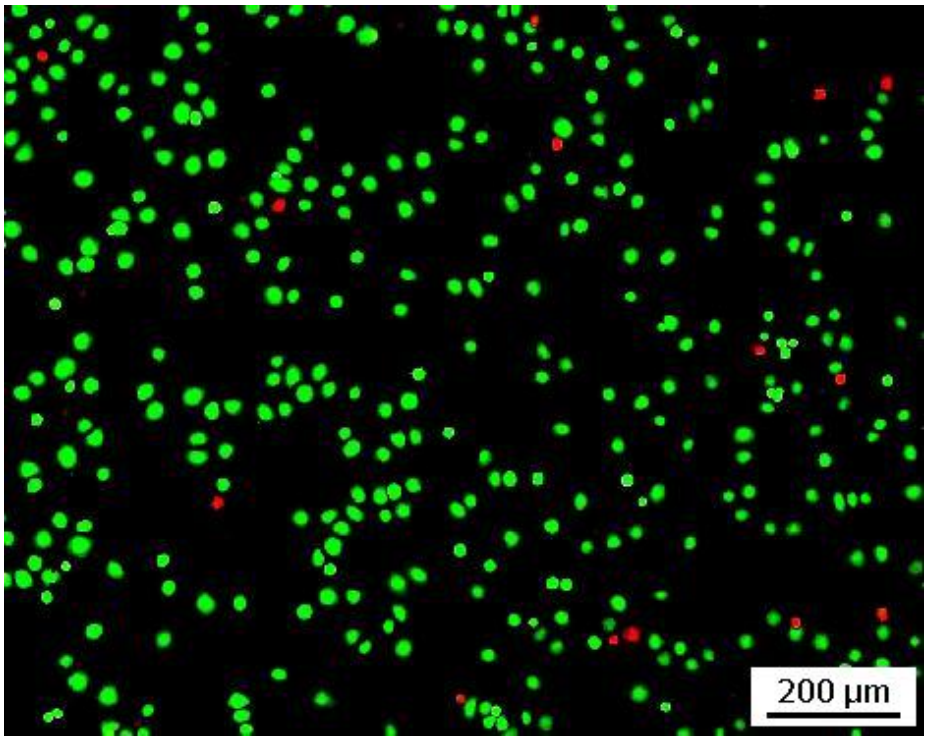

Fig. 5.5: Graph showing a 95% survival rate of L929 rat fibroblast cells stained with Calcein AM and Ethidium homodimer-1. Printed with an excitation pulse amplitude of 116 V, at a frequency of 1.5 kHz, with rising and falling times of 3 µs. The orifice used was 119 µm.

5.3.1.2 Cell Survivability: Effects of the Mean Shear Rate

Cell survivability after printing was quantitatively investigated by using the LIVE-DEAD Viability/Cytotoxicity Kit as explained above. Fig. 5.5 shows a stained sample which has a 95% survival rate.

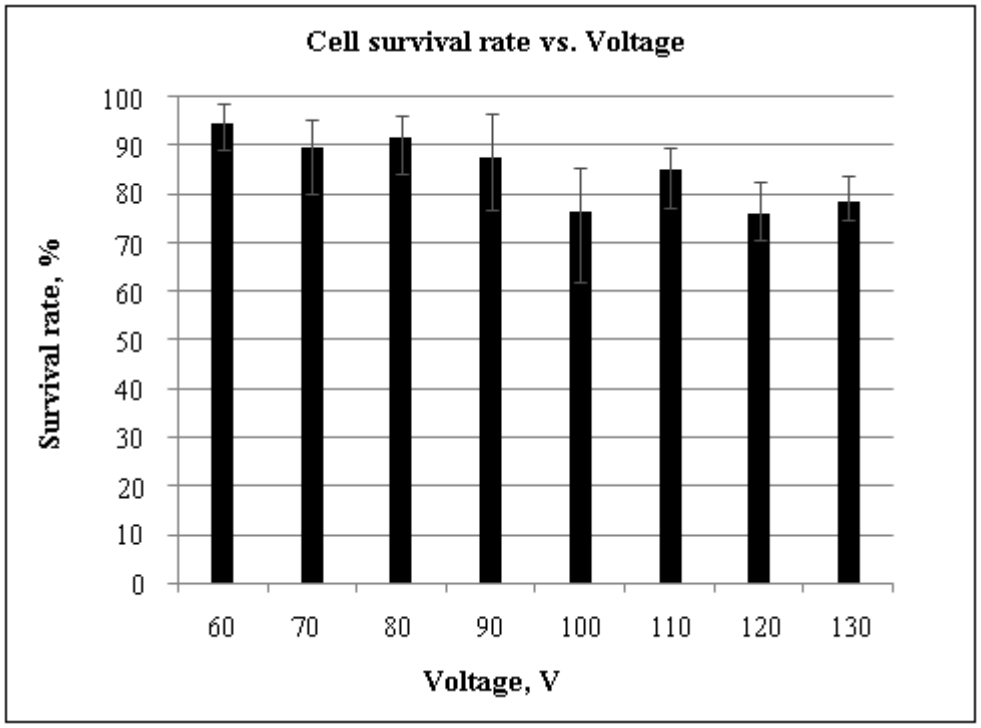

Fig. 5.6: Mean cell survival rate with respect to excitation pulse amplitude for the samples printed through the 36 μm orifice, with excitation pulse amplitude from 60 V to 130 V, at a frequency of 1.5 kHz, with rising and falling times of 3 μs. Error bars show the standard error from 5 replicates.

Fig. 5.6 shows the effects of excitation pulse amplitude on the mean cell survival rate, for the 36 μm nozzle. It is shown that the survival rate falls from 95% to 78% as the excitation pulse is increased from 60 to 130 V, and the lowest survival rate of 76% is observed when the highest voltage is approached. The excitation pulse amplitude represents the power for the piezoelectric actuator to dispense the droplets and this power directly affects the droplet velocity and thereby the shear stress in the liquid. In Fig. 5.7, the mean cell survival rates against excitation pulse amplitude for all of the three different orifices are drawn together to compare the effects of different orifice sizes on cell survivability.

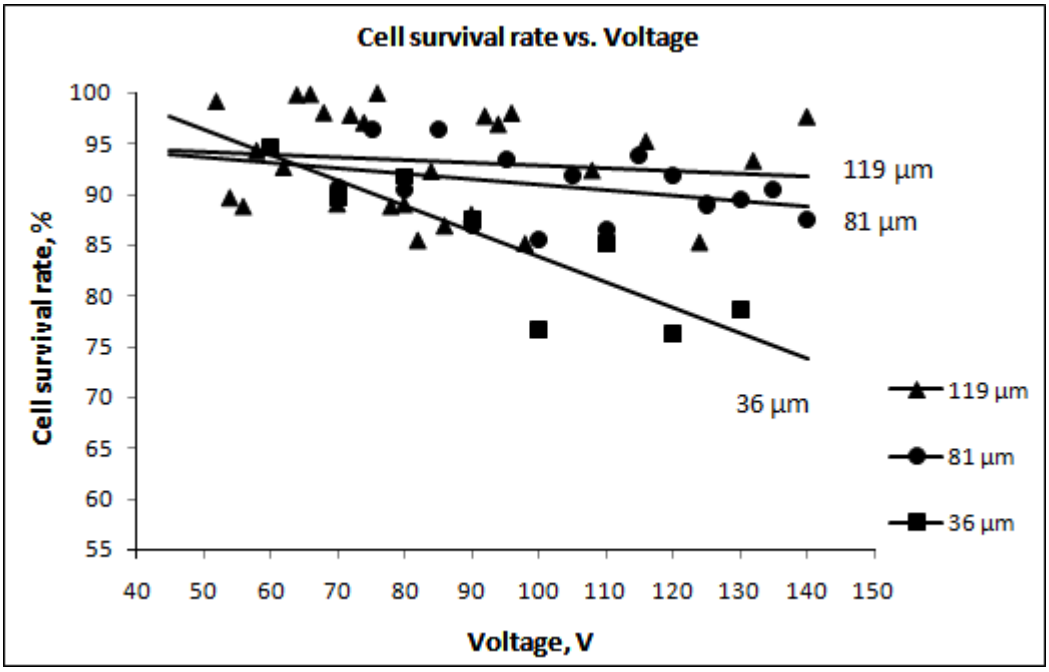

Fig. 5.7: Graph showing the mean cell survival rate against excitation pulse amplitude. Samples printed through orifices with the diameter of 36, 81 and 119 µm, with excitation pulse amplitude from 52 to 140 V, at frequency of 1.5 kHz, with rising and falling times of 3 µs. Each cell survival rate data was the average value from 5 replicates.

It shows that survival rates fall from 99% to 85% for the 119 µm nozzle and from 96% to 85% for the 81 µm nozzle. It can be seen that for the bigger orifices, especially the 119 µm one, the printing did not produce a significant reduction in cell survivability as the excitation pulse amplitude is increased. This may be due to the fact that the cells used here were much smaller than the two bigger orifices. The round-shaped L929 rat fibroblast cells are measured to have a diameter of approximately 20 µm. It is known that shear stress in a Newtonian fluid is proportioned to the velocity gradient in radial direction, thus the highest shear stress is always generated in the region near the wall during droplet dispensing. For the larger nozzles the fraction of cells moving next to the wall is reduced, on average the cells will therefore experience less shear stresses, which would ultimately lead to a higher survival rate.

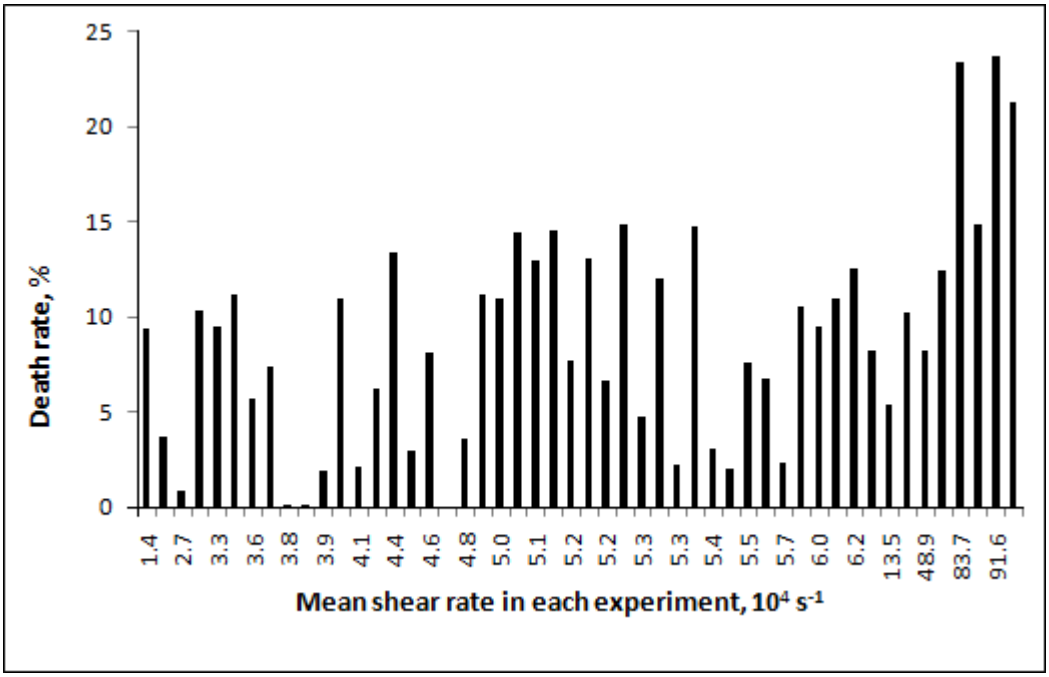

Fig. 5.8: Graph showing percentage of cell death against the mean shear rate. Samples printed through orifices with the diameter of 36 μm, 81 μm and 119 μm. Each cell death rate data was the average value from 5 replicates.

Comparing the 3 different trendlines in Fig. 5.7, we conclude that it is not the strength of the electric field which directly affects cell survival rate; rather it is the fluid shear stress. Due to the highly transient nature of the flow driven through the nozzle (see Fig. 5.2(a)), the detailed knowledge of the velocity profile within the droplet at the nozzle tip is lacked here. Thus the mean shear rate, which can be estimated by $\dot{\varepsilon} = v/r$, where v and r are the drop velocity and the nozzle radius, respectively, is used as a substitute for effective shear stresses. Fig. 5.8 shows the percentage of cells that died against the mean shear rate during the printing. It is shown that the cell death rate increases approximately from 5% to 24% as the mean shear rate increases from 1.4×10^4 s^{-1} to 9.2×10^5 s^{-1}. The trend is more evident for the last eight data points which correspond to the results for the 36 μm orifice. The results clearly show that cell death does occur during the printing, especially under the effects of high shear rates, above 5×10^5 s^{-1}.

One can roughly estimate the displacement thickness of the boundary layer δ using the time duration of the piezo-signal T and the kinematic viscosity of the liquid ν, with the well-known approximation [181], $\delta = 1.72(\nu T)^{1/2}$. The total duration of the signal is T = 76 μs and the viscosity of the cell ink is very similar to that of water, i.e. ν = 10^{-3} m^2/s, which gives δ = 15 μm. The two boundary layers therefore span 30 μm, which is close to the diameter of the smallest nozzle. The large velocity gradients inside the boundary layers are therefore likely to submit many of the cells to the high shear stresses. The geometry of the converging nozzle will certainly affect the true thickness of these boundary layers, but this simple calculation suggests that their size becomes quite significant for the smallest nozzle diameter of 36 μm.

5.3.2 The Number of Cells in Each Droplet

Having investigated cell viability from the inkjet printing, the next step in optimizing the use of such printing in tissue engineering is to uniformly position cells in desired configurations.

Fig. 5.9 shows sections of two adjacent straight lines printed with a 60 μm nozzle. The space between the lines is around 30 μm. There are between 1 to 5 cells observed in each droplet. This large deviation in cell numbers highlights the random distribution of the cells inside the medium when it reaches the nozzle, from which the droplets are dispensed. Therefore, a large average cell concentration will be needed in the suspension to guarantee at least one cell per droplet, with a certain high probability. To investigate the associated

probabilities, we performed a set of separate experiments described in what follows.

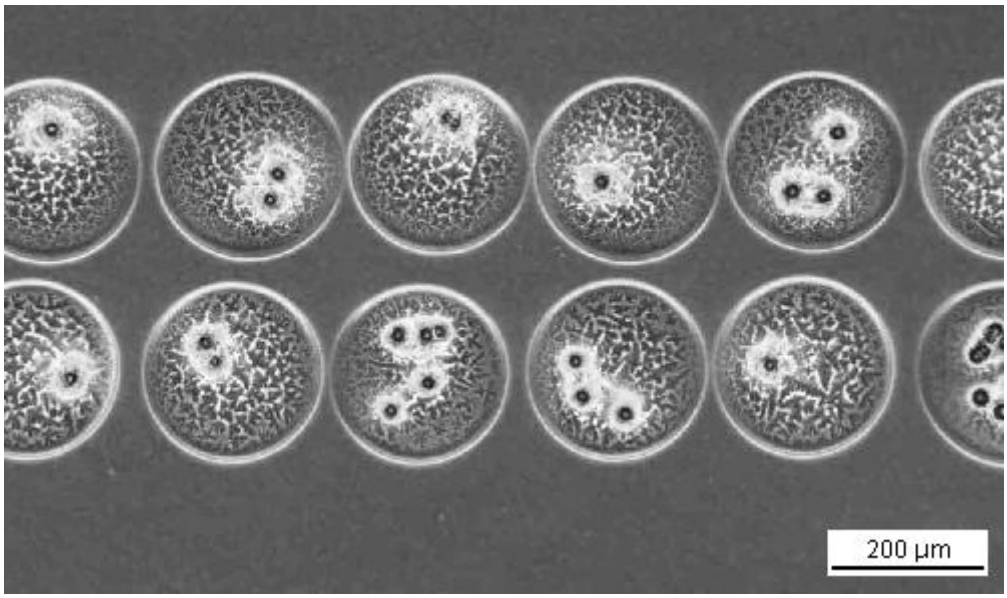

Fig. 5.9: Droplets printed onto a dry substrate from a suspension with a concentration of 2×10^6 cells per ml. Each droplet contains 1 to 5 cells. The orifice diameter of the nozzle used was 60 µm.

The number of cells in each droplet can be thought of as a random variable, whose distribution can then be estimated using basic probability theory [7]. The distribution of cells in the original medium is assumed to be random with a uniform probability density. With this assumption the printing simply represents random sampling of the liquid volume in the reservoir, with a sphere of the same volume as the droplet V_d. The aim is to determine the probability that a certain number of cells are present in this volume. This can be formulated in terms of a Bernoulli sequence of trials [182]. Each trial α consists of randomly assigning the position of the center of one cell inside the whole liquid volume of the media V_m. Successful trial occurs when the cell lands inside the specified droplet. The probability of success in each trial is therefore very small, i.e.

$$p = P(\alpha) = \frac{V_d}{V_m} \sim 10^{-6} \tag{5.1}$$

with a correspondingly very high probability of failure $q = 1-p$. We do however have a very large number of cells, i.e. a very large number of trials are performed. Elementary probability theory shows that the probability of getting *k* cells into a specific droplet in *n* trials becomes

$$P_n(k) = \binom{n}{k} p^n q^{(n-k)} \tag{5.2}$$

where $\binom{n}{k}$ are the binomial coefficients. In our treatment *n* is a very large number, i.e. essentially the total number of cells. In other words, $n = NV_m$, where *N* is the average cell concentration per unit volume. The above eq. 5.2 is therefore quite difficult to evaluate. However, the *Poisson theorem* can be utilized to simplify this calculation, which gives

$$P_n(k) = e^{-np} \frac{(np)^k}{k!} \tag{5.3}$$

where the product $np = NV_d$ now corresponds to the average number of cells per droplet volume, which is denote by N_d.

Fig. 5.10 shows this probability density function for a few different values of N_d, highlighting the variability of the number of cells in different droplets. As the concentration increases the most likely number of cells shifts to larger *k*, while the distribution also widens. The figure shows clearly, that there is a finite probability of producing droplets containing no cells. The above eq. 5.3 shows that the probability of "empty droplets" is

$$P_n(k = 0) = e^{-np} \tag{5.4}$$

which reduces exponentially with higher cell concentration in the medium. Using this formula, it can be seen that to guarantee, with a 99% probability, that each droplet contains at least one cell the average cell density in the

solution must be above $N_d = 4.6$ cells/drop-volume.

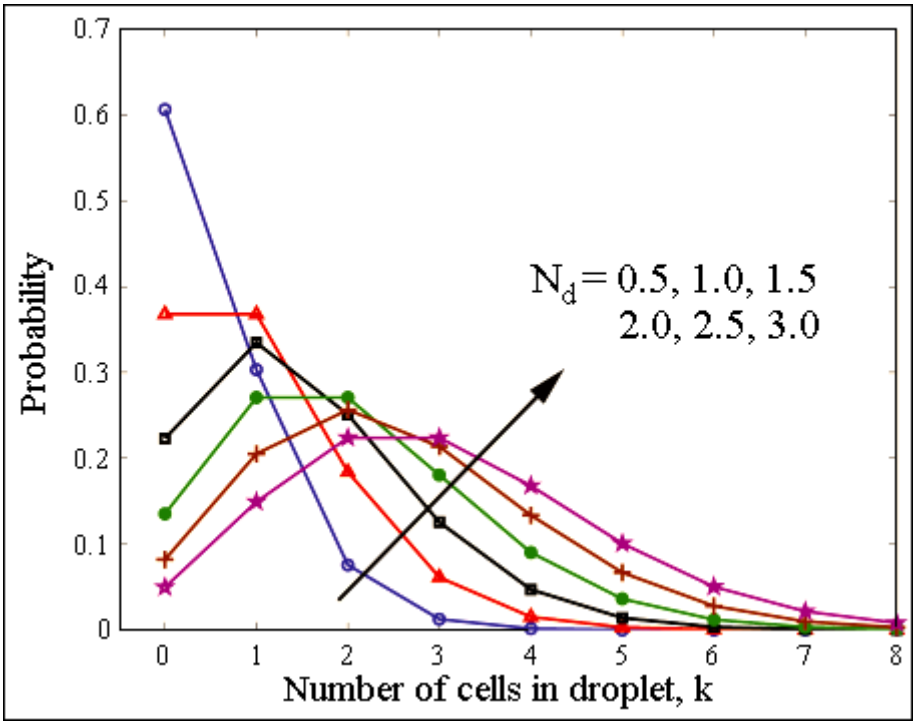

Fig. 5.10: Graph showing the probability density distribution of the number of cells in each droplet. For a range of different average cell concentration in the cell medium, from N_d = 0.5, 1.0, 1.5 … 3.0 cells per droplet.

To investigate the validity of our assumptions we carried out a set of experiments where thousands of droplets were printed onto dry Petri dishes. The diameter of the nozzle used was 130 µm, giving droplet diameter of 170 µm. The resulting diameter of the dry droplet residue was 268 µm, indicating a spreading factor of around 1.6. Therefore the average height of the liquid film was 46 µm. The drops dried out within about 1 min, leaving the dead cells (as compared to the living cells in Fig. 5.11, which adhere to the substrate and extend long filopodia) encased inside the remaining residue of dried medium, as is shown in Fig. 5.12(a). The number of cells inside each drop was then counted under the microscope.

Fig. 5.11: Optical micrographs of L929 rat fibroblast cells after 5 days in culture following printing. Cell division can be observed (indicated by green circle) apparently.

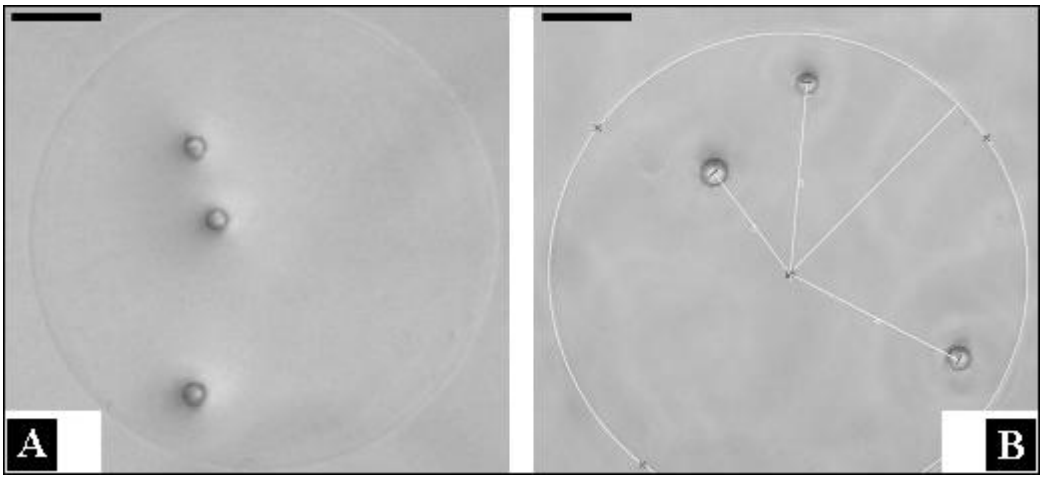

Fig. 5.12: Images of printed cells. (a). Cells inside dried droplet residues. The scale bar is 50 μm. (b). Schematic showing the measurement of the radial location of each cell, away from the center of the dried droplet residue.

Fig. 5.13 compares the distribution of the number of cells inside each droplet with the theory in eq. 5.3. The theory shows excellent agreement except that we observe slightly fewer empty drops that predicted and slightly more droplets containing only one cell. The theory shows perfect agreement for $k \geq 2$. Keep in mind that there are no free parameters in this relationship, with the mean cell concentration $N_d = 1.29$ coming directly from the experimental

results. This excellent agreement with the theory is expected to become even better when the average number of cells in the medium increases.

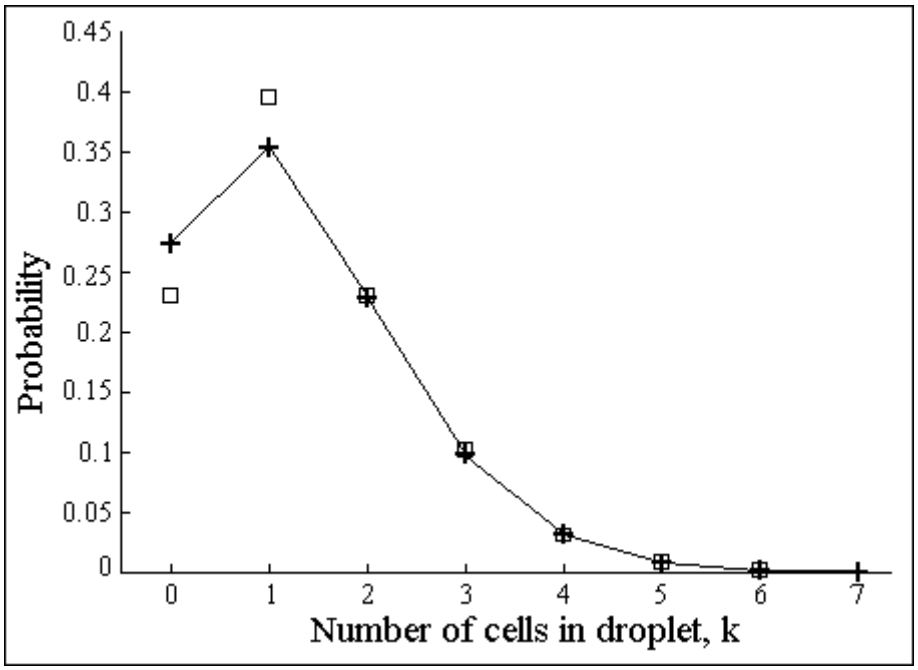

Fig. 5.13: Graph showing the probability density distribution of the number of cells in each droplet. The (□) stands for the experimental results and (--+--) stands for the values calculated from eq. 5.3. Determined from microscope counting of cells in 800 droplets, which were dispensed within the first 4 minutes.

5.3.3 The Location of Cells inside Each Droplet

The spatial distribution of the cells within the dried drop was also studied. Fig. 5.12(b) shows how the radial location of each cell, away from the center of the dried droplet residue, was measured. It is firstly verified that the horizontal motion of the substrate, during the printing, does not move the cells towards a specific direction. This might be introduced by the effective angle of impact of the droplet, which is always less than 6˚ from the vertical. The evaporation of the liquid during drying, could also introduce capillary-driven motions of the cells to the edge of the drop, as is well-known from the everyday experience of coffee stains [33, 34]. This was not observed in the resulting distribution of

cells in the dried spot, which is normalized by the area.

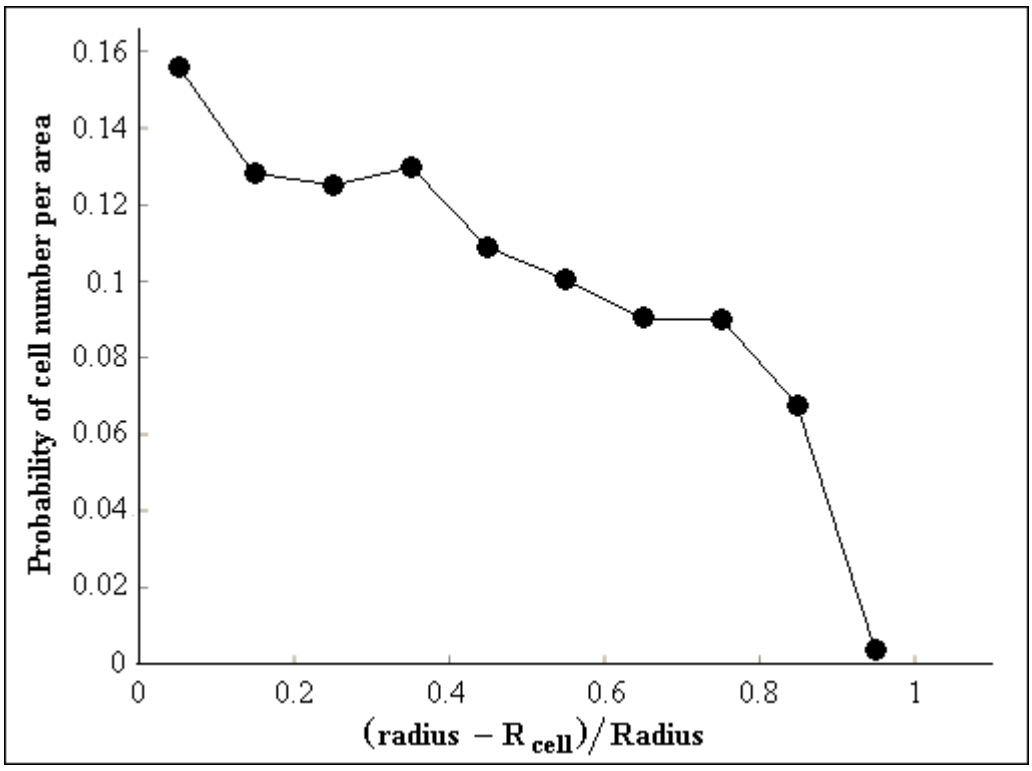

Fig. 5.14: Graph showing the probability of cell location within the dried droplet splatter. The "radius" is the distance from the center of the cell to the center of the dried droplet. The "Radius" is the radius of the dried droplet. "R_{cell}" is the radius of the round-shaped L929 rat fibroblast cells, which has a value of approximately 10 μm.

Fig. 5.14 shows that the cells are most likely to be located near the center, with clear reduction in cell numbers near the edge. This might be explained if the thin lamella of liquid which is generated by the impact and precedes the spreading, is of similar thickness as the cells. This is likely to occur in our setup, as the Reynolds number of the impacts $Re = \frac{\rho U_i D}{\mu} \approx 170$, suggesting a weak lamella traveling along the substrate. Here ρ and μ are respectively the liquid density and dynamic viscosity. U_i and D are the impact velocity and droplet diameter.

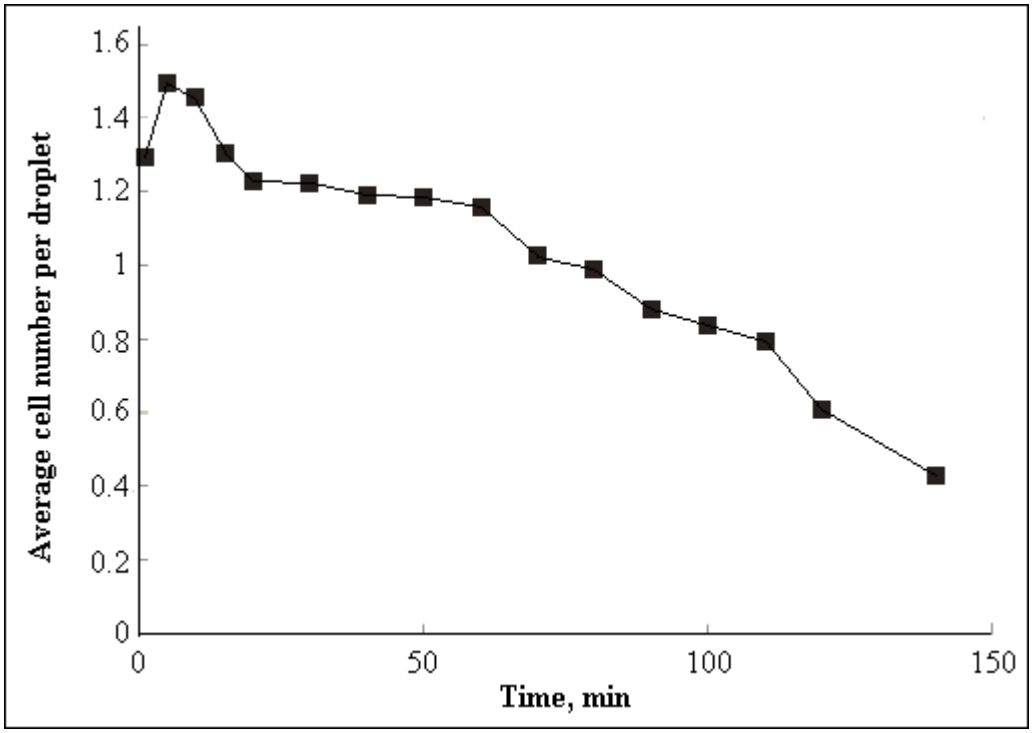

Fig. 5.15: Graph showing the average number of cells per droplet vs. time from start of printing. Printing was carried out continuously over a period of 2.5 hours, at 120 Hz driving frequency.

Fig. 5.15 shows the long-time evolution of the average number of cells in each droplet. The cell number is fairly uniform for the first hour and then reduces at approximately a uniform rate, which is probably due to slow coagulating or settling of the cells in the liquid chamber.

5.3.4 Printing Patterns

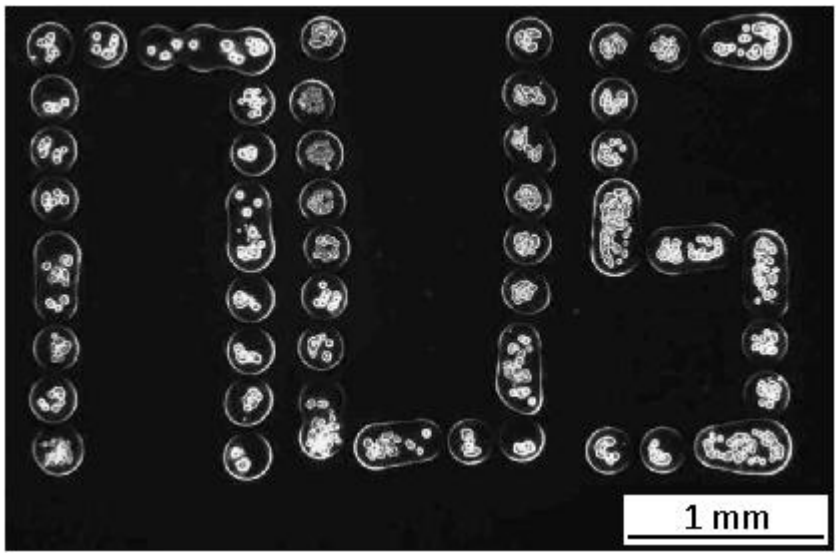

Fig. 5.16: Image showing cells printed onto a dry Petri-dish, forming an "NUS" pattern. Each droplet contains 2 to 6 cells. The orifice diameter of the nozzle used was 60 µm.

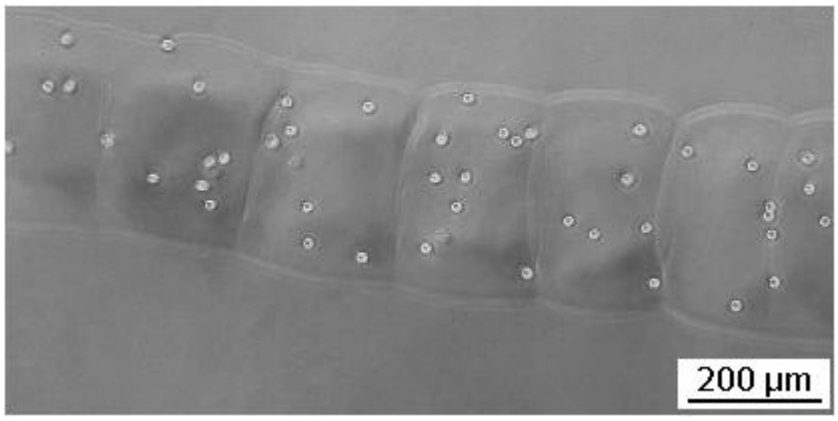

Fig. 5.17: Image showing a continuous line of overlapping droplets with around 6 to 8 cells per droplet in the crosslinked gel. The orifice diameter of the nozzle used was 60 µm.

For the printing of cell patterns, a manual micro-meter x-y-stage is used, for a proof-of-concept demonstration. Fig. 5.16 shows cells fired onto a dry Petri-dish through a 60 µm orifice, forming an "NUS" pattern. Using the manually operated stage and single-drop printing the formation of this entire pattern took about 5 min. As a result, most of the droplets dried up during the printing, leaving only dead cells (due to dehydration) inside the dried outline of the droplets. A viable substrate is necessary in order to maintain suitable moisture

to prevent cell death from dehydration. Fig. 5.17 shows the printed cells inside the crosslinked gel made from 1.0% (w/v) alginate and 0.5% (w/v) calcium chloride. (Alginate was coated onto a well-plate before printing, while calcium chloride was mixed within the cell ink). The overlapping droplets form a continuous straight edged line. It was subsequently found that fibroblast cells retained their spherical shape rather than extending filopodia, which meant that the cells failed to adhere to the alginate. The same result has also been reported by Kuo *et al.* [183].

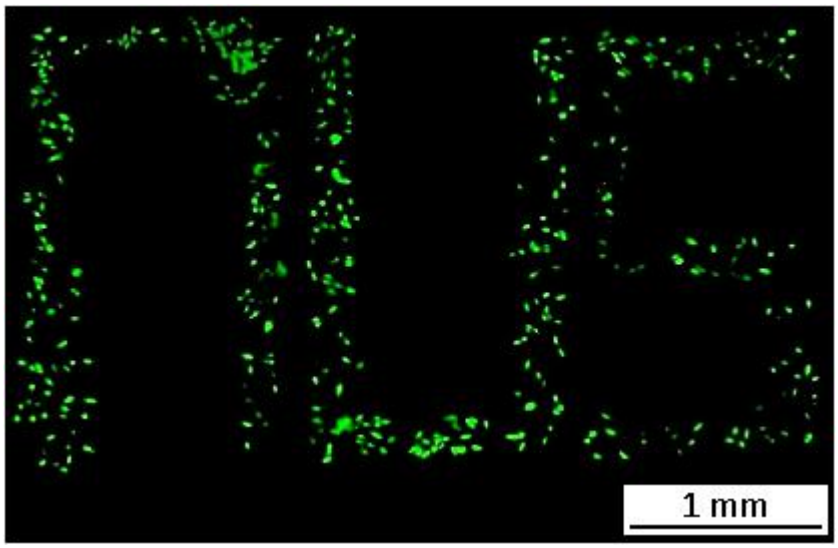

Fig. 5.18: Image showing live cells printed onto a collagen gel, forming an "NUS" pattern. The orifice diameter of the nozzle used was 60 μm. Picture taken 5 day after printing.

In Fig. 5.18, the same "NUS" pattern was created by dispensing the cells onto a collagen gel. Printed cells were immediately placed into an incubator. 1 hour following the printing, fresh medium was added into the well plates. The samples were transferred into the incubator again and observed under microscope at intervals. After 5 days, Live/Dead assay was applied to the samples. A bright green fluorescence was observed after incubation for 30 min. The cells were shown to survive after printing, adhere to the gel, spread and proliferate, forming a denser pattern. It is worth noting that the cells were

slightly moved from their initial position, perhaps caused by the addition of the fresh medium, thereby slightly reducing the resolution of the printing.

5.5 Conclusions

The study has demonstrated that piezoelectric DOD inkjet printing is able to successfully deliver L929 rat fibroblast cells through nozzles as small as 36 μm. There was no significant cell death when dispensing the cells through the 81 μm and the 119 μm nozzle, with the mean survival rates only reducing from 98% to 85%. This is in good agreement with the study of Saunders *et al.* [9], in which a commercial printer was used to print human fibroblast cells.

When the orifice was reduced to 36 μm, the corresponding cell survival rates fell from 95% to 76% when the excitation pulse amplitude increased from 60 V to 130 V. These results indicate that the droplet ejection out of the nozzle has exerted large shear stresses on the cells and possibly disrupted the cell membrane and killed about 20% of the cells. Mean shear rate was estimated by combining the effects of droplet velocity and orifice diameter and was correlated with the cell survival rate. A large range of mean shear rates from 1.3×10^{4} s^{-1} to 9.2×10^{5} s^{-1} were generated and cell survival rates were found to be strongly affected by the higher mean shear rates, especially when the shear rate exceeds 5×10^{5} s^{-1}.

The distribution of the number of cells within each droplet was also investigated. This was done to find the minimal cell concentration in the medium, which is required to avoid the appearance of empty droplets, since

droplets containing no cells may be detrimental to pattern printing. The distribution of cell numbers is found to have a binomial form, which consistent with a uniform distribution of cells inside the medium in the reservoir.

For pattern printing, L929 fibroblast cells were delivered by using a 60 μm nozzle. Printed cells successfully kept their patterns in the crosslinked gel made from 1.0% (w/v) alginate and 0.5% (w/v) calcium chloride. However, it was found that the cells failed to adhere to alginate. On the other hand, cells dispensed onto collagen gel were found to successfully maintain their viability, adhere to the gel, spread and proliferate, forming a denser pattern. However, unlike the crosslinked calcium-alginate which can immobilize cells quite rapidly, cell adhesion to collagen needs a relatively long time to get established. Therefore, some of the printed cells were slightly moved from their initial position when the sample was disturbed, by the addition of fresh medium or unintended shaking of the sample, which will reduce the resolution of the printing. The smallest nozzle, with orifice diameter of 36 μm, was not used for pattern printing, due to issues concerning the reliability of the printing process, as it can easily get clogged.

Future studies should involve experiment with more mammalian cell types. It is also of interest to check whether adding ligands or collagen into alginate (before the crosslinking reactions) will promote cell adhesion onto the substrate. If this can be successfully implemented, the accuracy of the pattern printing will be significantly improved.

6. RECOMMENDATIONS FOR FUTURE WORK

6.1 Printhead Design

As a manufacturing tool, high speed jetting is required to increase productivity of inkjet printing technology. For a specific printhead, its maximum jetting frequency is mainly depended on the construction of the printhead as well as the driving signal. Typical DOD printheads generate droplets at rates in the range 0.1-10 kHz. While the maximum jetting frequency for our in-house-developed printhead is only 3.6 kHz. Furthermore, our printhead has a relatively lower threshold frequency, above which jetting frequency starts to have great effects on droplet velocity and droplet diameter. This threshold frequency is also mainly determined by the construction of the prinhtead. Thus future work should include a systematic study of the relationship between this threshold frequency and printhead construction, to optimize the printhead design, which includes parameters such as the piezo-ceramic material, the dimensions of the piezo-element, the dimensions of the printhead chamber, the nozzle profile, *etc.*.

The dispensing of relatively high concentration of sodium alginate solutions shows that the printing behavior of non-Newtonian liquid is distinctly different from that of Newtonian liquids. Thus more experiments need to be carried out

to investigate the characteristics of our printhead for printing non-Newtonian liquids or even particle-laden liquids.

6.2 Reducing Droplet Size

The results in Chapter 3 show that by carefully control the driving signal, fine jets can be produced with a relatively bigger nozzle size. The results show the possibility of reducing droplet size (or improving printing resolution) without reducing nozzle size. However, the repeatability of the method is still far from perfect. It is interesting to find out whether the repeatability of the generation of such fine jet will be improved by adopting different nozzle profiles. Furthermore, current experiments are collected only from the printing of Newtonian liquids; more experiments also need to be carried out to investigate the generation of fine jets with non-Newtonian liquids.

6.3 Cell Printing

To fully understand the long-term effects of stress forces on cell viability, more experiments need to be carried out to collect quantitative data for cell adhesion, cell spreading and cell migration, and cell proliferation. It is also of interesting to compare our cell viability results with cells in other fluidic systems, under similar shear stress forces. Future studies could also involve experiment with more mammalian cell types. It is also of interest to check whether adding ligands or collagen into the alginate (before the crosslinking reactions) will promote cell adhesion onto the substrate. If this can be

successfully implemented, the accuracy of the pattern printing will be significantly improved.

Bibliography

1. Kyocera Corporation, *website cited:* http://global.kyocera.com/news/2009/0903_kdos.html

2. P. Calvert: "Printing cells", Science, Vol. 318, No. 5848, 2007, pp. 208-209.

3. R. Chang, J. Nam, W. Sun: "Effects of dispensing pressure and nozzle diameter on cell survival from solid freeform fabrication-based direct cell writing", Tissue Engineering Part A, Vol. 14, No. 1, 2008, pp. 41-48.

4. T. Xu, J. Jin, C. Gregory, J. J. Hichman, T. Boland: "Inkjet printing of viable mammalian cells", Biomaterials, Vol. 26, No. 1, 2005, pp. 93-99.

5. T. Xu, S. Petridou, E. H. Lee, E. A. Roth, N. R. Vyavahare, J. J. Hickman, T. Boland: "Construction of high-density bacterial colony arrays and patterns by the ink-jet method", Biotechnology and Bioengineering, Vol. 85, No. 1, 2004, pp. 29-33.

6. C. Y. Chen, J. A. Barron, B. R. Ringeisen: "Cell patterning without chemical surface modification: Cell-cell interactions between printed bovine aortic endothelial cells (BAEC) on a homogeneous cell-adherent hydrogel", Applied Surface Science, Vol. 252, No. 24, 2006, pp. 8641-8645.

7. J. A. Barron, D. B. Krizman, B. R. Ringeisen: "Laser printing of single cells: statistical analysis, cell viability, and stress", Annals of Biomedical Engineering, Vol. 33, No. 2, 2005, pp. 121-130.

8. M. Nakamura, A. Kobayashi, F. Takagi, A. Watanabe, Y. Hiruma, K. Ohuchi, Y. Iwasaki, M. Horie, I. Morita, S. Takatani: "Biocompatible inkjet printing technique for designed seeding of individual living cells", Tissue Engineering, Vol. 11, No. 11-12, 2005, pp. 1658-1666.

9. R. E. Saunders, J. E. Gough, B. Derby: "Delivery of human fibroblast cells by piezoelectric drop-on-demand inkjet printing", Biomaterials, Vol. 29, No. 2, 2008, pp. 193-203.

10. T. Xu, C. A. Gregory, P. Molnar, X. Cui, S. Jalota, S. B. Bhaduri, T. Boland: "Viability and electrophysiology of neural cell structures generated by the inkjet printing method", Biomaterials, Vol. 27, No. 19, 2006, pp. 3580-3588.

11. Cambridge Display Technology, Ltd., *website cited:* http://www.tinhoahoc.com/Semiconductor/IJ-PLED1.pdf

12. B. J. de Gans, P. C. Duineveld, U. S. Schubert: "Inkjet printing of polymers: state of the art and future developments", Advanced Materials, Vol. 16, No. 3, 2004, pp. 203-213.

13. S. E. Molesa: "Ultra-low-cost printed electronics", Ph.D thesis from University of California at Berkeley, 2006.

14. D. H. Redinger: "Solution processing techniques for low-cost circuit fabrication", Ph.D thesis from University of California at Berkeley, 2007.

15. C. W. Sele, T. von Werne, R. H. Friend, H. Sirringhaus: "Lithography-free, self-aligned inkjet printing with sub-hundred-nanometer resolution", Advanced Materials, Vol. 17, No. 8, 2005, pp. 997-1001.

16. D. J. Gundlach, T. N. Jackson, D. G. Schlom, S. F. Nelson: "Solvent-induced phase transition in thermally evaporated pentacene films", Applied Physics Letters, Vol. 74, No. 22, 1999, pp. 3302-3304.

17. J. Perelaer, B. J. de Gans, U. S. Schubert: "Ink-jet printing and microwave sintering of conductive silver tracks", Advanced Materials, Vol. 18, No. 16, 2006, pp. 2101-2104.

18. N. Stutzmann, R. H. Friend, H. Sirringhaus: "Self-aligned, vertical-channel, polymer field-effect transistors", Science, Vol. 299, No. 5614, 2009, pp. 1881-1884.

19. Y. Wang: "Applying drop-on-demand inkjet printing method to maskless lithography", Ph.D thesis from University of California at Berkeley, 2005.

20. H. Sirringhaus, T. Kawase, R. H. Friend, T. Shimoda, M. Inbasekaran, W. Wu, E. P. Woo: "High-resolution inkjet printing of all-polymer transistor circuits", Science, Vol. 290, 2000, pp. 2123-2126.

21. A. U. Chen, O. A. Basaran: "A new method for significantly reducing drop radius without reducing nozzle radius in drop-on-demand drop production", Physics of Fluids, Vol. 14, No. 1, 2002, pp. L1-L4.

22. A. A. Goghari, S. Chandra: "Producing droplets smaller than the nozzle diameter by using a pneumatic drop-on-demand droplet generator", Experiments in Fluids, Vol. 44, No. 1, 2008, pp. 105-114.

23. C. Rensch: "Creation of small microdrops", MicroFab Technologies Inc., Oct 2006.

24. H. Y. Gan, X. Shan, T. Eriksson, B. K. Lok, Y. C. Lam: "Reduction of droplet volume by controlling actuating waveforms in inkjet printing for micro-pattern formation", Journal of micromechanics and microengineering, Vol. 19, 2009, 055010.

25. N. Riefler, T. Wriedt: “Generation of monodisperse micron-sized droplets using free adjustable signals”, Particle & Particle Systems Characterization, Vol. 25, No. 2, 2008, pp. 176-182.

26. H. P. Le: “Progress and Trends in Ink-jet Printing Technology”, Journal of Imaging Science and Technology, Vol. 42, No. 1, 1998, pp. 49-62.

27. L. Rayleigh: “On the instability of jets”, Proceedings of the London Mathematical Society, Vol. 10, No. 4, 1878, pp. 4-13.

28. J. Heinzl, C. H. Hertz: “Ink-jet printing,” Advances in Electronics and Electron Physics, Vol. 65, 1985, pp. 91–171.

29. A. Mikalesen: “Ink jet apparatus and method employing phase change ink”, US Patent No. 4,742,364, 1988.

30. A. Benjeddou: “Shear-mode piezoceramic advanced materials and structures: a state of the art”, Mechanics of Advances Materials and Structures, Vol. 14, No. 4, 2007, pp. 263-275.

31. H. R. Kang: “Water-based ink-jet ink. 3. performances studies”, Journal of Imaging Science, Vol. 35, No. 3, 1991, pp. 195-201.

32. S. C. Chang, J. Liu, J. Bharathan, Y, Yang, J. Onohara, J. Kido: “Multicolor Organic Light-Emitting Diodes Processed by Hybrid Inkjet Printing”, Advanced Materials, Vol. 11, No. 9, 1999, pp. 734-737.

33. M. Singh, H. M. Haverinen, P. Dhagat, G. E. Jabbour: “Inkjet printing - progress and its applications”, Advanced Materials, Vol. 22, 2010, pp. 673-685.

34. R. D. Deegan, O. Bakajin, T. F. Dupont, G. Huber, S. R. Nagel, T. A. Witten: “Capillary flow as the cause of ring stains from dried liquid drops”, Nature, Vol. 389, 1997, pp. 827-829.

35. M. Ikegawa, H. Azuma: “Droplet behaviors on substrates in thin-film formation using ink-jet printing”, JSME International Journal Series B: Fluids and Thermal Engineering, Vol. 47, No. 3, 2004, pp. 490-496.

36. Xaar, *website cited:* http://www.xaar.com/printheads.aspx

37. MicroFab Technologies, Inc., *website cited:* http://www.microfab.com/equipment/systems.html

38. M. A. Groninger, P. G. M. Kruijt, H. Reinten, R. H. Schippers, J. M. M. Simons: “Method of controlling an inkjet printhead, an inkjet printhead suitable for use of said method, and an inkjet printer comprising said printhead”, US Patent 7,357,474, 2008.

39. K. S. Kwon: “Waveform design methods for piezo inkjet dispensers based on measured meniscus motion”, Journal of Microelectromechanical Systems, Vol. 18, No. 5, 2009, pp. 1118-1125.

40. K. S. Kwon, W. Kim: “A waveform design method for high-speed inkjet printing based on self-sensing measurement”, Sensors and Actuators: A, Vol. 140, 2007, pp. 75-83.

41. S. Bruner, D. Xu, C. Phillips: “Drop landing accuracy improvements in inkjet printed OLED displays”, SID Symposium Digest of Technical Papers, Vol. 38, 2007, pp. 1611-1612.

42. M. McDonald: “Manufacture of flat panel displays using piezoelectric drop-on-demand ink jet”, SID Symposium Digest of Technical Papers, Vol. 34, 2003, pp. 1186-1189.

43. T. Shimoda, K. Morii, S. Seki, H. Kiguchi: “Inkjet printing of light-emitting polymer displays”, MRS Bulletin, Vol. 28, 2003, pp. 821-827.

44. R. A. Street, W. S. Wong, S. E. Ready, M. L. Chabinyc, A. C. Arias, S. Limb, A. Salleo, R. Lujan: “Jet printing flexible displays”, Materials Today, Vol. 9, No. 4, 2006, pp. 32-37.

45. J. X. Zhou, J. Y. H. Fuh, H. T. Loh, Y. S. Wong, Y. S. Ng, J. G. Jeffrey, S. J. Chua: “Characterization of drop-on-demand microdroplet printing”, The International Journal of Advanced Manufacturing Technology, Vol. 48, 2010, pp. 243-250.

46. D. Soltman, V. Subramanian: “Inkjet-printed line morphologies and temperature control of the coffee ring effect”, Langmuir, Vol. 24, No. 5, 2008, pp. 2224-2231.

47. P. J. Smith, D. Y. Shin, J. E. Stringer, B. Derby, N. Reis: “Direct ink-jet printing and low temperature conversion of conductive silver patterns”, Journal of Materials Science, Vol. 41, 2006, pp. 4153-4158.

48. J. F. Dijksman: “Hydrodynamics of small tubular pumps”, Journal of Fluid Mechanics, Vol. 139, 1984, pp. 173-191.

49. J. E. Fromm: “Numerical calculation of the fluid dynamics of drop-on-demand jets”, IBM Journal of Research and Development, Vol. 28, No. 3, 1984, pp. 322-333.

50. E. B. Wylie, V. L. Streeter: “Fluid Transients”, New York: McGraw-Hill, 1978.

51. N. Reis, C. Ainsley, B. Derby: “Ink-jet delivery of particle suspensions by piezoelectric droplet ejectors”, Journal of Applied Physics, Vol. 97, 2005, 094903.

52. D. B. Bogy, F. E. Talke: “Experimental and theoretical study of wave propagation phenomena in drop-on-demand ink jet devices”, IBM Journal of Research and Development, Vol. 28, No. 3, 1984, pp. 314-321.

53. H. Wijshoff: “Free surface flow and acousto-elastic interaction in piezo inkjet”, Technical Proceedings of the 2004 NSTI Nanotechnology Conference and Trade Show, Vol. 2, 2004, 215-218.

54. H. C. Wu, H. J. Lin, W. S. Hwang: “A numerical study of the effect of operating parameters on drop formation in a squeeze mode inkjet device”, Modelling and Simulation in Materials Science and Engineering, Vol. 13, 2005, pp. 17-34.

55. H. C. Wu, T. R. Shan, W. S. Hwang, H. J. Lin: “Study of micro-droplet behavior for a piezoelectric inkjet printing device using a single pulse voltage pattern”, Materials Transactions, Vol. 45, No. 5, 2004, pp. 1794-1801.

56. R. Li, N. Ashgriz, S. Chandra: “Droplet generation from pulsed micro-jets”, Experimental Thermal and Fluid Science, Vol. 32, No. 8, 2008, pp. 1679-1686.

57. A. S. Yang, W. M. Tsai: “Ejection process simulation for a piezoelectric microdroplet generator”, Transactions of the American Society of Mechanical Engineers, Vol. 128, No. 6, 2006, pp. 1144-1152.

58. Y. Wang, J. Bokor, A. Lee: “Maskless lithography using drop-on-demand inkjet printing method”, Proceedings of SPIE, Vol. 5374, 2004, pp. 628-636.

59. B. J. de Gans, E. Kazancioglu, W. Meyer, U. S. Schubert: “Ink-jet printing polymers and polymer libraries using micropipettes”, Macromolecular Rapid Communications, Vol. 25, No. 1, 2004, pp. 292-296.

60. Microfab Technote 99-03: “Drive waveform effects on ink-jet device performance”, 1999.

61. S. L. Zoltan: “Pulse droplet ejection system”, US Patent 3,683,212, 1974.

62. K. A. M. Seerden, N. Reis, J. R. G. Evans, P. S. Grant, J. W. Halloran, B. Derby: “Ink-jet printing of wax-based alumina suspensions”, Journal of The American Ceramic Society, Vol. 84, No. 11, 2001, pp. 2514-2520.

63. H. Dong, W. W. Carr, J. F. Morris: “An experimental study of drop-on-demand drop formation”, Physics of Fluids, Vol. 18, 2006, 072102.

64. H. Dong, W. W. Carr, J. F. Morris: “Visualization of drop-on-demand inkjet: Drop formation and deposition”, Review of Scientific Instruments, Vol. 77, 2006, 085101.

65. H. J. Shore, G. M. Harrison: "The effect of added polymers on the formation of drops ejected from a nozzle", Physics of Fluids, Vol. 17, 2005, 033104.

66. F. G. Tseng, C. J. Kim, C. M. Ho: "A high-resolution high-frequency monolithic top-shooting microinjector free of satellite drops-Part I: concept, design, and model", Journal of Microelectromechanical Systems, Vol. 11, No. 5, 2002, pp. 427-436.

67. Boston Piezo-Optics Inc, *website cited*: http://bostonpiezooptics.com/?D=6

68. E. R. Lee: "Microdrop generation", London: CRC Press, 2003.

69. D. J. Hayes, D. B. Wallace: "Overview of small holes", Non Traditional Machining Conference, MS89184, Orlando, Florida, November 1989.

70. H. Robert: "Properties of crystalline silicon", London: The Institution of Electrical Engineers, 1999.

71. E. Bassous, H. H. Taub, L. Kuhn: "Ink jet printing nozzle arrays etched in silicon", Applied Physics Letters, Vol. 31, No. 2, 1977, pp. 135-137.

72. L. Kuhn, E. Bassous, R. Lane: "Silicon charge electrode array for ink jet printing", IEEE Transactions on Electron Devices, Vol. ED-25, No. 10, 1978, pp. 1257-1260.

73. T. Laurell, L. Wallman, J. Nilsson: "Design and development of a silicon microfabricated flow-through dispenser for on-line picolitre sample handling", Journal of Micromechanics and Micro engineering, Vol. 9, 1999, pp. 369-376.

74. R. F. Service: "Printable electronics that stick around", Science, Vol. 304, No. 5671, 2004, pp. 675.

75. H. E. Katz: "Recent advances in semiconductor performance and printing processes for organic transistor-based electronics", Chemistry of Materials, Vol. 16, No. 23, 2004, pp. 4748-4756.

76. J. A. Rogers, Z. Bao: "Printed plastic electronics and paperlike displays", Journal of Polymer Science: Part A: Polymer Chemistry, Vol. 40, No. 20, 2002, pp. 3327-3334.

77. J. A. Rogers, Z. Bao, K. Baldwin, A. Dodabalapur, B. Crone, V. R. Raju, V. Kuck, H. Katz, K. Amundson, J. Ewing, P. Drzaic: "Paper-like electronic displays: large-area rubber-stamped plastic sheets of electronics and microencapsulated electrophoretic inks", Proceedings of the National Academy of Science of the United States of America, Vol. 98, No. 9, 2001, pp. 4835-4840.

78. T. Sekitani, Y. Noguchi, U. Zschieschang, H. Klauk, T. Someya: "Organic transistors manufactured using inkjet technology with subfemtoliter accuracy", Proceedings of the National Academy of Sciences of the United States of America, Vol. 105, No. 13, 2008, pp. 4976-4980.

79. N. Zhao, M. Chiesa, H. Sirringhaus, Y. Li, Y. Wu, B. Ong: "Self-aligned inkjet printing of highly conducting gold electrodes with submicron resolution", Journal of Applied Physics, Vol. 101, No. 6, 2007, 064513.

80. J. Z. Wang, J. Gu, F. Zenhausern, H. Sirringhaus: "Low-cost fabrication of submicron all polymer field effect transistors", Applied Physics Letters, Vol. 88, No. 13, 2006, 133502.

81. J. Z. Wang, Z. H. Zheng, H. W. Li, W. T. S. Huck, H. Sirringhaus: "Dewetting of conducting polymer inkjet droplets on patterned surfaces", Nature Materials, Vol. 3, No. 3, 2004, pp. 171-176.

82. M. Caironi, E. Gili, T. Sakanoue, X. Cheng, H. Sirringhaus: "High yield, single droplet electrode arrays for nanoscale printed electronics", Acs Nano, Vol. 4, No. 3, 2010, pp. 1451-1456.

83. B. J. de Gans, S. Hoeppener, U. S. Schubert: "Polymer relief microstructures by inkjet etching", Journal of Materials Chemistry, Vol. 17, 2007, pp. 3045-3050.

84. C. Y. Kung, M. D. Barnes, N. Lermer, W. B. Whitten, J. M. Ramsey: "Single-molecule analysis of ultradilute solutions with guided streams of 1-μm water droplets", Applied Optics, Vol. 38, No. 9, 1999, pp. 1481-1487.

85. S. Temple: "Small fast inkdrop emission from a nozzle", 43rd European Study Group with Industry Technical Report, Lancaster University, UK 2002.

86. J. U. Park, M. Hardy, S. J. Kang, K. Barton, K. Adair, D. K. Mukhopadhyay, C. Y. Lee, M. S. Strano, A. G. Alleyne, J. G. Georgiadis, P. M. Ferreira, J. A. Rogers: "High-resolution electrohydrodynamic jet printing", Nature Materials, Vol. 6, No. 10, 2007, pp. 782-789.

87. S. N. Jayasinghe, M. J. Edirisinghe: "Electric-field driven jetting from dielectric liquids", Applied Physics Letters, Vol. 85, No. 18, 2004, pp. 4243-4245.

88. S. N. Jayasinghe, A. N. Qureshi, P. A. M. Eagles: "Electrohydrodynamic jet processing: an advanced electric-field-driven jetting phenomenon for processing living cells", Small, Vol. 2, No. 2, 2006, pp. 216-219.

89. I. Marginean, L. Parvin, L. Heffernan, A. Vertes: "Flexing the electrified meniscus: the birth of a jet in electrosprays", Analytical Chemistry, Vol. 76, No. 14, 2004, pp. 4202-4207.

90. G. Taylor: "Disintegration of water drops in an electric field", Proceedings of the Royal Society of London. Series A, Mathematical and Physical Sciences, Vol. 280, No. 1382, 1964, pp. 383-397.

91. J. F. de la Mora: "The fluid dynamics of Taylor cones", Annual Review of Fluid Mechanics, Vol. 39, 2007, pp. 217-243.

92. H. K. Choi, J. U. Park, O. O. Park, P. M. Ferreira, J. G. Georgiadis, J. A. Rogers: "Scaling laws for jet pulsations associated with high-resolution electrohydrodynamic printing", Applied Physics Letters, Vol. 92, No. 12, 2008, 123109.

93. K. Murata, J. Matsumoto, A. Tezuka, Y. Matsuba, H. Yokoyama: "Super-fine ink-jet printing: toward the minimal manufacturing system", Microsystem Technologies-Micro-and Nanosystems-Information Storage and Processing Systems, Vol. 12, 2005, pp. 2-7.

94. C. H. Chen, D. A. Saville, I. A. Aksay: "Scaling laws for pulsed electrohydrodynamic drop formation", Applied Physics Letters, Vol. 89, No. 12, 2006, 124103.

95. J. L. Li: "On the meniscus deformation when the pulsed voltage is applied", Journal of Electrostatics, Vol. 64, No. 1, 2006, pp. 44-52.

96. J. L. Li: "EHD sprayings induced by the pulsed voltage superimposed to a bias voltage", Journal of Electrostatics, Vol. 65, No. 12, 2007, pp. 750-757.

97. J. L. Li: "On the stability of electrohydrodynamic spraying in the cone-jet mode", Journal of Electrostatics, Vol. 65, No. 4, 2007, pp. 251-255.

98. W. Balachandran, W. Machowski, C. N. Ahmad: "Electrostatic atomization of conducting liquids using AC superimposed on DC fields", IEEE Transactions on Industry Applications, Vol. 30, No. 4, 1994, pp. 850-855.

99. Y. J. Kim, J. S. Lee, S. Y. Kim, S. E. Park, J. Hwang, Y. J. Kim: "Hybrid on demand jetting system for ultra fine droplet based on electrohydrodynamic and piezoelectric actuation", IEEE 22nd International Conference on Micro Electro Mechanical Systems, 2009, pp. 491-494.

100. Y. J. Kim, S. Y. Kim, J. S. Lee, J. Hwang, Y. J. Kim: "On-demand electrohydrodynamic jetting with meniscus control by a piezoelectric actuator for ultra-fine patterns", Journal of Micromechanics and Microengineering, Vol. 19, No. 10, 2009, 107001.

101. H. Yamazoe, T. Tanabe: "Cell micropatterning on an albumin-based substrate using an inkjet printing technique", Journal of Biomedical Materials Research: Part A, Vol. 91A, No. 4, 2009, pp. 1202-1209.

102. Y. Ito: "Surface micropatterning to regulate cell functions", Biomaterials, Vol. 20, No. 23-24, 1999, pp. 2333-2342.

103. S. Takahashi, Y. Tomikawa: "A study of handling of living mammalian cells using a piezoelectric dispensing head", Japanese Journal of Applied Physics, Vol. 42, 2003, pp. 3098-3101.

104. Y. Chisti: "Hydrodynamic damage to animal cells", Critical Reviews in Biotechnology, Vol. 21, No. 2, 2001, pp. 67-110.

105. C. Born, Z. Zhang, M. Alrubeai, C. R. Thomas: "Estimation of disruption of animal cells by laminar shear stress", Biotechnology and Bioengineering, Vol. 40, No. 9, 1992, pp. 1004-1010.

106. Z. Zhang, M. Alrubeai, C. R. Thomas: "Estimation of disruption of animal cells by turbulent capillary flow", Biotechnology and Bioengineering, Vol. 42, No. 8, 1993, pp. 987-993.

107. B. J. H. Zoro, S. Owen, R. A. L. Drake, M. Hoare: "The impact of process stress on suspended anchorage-dependent mammalian cells as an indicator of likely challenges for regenerative medicines", Biotechnology and Bioengineering, Vol. 99, No. 2, 2008, pp. 468-474.

108. R. E. Saunders, J. E. Gough, B. Derby: "Inkjet printing of mammalian primary cells for tissue engineering applications", In: Laurencin CT, Botchwey, EA, editors, Nanoscale Materials Science in Biology and Medicine, Boston: MRS, 2005, pp. 57-62.

109. H. J. Kong, M. K. Smith, D. J. Mooney: "Designing alginate hydrogels to maintain viability of immobilized cells", Biomaterials, Vol. 24, No. 22, 2003, pp. 4023-4029.

110. L. Shapiro, S. Cohen: "Novel alginate sponges for cell culture and transplantation", Biomaterials, Vol. 18, No. 8, 1997, pp. 583-590.

111. G. Klock, A. Pfeffermann, C. Ryser, P. Grohn, B. Kuttler, H. J. Hahn, U. Zimmermann: "Biocompatibility of mannuronic acid-rich alginates", Biomaterials, Vol. 18, No. 10, 1997, pp. 707-713.

112. E. Alsberg, K.W. Anderson, A. Albeiruti, R. T. Franceschi, D. J. Mooney: "Cell-interactive alginate hydrogels for bone tissue engineering", Journal of Dental Research, Vol. 80, No. 11, 2001, pp. 2025-2029.

113. A. D. Augst, H. J. Kong, D. J. Mooney: "Alginate hydrogels as biomaterials", Macromolecular Bioscience, Vol. 6, No. 8, 2006, pp. 623-633.

114. N. E. Fedorovich, J. Alblas, J. R. de Wijn, W. E. Hennink, A. J. Verbout, W. J. A. Dhert: "Hydrogels as extracellular matrices for skeletal tissue engineering: state-of-the-art and novel application in organ printing", Tissue Engineering, Vol. 13, No. 8, 2007, pp. 1905-1925.

115. B. K. Mann, A. T. Tsai, T. Scott-Burden, J. L. West: "Modification of surfaces with cell adhesion peptides alters extracellular matrix deposition", Biomaterials, Vol. 20, No. 23-24, 1999, pp. 2281-2286.

116. S. P. Massia, J. A. Hubbell: "Covalent surface immobilization of Arg-Gly-Asp- and Tyr-Ile-Glv-Ser-Arg-containing peptides to obtain well-defined cell-adhesive substrates", Analytical Biochemistry, Vol. 187, No. 2, 1990, pp. 292-301.

117. K. C. Olbrich, T. T. Andersen, F. A. Blumenstock, R. Bizios: "Surfaces modified with covalently-immobilized adhesive peptides affect fibroblast population motility", Biomaterials, Vol. 17, No. 8, 1996, pp. 759-764.

118. J. A. Rowley, G. Madlambayan, D. J. Mooney: "Alginate hydrogels as synthetic extracellular matrix materials", Biomaterials, Vol. 20, No. 1, 1999, pp. 45-53.

119. M. G. Patino, M. E. Neiders, S. Andreana, B. Noble, R. E. Cohen: "Collagen: an overview", Implant Dentistry, Vol. 11, No. 3, 2002, pp. 280-285.

120. F. H. Silver, G. Pins: "Cell-growth on collagen-a review of tissue engineering using scaffolds containing extracellular-matrix", Journal of Long-Term Effects of Medical Implants, Vol. 2, No. 1, 1992, pp. 67-80.

121. W. Sun: "Computer-aided tissue engineering, Part II", Tutorial Presentation at CAD/CG'05, Hong Kong University of Science and Technology, 2005.

122. R. Landers, U. Hübner, R. Schmelzeisen, R. Mülhaupt: "Rapid prototyping of scaffolds derived from thermoreversible hydrogels and tailored for applications in tissue engineering", Biomaterials, Vol. 23, No. 23, 2002, pp. 4437-4447.

123. W. Y. Yeong, C. K. Chua, K. F. Leong, M. Chandrasekaran: "Rapid prototyping in tissue engineering: challenges and potential", Trends in Biotechnology, Vol. 22, No. 12, 2004, pp. 643-652.

124. B. S. Kim, D. J. Mooney: "Development of biocompatible synthetic extracellular matrices for tissue engineering", Trends in Biotechnology, Vol. 16, No. 5, 1998, pp. 224-230.

125. A. Ovsianikov, M. Gruene, M. Pflaum, L. Koch, F. Maiorana, M. Wilhelmi, A. Haverich, B. Chichkov: "Laser printing of cells into 3D scaffolds", Biofabrication, Vol. 2, No. 1, 2010, 014104.

126. H. Lo, M. S. Ponticiello, K. W. Leong: "Fabrication of controlled release biodegradable foams by phase separation", Tissue Engineering, Vol. 1. No. 1, 1995, pp. 15-28.

127. A. G. Mikos, A. J. Thorsen, L. A. Czerwonka, Y. Bao, R. Langer, D. N. Winslow, J. P. Vacanti: "Preparation and characterization of poly (L-lactic acid) foams", Polymer, Vol. 35, 1994, pp. 1068-1077.

128. D. J. Mooney, D. F. Baldwin, N. P. Suh, J. P. Vacanti, R. Langer: "Novel approach to fabricate porous sponges of poly (D, L-lactic-co-glycolic acid) without the use of organic solvents", Biomaterials, Vol. 17, No. 14, 1996, pp. 1417-1422.

129. K. Whang, C. H. Thomas, K. E. Healy, G. Nuber: "A novel method to fabricate bioabsorbable scaffolds", Polymer, Vol. 36, No. 4, 1995, pp. 837-842.

130. P. X. Ma, R. Y. Zhang: "Microtubular architecture of biodegradable polymer scaffolds", Journal of Biomedical Materials Research, Vol. 56, No. 4, 2001, pp. 469-477.

131. D. W. Hutmacher: "Scaffold design and fabrication technologies for engineering tissues state of the art and future perspectives", Journal of Biomaterials Science, Polymer Edition, Vol. 12, No. 1, 2001, pp. 107-124.

132. R. Landers, R. Mülhaupt: "Desktop manufacturing of complex objects, prototypes and biomedical scaffolds by means of computer-assisted design combined with computer-guided 3D plotting of polymers and reactive oligomers", Macromolecular Materials and Engineering, Vol. 282, No. 1, 2000, pp. 17-21.

133. W. Sun, A. Darling, B. Starly, J. Nam: "Computer-aided tissue engineering: overview, scope and challenges", Biotechnology and Applied Biochemistry, Vol. 39, 2004, pp. 29-47.

134. R. A. Barry, R. F. Shepherd, J. N. Hanson, R. G. Nuzzo, P. Wiltzius, J. A. Lewis: "Direct-write assembly of 3D hydrogel scaffolds for guided cell growth", Advanced Materials, Vol. 21, No. 23, 2009, pp. 2407-2410.

135. T. Boland, X. Tao, B. J. Damon, B. Manley, P. Kesari, S. Jalota, S. Bhaduri: "Drop-on-demand printing of cells and materials for designer tissue constructs", Materials Science and Engineering C: Biomimetic and Supramolecular Systems, Vol. 27, No. 3, 2007, pp. 372-376.

136. T. Boland, V. Mironov, A. Gutowska, E. A. Roth, R. R. Markwald: "Cell and organ printing 2: fusion of cell aggregates in three-dimensional gels", Anatomical Record Part A: Discoveries in Molecular Cellular and Evolutionary Biology, Vol. 272A, No. 2, 2003, pp. 497-502.

137. V. Mironov, T. Boland, G. Forgacs, R. R. Markwald: "Organ printing: computer-aided jet-based 3D tissue engineering", Trends in Biotechnology, Vol. 21, No. 4, 2003, pp. 157-161.

138. *Website cited*: http://images.google.com.sg/imglanding?q=organ%20printing&imgurl=http://www.newscientist.com/data/images/ns/cms/dn3292/dn3292-2_587.jpg&imgrefurl=http://3d-print.in/%3Fp%3D10&usg=__x2XuY73RdyXWWQpViuXNmmpmDrI=&h=388&w=587&sz=35&hl=en&um=1&itbs=1&tbnid=0j4Vymt6KgiHhM:&tbnh=89&tbnw=135&prev=/images%3Fq%3Dorgan%2Bprinting%26um%3D1%26hl%3Den%26sa%3DN%26rlz%3D1R2ADFA_enSG346%26tbs%3Disch:1&um=1&sa=N&rlz=1R2ADFA_enSG346&tbs=isch:1&start=11#tbnid=0j4Vymt6KgiHhM&start=15

139. S. Moon, S. K. Hasan, Y. S. Song, F. Xu, H. O. Keles, F. Manzur, S. Mikkilineni, J. W. Hong, J. Nagatomi, E. Haeggstrom, A. Khademhosseini, U. Demirci: "Layer by layer three-dimensional tissue epitaxy by cell-laden hydrogel droplets", Tissue Engineering Part C: Methods, Vol. 16, No. 1, 2010, pp. 157-166.

140. E.Q. Li, S.T. Thoroddsen, J.Y.H. Fuh, S.C.H. Thian, Y.S. Wong, H.T. Loh, L. Lu, PET-based piezoelectric squeeze mode microjetting printhead with interchangeable nozzles, Provisional US Patent (2009) Serial No. 61/226781.

141. Y. Nishiyama, M. Nakamura, C. Henmi, K. Yamaguchi, S. Mochizuki, H. Nakagawa, K. Takiura: "Development of a three-dimensional bioprinter: construction of cell supporting structures using hydrogel and state-of-the-art inkjet technology", Journal of Biomechanical Engineering - Transaction of The ASME, Vol. 131, No. 3, 2009, 035001.

142. J. D. Kim, J. S. Choi, B. S. Kim, Y. C. Choi, Y. W. Cho: "Piezoelectric inkjet printing of polymers: stem cell patterning on polymer substrates", Polymer, 2010, article in press.

143. S. Ilkhanizadeh, A. I. Teixeira, O. Hermanson: "Inkjet printing of macromolecules on hydrogels to steer neural stem cell differentiation", Biomaterials, Vol. 28, No. 27, 2007, pp. 3936-3943.

144. E. A. Roth, T. Xu, M. Das, C. Gregory, J. J. Hickman, T. Boland: "Inkjet printing for high-throughput cell patterning", Biomaterials, Vol. 25, No. 17, 2004, pp. 3707-3715.

145. N. E. Sanjana, S. B. Fuller: "A fast flexible ink-jet printing method for patterning dissociated neurons in culture", Journal of Neuroscience Methods, Vol. 136, No. 2, 2004, pp. 151-163.

146. G. M. Whitesides, B. Grzybowski: "Self-assembly at all scales", Science, Vol. 295, No. 5564, 2002, pp. 2418-2421.

147. Z. C. Liu, Y. Su, K. Varahramyan: "Inkjet-printed silver conductors using silver nitrate ink and their electrical contacts with conducting polymers", Thin Solid Films, Vol. 478, No. 1-2, 2005, pp. 275–279.

148. W. Feng, J. Y. H. Fuh, Y. S. Wong: "Development of a drop-on-demand micro dispensing system", Materials Science Forum, Vol. 505-507, 2006, pp. 25-29.

149. B. M. Wu, S. W. Borland, R. A. Giordano, L. G. Cima, E. M. Sachs, M. J. Cima: "Solid free-form fabrication of drug delivery devices", Journal of Controlled Release, Vol. 40, No. 1-2, 1996, pp. 77-87.

150. T. Kawase, T. Shimoda, C. Newsome, H. Sirringhaus, R. H. Friend: "Inkjet printing of polymer thin film transistors", Thin Solid Films, Vol. 438, 2003, pp. 279-287.

151. K. X. Steirer, J. J. Berry, M. O. Reese, M. F. A. M. van Hest, A. Miedaner, M. W. Liberatore, R. T. Collins, D. S. Ginley: "Ultrasonically sprayed and inkjet printed thin film electrodes for organic solar cells", Thin Solid Films, Vol. 517, No. 8, 2009, pp. 2781-2786.

152. D. Xu, V. Sanchez-Romaguera, S. Barbosa, W. Travis, J. de Wit, P. Swan, S. G. Yeates: "Inkjet printing of polymer solutions and the role of chain entanglement", Journal of Materials Chemistry, Vol. 17, No. 46, 2007, pp. 4902-4907.

153. K. C. Fan, J. Y. Chen, C. H. Wang, W. C. Pan: "Development of a drop-on-demand droplet generator for one-drop-fill technology", Sensors and Actuators: A - Physical, Vol. 147, No. 2, 2008, pp. 649-655.

154. J. de Jong, G. de Bruin, H. Reinten, M. van den Berg, H. Wijshoff, M. Versluis, D. Lohse: "Air entrapment in piezo-driven inkjet printheads", Journal of Acoustical Society of America, Vol. 120, No. 3, 2006, pp. 1257-1265.

155. J. de Jong, H. Reinten, H. Wijshoff, M. van den Berg, K. Delescen, R. van Dongen, F. Mugele, M. Versluis, D. Lohse: "Marangoni flow on an inkjet nozzle plate", Applied Physics Letters, Vol. 91, No. 20, 2007, 204102.

156. B. Beulen, J. de Jong, H. Reinten, M. van den Berg, H. Wijshoff, R. van Dongen: "Flows on the nozzle plate of an inkjet printhead", Experiments in Fluids, Vol. 42, No. 2, 2007, pp. 217-224.

157. B. H. Kim, T. G. Kim, T. K. Lee, S. Kim, S. J. Shin, S. J. Kim, S. J. Lee: "Effects of trapped air bubbles on frequency responses of the piezo-driven inkjet printheads and visualization of the bubbles using synchrotron X-ray", Sensors and Actuators A: Physical, Vol. 154, No. 1, 2009, pp. 132-139.

158. S. J. Lee, D. H. Kwon, Y. S. Choi: "Dynamics of entrained air bubbles inside a piezodriven inkjet printhead", Applied Physics Letters, Vol. 95, No. 22, 2009, 221902.

159. J. de Jong, R. Jeurissen, H. Borel, M. van den Berg, H. Wijshoff, H. Reinten, M. Versluis, A. Prosperetti, D. Lohse: "Entrapped air bubbles in piezo-driven inkjet printing: Their effect on the droplet velocity", Physics of Fluids, Vol. 18, No. 12, 2006, 121511.

160. H. Wijshoff: "Structure- and fluid-dynamics in piezo inkjet printheads", Ph.D. Thesis, University of Twente, The Netherlands, 2008.

161. K.S. Kwon: "Methods for detecting air bubble in piezo inkjet dispensers", Sensors and Actuators A: Physical, Vol. 153, 2009, pp. 50-56.

162. A. M. Worthington: "A study of Splashes", Longmans and Green, London, 1908; reprint by Macmillan, Basingstoke, 1963.

163. M. Rein: "Phenomena of liquid drop impact on solid and liquid surfaces," Fluid Dynamics Research, Vol. 12, No. 2, 1993, pp. 61-93.

164. S. T. Thoroddsen, A. Q. Shen: "Granular jets," Physics of Fluids, Vol. 13, No. 1, 2001, pp. 4-6.

165. D. Lohse, R. Bergmann, R. Mikkelsen, C. Zeilstra, D. van der Meer, M. Versluis, K. van der Weele, M. van der Hoef, H. Kuipers: "Impact on soft sand: Void collapse and jet formation," Physical Review Letters, Vol. 93, No. 19, 2004, 198003.

166. J. R. Royer, E. I. Corwin, A. Flior, M.-L. Cordera, M. L. Rivers, P. J. Eng, H. M. Jeager: "Formation of granular jets observed by high-speed x-ray radiography," Nature Physics, Vol. 1, 2005, pp. 164-167.

167. A. Antkowiak, N. Bremond, J. Duplat, S. Le Dizes, E. Villermaux: "Cavity jets", Physics of Fluids, Vol. 19, No. 9, 2007, 091112.

168. A. Antkowiak, N. Bremond, S. Le Dizes, E. Villermaux: "Short-term dynamics of a density interface following an impact", Journal of Fluid Mechanics, Vol. 577, 2007, pp. 241-250.

169. J. O. Marston, S. T. Thoroddsen: "Apex jets from impacting drops", The Journal of Fluid Mechanics, Vol. 614, 2008, pp. 293-302.

170. S. T. Thoroddsen, K. Takehara, T. G. Etoh, C. D. Ohl: "Spray and microjets produced by focusing a laser into a hemispherical drop", Physics of Fluids, Vol. 21, No. 11, 2009, 112101.

171. S. T. Thoroddsen, T. G. Etoh, K. Takehara: "Microjetting from wave focusing on oscillating drops", Physics of Fluids, Vol. 19, No. 5, 2007, 052101.

172. A. L. Yarin: “Drop impact dynamics: Splashing, spreading, receding, bouncing”, Annual Review of Fluid Mechanics, Vol. 38, 2006, pp. 159-192.

173. D. Bartolo, C. Josserand, D. Bonn: “Singular jets and bubbles in drop impact”, Physical Review Letters, Vol. 96, No. 12, 2006, 124501.

174. B. W. Zeff, B. Kleber, J. Fineberg, D. P. Lathrop: “Singularity dynamics in curvature collapse and jet eruption on a fluid surface”, Nature, Vol. 403, No. 6768, 2000, pp. 401-404.

175. M. P. Brenner: “Fluid mechanics - jets from a singular surface”, Nature, Vol. 403, No. 6768, 2000, pp. 377-378.

176. T. G. Etoh, D. Poggemann, G. Kreider, H. Mutoh, A. J. P. Theuwissen, A. Ruckelshausen, Y. Kondo, H. Maruno, K. Takubo, H. Soya, K. Takehara, T. Okinaka, Y. Takano: “An image sensor which captures 100 consecutive frames at 1,000,000 frames/s”, IEEE Transactions on Electron Devices, Vol. 50, No. 1, 2003, pp. 144-151.

177. M. S. Barrow, S. W. J. Brown, P. R. Williams: “Extensional flow of liquid jets formed by bubble collapse in oils under cavitation-generated pressure waves”, Experiments in Fluids, Vol. 36, 2004, pp. 463-472.

178. S. T. Thoroddsen, T. G. Etoh, K. Takehara, N. Ootsuka: “On the coalescence speed of bubbles”, Physics of Fluids, Vol. 17, 2005, 071703.

179. F. H. Zhang, S. T. Thoroddsen: “Satellite generation during bubble coalescence”, Physics of Fluids, Vol. 20, No. 2, 2008, 022104.

180. L. Duchemin, S. Popinet, C. Josserand, S. Zaleski: “Jet formation in bubbles bursting at a free surface”, Physics of Fluids, Vol. 14, No. 9, 2002, pp. 3000-3008.

181. G. K. Batchelor: “An introduction to fluid dynamics”, London: Cambridge University Press, 1967.

182. A. Papoulis: “Probability, random variables, and stochastic processes”, 1st Edition, New York: McGraw-Hill, 1965.

183. C. K. Kuo, P. X. Ma: “Ionically corsslinked alginate hydrogels as scaffolds for tissue engineering: Part 1. Structure, gelation rate and mechanical properties”, Biomaterials, Vol. 22, 2001, pp. 511-521.

Publications

1. E. Q. Li, S. T. Thoroddsen, J. Y. H. Fuh, S. C. H. Thian, Y. S. Wong, H. T. Loh, L. Lu, PET-based piezoelectric squeeze mode microjetting printhead with interchangeable nozzles, Provisional US Patent (2009) Serial No. 61/226781.
2. F. H. Zhang, E. Q. Li, S. T. Thoroddsen: "Satellite formation during coalescence of unequal size drops", Physics Review Letters, Vol. 102, 104502, 2009.
3. E. Q. Li, J. Y. H. Fuh, Y. S. Wong, S. T. Thoroddsen: "Forming a fine jet in inkjet printing", American Physical Society, 62nd Annual Meeting of the APS Division of Fluid Dynamics, November 22-24, 2009.
4. E. Q. Li, Q. Xu, J. Sun, J. Y. H. Fuh, Y. S. Wong, S. T. Thoroddsen: "Design and fabrication of a PET/PTFE-based piezoelectric squeeze mode drop-on-demand inkjet printhead with interchangeable nozzle", Sensors and Actuators A: Physical, article accepted, 2010.
5. E. Q. Li, E. K. Tan, S. T. Thoroddsen: "Piezoelectric Drop-on-Demand Inkjet Printing of Rat Fibroblast Cells: Survivability Study and Pattern Printing", Biotechnology and Bioengineering, 2011. (In Preparation)